High-Sensitivity Silicon Nitride Torque Sensors for Dynamic Torque Magnetometry of Nanomaterials

Inauguraldissertation

zur
Erlangung der Würde eines Doktors der Philosophie
vorgelegt der
Philosophisch-Naturwissenschaftlichen Fakultät
der Universität Basel

von

Mathias Claus

2026

The original document is saved on the University of Basel document server
http://edoc.unibas.ch



© Mathias Claus, 2026. Unless otherwise indicated, this work is licensed under CC BY-NC-SA 4.0. Material reproduced or adapted from previously published sources is excluded from this license. To view a copy of this license, visit https://creativecommons.org/licenses/by-nc-sa/4.0/.

Genehmigt von der Philosophisch-Naturwissenschaftlichen Fakultät
auf Antrag von

Erstbetreuer: Prof. Dr. Martino Poggio

Zweitbetreuerin: Prof. Dr. Ilaria Zardo

Externer Experte: PD Dr. Alexander Eichler

Basel, den 17.02.2026

Prof. Dr. Heiko Schuldt
Dekan

To my parents,
for their support, encouragement and unbroken belief in me.

Contents

1 Introduction **3**

2 Background **7**
2.1 Nanomechanical resonators . . . 7
2.1.1 Mechanical resonance frequency . . . 7
2.1.2 Mechanical dissipation and quality factor . . . 10
2.1.3 Torque sensitivity for a torsional mode . . . 12
2.1.4 Mechanical dissipation mechanisms . . . 12
2.1.5 Phononic band-gap engineering, dissipation dilution, and soft-clamping . . . 15
2.2 Magnetism at the nanoscale . . . 17
2.2.1 Magnetic free energy . . . 18
2.2.2 Magnetism in 2D materials . . . 21
2.2.3 Magnetism in magnetite nanoparticles . . . 22
2.3 Dynamic Torque Magnetometry . . . 23
2.3.1 Experimental setup . . . 23
2.3.2 Theoretical framework . . . 24
2.3.3 Experimental procedure and observables . . . 26
2.3.4 Connecting dynamic torque and magnetization . . . 26

3 Micro- and nanofabrication **29**
3.1 Introduction . . . 29
3.2 Fabrication of torque transducers made from silicon nitride . . . 30
3.2.1 Plasma-enhanced chemical vapor deposition of SiN_x . . . 31
3.2.2 Patterning the SiN_x mask layer . . . 32
3.2.3 Si wet etching using the SiN_x mask layer as etch mask . . . 33
3.2.4 Patterning the SiN_x device layer . . . 35
3.2.5 Suspending the SiN_x device layer . . . 35
3.2.6 Attachment of magnetic sample . . . 36
3.2.7 Reshaping the SiN_x transducer by gallium FIB milling . . . 36
3.2.8 Torque transducer designs . . . 36
3.3 Preparation of few-layer samples from vdW materials . . . 37
3.3.1 Exfoliation from bulk vdW crystal . . . 37
3.3.2 Isolation of flakes . . . 39
3.3.3 Protection of vdW materials . . . 39
3.4 Results . . . 43
3.4.1 Standalone torsional paddles . . . 43
3.4.2 Torsional paddles embedded in a PnC . . . 44
3.4.3 Few-layer samples from vdW materials . . . 46
3.5 Discussion . . . 46

4 Mechanical characterization of torque transducers **49**
4.1 Introduction . . . 49

4.2 Characterization procedure . . . 49
4.3 Results . . . 50
4.3.1 Mechanical properties of torsion paddle 1 . . . 50
4.3.2 Torque sensitivity and mechanical properties of torsion paddles 1 and 2 . . . 51
4.3.3 Dynamic torque magnetometry with torsion paddles 1 and 2 . . . 53
4.3.4 Mechanical properties of PnC paddle 1 . . . 55
4.3.5 Mechanical properties of PnC paddle 2 . . . 57
4.3.6 Torque sensitivity and mechanical dissipation of PnC paddle 2 . . . 59
4.3.7 Dynamic torque magnetometry with PnC paddle 2 . . . 60
4.3.8 Mechanical properties of PnC beam 1 . . . 60
4.4 Discussion . . . 63

5 Magnetic properties of an individual *Magnetospirillum gryphiswaldense* cell 65
5.1 Summary . . . 65
5.2 Introduction . . . 65
5.3 Dynamic cantilever magnetometry . . . 66
5.4 Data acquisition and processing . . . 67
5.5 Sample preparation and cantilever properties . . . 67
5.6 Measurements . . . 68
5.7 Magnetosome chain . . . 69
5.7.1 Structural model . . . 69
5.7.2 Micromagnetic model . . . 70
5.8 Results . . . 71
5.9 Discussion . . . 74

6 Conclusions and Outlook 75

Appendices 77

A Supplemental material: Micro- and nanofabrication 77
A.1 Fabrication details . . . 77
A.1.1 Protocol: Torsion paddles 1 and 2 . . . 77
A.1.2 Protocols: PnC devices . . . 79
A.2 Determination of SiN_x thickness after device fabrication . . . 84
A.3 Original micrographs prior to cosmetic editing . . . 85

B Supplemental material: Mechanical characterization of torque transducers 87
B.1 Ring-down measurements . . . 87
B.1.1 Torsion paddles 1 and 2 . . . 87
B.1.2 PnC paddle 2 . . . 90
B.2 Temperature-weighted drift correction . . . 91

C Supplemental material: Magnetic properties of a single *M. gryphiswaldense* cell 93
C.1 List of magnetosomes . . . 93
C.2 Transmission electron microscopy images of magnetosomes . . . 94

Bibliography 97

Acknowledgements 111

List of publications 113

1

Introduction

Over the past half-century, information technology has become the infrastructure of technological innovation across disciplines.[1,2] It has enabled unprecedented progress in fundamental and applied research, driving development of cutting-edge technologies as well as many of the everyday conveniences that characterize modern life—most recently complemented by the emergence of powerful AI tools.[2–4] The world's first program-controlled digital computer, the Z3, was conceptually developed by Konrad Zuse, and realized in the year 1941, however, the electromechanical architecture was large, power-hungry, and very slow.[5–8] The subsequent development of the point-contact transistor by Bardeen and Brattain at Bell Labs in 1948 marked a key inflection point toward modern computing, providing a compact solid-state switch and amplifier that enabled scalable electronic logic.[9,10] Although early transistorized computers delivered substantial gains in scaling, energy-efficiency, and a clock-speed increase of many orders of magnitude, these machines remained relatively large.[11,12] The key milestone enabling dense, energy-efficient logic for small-form-factor integrated circuits in the modern sense was catalyzed by the development of the MOSFET (metal–oxide–semiconductor field-effect transistor) by Atalla and Kahng at Bell Labs in 1959.[13–16]

Since then, advances in manufacturing have steadily pushed transistor scaling closer toward fundamental physical limits in pursuit of Moore's "law".[17–21] At today's dimensions and integration densities, high-speed operation is increasingly constrained by power dissipation and thermal management, and also by signal integrity.[22–24] Heat generation arises primarily from dynamic charging and discharging of gate and interconnect capacitances, as well as from leakage and resistive losses.[25,26] Moreover, parasitic coupling between neighboring devices and interconnects leads to crosstalk and cell-to-cell interference in dense logic and memory.[27–29] These effects limit reliable high-speed operation and motivate device concepts that reduce energy consumption, mitigate heating, and improve scalability at high packing density by reducing cross-talk.

Taken together, these power, thermal, and signal-integrity constraints increasingly limit further gains from conventional charge-based scaling, especially as the energy cost and latency of moving data between memory and compute also become system-level bottlenecks.[30,31] This drives interest in architectures that co-locate memory and logic and utilize alternative state variables such as electron spin.[32–34] In this context, atomically thin magnetic two-dimensional (2D) materials are promising building blocks for scalable, non-volatile spintronic functionality, while their van der Waals (vdW) nature enables layer-by-layer assembly into three-dimensional vertical stacks with ultrathin active regions.[35–37] Furthermore, stacking dissimilar 2D crystals into vdW heterostructures provides a modular route to combine electronic, optical, and magnetic functionalities within a single device element, allowing the properties of each constituent to be leveraged and thereby strongly motivating exploration of 2D materials, vdW heterostructures, and in particular the control of magnetism in the 2D limit.[37–40]

Magnetism in 2D materials is commonly characterized using a complementary set of experimental

platforms.[35,36,41] Bulk vibrating SQUID magnetometry (SQUID-VSM) measures sample-averaged magnetization as a function of field and temperature, enabling extraction of hysteresis parameters and magnetic ordering temperatures.[42,43] Magneto-optical probes such as Kerr rotation (MOKE),[44–46] magnetic circular dichroism (MCD),[46,47] among others, provide sensitive optical readout of magnetic order and, in microscopic implementations, domain-resolved imaging.[48] In device geometries, electrical transport—most notably the anomalous Hall effect and magnetoresistance—connect magnetic switching to an electrical signal.[49,50] To resolve spatial inhomogeneity and magnetic microstructure, local scanning-probe techniques—in particular scanning NV-magnetometry (SNVM),[46,51,52] scanning SQUID microscopy (SOT[53–57]/SOL[58–60]), and (nanowire) magnetic force microscopy ((NW)-MFM)[61–66]—are widely used to image domains, stray fields, and emergent textures.[67]

Dynamic torque magnetometry—best known as dynamic cantilever magnetometry (DCM)—is broadband and can access both magnetostatic effects and magnetization dynamics, including spin resonance and relaxation processes.[68–71] It offers excellent sensitivity for probing hysteresis, anisotropy energy, and phase transitions, and is particularly suited for the investigation of nanometer-scale magnets as has been demonstrated for nanowires,[72] nanotubes,[70,73,74] thin films,[75] and mesocrystals.[76] In 2D systems, however, the magnetic volume becomes vanishingly small, such that signal-to-background constraints—and the need for accurate quantitative extraction of these properties—motivate the development of improved micro- and nanomechanical resonators for ultrasensitive dynamic torque measurements.

For a nanomechanical resonator, the smallest detectable torque in a thermomechanically limited measurement is set by its geometry (inertia and stiffness), mechanical dissipation, and temperature.[77] The noise floor is set by two fundamental effects: thermal fluctuations, which randomly perturb the resonator motion, and mechanical losses, which drain vibrational energy and limit how sharply the device responds.[78,79] Because these thermal fluctuations and dissipative losses are inherently linked, reducing mechanical losses directly improves sensitivity. Therefore, sensitivity of a mechanical transducer can be improved by reducing its size and defect-density, and by suppressing radiation of elastic energy to the surrounding substrate via the supports.[77,80,81] A particularly effective strategy to prevent acoustic radiation of energy is to embed the resonator in a phononic crystal (PnC)—a microstructured region engineered to inhibit the propagation of elastic waves in a targeted frequency range—thereby providing strong acoustic isolation and enhancing the resonator's quality factor.[82–85] Importantly, the PnC architecture incorporates the possibility to integrate electrical contacts to the sample, a capability which has been challenging with the most sensitive cantilever-based torque transducers used in DCM.[86] Together, improved mechanical sensitivity and the ability to electrically contact the sample are envisioned to enable a broad range of new experiments, including the detection of superconducting and magnetic phase transitions in atomically thin 2D crystals and vdW heterostructures.[39,87,88]

In this thesis, we develop, fabricate, and characterize nanomechanical torsional and flexural resonators based on non-stoichiometric amorphous silicon nitride. By reducing the resonator dimensions and embedding the devices as defect modes within a PnC structure, we aim to suppress mechanical dissipation and thereby address key challenges in ultrasensitive torque sensing of vdW crystal in the 2D limit.

This thesis is structured as follows:

Chapter 2 introduces the background relevant to this thesis. It begins by outlining the theoretical concepts that govern the mechanical properties of micro- and nanomechanical resonators, then introduces magnetism at the nanoscale, and concludes by describing dynamic torque magnetometry as a probe for nanomagnets.

Chapter 3 describes the design and fabrication of torque transducers, including plain torsional resonators in unstructured membranes as well as torsional and flexural resonators embedded in PnC patterned membranes. Simulations are used to optimize the PnC and defect design such that the fundamental defect-mode resonances lie within the phononic band gap. In addition, we employ the widely used micromechanical cleavage method to exfoliate magnetic 2D materials, establishing in our

group first-hand experience with the fabrication of ultrathin, air-sensitive samples near the ultimate 2D limit, including few-layer flakes down to the bilayer.

Chapter 4 present the characterization of the mechanical properties of the fabricated transducers, and assesses their dynamic torque sensing performance using our custom-built DCM setup. By comparing the dissipation of plain devices with that of devices acoustically isolated by a PnC, we identify the dominant mechanical loss channels that limit the minimal detectable torque.

Chapter 5 demonstrates DCM as a tool to study a single *Magnetospirillum gryphiswaldense* cell to probe the magnetic properties of its nanomagnets. Use a commercially available SiN cantilever, we perform rotation and hysteresis measurements. By combining ultrasensitive torque magnetometry with transmission electron microscopy and micromagnetic simulations, we determine the magnetic moment of an individual bacterium, its saturation magnetization, and its effective easy-axis anisotropy.

Lastly, Chapter 6 concludes by summarizing the results presented in Ch. 3 to 5 and discussing future prospects toward realizing dynamic torque magnetometry of ultrathin magnetic 2D materials and vdW heterostructures.

2

Background

This chapter establishes the physical background for using nanomechanical resonators to probe magnetism in nano- to micrometer-scale magnets. It begins with a description of micro- and nanomechanical resonators in Sec. 2.1, emphasizing the mechanical figures of merit—resonance frequency, dissipation, and quality factor—that ultimately set the torque sensitivity. It then reviews magnetism in nano- to micrometer-sized objects in Sec. 2.2, and concludes by introducing the central ideas of dynamic torque magnetometry in Sec. 2.3, which relates magnetic torque in an applied field to a measurable shift of the resonance frequency.

2.1 Nanomechanical resonators

Mechanical detection of the minute magnetic moment of a micro- or nanoscale magnet requires an ultrasensitive mechanical resonator. As discussed in Sec. 2.3, dynamic torque magnetometry senses magnetic moments by measuring the torque-induced shift of a resonator's eigenfrequency when a magnet is attached to the resonator. This frequency shift is determined by the magnetic torque acting on the magnet–resonator assembly in response to an externally applied magnetic field. Since this thesis focuses on the development and characterization of double-clamped resonators, the following discussion concentrates on this device architecture and on the fundamental mechanical properties that ultimately determine the achievable torque sensitivity.

This section first introduces the key mechanical properties of nanomechanical resonators for magnetic torque sensing: the mechanical resonance frequency in Sec. 2.1.1, the mechanical quality factor Q and dissipation in Sec. 2.1.2, and the thermal torque sensing limit in Sec. 2.1.3. It then discusses mechanical dissipation mechanisms under cryogenic, high-vacuum conditions in Sec. 2.1.4. Finally, more advanced concepts—including phononic-crystal (PnC) engineering, dissipation dilution, and soft clamping—are introduced in Sec. 2.1.5.

2.1.1 Mechanical resonance frequency

Micro- and nanomechanical resonators sustain a discrete set of normal modes whose eigenfrequencies are set by the device geometry, boundary conditions, and material parameters. The fundamental frequency f_0 is the lowest nonzero resonance frequency of the structure and it also sets the baseline for transduction bandwidth and quality-factor engineering in sensing applications.[77,89,90] For cantilevers and double-clamped torsional devices with a central platform, two modal families are especially important: flexural (transverse) bending and torsional twisting about the long axis. In what follows, we derive (i) the fundamental frequency for the torsional mode of a double-clamped beam that carries a central platform, i.e. a torsional paddle, and (ii) the flexural modes of a uniform cantilever.

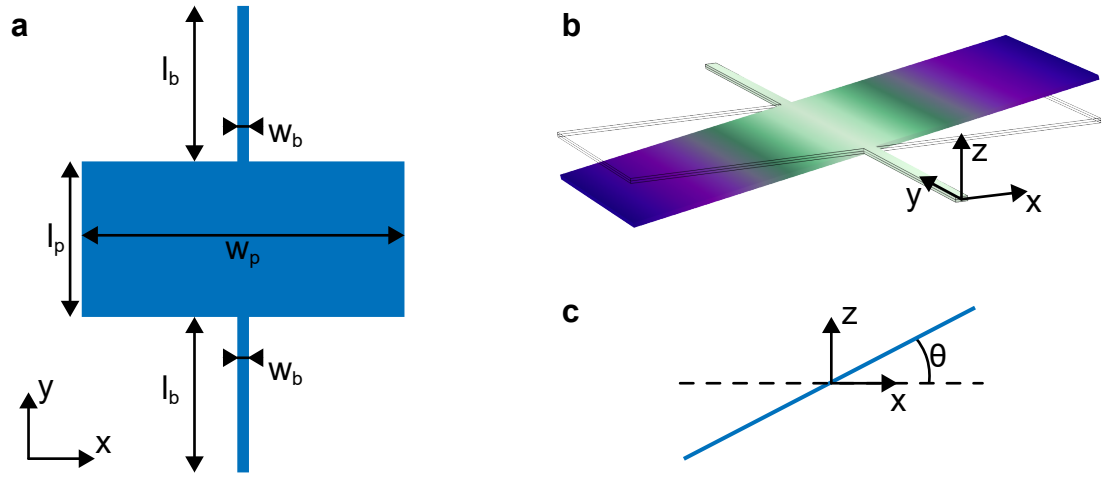


Figure 2.1: A torsional resonator in the shape of a double-clamped torsional paddle. (**a**) Lateral device dimensions. (**b**) 3D model of the fundamental torsional mode of a paddle microbridge. (**c**) Angular displacement of the paddle cross-section at midline ($y = l_\mathrm{b} + l_\mathrm{p}/2$).

Torsional vibration of a paddle resonator

In the continuum description, torsional vibrations of a slender prismatic bar can be formulated in the Saint-Venant framework.[91] This framework provides two important ingredients by which the torsion problem of a solid body can be simplified: (i) The Saint-Venant principle states that, far from the load application region, the stress/strain field generated by two statically equivalent loadings is governed only by the resultant net force and net moment, and not by the detailed traction distribution.[92] (ii) The Saint-Venant bar theory reduces the three-dimensional elasticity problem to a two-dimensional cross-section problem, for example via the Prandtl stress function.[93] For static, linear elastic Saint-Venant torsion, the Prandtl stress function $\phi(x, z)$ is a scalar stress potential defined on the cross-section of area A such that it encodes the shear-stress field, and the net torque follows from $\tau = 2\int_A \phi \, dA$ (for a simply connected cross-section).[92,93] The Saint-Venant torsion constant J_T is a geometric factor that links torque to twist rate along the torsion axis by $\tau = GJ_T\theta'$, and is obtained as $J_T = \frac{2}{G\theta'}\int_A \phi \, dA$. For a uniform bar this leads to the dynamic one-dimensional torsional wave equation

$$\rho I_\mathrm{p} \frac{\partial^2 \theta}{\partial t^2} - GJ_T \frac{\partial^2 \theta}{\partial y^2} = 0, \tag{2.1}$$

where $\theta(y, t)$ is the twist angle, $GJ_T(y)$ the torsional stiffness with G, the shear modulus, and $\rho I_\mathrm{p}(y)$ the polar mass moment of inertia per unit length given by mass density ρ times the polar second moment of area I_p for rotation about the y axis, in accordance with the coordinate system defined in Fig. 2.1.[93,94] For uniform cross-sections, J_T is known in closed form for only a few shapes. For non-uniform or composite cross-sections, and in particular for the torsional paddle geometry with strongly varying and discontinuous width studied in this work, the Saint-Venant problem becomes a piecewise three-dimensional elasticity problem and solving it typically requires numerical or finite-element methods.[95–97] In resonant sensing applications one is, however, almost exclusively interested in the fundamental mode. In that regime, energy methods provide an efficient alternative to solving Eq. (2.1) directly. Castigliano's displacement theorem allows one to compute torsional stiffness from strain energy, while Rayleigh's method yields an approximate fundamental frequency by equating maximum potential and kinetic energies for an assumed mode shape.[91,98] These approaches can be combined into a fully compliant, yet lumped-parameter description of torsion-paddle microresonators.

Consider a torsional paddle microbridge as sketched in Fig. 2.1a which is composed of three beam-like segments with uniform thickness d and spatially varying width $w(y)$, defining the two distally clamped bridge segments and the central suspended paddle. The torsional compliance of a single uniform segment of length l is given by $\int_0^l 1/(GJ_T)\, dy$, i.e., by integrating the local compliance along the segment axis. For a thin rectangular cross-section with $d < w$, the Saint-Venant torsion constant

is well approximated by $J_T \approx wd^3(\frac{1}{3} - 0.63\frac{d}{w})$,[99] and the effective torsional compliance $C_{t,\mathrm{eff}}^{1/2}$ of half a torsional paddle microbridge with length $L/2 = l_\mathrm{b} + l_\mathrm{p}/2$ follows from Castigliano's theorem as[100]

$$C_{t,\mathrm{eff}}^{\mathrm{half}} = \frac{1}{G}\int_0^{L/2} \frac{dy}{J_T(y)} \approx \frac{1}{Gd^3}\left[\frac{1}{0.33w_\mathrm{b} - 0.21d}\int_0^{l_\mathrm{b}} dy + \frac{1}{0.33w_\mathrm{p} - 0.21d}\int_0^{l_\mathrm{p}/2} dy\right]. \tag{2.2}$$

For a complete torsional paddle, the effective torsional stiffness seen at the paddle center is then obtained by combining two lumped half-bridge segments in series leading to[100]

$$k_{t,\mathrm{eff}} = \frac{2}{C_{t,\mathrm{eff}}^{\mathrm{half}}} \approx \frac{4Gd^3(0.33w_b - 0.21d)(0.33w_p - 0.21d)}{0.33(2l_b w_p + l_p w_b) - 0.21d(2l_b + l_p)}. \tag{2.3}$$

To capture the dynamics, the distributed torsional inertia is represented by an energy-equivalent moment of inertia. Imposing harmonic solutions of the form $\Theta(y,t) = \theta(t)q(y)$ with $\theta(t) = e^{-i\omega t}$, the distributed kinetic energy can be related to the lumped model as

$$E_\mathrm{kin} = \frac{1}{2}\int_0^L \rho I_\mathrm{p}(y)\,\dot{\Theta}(y,t)^2\,dy = \frac{1}{2}\dot{\theta}^2\int_0^L \rho I_\mathrm{p}(x)\,q^2(x)\,dy \equiv \frac{1}{2}J_\mathrm{eff}\dot{\theta}^2, \tag{2.4}$$

which defines the effective moment of inertia about the torsional axis, J_eff. Following Lobontiu,[100] $q(y)$ is chosen as a low-order polynomial that satisfies the fixed–fixed boundary conditions and the symmetry of the paddle structure, for example a parabolic shape

$$q(y) = \frac{4y(L-y)}{L^2} \qquad \text{with} \quad 0 \le y \le L = 2l_\mathrm{b} + l_\mathrm{p}, \tag{2.5}$$

which vanishes at the clamps, is smooth, and reaches unity at the center of the paddle. Rayleigh's principle ensures that the fundamental torsional frequency obtained with such an admissible $q(y)$ is an upper bound to the true fundamental frequency of the continuous system.[91,101]

For thin rectangular cross-sections one may write $I_\mathrm{p} = \frac{1}{12}(w^3 d + w d^3)$ which in combination with Eq. (2.4) and (2.5) yields the effective moment of inertia

$$\begin{aligned} J_\mathrm{eff} &= \frac{\rho d}{12}\int_0^L q^2(y)\big[w(y)^3 + w(x)d^2\big]\,dy \\ &= \frac{2\rho d}{45(2l_\mathrm{b} + l_\mathrm{p})^4}\Big[2l_\mathrm{b}^3 w_\mathrm{b}(w_\mathrm{b}^2 + d^2)(16l_\mathrm{b}^2 + 25l_\mathrm{b}l_\mathrm{p} + 10l_\mathrm{p}^2) \\ &\qquad + l_\mathrm{p}w_\mathrm{p}(w_\mathrm{p}^2 + d^2)(30l_\mathrm{b}^4 + 60l_\mathrm{b}^3 l_\mathrm{p} + 40l_\mathrm{b}^2 l_\mathrm{p}^2 + 10l_\mathrm{b}l_\mathrm{p}^3 + l_\mathrm{p}^4)\Big]. \end{aligned} \tag{2.6}$$

Combining the effective stiffness Eq. (2.2) and inertia Eq. (2.6) yields the fundamental torsional angular frequency of a torsional paddle as

$$\omega_{t,0} \approx \sqrt{\frac{k_{t,\mathrm{eff}}}{J_\mathrm{eff}}}, \tag{2.7}$$

which incorporates the full compliance and inertia of both bridge segments and the paddle. This fully compliant, energy-based lumped model provides accurate estimates of the fundamental torsional resonance for typical paddle geometries, without the need to solve the Saint-Venant partial differential equation for torsion Eq. (2.1).

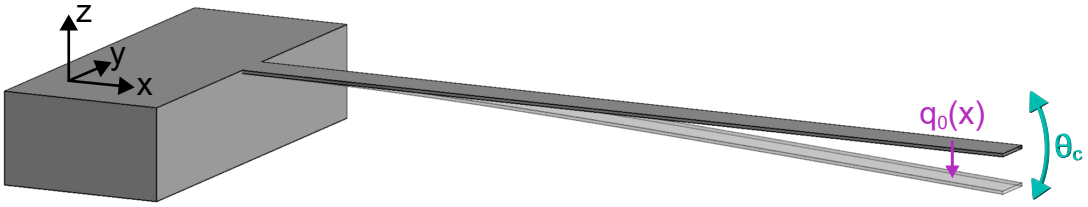


Figure 2.2: A uniform cantilever. Fundamental flexural mode, showing an angular deflection θ_c of the free end and transverse displacement $q_0(x)$ in the z-direction.

Flexural vibration of a cantilever

The flexural dynamics of prismatic beams is governed by the Euler–Bernoulli beam model. For a prismatic beam of length L the flexural displacement $u(x,t)$ obeys

$$EI\,\frac{\partial^4 u(x,t)}{\partial x^4} + \rho A\,\frac{\partial^2 u(x,t)}{\partial t^2} = 0, \tag{2.8}$$

where E is the Young's modulus, I the second moment of area, ρ the mass density, and A the cross-sectional area.[89] The solutions for cantilevers as depicted in Fig. 2.2 are found up to a normalization factor C_n as

$$q_n(x) = C_n\Big[\big(\cosh\beta_n x - \cos\beta_n x\big) - \alpha_n\big(\sinh\beta_n x - \sin\beta_n x\big)\Big], \tag{2.9}$$

with $\beta = \left(\frac{\rho A\,\omega^2}{EI}\right)^{\frac{1}{4}}$ and $\alpha_n = \frac{\cosh\beta_n L + \cos\beta_n L}{\sinh\beta_n L + \sin\beta_n L}$. The characteristic wavenumbers β_n must satisfy

$$\cosh(\beta_n L)\cos(\beta_n L) + 1 = 0 \tag{2.10}$$

which has the first three roots $\beta_n L = \{1.8751,\ 4.6941,\ 7.8548,\ \dots\}$. The corresponding flexural angular eigenfrequencies are

$$\omega_n = \beta_n^2\sqrt{\frac{EI}{\rho A}}\,. \tag{2.11}$$

These standard solutions provide the usual expressions for eigenfrequencies, mode shapes, and derived quantities including effective mass m_{eff} and spring constants. Since the mechanics of cantilevers has been treated extensively in the theoretical and experimental literature, we omit the full derivation and refer the reader to standard references.[77,89,91–93,102]

Damped harmonic oscillator

Once the effective spring parameters have been determined for a given the torsional mode of a double-clamped torsional paddle or a flexural mode of a cantilever, their time-dependent motion can be described using the well-known framework of the classical damped harmonic oscillator according to

$$J_{\text{eff},n}\ddot{\theta}_n(t) + J_{\text{eff},n}\Gamma_{\text{m},n}\dot{\theta}_n(t) + J_{\text{eff},n}\omega_n^2\theta_n(t) = 0\,, \tag{2.12}$$

and

$$m_{\text{eff},n}\ddot{z}_n(t) + m_{\text{eff},n}\Gamma_{\text{m},n}\dot{z}_n(t) + m_{\text{eff},n}\omega_n^2 z_n(t) = 0\,, \tag{2.13}$$

for a torsional and a flexural resonator, respectively, where $\Gamma_{\text{m},n}$ denotes the mechanical damping rate.

2.1.2 Mechanical dissipation and quality factor

Mechanical nano- and micro-resonators are key elements in sensing, signal processing and experiments at the quantum–classical boundary. By putting them in a controlled environment in high-vacuum ($p < 10^{-6}$ mbar) and cryogenic conditions at few kelvin, their performance is often limited not by external noise, but by intrinsic mechanical dissipation that sets the thermal noise floor and bounds

the achievable coherence time.[89, 103] This property is guided by the mechanical damping rate Γ_m of a mechanical resonator and the corresponding quality factor Q.

Quality factor and dissipation

For an under-damped mechanical mode n with angular resonance frequency ω_n, the quality factor Q_n is defined as the ratio of energy stored to the energy lost per oscillation cycle,

$$Q_n \equiv 2\pi \frac{\text{total energy stored}}{\text{energy lost/cycle of mode } n} = 2\pi \frac{U_\mathrm{tot}}{\Delta U_n}, \tag{2.14}$$

where U_tot is the maximum strain energy stored in the mode of an elastic material and ΔU_n is the energy dissipated in one oscillation cycle of mode n.[89, 104] Equivalently, the mode amplitude of a weakly damped resonator decays exponentially as[78, 104]

$$\theta_n(t) \propto e^{-\frac{\Gamma_{\mathrm{m},n} t}{2}} \cos(\omega_n t)\,, \tag{2.15}$$

the stored energy decays as $U(t) \propto e^{-\Gamma_{\mathrm{m},n} t}$, and one finds $Q_n = \frac{\omega_n}{\Gamma_{\mathrm{m},n}}$. In the framework of the parallel loss model, the total quality factor of a mechanical mode can be written as

$$Q_\mathrm{tot}^{-1} = \sum_i Q_i^{-1}\,, \tag{2.16}$$

where $\sum Q_i^{-1}$ collects all dissipative contributions acting on the mechanical resonator.[103]

The quality factor Q_n directly controls the thermal torque noise of the mode. For a linear torsional mode coupled to a thermal bath at finite temperature T, the single-sided thermal torque noise spectral density is[78, 103]

$$S_{\tau\tau,n}^\mathrm{th} = 4k_\mathrm{B} T J_{\mathrm{eff},n} \Gamma_{\mathrm{m},n} = 4k_\mathrm{B} T J_{\mathrm{eff},n} \frac{\omega_n}{Q_n}. \tag{2.17}$$

Thus, decreasing $\Gamma_{\mathrm{m},n}$ lowers the thermal torque noise floor and thereby improves the minimum detectable torque signal, making high-Q resonators particularly advantageous for sensing[105] and also for approaching the quantum limit.[106–108]

Complex stiffness and mechanical loss angle

Mechanical dissipation can be described by allowing the elastic moduli (or spring constants) to become complex. For a simple mechanical spring element with conservative stiffness κ' and a lossy stiffness κ'', one can formulate the complex shear modulus

$$\kappa^*(\omega) = \kappa'(\omega) + i\,\kappa''(\omega) = \kappa'(\omega)\,[1 + i\,\phi_n(\omega)]\,, \tag{2.18}$$

where $\phi_n(\omega)$ is the mechanical loss angle which quantifies the phase lag between stress and strain in the material under cyclic loading.[109–111] For homogeneous, frequency-independent structural damping, i.e. $\phi_n \ll 1$ the quality factor is simply the inverse of the loss angle following[78, 110]

$$Q_n^{-1} = \frac{\kappa''(\omega)}{\kappa'(\omega)} = \tan(\phi_n) \approx \phi_n\,. \tag{2.19}$$

For extended structures with spatially varying strain, the total modal loss angle is a strain-energy-weighted average of the local loss angle $\phi_n(\mathbf{r})$ which follows

$$\phi_{\mathrm{tot},n} = \frac{\int \phi_n(\mathbf{r})\, u_{\mathrm{el},n}(\mathbf{r})\, \mathrm{d}V}{\int u_{\mathrm{el},n}(\mathbf{r})\, \mathrm{d}V}, \tag{2.20}$$

where $u_{\mathrm{el},n}(\mathbf{r})$ is the local elastic energy density.[104, 112] This framework connects localized high-loss regions, as e.g. surfaces, clamps, and coatings to the global quality factor.

2.1.3 Torque sensitivity for a torsional mode

As a mechanical torque transducer is not an isolated system, it couples mechanically to the environment. Despite operation at low temperature of only few Kelvin and in high-vacuum, thermal fluctuations occur. These are caused by phonons which couple from the substrate via the anchors, and to a minor degree by random collisions of gas molecules with the resonator under high-vacuum conditions. Thus, even when the mechanical motion is not actively driven, the torsional paddle is subject to random thermal forces/torques which displace it from the resting position while in thermal equilibrium with a bath at finite temperature T. For a thermally limited classical force or torque sensing experiment, the minimum observable signal is entirely governed by such thermomechanical noise. In-depth discussions of mechanical force and torque detection—including mechanical susceptibility, thermal force/torque noise, and force/torque sensitivity—can be found in the scientific literature.[77, 102, 113–116]

Adapting these concepts to torque sensing using the fundamental torsional mode, the single-sided torque noise power spectral density (PSD) can be expressed as

$$S_{\tau\tau}^{\mathrm{th}}(\omega) = 4k_B T J_{\mathrm{eff}} \Gamma_{\mathrm{m}} \tag{2.21}$$

where k_B denotes Boltzmann's constant and Γ_{m} represents the mechanical damping rate. Mechanical dissipation is mode-dependent and a function of the mode's frequency ω_n, the effective moment of inertia J_{eff}, and quality factor Q. As a consequence, the measured signal power $P(\omega_d)$ is composed of the torque of interest τ_d and the torque noise according to

$$P(\omega_d) = |\chi(\omega_d)|^2 S_{\tau\tau}^{\mathrm{th}} \cdot \mathrm{BW} + |\chi(\omega_d)|^2 \tau_d^2 \tag{2.22}$$

where $\chi(\omega_d)$ denotes the resonator's mechanical susceptibility to a monochromatic torque signal at frequency ω_d, and BW is the measurement bandwidth centered around ω_d. The standard definition of the signal-to-noise power ratio (SNR) of a torque signal is given by $\mathrm{SNR} = \tau_d^2/(S_{\tau\tau}^{\mathrm{th}} \cdot \mathrm{BW})$. Employing the conventional limit condition for detection of a signal, i.e. $\mathrm{SNR} = 1$, and under the assumption that the SNR is independent of the driving frequency, the minimum detectable torque is

$$\tau_{\mathrm{min,BW}} = \sqrt{S_{\tau\tau}^{\mathrm{th}} \cdot \mathrm{BW}} = \sqrt{4k_B T J_{\mathrm{eff}} \Gamma_{\mathrm{m}} \cdot \mathrm{BW}}\,. \tag{2.23}$$

Correspondingly, a torsional resonator's thermomechanically limited torque sensitivity can be expressed in a generalized form independently from the resolution bandwidth, and thereby, also from the integration time as

$$\tau_{\mathrm{min}} = \sqrt{S_{\tau\tau}^{\mathrm{th}}} = \sqrt{4k_B T J_{\mathrm{eff}} \Gamma_{\mathrm{m}}} = \sqrt{4k_B T J_{\mathrm{eff}} \frac{\omega}{Q}} \tag{2.24}$$

in units of $\mathrm{Nm}/\sqrt{\mathrm{Hz}}$.

2.1.4 Mechanical dissipation mechanisms

Mechanical dissipation in nano- and micro-resonators arises from several types of mechanisms:

(i) Internal (volume and surface) losses

(ii) Clamping/anchor and radiative (phonon-tunneling) losses

(iii) Thermoelastic damping

(iv) Fluidic (gas) damping

(v) Extrinsic losses associated with actuation/readout and surrounding circuitry

(vi) Nonlinear and amplitude-dependent damping

Systematic surveys for NEMS/MEMS consistently find that in high-vacuum and at cryogenic temperatures internal and anchor-related losses dominate, while gas and thermoelastic damping are strongly suppressed.[80, 103, 104, 117] In the following, the loss mechanisms listed above are introduced and their relevance at cryogenic high-vacuum conditions is assessed.

(i) Internal (volume and surface) losses

Bulk internal friction is associated with anelastic relaxation of defects, dislocations, impurities, and phonon–phonon interactions in the resonator material. Classical anelasticity theory (Zener model) describes these processes as ensembles of relaxation modes with characteristic relaxation times τ, leading to frequency- and temperature-dependent loss peaks of the form[89, 110, 111, 118]

$$\phi(\omega) \propto \frac{\omega\tau}{1+(\omega\tau)^2}, \tag{2.25}$$

with ω being the angular frequency. In crystalline materials, phonon–phonon scattering and defect motion dominate at elevated temperatures, whereas at cryogenic temperatures tunneling two-level systems (TLS) and impurity-related processes become important, especially in amorphous or partially disordered materials such as non-stoichiometric SiN.[103, 119]

Nano- and micro-resonators exhibit large surface-to-volume ratios, so dissipation associated with surface oxides, adsorbates, dangling bonds, and near-surface damage Q_{surf}^{-1} can outweigh bulk (volume) losses Q_{vol}^{-1}. Experimentally, the internal loss of thin pre-stressed silicon nitride resonator scales approximately with inverse thickness d and surface loss parameter β according to

$$Q_{\mathrm{int}}^{-1} = Q_{\mathrm{vol}}^{-1} + Q_{\mathrm{surf}}^{-1} \approx Q_{\mathrm{vol}}^{-1} + \frac{1}{\beta d}, \tag{2.26}$$

consistent with a thin lossy surface layer of fixed thickness.[103, 117] For Si_3N_4 resonators, a systematic analysis of beams, strings and membranes showed that surface loss is a ubiquitous limiting mechanism in thin devices with a nearly universal surface-Q proportional to thickness.

At cryogenic temperatures of few kelvin, bulk thermo-activated processes are strongly suppressed, but TLS-related and surface-related losses typically remain significant and often determine the observed quality factor.[103, 104] At cryogenic and high-vacuum conditions, dissipation due to interaction with the environment is strongly suppressed, such that internal, i.e. volume and surface, dissipation is expected to be one of the dominant limitations of Q.

(i) Clamping and radiative losses

Even if the material itself were perfectly elastic, energy can escape through the supports into the substrate as elastic waves known as clamping or anchor loss. In simple terms, the vibrating resonator shakes its anchors, launching phonons into the bulk that do not return.[89, 104]

For nanomechanical beams and strings, the importance of anchor loss depends strongly on geometry (aspect ratio, support shape) and acoustic mismatch between resonator and substrate. Experiments on SiN string and beam resonators show that radiation through the supports can dominate at high frequencies and small aspect ratios, and can be strongly reduced by engineering the clamp geometry.[80, 117, 120, 121]

More generally, clamping loss can be understood in terms of phonon tunneling. Mechanical energy leaks through finite-stiffness supports into a continuum of substrate modes. Efficient numerical methods based on this picture accurately predict design-limited Q and highlight the strong geometric dependence of this loss channel.[121] Phononic band-gap shields and soft-clamping make use of this to suppress support-induced radiation by many orders of magnitude.[84, 120, 122, 123]

Clamping and radiative losses are largely independent of pressure and only weakly dependent on temperature through changes in elastic constants and sound speeds. Therefore, at cryogenic temperatures and in high-vacuum anchor loss is typically the other main competitor to internal loss, unless it is deliberately suppressed by phononic engineering or optimized support design.

(ii) Thermoelastic damping

Thermoelastic damping (TED) arises from the coupling between elastic strain and temperature. As regions under compression heat up, and regions under tension cool down, irreversible heat flow between them dissipates energy.[109–111, 124] For flexural modes of beams and plates, TED can often be described by Zener's model, in which the loss peaks when the thermal diffusion time across the

structure matches the oscillation period.[109,124,125] For many MEMS geometries at room temperature, TED sets an upper bound on achievable Q even for ideal crystalline materials.[104,109] However, TED scales with the thermal expansion coefficient, specific heat and thermal conductivity, all of which change strongly at low temperature. For common resonator materials, as e.g. Si, SiN, and SiO_2, TED decreases rapidly upon cooling and is strongly suppressed at cryogenic temperatures, especially for sub-micron thicknesses where the relevant thermal relaxation times become much shorter than the oscillation period.[104,109]

Hence, when considering cryogenic high-vacuum conditions, TED is expected to be a minor contribution compared to internal and clamping loss, unless a structure is unusually thick or operated at very high frequencies.

(iii) Fluid (gas) damping

Fluid or gas damping arises from viscous and inertial forces exerted by a surrounding gas or liquid. At moderate and high pressures, continuum hydrodynamics (Navier–Stokes) and squeeze-film models describe the interaction, while at low pressures the gas enters the free molecular regime where damping is governed by individual molecules impacting on the resonator.[126–129] For nanomechanical resonators, the gas-limited quality factor scales approximately as $Q_{\mathrm{gas}} \propto 1/p$ in the molecular flow regime and can exceed 10^7–10^8 already at pressures of 10^{-4} – 10^{-5} mbar, depending on geometry and frequency.[127,128] Analytical models based on momentum transfer agree well with experiments and confirm that, once in the deep molecular regime and beyond gas damping is negligible.[126,130] At cryogenic high-vacuum conditions, nano- and micro-resonators are firmly in the free molecular regime, and therefore gas damping is extremely small. This corresponds to gas-limited quality factors far above 10^8, well beyond the range set by internal and clamping losses.[126,128]

(iv) Losses associated with actuation and readout

Additional mechanical dissipation can be introduced by the specific transduction scheme and surrounding structures. This includes:

- Dielectric and electrostatic losses: Motion in inhomogeneous electric fields can dissipate energy via dielectric relaxation or resistive heating in electrodes and wiring.[89,103]
- Magnetomotive and eddy-current damping: In magnetic-field-based actuation, induced currents in conductive elements dissipate energy resistively.[89]
- Optomechanical damping: Strong optical fields can cool or amplify motion via dynamic backaction and absorption-induced heating can introduce additional TED.[84,104]

These mechanisms are highly device-specific and can be relevant irrespective of cryogenic cooling and high-vacuum. However, careful circuit and optical design usually limits their contribution below internal and anchor losses.

(v) Nonlinear and amplitude-dependent dissipation

At large vibration amplitudes many nano- and micro-resonators exhibit nonlinear damping where the effective loss angle ϕ and thus Q depend on oscillation amplitude.[131–134] Proposed microscopic origins include:

- Strain-dependent TLS relaxation and saturation.
- Nonlinear coupling between modes.
- Amplitude-dependent surface defect motion.
- Geometric nonlinearities that enhance strain within lossy regions.

In some low-dimensional resonators such as carbon nanotubes and graphene membranes, nonlinear damping can dominate over linear damping, causing the quality factor to become strongly amplitude dependent.[131,133] Under typical small-displacement conditions used to characterize the linear response, nonlinear damping can be neglected.

2.1.5 Phononic band-gap engineering, dissipation dilution, and soft-clamping

In recent years, three largely complementary design tools have been established to improve the quality factor of nano- and micromechanical resonators:

(i) Acoustic isolation via phononic band gap

(ii) Dissipation dilution via strain engineering

(iii) Soft-clamping of localized modes

In modern ultracoherent nanomechanical devices, all three strategies are applied together: high tensile stress for dissipation dilution, phononic crystal (PnC) structures for acoustic isolation, and soft-clamped defect modes to minimize bending and coupling at the supports. This combination has enabled room-temperature and cryogenic quality factors approaching or exceeding 10^9 in the kHz–MHz range, setting the present benchmark for low-dissipation nano- and micro-mechanical resonators.[83,84,122,123,135–138] In the following, these three concepts for improving the quality factor are briefly introduced.

(i) Acoustic isolation via phononic band gap

Acoustic isolation is a design strategy that specifically targets Q_{clamp}. By surrounding the resonator with a periodic elastic phononic crystal (PnC) whose band structure exhibits a band gap at the mode frequency, vibrational energy is confined to a defect region and cannot propagate into the bulk. As a result, radiation losses are suppressed by many orders of magnitude, strongly enhancing $Q_{\mathrm{clamp}} \to \infty$ in the ideal case and leaving Q_{int} as the dominant limitation. Phonon-tunneling theory and experiments quantitatively showed how support-induced losses depend on geometry, and how phononic engineering can strongly reduce radiation into the substrate.[121] In Si_3N_4 membranes, two-dimensional PnC structures have been used to provide a phononic band gap around the mode frequency, observing that the mechanical lifetime increases exponentially with the number of PnC periods until internal losses become dominant and Q exceeds 10^8 at $\sim$1 MHz at room temperature.[84] Similarly, MacCabe *et al.* realized a GHz nano-acoustic cavity with a one-dimensional phononic band-gap structure and showed that the phonon lifetime grows exponentially with the length of the acoustic shield, reaching ringdown times on the order of seconds and quality factors $\sim 10^{10}$ at $\sim$5 GHz and millikelvin temperature.[83]

For sensing applications that use the fundamental mode, phononic band-gap concepts demand that the band gap must be engineered such that this fundamental mode is either the localized defect mode itself or is supported by tethers embedded in a phononic shield. Such phononic band-gap isolation

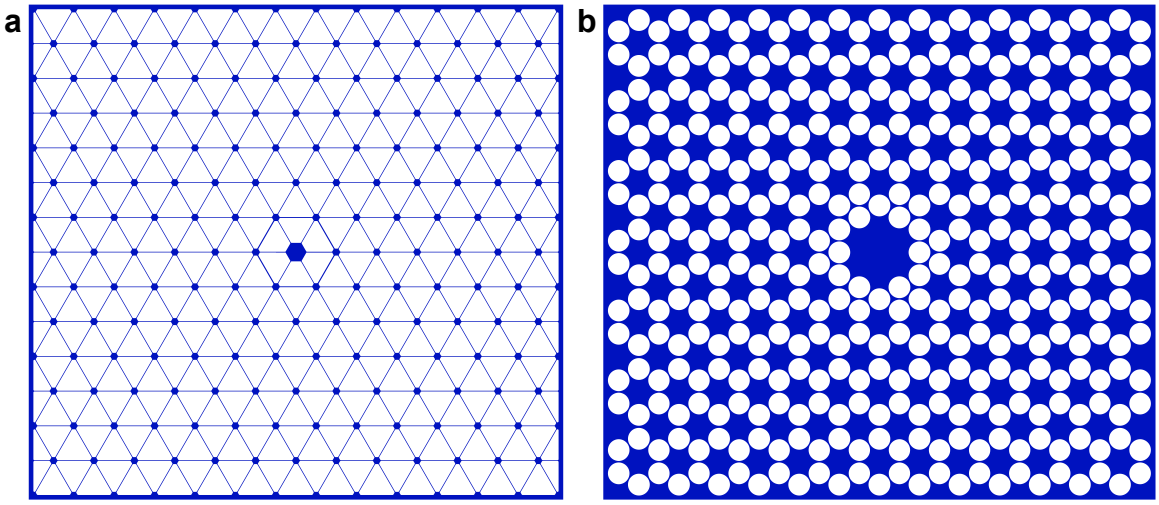


Figure 2.3: 2D PnC structures. Schematics of (**a**) high-contrast and (**b**) low-contrast geometries.

typically requires adding periodic shield structures to the supports or embedding the fundamental mode in a deliberately designed defect region. A comprehensive study of core design principles for making a PnC is reported by Reetz *et al.*,[138] where the 2D PnC is treated as a one-dimensional periodic string with alternating pad and tether segments. This is characterized by a single contrast parameter $V = v_t/v_p$, i.e., the ratio of tether to pad wave speeds in the PnC, which sets the band structure and the band-gap width. Exemplary high- and low-contrast PnC designs are shown in Fig. 2.3. Increasing V widens the phononic band gap and shortens the evanescent decay length of defect modes into the PnC which improves phononic isolation, and thus, the radiation-limited quality factor Q_{rad}. But simultaneously this compresses the mode spatially and increases bending near the defect, which lowers the bending-limited quality factor Q_{bend}. Optimal designs therefore work at an intermediate contrast where the band gap is wide enough to isolate the defect mode but not so wide that soft-clamping is diminished by excessive curvature.

In summary, phononic band-gap engineering improves Q_{clamp} by removing energy radiation to the environment while Q_{int} remains unchanged, and therefore $Q_{\mathrm{tot}} \approx Q_{\mathrm{int}}$ in the ideal limit .

(ii) Dissipation dilution via strain engineering

Instead of blocking energy from leaving through the supports, dissipation dilution reduces the effective loss angle ϕ_{eff} of a given mode by storing a large fraction of its elastic energy in an almost lossless tensile potential. For a strained resonator, one may write

$$\phi_{\mathrm{eff}} = \frac{1}{D_Q}\,\phi_{\mathrm{int}} \quad \Leftrightarrow \quad Q_{\mathrm{eff}} = D_Q\, Q_{\mathrm{int}}, \tag{2.27}$$

where ϕ_{int} is the intrinsic material loss angle and $D_Q \equiv \frac{U_{\mathrm{tot}}}{U_{\mathrm{lossy}}} \geq 1$ is the dilution factor, with U_{tot} the total strain energy and U_{lossy} the energy in lossy degrees of freedom.[84,123,137] High-stress beams and membranes realize large D_Q because the static tensile strain combined with geometric nonlinearity in the stress-strain coupling for a given mode stores a lot of energy without adding dissipation, while the lossy bending strain accounts for only a small fraction of the total energy.

Fedorov *et al.* developed a general theory of dissipation dilution that applies to arbitrary strained resonator geometries and clarified that the lossless potential responsible for dilution arises from the combination of static tension and geometric nonlinearity in the strain-displacement relation.[123] They showed analytically how the dilution factor can be maximized in non-uniform beams via geometric strain engineering, for example by tapering and clamp thinning. Experimentally, nanoscale strain engineering in non-uniform Si_3N_4 nanobeams and membranes has achieved dilution factors of order 10^4 and room-temperature quality factors up to $Q \approx 8 \cdot 10^8$ in the MHz range.[84,137] Beccari *et al.* extended this approach to tensioned crystalline silicon nanostrings, achieving quality factors above 10^{10} at cryogenic temperatures, consistent with extremely strong dissipation dilution in a stoichiometric Si_3N_4.[135] Just recently, the concept has been extended to torsional modes of high-stress Si_3N_4 nanoribbons achieving $Q \approx 10^8$ and torque sensitivities of the order of $10^{-20}\,\mathrm{Nm}/\sqrt{\mathrm{Hz}}$ in the low kHz range.[139–141]

For a uniform double-clamped beam, increasing the film stress improves D_Q through two distinct mechanisms that have different implications for the mechanical damping rate Γ_{m}, which sets the sensitivity limit (Eq. (2.24)): (i) reducing U_{lossy} and (ii) increasing U_{tot}.[123] In the low-stress regime, the beam stiffness is dominated by the material's Young's modulus, so both the resonance frequency ω and the dissipation are essentially independent of stress. With increasing stress, U_{tot} and the resonance frequency rise together and these changes largely cancel, leaving Γ_{m} approximately unchanged. However, the mode shape simultaneously becomes more sinusoidal, concentrating curvature—and thus bending loss—near the clamps. This reduces U_{lossy} and therefore initially lowers Γ_{m}. Once the mode shape asymptotically approaches the sinusoidal limit, this dilution effect saturates; further increases in film stress mainly raise U_{tot}, increasing Q and ω proportionally while leaving Γ_{m} essentially unchanged.

For sensing with the fundamental flexural mode of highly stressed membranes or strings, dissipation dilution is directly applicable and typically provides a large enhancement of Q, because the fundamental

flexural mode stores most of its energy in tension. Therefore, mostly transverse flexural modes—and in some suitably engineered geometries also torsional modes as reported for nanoribbons[141]—exhibit strong dilution, whereas longitudinal/breathing modes do not.[142] Importantly, dissipation dilution does not require a phononic band gap as a uniform highly stressed string or membrane can already exhibit dilution. Conversely, a phononic band-gap device without tension does not exhibit dissipation dilution.

(iii) Soft-clamping of localized modes

Soft-clamping is often realized with phononic band-gap structures, but is conceptually distinct from band-gap-based isolation. In a conventional beam or membrane, the vibrational mode shape typically has large curvature at the rigid supports, which concentrates bending strain near the clamps, and therefore enhances local dissipation and radiation of energy into the substrate. Soft-clamping suppresses this loss channel by shaping the structure—and therefore the mode shape—such that the effective support region of the localized mode is compliant rather than rigid. In this case, the curvature and strain at the boundary of the localized mode are strongly reduced, and the mode decays evanescently into the surrounding structure and the curvature remains small.

Tsaturyan *et al.* introduced soft-clamped defect modes in a two-dimensional Si_3N_4 PnC membrane, where the mode is localized in a central defect cell, but instead of terminating on a rigid frame it extends a few lattice constants into the surrounding PnC. This way, the effective clamping region has low curvature and the clamping loss is substantially reduced.[84] In one-dimensional Si_3N_4 nanobeams, soft-clamping has been realized by patterning a non-uniform phononic crystal beam in which the localized mode has near-zero slope at the physical supports, again strongly reducing bending strain at the clamp.[137] Further soft-clamping has been applied to hierarchical "binary tree" tensile structures, where the fundamental flexural mode itself is soft-clamped by a network of compliant links, yielding $Q \approx 10^9$ at 107 kHz in combination with dissipation dilution, and excellent force sensitivity of $F_{\mathrm{min}} = 10^{-20}\,\mathrm{N}/\sqrt{\mathrm{Hz}}$ at cryogenic temperature.[122] Based on similar hierarchical "fractal-like" string resonators in which the mode shape is soft-clamped at fixed material, size and tensile stress, it has been shown that soft-clamping alone enhances Q of the fundamental mode by up to two orders of magnitude compared to a string with the same dimension and tension.[85]

In many phononic membrane implementations, soft-clamping is realized for higher-order localized defect modes rather than for the fundamental mode of the full membrane. However, as the hierarchical binary-tree and fractal-like structures demonstrate, it is possible to design the fundamental mode of a resonator to be soft-clamped.[85,122] Therefore, soft-clamping can in principle be fully compatible with using the fundamental flexural mode for sensing, provided the overall geometry is tailored for that purpose.

Conceptually, soft-clamping modifies the mode shape and boundary conditions to (i) suppress curvature and therefore internal loss near the supports, and (ii) reduce coupling to substrate modes. In the language of the loss budget, it simultaneously increases Q_{clamp} by shifting elastic energy away from highly lossy clamping regions, but it is not synonymous with either pure band-gap shielding or pure strain engineering.

2.2 Magnetism at the nanoscale

Already in the sixth century BC, Thales of Miletus invoked a "soul" to explain why lodestone (naturally magnetized magnetite) can set iron in motion. Since then, magnetism has become central to modern technology, underpinning applications ranging from electric motors and magnetic-field sensors to non-volatile data storage and spintronic memory. It continues to drive advances as magnetic materials are miniaturized to nanometer dimensions and even the 2D limit. This section introduces the energetic contributions that govern magnetic states in Sec. 2.2.1, surveys magnetism in 2D materials in Sec. 2.2.2, and finally discusses magnetism in magnetite nanoparticles in Sec. 2.2.3 as a representative nanoscale ferrimagnetic system relevant to this thesis.

2.2.1 Magnetic free energy

For a micro- to nanometer-sized permanent magnet, the global magnetization and the underlying micromagnetic configuration are determined by minimizing the sample's total magnetic free energy. In the following we use the term "magnetic energy" for the micromagnetic energy functional, which at fixed temperature plays the role of an effective magnetic free energy. In the standard micromagnetic approximation, this energy is written as the sum of four principal contributions: the Zeeman energy E_{Z}, the exchange energy E_{ex}, the anisotropy energy E_{a}, and the magnetostatic energy E_{ms}. Correspondingly, the total magnetic energy can be expressed as[143,144]

$$E_{\mathrm{tot}} = E_{\mathrm{Z}} + E_{\mathrm{ex}} + E_{\mathrm{ms}} + E_{\mathrm{a}}, \tag{2.28}$$

which can be considered a minimal micromagnetic model. It neglects additional energy terms that are absent or expected to be very small in the systems considered in this work. Depending on the specific material and geometry, this minimal form can be extended on demand in a straightforward way by adding further contributions as for example Dzyaloshinskii–Moriya (DMI), magnetoelastic, or interlayer exchange terms whenever these are known to be relevant. For layered two-dimensional magnets for example, an interlayer exchange (RKKY) coupling term may also be relevant. In the context of dynamic torque magnetometry, the magnetic energy determines both the equilibrium magnetization configuration and the field-dependent magnetic contribution to the effective spring constant as will be discussed in more detail later in Secs. 2.3.2 and 2.3.4. The magnetic energy terms included in Eq. (2.28) are introduced in the following.

Zeeman energy

In the presence of a uniform external magnetic field $\mathbf{H}_{\mathrm{ext}}$, magnetic moments inside a body tend to align with the applied field in order to lower the Zeeman energy. This contribution to the total magnetic energy is given by[143,145,146]

$$E_{\mathrm{Z}} = -\mu_0 \int_V \mathbf{M}(\mathbf{r}) \cdot \mathbf{H}_{\mathrm{ext}}\, dV, \tag{2.29}$$

where $\mathbf{M}(\mathbf{r})$ is the magnetization field and μ_0 denotes the vacuum permeability. Accordingly, the Zeeman energy is minimized when $\mathbf{M}(\mathbf{r})$ is parallel to $\mathbf{H}_{\mathrm{ext}}$.

Exchange energy

In general, the bilinear exchange interaction between localized moments can be decomposed into a symmetric part, which includes the usual Heisenberg exchange, and an antisymmetric part, which guides the Dzyaloshinskii–Moriya interaction (DMI).[143,145,147] The symmetric part is responsible for ferromagnetic (FM), ferrimagnetic (FiM), and antiferromagnetic (AFM) order, depending on the sign and spatial pattern of the exchange constant. The antisymmetric part is the DMI, which tends to cant neighboring moments and can favor approximately perpendicular alignment with a fixed chirality. In the following, the discussion is restricted to the more common and often dominant symmetric case, in which the exchange energy is minimized when neighboring moments are aligned parallel or antiparallel, depending on the sign of the exchange constant.

For most materials there is no simple analytical expression for the Heisenberg exchange integral J_{ij}, which quantifies the coupling strength between moments on sites i and j. In practice, J_{ij} is therefore treated as a phenomenological parameter that is determined either from experiment or from first-principles electronic-structure (DFT) calculations. Qualitatively, the exchange energy is an effective interaction between neighboring electron spins that arises from the combination of Coulomb repulsion and the Pauli exclusion principle. In the Heisenberg model it is written as[143,147,148]

$$E_{\mathrm{ex}} = -2 \sum_{i,j} J_{ij}\, \mathbf{S}_i \cdot \mathbf{S}_j, \tag{2.30}$$

where $\mathbf{S}_i$ and $\mathbf{S}_j$ denote the dimensionless total spin of the localized moments on atoms i and j,

respectively. For $J_{ij} > 0$ the ground state favors parallel alignment of neighboring spins, i.e. FM ordering, while for $J_{ij} < 0$ an AFM arrangement with antiparallel neighboring spins is obtained. For direct and superexchange in insulating magnets the magnitude of J_{ij} decreases rapidly with increasing distance, so that only nearest, and sometimes also next-nearest, neighbors contribute significantly. In metallic systems, longer-range indirect (RKKY-type) exchange can also play a role, but the Heisenberg interaction itself remains intrinsically short-ranged. It is worth noting that the isotropic Heisenberg term does not encode any globally preferred direction for the magnetization: a uniform rotation of all spins leaves E_{ex} unchanged.

Treating the magnetic specimen as a continuous medium and assuming that the magnetization magnitude is spatially uniform, a continuous magnetization vector field can be defined as $\mathbf{M}(\mathbf{r}) \equiv M_{\mathrm{s}}\,\hat{\mathbf{m}}(\mathbf{r})$ with $|\hat{\mathbf{m}}(\mathbf{r})| = 1$. In this micromagnetic continuum approximation the symmetric exchange interaction then takes the form[143,145–147]

$$E_{\mathrm{ex}} = A_{\mathrm{ex}} \int \left[\nabla \hat{\mathbf{m}}(\mathbf{r})\right]^2 dV, \tag{2.31}$$

where A_{ex} is the exchange stiffness, a continuum material parameter with units of energy per unit length that measures the energy cost of spatial non-uniformity of the magnetization, and $M_{\mathrm{s}}(T)$ is the temperature-dependent saturation magnetization. For a FM or FiM material, the Curie temperature T_C is the temperature above which spontaneous magnetic order disappears in the absence of an external field. In analogy, the Néel temperature T_N is the temperature at which spontaneous magnetic order is suppressed in AFM matter.

Magnetostatic energy

The magnetostatic (dipolar) energy describes the energy associated with the magnetic field generated by the magnetization itself. It is long-ranged and plays a key role in determining domain structures and shape effects.[145] In micromagnetics it can be written as[144,147]

$$E_{\mathrm{ms}} = -\frac{\mu_0}{2} \int_V \mathbf{M}(\mathbf{r}) \cdot \mathbf{H}_{\mathrm{d}}(\mathbf{r})\, dV, \tag{2.32}$$

where $\mathbf{H}_{\mathrm{d}}(\mathbf{r})$ denotes the demagnetizing field produced by $\mathbf{M}(\mathbf{r})$. The magnetic field generated by a magnet extends throughout space. Outside the magnet it is referred to as the stray field, while inside the body it acts back on (opposes) the magnetization and is referred to as the demagnetizing field.[145,147] In the absence of free currents, $\mathbf{H}_{\mathrm{d}}$ is determined by the magnetostatic Maxwell equations.[143,147] In general, finding $\mathbf{H}_{\mathrm{d}}$ for arbitrary sample shapes and nonuniform $\mathbf{M}$ requires numerical methods.[144] Although closed-form results for $\mathbf{H}_{\mathrm{d}}$ are only available for a few high-symmetry cases, ellipsoids are particularly useful because a uniformly magnetized ellipsoid yields a uniform internal demagnetizing field.[143,145] Approximating a given geometry by an ellipsoid with equal volume therefore provides a convenient macrospin estimate of the global magnetostatic (shape) energy. Thus, elongated samples with strong uniaxial shape anisotropy can often be modeled as prolate ellipsoids, whereas ultrathin films and layered 2D magnets can be approximated by oblate ellipsoids, capturing the dominant easy-axis or easy-plane character, but it neglects edge effects and possible domain formation in finite-sized structures.[143,147]

Let $a = b$ and c denote the semi-axes of an ellipsoid of revolution along its principal axes. For a uniformly magnetized ellipsoid, the demagnetizing field is also uniform inside the sample and can be written as[143,147]

$$\begin{pmatrix} H_{\mathrm{d},a} \\ H_{\mathrm{d},b} \\ H_{\mathrm{d},c} \end{pmatrix} = - \begin{pmatrix} D_a & 0 & 0 \\ 0 & D_b & 0 \\ 0 & 0 & D_c \end{pmatrix} \begin{pmatrix} M_a \\ M_b \\ M_c \end{pmatrix}, \tag{2.33}$$

where D_i $(i = a, b, c)$ are the demagnetizing factors, with $D_a + D_b + D_c = 1$. Inserting Eq. (2.33) into Eq. (2.32) yields[143]

$$E_{\mathrm{ms}} = \frac{\mu_0}{2} V \left(D_a M_a^2 + D_b M_b^2 + D_c M_c^2\right). \tag{2.34}$$

In the prolate limit $c \gg a$ one finds $D_c \to 0$ and $D_a = D_b \to \frac{1}{2}$, corresponding to an easy axis along

the long axis. In the oblate limit $c \ll a$ one finds $D_c \to 1$ and $D_a = D_b \to 0$, corresponding to an easy plane perpendicular to the short axis.[143]

Anisotropy energy

Magnetic anisotropy describes a system's preference for particular orientations of its magnetic moments. Correspondingly, the anisotropy energy quantifies the energy cost of rotating the moments away from these preferred directions. The orientations that minimize the anisotropy energy define the magnetic easy axis or, in case of an easy-plane system, the easy plane. Magnetic anisotropy is crucial because it shapes a sample's hysteresis and ultimately governs the stability of a given magnetization configuration against external perturbations. The effective anisotropy generally comprises several contributions—depending, for example, on crystallinity, geometry, dimensionality, growth, and sample preparation—including magnetocrystalline, shape, magnetoelastic, and surface anisotropy.[145,147]

Magnetocrystalline anisotropy has its origin in spin-orbit coupling (SOC), which links the spin direction to the electronic orbital character, while the orbital character is constrained by the crystal field and chemical bonding.[148] As a consequence, a uniform rotation of the magnetization direction $\hat{\mathbf{m}}(\mathbf{r})$ relative to the crystal lattice changes the electronic energy and introduces preferred crystallographic directions (easy axes) or planes (easy planes). For cubic crystals such as magnetite (Fe_3O_4), a standard low-order expression for the magnetocrystalline anisotropy energy up to second order is[145,147]

$$E_{\mathrm{MCA}} = \int_V \Big[K_{c1}\big(\alpha_1^2\alpha_2^2 + \alpha_2^2\alpha_3^2 + \alpha_3^2\alpha_1^2\big) + K_{c2}\,\alpha_1^2\alpha_2^2\alpha_3^2 \Big]\, dV\,. \tag{2.35}$$

Here K_{c1} and K_{c2} are the first- and second-order cubic anisotropy constants, V is the magnetic volume, and $\alpha_i \equiv \hat{\mathbf{m}}(\mathbf{r})\cdot\hat{\mathbf{e}}_i$ (with $i = 1, 2, 3$), where $\hat{\mathbf{e}}_i$ are unit vectors along the cubic crystallographic axes. Depending on the material under investigation, the second-order term proportional to K_{c2} is in many cases much smaller than the leading K_{c1} contribution, and therefore is often neglected.[145]

Surface or interface anisotropy is closely related to magnetocrystalline anisotropy, but is localized near surfaces and interfaces, where the reduced coordination and broken symmetry modify the local electronic environment and thereby the SOC induced anisotropy.[145,147] This contribution becomes particularly important in nanoscale structures with large surface-to-volume ratio and in ultrathin films and layered 2D magnets, where it may dominate the effective anisotropy by selecting an easy axis or easy plane.[147] A commonly used phenomenological form for surface anisotropy energy up to second order is[145]

$$E_{\mathrm{surf}} = -\int_S \Big[K_{s1}\big(\hat{\mathbf{m}}(\mathbf{r})\cdot\hat{\mathbf{n}}_s(\mathbf{r})\big)^2 + K_{s2}\big(\hat{\mathbf{m}}(\mathbf{r})\cdot\hat{\mathbf{n}}_s(\mathbf{r})\big)^4 \Big]\, dS\,. \tag{2.36}$$

where K_{s1} and K_{s2} are the first- and second-order surface anisotropy constants, $\hat{\mathbf{n}}_s(\mathbf{r})$ is the local surface-normal unit vector, and S denotes the magnet's surface.

Shape anisotropy refers to the directional preference induced through dipolar (magnetostatic) self-interactions, and therefore depends on a magnet's geometry.[143,147] In the strict micromagnetic decomposition this contribution is contained in E_{ms}. However, in many situations—for example, in macrospin-like descriptions where $\mathbf{M}(\mathbf{r}) \equiv \mathbf{M}$—the net easy-axis or easy-plane effect can be modeled as an effective uniaxial anisotropy energy.[145,147] In practice, this behavior can be summarized by an effective uniaxial anisotropy energy up to second order of the form

$$E_u = -\int_V \Big[K_{u1}\,(\hat{\mathbf{m}}\cdot\hat{\mathbf{n}})^2 + K_{u2}\,(\hat{\mathbf{m}}\cdot\hat{\mathbf{n}})^4 \Big]\, dV\,. \tag{2.37}$$

where K_{u1} and K_{u2} are the first- and second-order uniaxial anisotropy constants, and $\hat{\mathbf{n}}$ is the unit vector along the uniaxial easy direction. Correspondingly, this energy term is minimized when magnetic moments align parallel or antiparallel with respect to the uniaxial anisotropy axis in the case when $K_{u1} > 0$ and in the absence of higher-order terms.[145]

Magnetoelastic anisotropy arises when strain modifies the local crystal field and thereby the SOC-induced anisotropy.[147] Phenomenologically, it can be treated as an additional strain-dependent

anisotropy term, often of approximately uniaxial character, whose strength depends on the sample's elastic state—for example, through epitaxial strain in thin films, strain from sample preparation, or from deliberately applied external stress.[145]

2.2.2 Magnetism in 2D materials

2D materials—also referred to as van der Waals materials—are layered solid materials in which layers are not covalently connected with each other but are held together solely by much weaker van der Waals interaction. This allows their exfoliation from bulk crystals. Since their discovery and the initial isolation of graphene and the demonstration of a pronounced electric-field effect in atomically thin (monolayer) carbon films in 2004, the study of 2D materials has become a major research field.[149] The ability to deterministically stack layers of different 2D materials into so-called vdW heterostructures further expanded the field into a versatile platform where electronic, optical, and magnetic properties can be combined and new properties emerge.[37,38]

From a fundamental viewpoint, magnetism in the strict 2D limit is non-trivial. For systems with short-range exchange and continuous spin-rotation symmetry, the Mermin–Wagner theorem excludes conventional finite-temperature long-range FM or AFM order in the thermodynamic limit, because long-wavelength thermal fluctuations destabilize magnetic order.[150] Importantly, real materials are rarely perfectly isotropic. Magnetic anisotropy induced by magnetocrystalline and dipolar interactions reduces the symmetry and can open a spin-wave gap, thereby stabilizing magnetic order in atomically thin crystals, inducing Ising-type easy-axis character, or enabling topological finite-temperature phases in XY-type easy-plane systems.[35,36,150]

Intrinsic magnetism in atomically thin vdW crystals was experimentally demonstrated in 2017 in CrI_3, showing that FM order persists down to the monolayer limit with strong out-of-plane (Ising-like) character.[44] A pronounced even–odd layer dependence, consistent with AFM interlayer coupling, was later supported by tunneling and spin-filter measurements.[50,151] At about the same time, intrinsic out-of-plane FM order was also observed in bilayer and thicker few-layer samples of the soft magnet $Cr_2Ge_2Te_6$, demonstrating FM interlayer coupling, a strong layer-number dependence of T_C, and field-induced control of the transition temperature.[152] More generally, these works highlight how magnetic anisotropy—whether intrinsic or effectively enhanced by external fields—counteracts thermal fluctuations in the 2D limit. Together, these reports marked the beginning of intrinsic 2D magnetism in vdW materials.[35,36,39]

Since then, 2D magnets have developed into a rich playground for the study of spin physics in systems with reduced dimensionality, where magnetic order and anisotropy can be tuned. For example, gate-controlled switching between layered AFM and FM configurations has been demonstrated in bilayer CrI_3, and ionic gating has been shown to raise T_C of trilayer Fe_3GeTe_2 up to room temperature beyond the bulk transition temperature.[45,49] Further, twisted stacking has been applied to produce moiré superlattices that can induce spatially varying exchange interaction and anisotropy, leading to emergent magnetic textures and so-called moiré magnetism as directly visualized for twisted CrI_3.[46] Today, a large number of metallic, semiconducting and insulating vdW FM and AFM exists, and a versatile toolbox has been introduced for controlling magnetism via thickness, gating, strain-engineering, stacking, and twisting.[35,36,39] Key limitations for integrating 2D materials into functional vdW heterostructure devices are air sensitivity,[153] monolayer yield and reliable monolayer access,[153,154] clean interfaces,[155] scalable and reproducible synthesis,[154,156] CMOS-compatible processing,[156] and the scarcity of intrinsic 2D magnets with ordering temperatures approaching room temperature.[157]

The vdW heterostructure approach is particularly important for magnetism because it enables interface-driven functionality, allowing combination of magnetic layers for example with graphene contacts, semiconducting transition-metal dichalcogenides, or topological materials to realize proximity exchange, spin filtering, and gate-tunable magnetic tunnel junctions.[36–39] An exemplary landmark device demonstration is the realization of CrI_3-based spin-filter tunnel junctions exhibiting very large tunneling magnetoresistance, and the use of vertical tunneling as an electrical probe of layered magnetic order and excitations.[50,151] Such results motivate the view that 2D magnets can serve not only as model systems for the study of emergent low-dimensional spin-physics, but also as functional

building blocks for ultrathin spintronic elements.[35,36,39]

From a technology perspective, the interest in 2D magnetism is tightly linked to computing and information technologies, where magnetism is already central today. Magnetoresistive read heads based on giant magnetoresistance (GMR) enabled major increases in hard-disk areal density and became a core technology for data storage, illustrating how fundamental spin-transport effects can translate into abundant technologies for the consumer market.[158,159] In modern non-volatile memories, magnetic tunnel junctions (MTJ) are the key component of MRAM concepts. Spin-Transfer-Torque (STT-)MRAM is being actively developed for CMOS integration, with applications ranging from standalone memory chips to embedded non-volatile memory on logic devices.[160] In this context, the use of 2D magnets promises atomic-thickness scaling, low-energy voltage control, and a modular heterostructure platform that integrates transport, optics, and magnetism.[37,39,45,161] AFM vdW materials, in particular, provide an additional device-motivated research direction: with (nearly) zero net magnetization, AFMs generate negligible stray fields and are therefore promising for high-density device arrays with reduced magnetic crosstalk. In addition, they exhibit intrinsic spin dynamics in the GHz–THz range, which is attractive for high-speed operation in memory and logic concepts.[162–164] Thus, substantial effort is devoted to understanding, tuning, and controlling AFM order and related spin dynamics in layered 2D crystals.[35,36,39,161,165]

Overall, 2D magnetism has progressed from the realization of stable atomically thin crystals[149] and vdW stacking,[37] through the experimental discovery of intrinsic magnetism down to the few- and monolayer limit in vdW magnets,[44,152] to today's broad landscape of tunable magnetic phases and interface-induced phenomena in vdW heterostructures.[36] While most intrinsic 2D magnet devices remain at the laboratory and prototype stage,[45,50] the rapid pace of progress—together with the proven commercial relevance of MRAM technologies, from GMR[158] to STT-MRAM and MTJ-based embedded memory[160]—makes 2D magnets a compelling research direction toward future low-power, scalable, and functionally integrated spin-based technologies.

2.2.3 Magnetism in magnetite nanoparticles

Magnetite (Fe_3O_4) is a soft FiM crystal with cubic inverse spinel structure (AB_2O_4) above its Verwey transition, where Fe^{2+} occupy octahedral sites and Fe^{3+} are split, half on tetrahedral and half on octahedral sites.[166–169] At room temperature, bulk magnetite forms a multi-domain grain-structure to reduce its magnetostatic energy at the cost of domain-wall formation. For small particles, experimental studies of individual grains[170,171] and analytical/micromagnetic modeling of isolated cubic particles indicate single-domain formation below the size of $\sim$0.1 µm.[172,173] The exact size threshold for single-domain formation, however, depends strongly on a particle's morphology, magnetic anisotropy, and degree of crystallinity. When the particle size is reduced below 20 – 35 nm, the effective anisotropy energy barrier—set by magnetocrystalline, shape/magnetostatic, surface, and magnetoelastic contributions—becomes comparable to k_BT, so the magnetic moment undergoes thermally activated reversals and the particles become superparamagnetic.[171,174,175]

Magnetite nanoparticles can be produced synthetically in various shapes and sizes, and several routes for surface functionalization and bioconjugation have been described.[176,177] An alternative route to obtain magnetite nanocrystals is biogenic production.[178] Many magnetotactic bacteria (MTB) have been reported that synthesize magnetite particles—the so-called magnetosomes—within their cell body and arrange them in quasi-linear chains as shown in Fig. 2.4, in which the magnetic moment is stabilized via dipolar interaction which induces an effective uniaxial anisotropy.[179–181] Magnetosomes exhibit a species-specific mature morphology and size between 35 – 120 nm,[182] and therefore typically fall in the stable single-domain range. Biomineralization comes with several strong advantages: crystals are typically highly crystalline, chemically pure, and narrow in size/shape distribution, with reproducible magnetic properties that arise from biological control over nucleation and growth.[179,180] Another practically important advantage is the native magnetosome membrane, which promises great biocompatibility[183,184] and provides a built-in biointerface that can facilitate colloidal handling and bioconjugation strategies compared with bare synthetic iron oxides. And ultimately, biogenic synthesis comes with the potential to tailor properties via genetic modification of

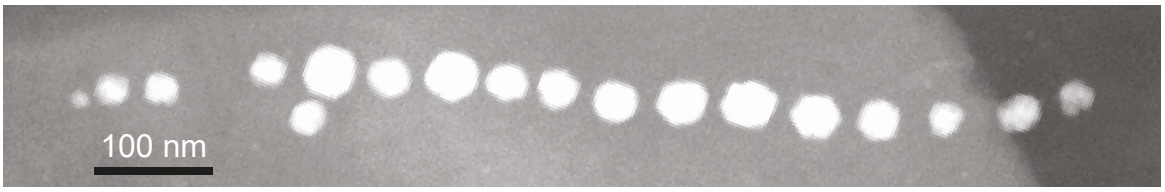


Figure 2.4: Bacterial magnetite particles. Cuboctahedral magnetite crystals forming a magnetosome chain in *Magnetospirillum gryphiswaldense*.

the underlying metabolic pathways, and thereby enable targeted optimization and design of single magnetite nanoparticles, magnetosome chains, and whole MTB cells toward specific technological applications.[185–187]

The discovery of MTB and MTB-derived magnetite nanoparticles has inspired numerous applications in fundamental research and the applied sciences, including the use of single magnetosomes, isolated magnetosome chains, and even whole MTB cells.[178,188–190] Most of these ideas are still at the laboratory or preclinical stage; however, magnetosome-based technologies offer a remarkably rich pipeline for future applications across many disciplines, motivating continued research. This includes a number of biomedical applications,[191–196] including using them as nano-robots with magnetic actuation[197–200] as sensing devices,[201] as mediators of magnetic hyperthermia for cancer therapy,[202–205] or as high-contrast agents for magnetic resonance[187,206] and magnetic particle imaging.[207–210] The biomineralization process governing the formation of magnetosome chains is also of great interest for finding new routes of material generation.[211] More exotic research directions include the use of MTB in waste water treatment,[212] in the realization of magnonic quantum states at room temperature for magnonic computing,[213] or studies linking the presence of magnetite nanoparticles—similar to those making up magnetosomes—in meteorites from Mars to potential presence of ancient life on that planet[i].[214–216]

2.3 Dynamic Torque Magnetometry

Dynamic torque magnetometry has evolved into a powerful tool for studying magnetism in ever smaller systems, from bulk single crystals down to individual nanomagnets.[217–219] In essence, the technique converts field-dependent changes in a sample's magnetic energy into measurable shifts of a mechanical resonator's eigenfrequency and dissipation. Early implementations relied on macroscopic torsion fibers and cantilevers, while modern realizations use ultra-compliant micro- and nanomechanical resonators.[69,220] These methods achieve exquisite torque sensitivity and give access to a broad range of magnetic phenomena including anisotropy, hysteresis, and phase transitions.[70,73,221] A particularly successful implementation is Dynamic Cantilever Magnetometry (DCM), in which a magnetic specimen is rigidly attached to a flexural resonator and the resulting magnetic torque modifies its effective spring constant.[69,70,75] In the following, we adapt this general concept to the use of a torsional paddle microbridge. Section 2.3.1 introduces the experimental setup, while Sec. 2.3.2 develops the theoretical framework relating the measured frequency shift and dissipation to the curvature of the sample's magnetic energy landscape. We then describe the experimental procedure and associated observables in Sec. 2.3.3. The discussion concludes in Sec. 2.3.4 with analytical and numerical modeling that connects the measured dynamic torque to the sample's magnetization.

2.3.1 Experimental setup

The torque transducer consists of a double-clamped torsional paddle resonator with a large central platform suspended by lateral tethers as sketched in Fig. 2.5. The magnetic sample is attached at the paddle center where the fundamental torsional mode has maximum angular displacement. Typically, the magnetic specimen is oriented such that its easy anisotropy axis lies in the plane and is aligned roughly perpendicular to the paddle's axis of rotation. The out-of-plane displacement of the magnet-on-resonator system is tracked with an optical fiber interferometer readout operated at powers

[i]Paragraph partially adapted from Claus, M. M. *et al.*, *Phys. Rev. E* **113**, 014408 (2026)

between 100 – 250 nW and telecom wavelength of 1550 nm, yielding an optical signal that is converted into a photo-induced voltage by a photodetector, and the voltage signal is detected using a lock-in amplifier.[222] The coordinate system is defined such that the paddle rotates about the y-axis (neutral axis), the z-axis points out of plane, and the x-axis lies in plane, perpendicular to the rotation axis. Furthermore, the measurement setup includes a rotatable superconducting bore magnet that can be oriented within the xz-plane over an angular range of 225°, providing magnetic fields **H** of up to 4.5 T. The orientation of **H** is described by θ_h which measures the angle with respect to the z-axis and θ_p denotes the angular displacement of the paddle. The transducer is mounted in a vibration-isolated closed-cycle helium cryostat (Montana Instruments) which allows temperature control in the range from ∼4 – 300 K depending on thermal coupling. Ideally, thermal fluctuations are sufficient to excite resonator motion above the thermal noise floor for high-Q resonators. However, if this is not the case, resonator motion can be actively driven. This can be achieved either by a piezoelectric element, which shakes the entire chip in an out-of-plane motion, or by magnetic torque driving, where a coil generates an AC magnetic field H_z that couples primarily to the paddle's torsional modes via the magnetic specimen. For active actuation schemes, the drive frequency is swept across a resonance peak at constant drive amplitude, and the signal is fitted and the resonance frequency can be extracted accordingly.

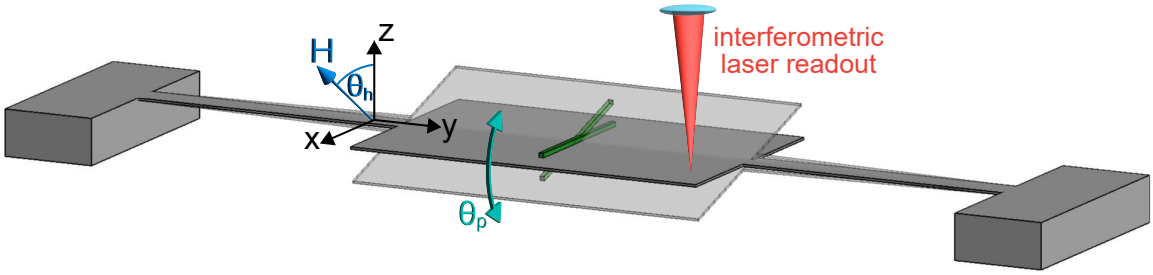


Figure 2.5: Dynamic torque magnetometry with a torsional resonator and interferometric displacement detection. Sketch of the magnet-on-paddle system, the coordinate system, and 1550 nm laser for detection of the resonator deflection. **H** denotes the magnetic field vector and θ_h sets its orientation within the xz-plane. θ_p is the angular displacement of the paddle due to rotational twist about the y-axis. A putative magnetic sample is depicted in green.

2.3.2 Theoretical framework

Dynamic torque magnetometry allows non-invasive characterization of extremely small magnetic specimen with dimensions of only few tens to few hundreds of nanometers.[223] The technique is based on attaching a magnetic sample to a mechanical resonator, thereby coupling the magnetic and mechanical energies. Typically, ultra-soft cantilevers have been employed as mechanical resonators, and the underlying DCM measurement principle has been extensively discussed in the theoretical and experimental literature.[70,74,217,224–227] Here, the physical framework of DCM is adapted to the use of a paddle micro-bridge, as sketched in Fig. 2.5, whose fundamental torsional mode is used for Dynamic Paddle Magnetometry (DPM), instead of the fundamental flexural mode used for DCM.

The magnetic torque $\boldsymbol{\tau}$ exerted on a resonator in response to the probe's magnetic moment $\mathbf{m}(\mathbf{H})$ coupling to the externally applied magnetic field **H** follows $\boldsymbol{\tau} = \mathbf{m}(\mathbf{H}) \times \mu_0 \mathbf{H}$. With τ_m denoting the component of magnetic torque about the y-axis, acting on the center of the paddle micro-bridge, Eq. (2.12) becomes a damped driven harmonic oscillator equation of motion. For the fundamental torsional mode, it can be written as a Langevin equation of the form

$$J_\mathrm{eff}\,\ddot{\theta} + J_\mathrm{eff}\Gamma_\mathrm{m}\dot{\theta} + k_{t,\mathrm{eff}}\,\theta = \tau_\mathrm{m}\,. \tag{2.38}$$

The total energy E_tot of the magnet-on-resonator system combines the mechanical and magnetic energy E_m according to

$$E_\mathbf{tot} = \frac{1}{2}\,k_{t,\mathrm{eff}}\,\theta_\mathrm{p}^2 + E_\mathrm{m}\,. \tag{2.39}$$

The coordinate system is chosen such that **H** lies in the xz-plane and the y-axis coincides with the paddle's axis of rotation. Hence, θ_p is a function of the torque along y given by $\tau = -\left(\frac{\partial E_\mathrm{tot}}{\partial \theta_\mathrm{p}}\right)$. By expanding E_m around $\theta_\mathrm{p} = 0$, while keeping terms only up to first order and solving Eq. (2.38) for τ, the torque along the micro-bridge's axis of rotation can be rewritten as

$$\tau(\theta_\mathrm{p}) = -\left(\frac{\partial E_\mathrm{m}}{\partial \theta_\mathrm{p}}\bigg|_{\theta_\mathrm{p}=0}\right) - \left[k_{t,\mathrm{eff}} + \left(\frac{\partial^2 E_\mathrm{m}}{\partial \theta_\mathrm{p}^2}\bigg|_{\theta_\mathrm{p}=0}\right)\right]\theta_\mathrm{p}\,. \tag{2.40}$$

Thus, by combining Eq. (2.38) and (2.40) the equation of motion becomes

$$\begin{aligned} & J_\mathrm{eff}\,\ddot{\theta}_\mathrm{p} + J_\mathrm{eff}\Gamma_\mathrm{m}\dot{\theta}_\mathrm{p} = \tau(\theta_\mathrm{p}) \\ \Rightarrow\quad & J_\mathrm{eff}\,\ddot{\theta}_\mathrm{p} + J_\mathrm{eff}\Gamma_\mathrm{m}\dot{\theta}_\mathrm{p} + \Bigg[k_{t,\mathrm{eff}} + \underbrace{\left(\frac{\partial^2 E_\mathrm{m}}{\partial \theta_\mathrm{p}^2}\bigg|_{\theta_\mathrm{p}=0}\right)}_{k_\mathrm{m}}\Bigg]\theta_\mathrm{p} = \underbrace{-\left(\frac{\partial E_\mathrm{m}}{\partial \theta_\mathrm{p}}\bigg|_{\theta_\mathrm{p}=0}\right)}_{\tau_\mathrm{m}}. \end{aligned} \tag{2.41}$$

As can be seen from to Eq. (2.41), the coupling between the probe's magnetic moment and the externally applied magnetic field gives rise to a magnetic spring constant k_m and a static magnetic torque τ_m.

In approximation, contributions from dissipation Γ_m are negligible for high-Q resonators, and hence, the change in spring constant translates into a shift in angular resonance frequency from

$$\omega_{t,0} \approx \sqrt{\frac{k_{t,\mathrm{eff}}}{J_\mathrm{eff}}} \quad\longrightarrow\quad \omega_{t,\mathrm{m}} \approx \sqrt{\frac{k_{t,\mathrm{eff}} + k_\mathrm{m}}{J_\mathrm{eff}}}. \tag{2.42}$$

Expanding $\Delta\omega_t = \omega_{t,\mathrm{m}} - \omega_{t,0}$ up to first order in k_m in the regime $k_\mathrm{m} \ll k_{t,0}$, and using $\omega = 2\pi f$, the magnetic shift of the resonant torsional frequency yields

$$\Delta f_t = \frac{f_{t,0}}{2k_{t,\mathrm{eff}}}\left(\frac{\partial^2 E_\mathrm{m}}{\partial \theta_\mathrm{p}^2}\bigg|_{\theta_\mathrm{p}=0}\right). \tag{2.43}$$

Equation (2.43) is a resource to probe the curvature of the magnetic energy by measuring Δf in response to an external field **H**, which is proportional to the curvature of the magnetic energy landscape defined by E_m. As such, dynamic torque magnetometry probes the sample's net magnetization. However, when combined with micromagnetic simulations, it does provide detailed insight into the underlying (micro-)magnetic texture as will be discussed in Sec. 2.3.4.

During a DPM measurement re-orientation of the probes magnetization in an external field occurs much faster than changes in the oscillator's resonance frequency, and therefore magnetization can be considered in an equilibrium state at any given deflection angle θ_p. According to Eq. (2.43), a positive Δf_t corresponds to a local minimum in the magnetic energy with respect to θ_p. Thus, given the alignment of the probe's magnetization, its orientation in the xy-plane is energetically favorable as a change in θ_p is associated with an increase in E_m. Small displacement away from θ_p, therefore induces a spring-like magnetic restoring force which stabilizes the probe's magnetization. This in turn, causes an effective stiffening of the spring constant which manifests in a positive Δf_t.

In contrast, a negative Δf_t is indicative of a local maximum in $E_\mathrm{m}(\theta_\mathrm{p})$. Correspondingly, given the alignment of the probe's magnetization, its orientation in the xy-plane is energetically unfavorable. Therefore, the resonator experiences an effective softening of the spring constant, leading to a decrease in Δf_t. Even though an exact expression for E_m is required to predict the DPM response, certain limits can already be understood from approximating the magnetic energy, and we will follow up on this in Sec. 2.3.4

2.3.3 Experimental procedure and observables

The experimental setup described in Sec. 2.3.1 provides three independent control parameters: the externally applied magnetic field $\mathbf{H}$, the field angle θ_h, and the temperature T. This affords a rich experimental toolbox, enabling:

- Field sweeps at fixed angle $\Delta f(\mathbf{H})$ to probe hysteresis.
- Angle sweeps at fixed field $\Delta f(\theta_\mathrm{h})$ to probe magnetic anisotropy.
- Temperature sweeps at fixed field and angle $\Delta f(T)$ to probe temperature dependence.
- And combinations thereof to map out phase diagrams $\Delta f(\mathbf{H}, \theta_\mathrm{h}, T)$.

In this work, we employ dynamic torque magnetometry based on the first two measurement protocols listed above, which are briefly discussed in the following.

Performing hysteresis measurements along specific anisotropy axes clearly requires knowledge of their spatial orientation. Consequently, the characterization of a new magnetic sample typically begins with an angle-dependent measurement of $\Delta f(\theta_\mathrm{h})$ at a fixed field $\mathbf{H}$ chosen sufficiently large that the frequency shift lies well within the high-field regime and thus approximates Δf_hf, as given in Eq. (2.46). This not only probes the direction, but also the type of anisotropy present in the sample. Based on the result, the field angle θ_h is then oriented and fixed to address a specific anisotropy axis, and the field is swept from $\pm 4.5\,\mathrm{T}$ to $\mp 4.5\,\mathrm{T}$ and back, while measuring $\Delta f(\mathbf{H})$.

Resonator motion is driven either at a constant oscillation amplitude or with a constant driving amplitude. In both cases, the mechanical dissipation coefficient can be deduced in addition to the frequency shift Δf (dynamic torque, Eq.(2.43)) and the static torque τ_m. When operating the resonator at a constant oscillation amplitude, it must be driven with a torque $\tau_\mathrm{drive} = J_\mathrm{eff}\Gamma_\mathrm{m}\dot{\theta}_\mathrm{p}$ such that dissipative losses are compensated. The total dissipation of the magnet-on-resonator system can be written as $\Gamma = \Gamma_\mathrm{m} + \Gamma_\mathrm{mag}$, where Γ_m denotes mechanical losses of the resonator and Γ_mag captures magnetic relaxation processes in the sample.[228] The magnetic contribution produces sharp dips or jumps in Γ at magnetic phase transitions, making the dissipation signal (or driving voltage) a sensitive complementary probe to the frequency shift.[73,88,229,230]

2.3.4 Connecting dynamic torque and magnetization

The measured frequency shift Δf alone does not directly reveal the sample's magnetization. To address this, a complementary theoretical framework is needed that relates Δf to the magnetization $\mathbf{M}$, and thus to E_m, based on Eq. (2.43). Under certain conditions—specifically, at low and high applied fields and for magnetic samples with suitable properties—analytical models can be easily obtained. A comprehensive analysis of the dynamic magnetic torque signal in the intermediate field-range for prolate and oblate ellipsoid-shaped FM samples is reported by S. Philipp.[223] For samples with more complex magnetic behavior the mono-domain approximation breaks down, and thus, establishing a quantitative relationship requires micromagnetic modeling combined with numerical simulations of the dynamic torque. In what follows, both, analytical and numerical micromagnetic modeling approaches are introduced.

Analytical model

For small FM samples with uniaxial anisotropy, in which the exchange interaction forces individual spins to orientate parallel to each other, the collective magnetization can be treated as a single-domain macrospin using the Stoner-Wohlfarth model. In this simplified model, magnetization is assumed to be uniform across the entire magnetic volume V and is described by the magnetization unit vector $\hat{\mathbf{m}}$. In this regime, E_m can be approximated by considering only the Zeeman and the uniaxial anisotropy energies as[230]

$$E_\mathrm{m} = -\mu_0 V \mathbf{M} \cdot \mathbf{H}_\mathrm{ext} - K_\mathrm{u} V (\hat{\mathbf{m}} \cdot \hat{\mathbf{n}})^2 \,, \tag{2.44}$$

where μ_0 is the vacuum permeability, K_u the uniaxial anisotropy constant, and $\hat{\mathbf{n}}$ denotes the unit vector of the anisotropic easy axis. The easy axis represents the preferred orientation of $\hat{\mathbf{m}}$ in the

absence of an external field, and thus, minimizes the anisotropy energy. For $K_\mathrm{u} > 0$, the anisotropy term is minimized when $\hat{\mathbf{m}}$ aligns parallel or antiparallel to $\hat{\mathbf{n}}$. Again, it must be emphasized that in this simplified model higher order shape, as well as magnetocrystalline, and magnetoelastic anisotropy contributions are neglected. For samples with a high aspect ratio, as for example very long and thin magnets with strong uniaxial shape anisotropy, this is a valid and also powerful model, that allows analytical description of the resulting dynamic torque within the low- and high-field limit.

In the low-field limit, i.e. $H \ll \frac{K_\mathrm{u}}{M}$, E_m is dominated by the anisotropy term which induces parallel or anti-parallel orientation of $\mathbf{M}$ with respect to the easy axis. Thus, in this regime, DPM probes the curvature of the first magnetic energy term of Eq. (2.44). Differentiating twice the magnetic energy with respect to the angular displacement and inserting into Eq. (2.43) yields the torsional frequency shift in the low-field limit[70]

$$\Delta f_\mathrm{lf} = -\frac{f_{t,0}}{2k_{t,0}}\mu_0 V H \left.\frac{\partial^2 M_z}{\partial \theta_\mathrm{p}^2}\right|_{\theta_\mathrm{p}=0} = \frac{f_{t,0}\mu_0 V}{2k_{t,0}} H M_z \,, \tag{2.45}$$

and thus, $\Delta f_t \propto H_\mathrm{ext}$ and M_z can be determined from the measured response.

In the high-field limit, i.e. $H \gg \frac{K_\mathrm{u}}{M}$, the Zeeman term dominates and the probe's magnetization $\mathbf{M}$ is forced to be parallel with the field $\mathbf{H}$. Again, differentiating twice the expression for E_m in the high-field limit, and after inserting in Eq. (2.43) the frequency shift in the high-field limit is found[70]

$$\Delta f_\mathrm{hf} = \frac{f_{t,0}}{k_{t,0}}\mu_0 V K_\mathrm{u}(\cos^2\theta_n - \sin^2\theta_n \cos^2\phi_n) \,, \tag{2.46}$$

where θ_n and ϕ_n denote spherical angles of the easy axis $\hat{\mathbf{n}}$ relative to $\mathbf{H}$ and $\mathbf{M}$, respectively. This result is independent of the applied field and Δf_t approaches a horizontal asymptote referred to as the high-field limit Δf_hf. In this regime, DPM probes the curvature of the second term of Eq. (2.44), and Δf_hf is directly proportional to the magnet's anisotropy constant, and thus, allows quantification of the anisotropy energy.

Numerical model with micromagnetic simulation

Many of the structures investigated by DCM—such as nanotubes,[70,73,74] mesocrystals,[76] and other magnets with complex exchange-bias or shape anisotropy—cannot be faithfully described by a single macrospin. Even when the DPM response is ultimately sensitive only to the net torque and the curvature of the total magnetic energy, these quantities reflect non-uniform magnetization textures, domain walls, and vortex or flux-closure states.[74] In this regime, the micromagnetic description introduced by Brown and widely used in the DCM literature becomes essential.[70,73–76,146]

In micromagnetics, the magnetization is treated as a continuous vector field described by the magnetization unit vector $\hat{\mathbf{m}}(\mathbf{r})$, coarse-grained over a length scale large compared to the lattice constant, but comparable to intrinsic micromagnetic length scales such as for example the exchange length $l_\mathrm{ex} = \sqrt{2A_\mathrm{ex}/\mu_0 M_\mathrm{s}^2}$.[144,147] The magnetic energy functional includes Zeeman, exchange, anisotropy, and demagnetizing energy, and may have additional contributions as discussed in Sec. 2.2.1. The associated dynamics are governed by the Landau–Lifshitz–Gilbert equation

$$\frac{\partial \hat{\mathbf{m}}}{\partial t} = -\gamma\, \hat{\mathbf{m}} \times \mu_0 \mathbf{H}_\mathrm{eff} + \alpha\, \hat{\mathbf{m}} \times \frac{\partial \hat{\mathbf{m}}}{\partial t} \,, \tag{2.47}$$

where γ is the gyromagnetic ratio, α the Gilbert damping parameter, and $\mathbf{H}_\mathrm{eff}$ the effective field derived from the derivative of E_m with respect to $\hat{\mathbf{m}}$. In the context of DPM, however, the mechanical oscillation is slow compared to the internal precession and relaxation rates, so that the magnetization can be assumed to be in a quasi-static equilibrium configuration for each instantaneous value of the applied field $\mathbf{H}$ and torsional angle θ_p.

Adapting the cantilever-based micromagnetic treatment developed for DCM of systems such as nanotubes,[70,73,74] nanowires,[72] mesocrystals,[76] and thin films[75] to torsional DPM is straightforward.

Instead of a flexural deflection angle of a beam, the relevant analogous coordinate is now the rotation angle θ_p of the paddle. For a rigidly attached magnet, a small torsional oscillation is equivalent to a small rotation of the sample—and thus of its anisotropy and demagnetizing axes—with respect to the external field. For each field value, the magnetization is relaxed to an equilibrium configuration at small tilting angles using a micromagnetic solver such as *MuMax3*[231,232] or *Nmag*.[233] In practice, this is implemented by rotating the field by a small angle $\pm\delta\theta_\mathrm{p}$ relative to the sample, relaxing the magnetization in each position, and recording the corresponding total magnetic energies $E_\mathrm{m}(-\delta\theta_\mathrm{p})$, $E_\mathrm{m}(0)$, and $E_\mathrm{m}(+\delta\theta_\mathrm{p})$.[73,223,234] The resulting equilibrium energies $E_\mathrm{m}(\theta_\mathrm{p})$ encode both the net magnetic moment and the internal spin texture.

From these three energies—$E_\mathrm{m}(-\delta\theta_\mathrm{p})$, $E_\mathrm{m}(0)$, and $E_\mathrm{m}(+\delta\theta_\mathrm{p})$—the curvature $\partial^2 E_\mathrm{m}/\partial\theta_\mathrm{p}^2|_{\theta_\mathrm{p}=0}$ is obtained numerically using a central finite-difference scheme, as illustrated for flexural DCM.[115,223,224] Explicitly, the corresponding differential quotient is evaluated as

$$\left.\frac{\partial^2 E_\mathrm{m}}{\partial\theta_\mathrm{p}^2}\right|_{\theta_\mathrm{p}=0} \approx \frac{E_\mathrm{m}(+\delta\theta_\mathrm{p}) - 2E_\mathrm{m}(0) + E_\mathrm{m}(-\delta\theta_\mathrm{p})}{\delta\theta_\mathrm{p}^2}\,. \tag{2.48}$$

Inserting this curvature into Eq. (2.43) derived in Sec. 2.3.2, together with the independently measured bare resonance frequency $f_{t,0}$ and effective torsional stiffness $k_{t,\mathrm{eff}}$, yields the simulated field-dependent frequency shift $\Delta f_t(\mathbf{H})$ for the chosen set of micromagnetic parameters A_ex and M_s. The torsional spring constant $k_{t,\mathrm{eff}}$ is deduced from finite-element modeling of the mechanical resonator including the weight of the magnetic sample in *COMSOL Multiphysics* software.

In this way, micromagnetic modeling provides the bridge between complex real-space micromagnetic textures and the integrated DPM signals, enabling for example identification of vortex formation, flux-closure states, or domain-wall motion as specific features in the modeled $\Delta f(\mathbf{H})$, in direct analogy with the analyses reported for nanotubes,[70,73,74] nanowires,[72] exchange biased Janus particles,[75] and maghemite mesocrystals.[76]

Finally, the numerical DPM curves are compared with the experimental data and optimized for agreement, typically by first using the high-field asymptotes to constrain the combination of saturation magnetization, magnetic volume, and anisotropy, and then refining the model to reproduce low-field switching features and hysteresis. This strategy mirrors the procedure successfully employed in many DCM studies and provides a robust, broadly applicable framework for interpreting dynamic torque magnetometry measurements in terms of the underlying micromagnetic states.

3

Micro- and nanofabrication

This chapter describes the nanofabrication methods and process strategy for production of standalone torsional resonators in unstructured membranes, as well as torsional and flexural resonators embedded in a PnC structured membrane made from PECVD silicon nitride, as detailed in Sec. 3.2. It also outlines the key techniques commonly used to prepare magnetic vdW materials near the 2D limit, presented in Sec. 3.3. The fabrication outcomes are summarized in Sec. 3.4 and results are discussed in Sec. 3.5

3.1 Introduction

Recent advances in the fabrication of nanomechanical resonators have enabled measurements of mass, force, and torque with exceptional sensitivity. A major driver of this progress has been the substantial miniaturization of mechanical transducers over the past three decades, extending to devices based on individual carbon nanotubes.[235] Reducing device dimensions and defect density lowers mechanical dissipation and thereby improves transducer sensitivity.[236] More recently, phonon engineering has been employed to further suppress mechanical losses by patterning the supports to create a phononic band gap around the resonator's mechanical frequency.[84] In addition, support geometries can be designed to realize optimized clamping conditions, which further reduce dissipation. These concepts have enabled high-Q optomechanical devices,[237,238] and are now starting to be adopted in the design of high-sensitivity force sensors.[239–242] To the best of our knowledge, phononic band-gap shielding engineered for acoustic isolation has not yet been applied to ultrasensitive torsional-resonator torque transducers.

Here, we aim to transfer this approach for suppression of mechanical dissipation to the development of ultrasensitive mechanical torque transducers, tailoring their design and and improving their sensing performance for studies of 2D materials, including 2D magnets and vdW heterostructures. Beyond aiming to provide the sensitivity required to detect the tiny magnetic torque exerted by ultrathin samples near the 2D limit, devices are designed to support electrical contacting of the specimen, which has remained practically challenging in the most sensitive cantilever-based torque magnetometers. To achieve this, we (i) fabricate a transducer with minimal dimensions to reduce inertia and stiffness, and (ii) acoustically isolate the resonator using a PnC surround to suppress mechanical dissipation, thereby improving the quality factor Q. Devices are fabricated from non-stoichiometric amorphous PECVD silicon nitride in the form of torsional paddles and flexural beams, both with and without a surrounding PnC.

In addition, we investigate protocols for exfoliating the vdW magnets $MnPSe_3$ and VBr_3 from bulk crystals and for protecting the resulting flakes with hBN, enabling sample preparation near the ultimate 2D limit, including few-layer flakes down to the bilayer. Finally, we demonstrate that vdW materials can be transferred onto suspended SiN_x membranes without rupturing them. This observation suggests that vdW magnets can be stamped onto the SiN_x film after definition of the PnC

but prior to final suspension, when the remaining Si support layer still provides mechanical robustness. Beyond protecting an air-sensitive material, hBN encapsulation can also act as a protective barrier during the aqueous KOH release step used to suspend the PnC device.

3.2 Fabrication of torque transducers made from silicon nitride

Fabricating mechanical resonators with lateral dimensions of only a few micrometers and thicknesses of a few hundred nanometers is inherently challenging. A generalized process flow is shown in Fig. 3.1. The specific fabrication routes for the different device types—simple torsional paddles and more complex resonators embedded in a PnC—follow this workflow with minor variations. Detailed fabrication protocols for all devices presented in this work are provided in App. A.1. The generalized fabrication procedure can be divided into six main steps:

(i) Deposition of SiN_x films on both sides of the Si substrate by PECVD.

(ii) Patterning of the mask-layer SiN_x by optical lithography and RIE to define the wet-etch mask.

(iii) Wet etching of Si to form alignment markers and partially open cavities.

(iv) Patterning of the device-layer SiN_x by optical lithography and RIE to define the transducers.

(v) Wet etching of Si to remove the remaining Si and suspend the transducers.

(vi) Optional refinement of transducer geometry by focused ion beam (FIB) milling.

First, SiN_x films are deposited on both sides of a Si wafer by PECVD. The backside SiN_x—referred to as the *mask layer*—is then patterned by optical lithography and reactive ion etching (RIE) to define the wet-etch mask used to form alignment markers and the cavities that will later become the SiN_x membrane windows. In the window regions, the mask is designed to delay the Si etch relative to the fully opened alignment-marker areas. Backside patterning is followed by a Si wet-etch step that transfers the alignment markers to the front side, while leaving a residual Si layer of

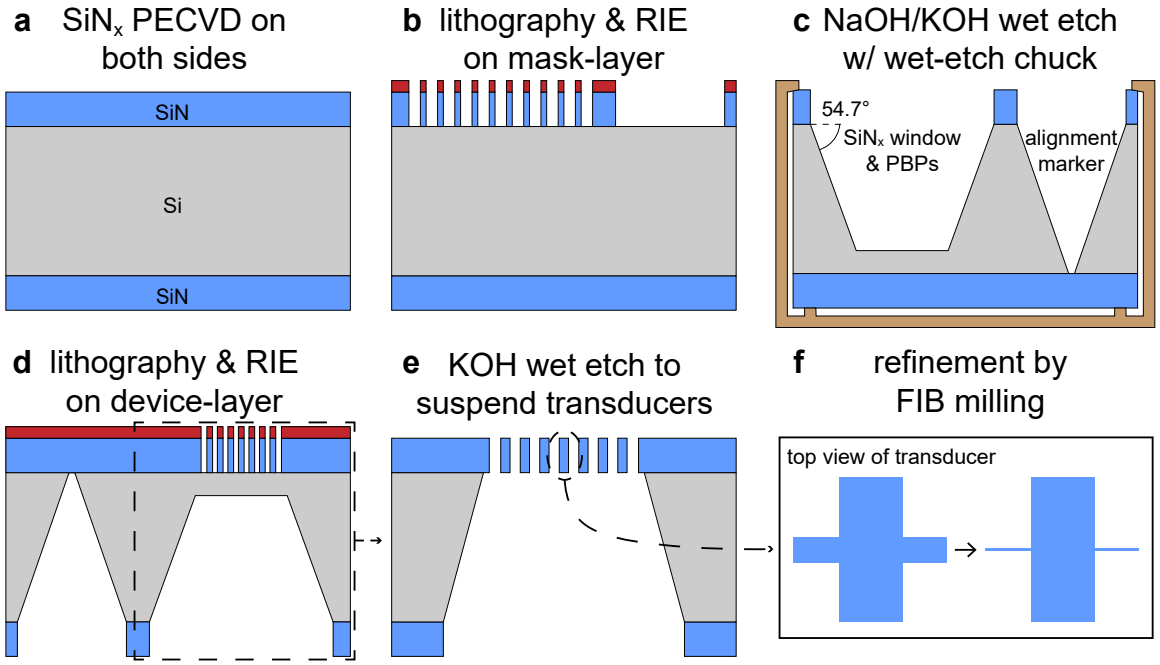


Figure 3.1: General fabrication route (chip cross-section). (**a**) PECVD of SiN_x on both sides of a Si substrate. (**b**) Patterning of mask-layer SiN_x. (**c**) Alkaline Si wet etch from backside with protection of device-layer SiN_x. (**d**) Patterning of the device-layer SiN_x. (**e**) Alkaline Si wet etch to suspend the transducers. (**f**) Optional FIB milling.

approximately 60 µm to mechanically support the front-side SiN_x over the future membrane windows and the predetermined breaking points (PBPs). This remaining Si also provides sufficient thermal conduction for uniform photoresist baking, which is required for subsequent patterning of the device layer.

The wafer is then flipped and the front-side SiN_x—referred to as the *device layer*—is also patterned by optical lithography and RIE to define the transducers. After the transducer geometries are defined, a final alkaline Si wet etch is carried out under milder conditions to release and gently suspend the device layer. Finally, the lateral dimensions of the SiN_x resonators can optionally be further reduced by focused ion beam (FIB) milling.

In the following, each fabrication step in this workflow is described in greater technical detail, including PECVD of silicon nitride in Sec. 3.2.1, optical lithography and RIE patterning of silicon nitride in Secs. 3.2.2 and 3.2.4, alkaline Si wet etching in Secs. 3.2.3 and 3.2.5, and FIB milling in Sec. 3.2.7. Fabrication results are summarized in Sec. 3.4.

3.2.1 Plasma-enhanced chemical vapor deposition of SiN_x

We begin the fabrication by depositing amorphous SiN_x films on both sides of a Si wafer, as sketched in Fig. 3.1a. SiN_x offers excellent mechanical performance, combining high hardness and durability with the potential for high mechanical quality factors.[77] In addition, SiN_x is significantly more resistant to alkaline etchants such as aqueous NaOH and KOH than Si, which is readily removed under these conditions. This combination allows the SiN_x to serve both as the structural material for the mechanical resonators and as wet-etch mask for backside patterning.

The SiN_x films are deposited in a PlasmaPro 80 PECVD reactor (Oxford Instruments). In this plasma-assisted process, an AC voltage is applied between the sample stage (bottom electrode) and the conductive chamber walls (top electrode) to sustain the discharge. Film growth proceeds via plasma-induced dissociation of silane (SiH_4) and ammonia (NH_3) and subsequent surface reactions of the activated species. The overall stoichiometric reaction for Si_3N_4 formation can be written as

$$3\,SiH_4(g) + 4\,NH_3(g) \rightarrow Si_3N_4(s) + 12\,H_2(g)\,. \tag{3.1}$$

The precursor gases are dissociated and partially ionized by the oscillating electric field, generating reactive radicals and ions that are accelerated in the plasma sheath. Upon impingement on the substrate, these species undergo surface reactions that result in the deposition of a conformal silicon nitride film. Notably, the composition of PECVD silicon nitride is generally non-stoichiometric and hydrogen-rich, in contrast to the stoichiometric Si_3N_4 product implied by Eq. (3.1). In practice, PECVD yields SiN_x:H; therefore, Eq. (3.1) should be regarded as an idealized net reaction.[243] We accordingly refer to the deposited material as SiN_x to emphasize its non-stoichiometric composition.

The films are deposited at 300 °C, 650 mTorr, and 20 W, using gas flow rates of 20 sccm SiH_4, 20 sccm NH_3, and 980 sccm N_2. During deposition, the excitation alternates between a high-frequency mode at 13.56 MHz and a low-frequency mode at 18 kHz. The high-frequency phase yields a tensile SiN_x film, whereas the low-frequency phase promotes compressive stress.[244] By alternating 16 s at high frequency with 4 s at low frequency, we obtain an overall low-stress SiN_x film.

Finally, the PECVD deposition rate depends on substrate temperature, and the heated stage exhibits a radial temperature gradient that decreases from the center toward the periphery. To maximize thickness uniformity, we therefore process a single wafer per run and position it at the center of the stage.

While alkaline wet etching of stoichiometric LPCVD Si_3N_4 is often reported to be negligible,[244,245] PECVD SiN_x exhibits a small but finite etch rate in aqueous KOH and NaOH. This rate depends on the deposition conditions, which determine the film composition and in particular the hydrogen content.[246–248]

For the specific PECVD SiN_x process used in this work, the etch rate was quantified by de Vito.[249] Using ellipsometry to track thickness during exposure to 25 w% aq. KOH at 80 °C, he reported a slow etch rate of ∼0.5 nm/min, while maintaining high selectivity of Si over SiN_x. To ensure the integrity of the wet-etch mask throughout the full etch duration, we therefore deposit the mask layer with a

thickness of at least 200 nm. The device-layer thickness is chosen based on the target thickness plus the expected thickness loss during the final KOH release step used to suspend the resonator. Exact deposition times and thicknesses for each device are given in App. A.1.

3.2.2 Patterning the SiN_x mask layer

After depositing SiN_x on both sides of the Si substrate, the backside mask layer is patterned by photolithography and RIE to form a wet-etch mask. This fabrication step is illustrated in Fig. 3.1,**b**. The mask comprises three distinct regions: alignment markers, SiN_x windows, and predetermined breaking points (PBPs). The alignment markers enable back-to-front alignment; the windows define the areas in which free-standing SiN_x transducers are formed from the device layer; and PBPs are incorporated to facilitate separation of the chips from the surrounding substrate. The alignment markers are realized as simple openings in the SiN_x mask. By contrast, the SiN_x windows and PBPs are covered with a densely meshed SiN_x grid that provides a controlled etch delay, as shown in Fig. 3.2. Within the grid-patterned areas, the wet-etch progression along the ⟨100⟩ direction is delayed, whereas the formation of alignment markers can proceed without impediment.[250] First, a dry-etch mask is defined on the mask layer using the photoresist MICROPOSIT™ S1805 G2 (micro resist technology) in combination with the adhesion promoter AR 300-80 new (Allresist). This liquid primer is compatible with S1805 and substantially improves the adhesion of the photoresist to the substrate. AR 300-80 new is applied by spin coating at 2000 rpm for 40 s, followed by a soft bake at 95 °C for 2 min on a hotplate. Subsequently, S1805 is spin coated at 4500 rpm for 40 s to yield a resist thickness of approximately 430 nm, and the coating is cured for 2 min at 125 °C.

Optical lithography is carried out using a µPG101 µMLA laser writer (Heidelberg Instruments) operating at a wavelength of 405 nm. The lithography pattern is aligned horizontally with the substrate's ⟨110⟩ direction using the primary flat in a two-step procedure. First, the wafer is placed on the writer stage using the alignment pins. Second, a tilt correction is applied based on the coordinates of two widely separated points on the primary flat, selected with the integrated camera. In addition, the exposure field is centered on the substrate using the laser writer's automatic edge-detection function. The substrate is focused using the "fast optical focus" function of the control software. After completion of the alignment and focusing steps, the resist is exposed and subsequently developed in MICROPOSIT™ MF-319 Developer (micro resist technologies) for 60 s at room temperature.

In the final step of mask-layer processing, the resist-defined pattern is transferred into the SiN_x layer by reactive ion etching (RIE) using a PlasmaPro 80 system (Oxford Instruments). The SiN_x is etched in a CHF_3/O_2 gas mixture at flow rates of 50 sccm and 5 sccm, respectively. The chamber pressure is set to 55 mTorr, the stage temperature to 20 °C, and the plasma is operated at a forward RF power of 150 W. Under these conditions, SiN_x is removed at a rate of approximately 22 nm/min,

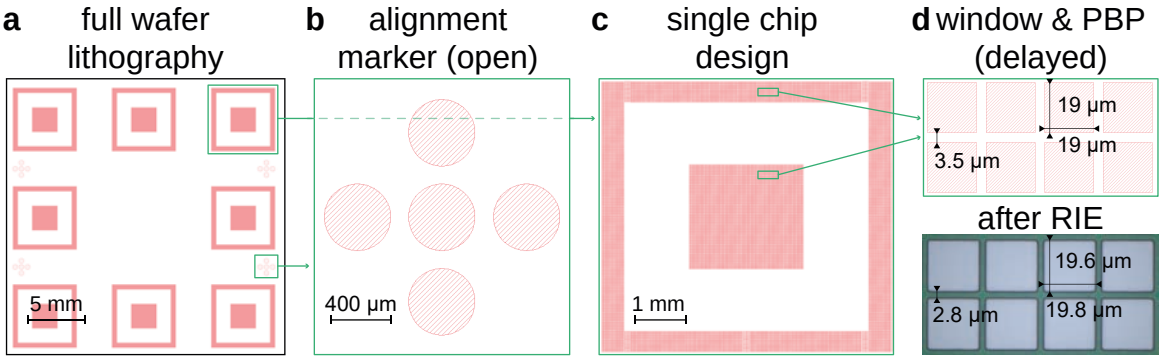


Figure 3.2: Lithography design for patterning the mask-layer SiN_x. (**a**) The full layout comprises eight chips and four alignment markers. (**b**) The alignment markers are used for back-to-front lithography alignment. (**c**) Each chip includes a central cavity and predetermined breaking points (PBPs) around the perimeter; both are patterned as a tightly meshed SiN_x grid to delay wet etching relative to the alignment markers. (**d**) Detail of the SiN_x grid. The grid dimensions are chosen such that a ∼25 µm thick Si layer remains in the cavity windows and PBPs when the alignment markers are fully etched.

and the etch duration is chosen such that the full mask layer is cleared and the underlying Si is exposed. After defining the wet-etch mask, residual photoresist is removed from both the mask and device layers using a mild O_2 plasma (20 sccm, 60 mTorr, 60 W). Removing the remaining resist by plasma etching rather than dissolution in acetone results in cleaner SiN_x surfaces—particularly important for the device layer—because it avoids re-deposition of dissolved resist during rapid acetone evaporation. Once such residues form, they are difficult to remove using standard solvents or RIE. Because mask-layer RIE requires placing the wafer with the device layer facing down, a polished 4" Si wafer is used as an intermediate carrier to prevent scratching from direct contact with the rough RIE stage surface.

3.2.3 Si wet etching using the SiN_x mask layer as etch mask

Etching is fundamentally an electrochemical process governed by the redox potential between the constituent reactants, provided that the reaction proceeds outside the diffusion-limited regime.[251] Wet anisotropic etching using alkaline solutions of potassium hydroxide (KOH)—and, to a lesser extent, sodium hydroxide (NaOH)—is a well-established MEMS method for etching crystalline silicon, particularly ⟨100⟩ and ⟨110⟩ wafers. This approach exploits the crystal-orientation dependence of Si etch rates, enabling the fabrication of precision structures such as v-grooves,[252] cavities,[253] and diaphragms.[254,255] Compared with highly toxic etchants such as tetramethylammonium hydroxide (TMAH) and ethylenediamine–pyrocatechol (EDP), alkaline KOH and NaOH solutions are relatively non-toxic, can be handled safely under standard laboratory conditions, and are easier to dispose of, thereby posing a lower risk to human health and the environment. Regardless of whether aqueous KOH or NaOH is used, the etch process follows the same reaction mechanism, with the dissolved hydroxide ion (OH^-) acting as the active species, as described by the reaction equation.[256]

$$Si_{(s)} + 2\,OH^-_{(aq)} + 2\,H_2O_{(l)} \longrightarrow SiO_2(OH)^{2-}_{2(aq)} + 2\,H_{2(g)}$$

After dissociation of the alkali hydroxide species in DI water, dissolved OH^- first attack exposed Si-H surface bonds followed by Si-Si bulk bonds, leading to the formation of stable, soluble silicate ions ($SiO_2(OH)^{2-}_2$) and H_2. Gaseous H_2 produced during the reaction nucleates as bubbles whose release and buoyant rise can, at sufficiently high rates, induce vigorous mixing and turbulence. A detailed discussion of anisotropic Si wet etching in alkaline solution is available by Seidel *et al.*[256] Anisotropic etching in alkaline solution removes Si at different rates from the different exposed crystallographic planes. Etch rates follow the order {110}>{100}> {111}, with the {111} plane etching at a substantially lower rate than {110} and {100}. Consistent with this behavior, patterns etched into a Si⟨100⟩ substrate using alkali hydroxides feature sidewalls defined by {111} planes that are tilted by ∼54.7° relative to the {100} plane, i.e., the wafer's surface.[257,258] For the substrates used in this work, we observe a slightly larger angle of ∼56°, which indicates that the wafers are slightly thinner than their nominal thickness. In addition to depending on the etchant, the anisotropy ratio and the overall etch dynamics exhibit a strong dependence on concentration and

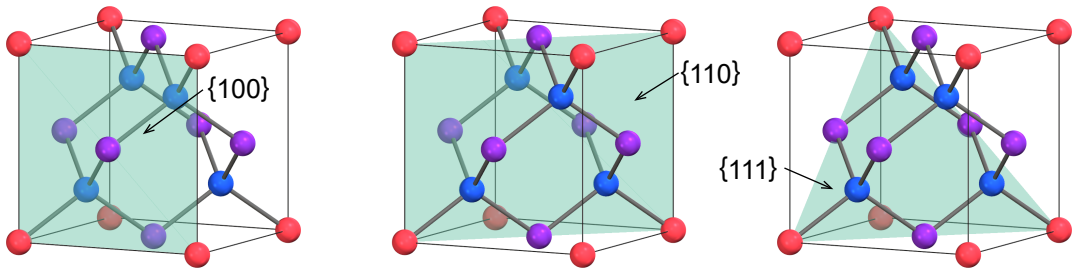


Figure 3.3: Packing densities of Si atoms in different crystallographic planes. Denser packing imposes greater steric hindrance for attack of bulk Si-Si backbonds. Correspondingly, with Si atoms being packed most densely in {111}, followed by {100} and then {110}, etch rates in aqueous KOH or NaOH follow the trend $R_{\{110\}}>R_{\{100\}}>R_{\{111\}}$.

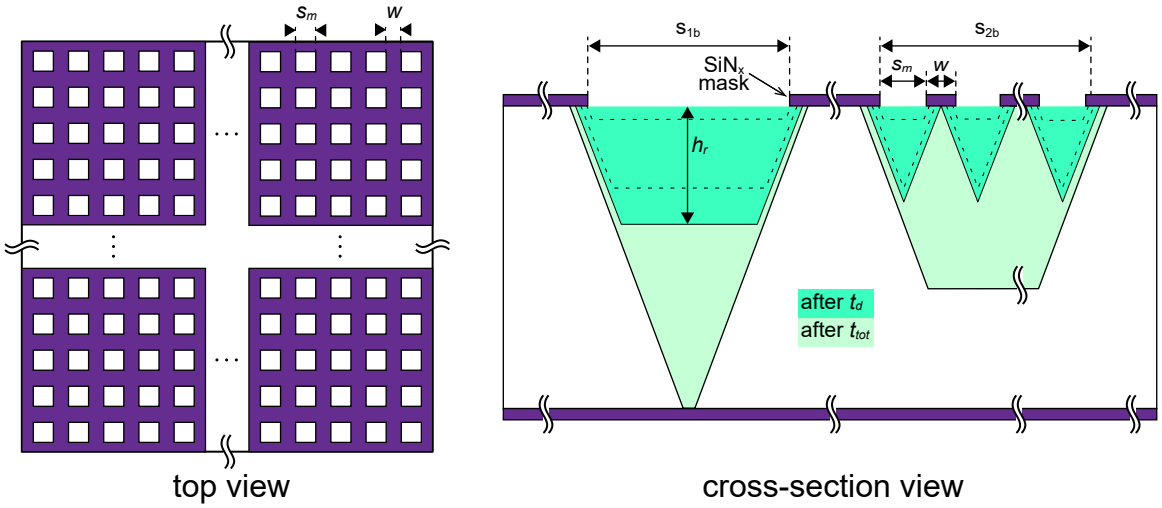


Figure 3.4: Resist-patterned delay of the wet etch. A tightly meshed resist pattern locally suppresses Si removal along the fast-etching {100} planes. The cross-section schematically illustrates etch progression in openly exposed features (s_{1b}) and in features with a delayed etch (s_{2b}).

temperature.[259] While diffusion does not limit the overall etch rate, the temperature dependence of the reaction kinetics is expected to follow an Arrhenius-type law, leading to higher etch rates at elevated temperatures.[260] Moreover, surfaces etched at temperatures above 80 °C exhibit approximately tenfold reduced roughness compared with etching at lower temperature.[261] With respect to concentration, the etch rate increases with the addition of etchant in the low-concentrations regime, as the higher abundance of hydroxide ions accelerates the process. However, for concentrations above ∼20 %, the etch rate levels off and subsequently decreases.

In combination, high temperature and high concentration yield smooth surfaces. At 80 °C and 25 % KOH, the etch-rate ratio $R_{\{100\}}/R_{\{111\}}$ has been reported to be ∼100, making KOH an ideal reagent for many applications that require minimal undercut formation.[252,256] Wet etching of Si with NaOH is slightly less anisotropic, with an etch-rate ratio $R_{\{100\}}/R_{\{111\}}$ of ∼40.[249,262] Using 20 w% aqueous NaOH has been reported to etch Si from {100} faces at a rate of 1.2 µm/min at 80 °C.[249] The anisotropic etch behavior in alkaline solutions can be understood in terms of the plane-dependent packing density of Si atoms and the corresponding accessibility of Si backbonds, as illustrated in Fig. 3.3.

Backside wet etching is sketched in Fig. 3.1c and is performed in two stages. First, the sample is etched at 85 °C in 20 w% (weight-%) aqueous NaOH (Sigma-Aldrich), which enables dynamic etch-rate control through the use of a close-meshed grid, as shown in Fig. 3.2d. While Si is etched at the nominal rate in the alignment-marker regions, etch progression within the larger windows and PBPs is delayed by the close-meshed SiN_x grid.[250] The delay depends on the grid linewidth, the spacing between the grid elements, and the anisotropic etch rates $R_{\{hkl\}}$ of the crystallographic planes; the method is schematically illustrated in Fig. 3.4.

Initially, Si is etched at the same rate across all exposed areas. Once the etch cones (cyan, area S_{2b}) have fully formed, however, the fast-etching (100) plane is no longer exposed, because sidewalls defined by {111} planes meet at the tip. This temporarily halts etching along the [100] direction until time t_d, when the SiN_x grid has been fully underetched by the much slower lateral etching of {111} planes. From this point onward, the etchant can again access the (100) plane without restriction. While the (100) face is temporarily protected by the SiN_x grid, openly exposed features, such as the alignment markers, can continue etching at the nominal rate (cyan, region S_{1b}); consequently, a delay h_r is introduced between the etch fronts. Thus, by the time the openly exposed features have etched through the substrate, a thin Si layer remains within the delayed features (light green). The resulting thickness h_r of the remaining substrate depends on the applied grid geometry: the grid linewidth w, the width of the exposed openings s_m, and also the etch-rate ratio $R_{\{100\}}/R_{\{111\}}$. When a small

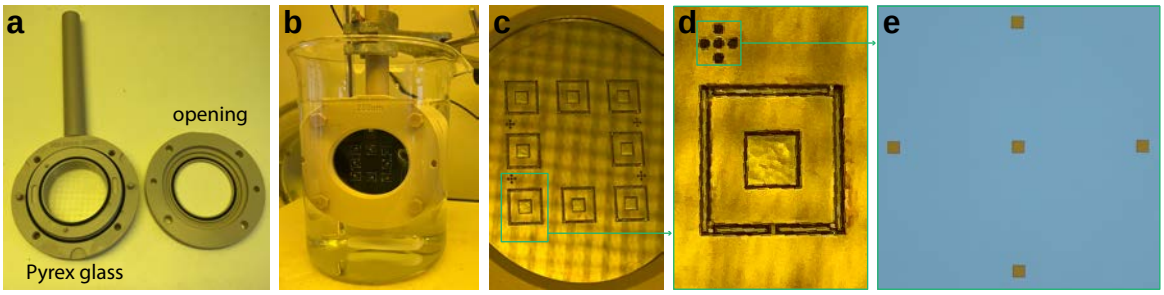


Figure 3.5: Si wet etching using SiN_x device layer as an etch mask. (**a**) A wet-etch chuck protects the device-layer SiN_x during (**b**) the alkaline wet-etch procedure. (**c**) Photograph of the full wafer and (**d**) close-up view of a single chip showing the etched features, including the SiN_x window, PBPs, and alignment markers. (**e**) Micrograph of an alignment marker as observed on the device layer.

delay is desired, lower ratios are favorable, since $h_r \propto R_{\{100\}}/R_{\{111\}}$. Owing to its lower anisotropy compared with KOH, NaOH undercuts the SiN_x grid before the etch front in the alignment-marker regions reaches the opposite substrate face. After underetching the SiN_x grid in aqueous NaOH, the reaction is quenched, the sample is rinsed, and subsequently transferred to a 25 w% aqueous KOH solution at the same temperature. The sample is then etched in KOH with reduced undercut formation until the alignment markers become fully transparent. For both reactions, in KOH and NaOH, the etch rate $R_{\{100\}}$ of Si at 85 °C is approximately 1.55 µm/min.[251] Figure3.5 shows the sample after wet etching and the wet-etch chuck (AMMT, Single OW) used to protect the device layer from the etch solution.

3.2.4 Patterning the SiN_x device layer

With alignment markers in place for back-to-front alignment of the features—namely, the backside-opened windows and the transducers defined in the frontside device layer—the device layer can be patterned. This fabrication step is sketched in Fig. 3.1d. The SiN_x device layer is machined using the same techniques as for preparation of the mask layer, and the procedure follows the same sequence: spin coating of the adhesion promoter AR 300-80 new, followed by spin coating of the photoresist S1805, photolithography, development in MF-319, and a final dry-etch sequence to (i) shape the transducers using a CHF_3/O_2 mixture and (ii) remove residual resist with a mild O_2 plasma to obtain a clean SiN_x surface.

3.2.5 Suspending the SiN_x device layer

With the SiN_x transducers defined in the device layer, the individual chips are broken off from the substrate, and subsequent processing is performed on single chips, as shown in Fig. 3.6a. To suspend the device layer, the sample is etched again in 25 % aqueous KOH, however at a reduced temperature of 65 – 75 °C. This lowers the reaction rate and, consequently, the rate of H_2 generation, thereby providing the mild conditions required to suspend the device layer gently without breakage. During suspension, the SiN_x of the device layer is freely exposed and etched at a very low rate of approximately 0.15 – 0.3 nm/min, depending on temperature. This material loss is compensated by initially depositing a thicker SiN_x film than the target thickness. The reaction is stopped once the windows become fully transparent.

Afterwards, the etchant is diluted with 65 °C warm DI water to a target concentration of <0.1 %, while keeping the sample immersed at all times. The reaction is then quenched in DI water for 40 min before performing a second solvent exchange: the DI water is replaced with 50 °C warm IPA—again keeping the sample immersed at all times—until the solution reaches a water concentration of <0.5 %. The sample is then kept in 50 °C warm isopropyl alcohol (IPA) for 10 min to allow residual H_2O to desorb from the SiN_x surface. Finally, the sample is lifted out of the solvent and held just above the solvent level for an additional 10 min, allowing it to dry gently in an IPA-enriched atmosphere and thereby reducing stress induced by the solvent's surface tension. The result is sketched in Fig. 3.1e, and exemplary structures obtained after suspension are shown in Fig. 3.6b – d.

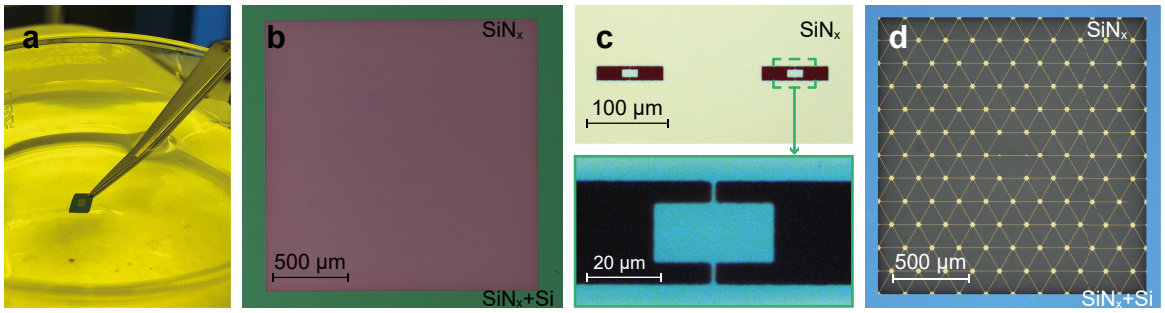


Figure 3.6: Suspending SiN_x structures using Si wet etching. (**a**) Devices are released by Si wet etching of single chips. The approach is applicable for suspension of (**b**) unpatterned SiN_x membranes as well as patterned films, such as (**c**) simple torsional paddles or (**d**) more complex architectures incorporating a PnC.

3.2.6 Attachment of magnetic sample

After successful fabrication of the SiN_x transducers, a magnetic nanotube (NT) is transferred onto the transducer using a micromanipulator (Narishige) and attached with UV-curable glue (Norland Optical Adhesive, NOA 60). The NT consists of amorphous cobalt iron boron ($Co_{20}Fe_{60}B_{20}$) surrounding a non-magnetic gallium arsenide (GaAs) core with a hexagonal cross-section. The NT has an outer diameter of approximately 260 nm, including the ferromagnetic CoFeB shell, which is (30 ± 2) nm thick.[70]

The micromanipulator system is a hydraulic apparatus that enables controlled motion of the manipulator arms in the x, y, and z directions with sub-µm precision. For this application, the manipulator arms are equipped with extremely fine glass needles. The needles are fabricated from glass rods (Narishige, G-1000) using a needle puller (Narishige, PC-100), yielding tips with a diameter of ∼0.5 µm.

3.2.7 Reshaping the SiN_x transducer by gallium FIB milling

FIB milling is a highly versatile technique in science and industry for shaping solid materials on the micro- to nanometer scale. This fabrication step is sketched in Fig. 3.1,**f**. We use a dual-beam FIB-SEM (FEI Helios Nano Lab 650) at the Nano Imaging Lab (University Basel) to mill the SiN_x surface and remove material. The system employs gallium ions (Ga^{3+}) and provides acceleration voltages of up to 30 kV. FIB milling enables the creation of precise features, such as high-aspect-ratio holes and conical geometries, for applications including nanopore fabrication,[263,264] biosensors,[265] and sample preparation for transmission electron microscopy (TEM), e.g., lamella cutting.[266] However, patterning suspended SiN_x films with a gallium FIB can be challenging due to ion-beam-induced charging of the target, re-deposition, thermal damage, and material swelling caused by ion implantation.[267,268] Mitigating these effects requires careful tuning of FIB parameters, such as beam focus, acceleration voltage, and ion current, depending on the task.

In this work, FIB milling is used to reshape and refine transducers that were previously fabricated using PECVD, photolithography, and RIE, as described in Sec. 3.2.1 – 3.2.5. Prior to FIB milling, a thin 2 nm-thick gold film is sputtered onto the existing transducer to protect the SiN_x structure from damage due to electrostatic charging.

3.2.8 Torque transducer designs

This section describes the designs of all SiN_x-based torque transducers that were fabricated and experimentally characterized in the course of this thesis.

Simple torsional paddles

In a first attempt, we fabricate simple torsional paddles without a phononic crystal. The lithography design is shown in Fig. 3.7, together with optical images of the resulting torsional paddle embedded in a free-standing SiN_x membrane. After mechanical characterization of this initial device, its lateral

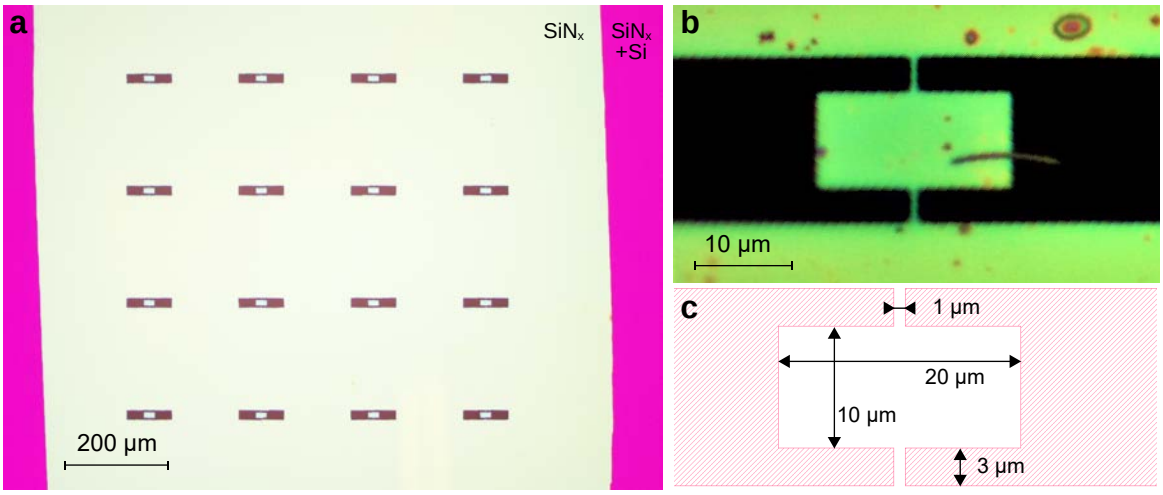


Figure 3.7: First fabricated torque transducer: torsion paddle 1. (**a**) Free-standing SiN_x film featuring a 4×4 array of identical torsional paddles. (**b**) Optical micrograph after attachment of a magnetic CoFeB nanotube. (**c**) Optical lithography layout used for the fabrication of the torque transducers.

dimensions are further refined by gallium FIB milling, with the aim of reducing the span width to ∼200 nm. We refer to the first device as torsion paddle 1 and to the second device, produced by FIB milling, as torsion paddle 2. More detailed SEM images, including measured dimensions, are provided in Fig. 3.16 and 3.17 in Sec. 3.4.1.

Torque transducers embedded in a PnC

After successfully fabricating the simple torsional paddles, we proceed to transducers embedded in a PnC. The three lithography designs used to pattern the device layer are shown in Fig. 3.8. The first device, PnC paddle 1, incorporates a PnC composed of 13×7 unit cells. The other two devices, PnC paddle 2 and PnC beam 1, incorporate a PnC with 10×6 unit cells. For all devices, the unit cell measures 175 µm × 301 µm. The hexagonal PnC platforms are 30 µm across, and the tethers are designed to be 3 µm wide. PnC paddle 1 and 2 use a torsional paddle as the defect center, whereas PnC beam 1 uses a double-clamped beam. For PnC paddle 2, seven torsional paddles with varying bridge span widths are fabricated in parallel, increasing the probability of obtaining a torsional paddle with the target span width of ∼2.0 µm.

3.3 Preparation of few-layer samples from vdW materials

Van der Waals (vdW) materials are uniquely suited for fabrication of so-called 2D materials with only few atomic layers due to their strong covalent intra-plane bonding in concert with their comparatively weak inter-layer adhesion solely by weak van der Waals interaction. This combination makes them ideal for cleavage along the atomic plane to yield few- or even mono-layers which can be re-combined with pristine interfaces to create heterostructures with unprecedented thermal, optical, electronic, and magnetic properties.[37] Exploration of this extremely rich zoo of low-dimensional combined materials and their behavior holds the prospect to control and engineer their physical properties and tailor them towards improvement of existing devices and development of new technologies.

3.3.1 Exfoliation from bulk vdW crystal

Production of vdW heterostructures starts with exfoliation of bulk crystal by micro-mechanical cleaving. By this method, the thickness of the starting material is gradually reduced down to only few layers or even a mono-layer.[149,269] In this form, extremely fragile vdW materials—as for example VBr_3 sample which is highly hygroscopic—can be encapsulated with hBN for protection. Since hBN is inert under ambient conditions, it can be easily exfoliated in atmosphere. Highly air-sensitive materials on the other hand, must to be handled inside a protective environment at all times prior

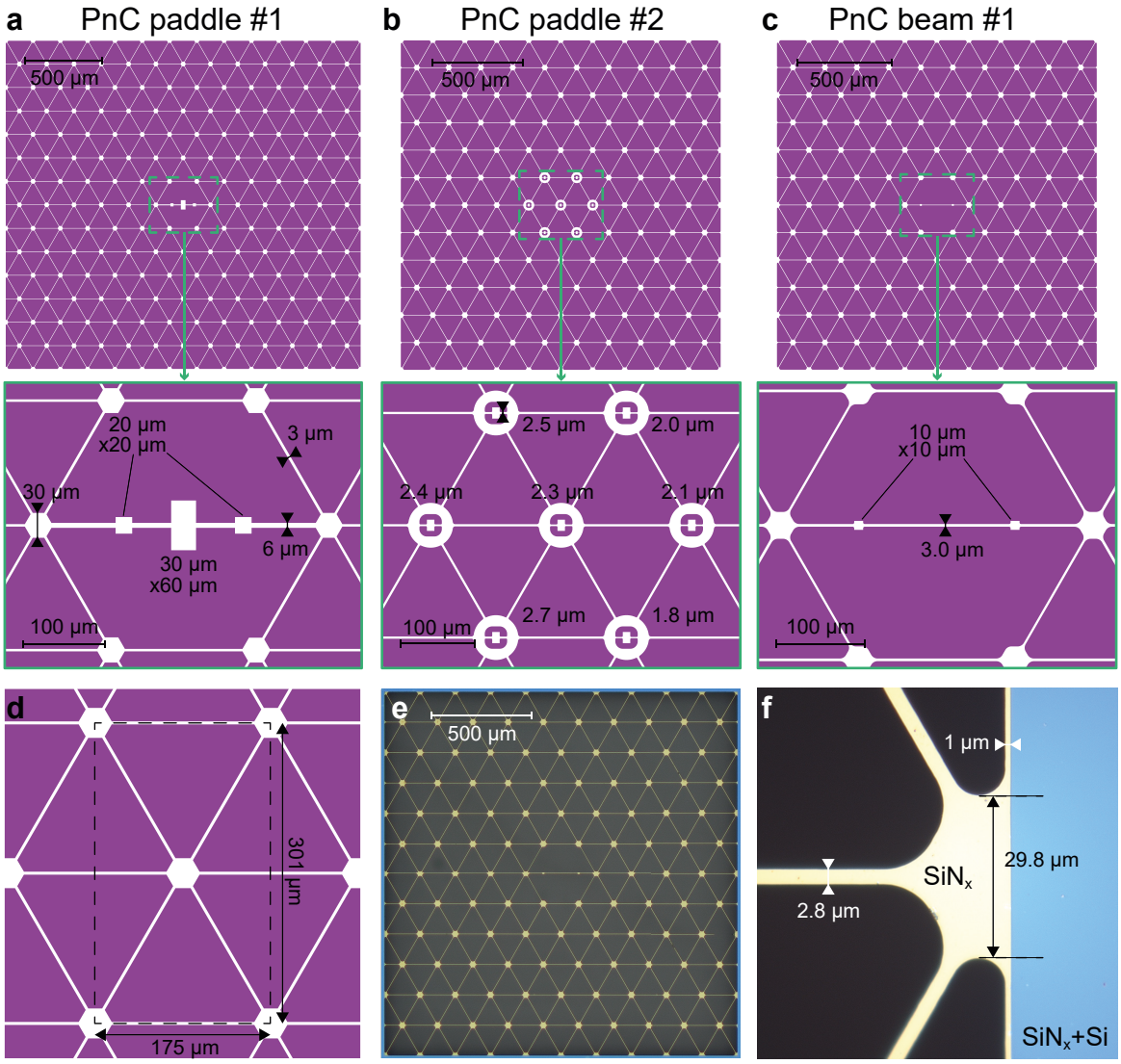


Figure 3.8: Torque transducer designs with PnC surround. Lithography mask layouts of (**a**) PnC paddle 1, (**b**) PnC paddle 2, (**c**) PnC beam 1, and (**d**) the PnC unit cell. PnC paddle 2 integrates seven torsional paddles. Each paddle consists of a 15 µm × 10 µm central platform (width×length) connected by a 10 µm-long bridge on either side, with bridge widths varied between paddles. Optical micrographs show (**e**) a complete PnC device and (**f**) a ∼1 µm mismatch between the Si frame and the PnC pattern.

to encapsulation. Hence, such materials are exfoliated inside a dedicated inert gas glovebox system (Braun UNIlab pro) under N_2-atmosphere with O_2- and H_2O-levels controlled below 2 ppm. Under these conditions, thin-layers of VBr_3 and especially its mono-layer specimen still degrades within 24 h. This requires VBr_3 to be exfoliated and encapsulated on the same day.

hBN is exfoliated using adhesive tape (Nitto, ELP BT-130E-SL), while regular adhesive tape (Scotch Magic Tape) is used for exfoliation of VBr_3. For both materials, it is recommended to use two separate pieces of tape for exfoliation instead of using a single piece which is then folded onto itself. Using two separate pieces improves yield of larger flakes. One of the tapes is fixed on the bench using double-sided tape, and a bulk piece of vdW crystal is place on it. Then, the second tape is placed on top of the bulk crystal, and after making good contact it is exfoliated once, and the bigger of the two exfoliated bulk pieces is removed from the tape with tweezers. The vdW material remaining on the tapes can now be thinned down by repeating exfoliation. It is best to keep the contact angle as low as possible when separating the tapes to reduce the risk of cracking flakes. Once the few-layer regime has been achieved—i.e., when exfoliated material on the adhesive tape are almost invisible by eye—the flakes are transferred to a Si substrate with a 285 nm SiO_2 layer (NOVA Electronic

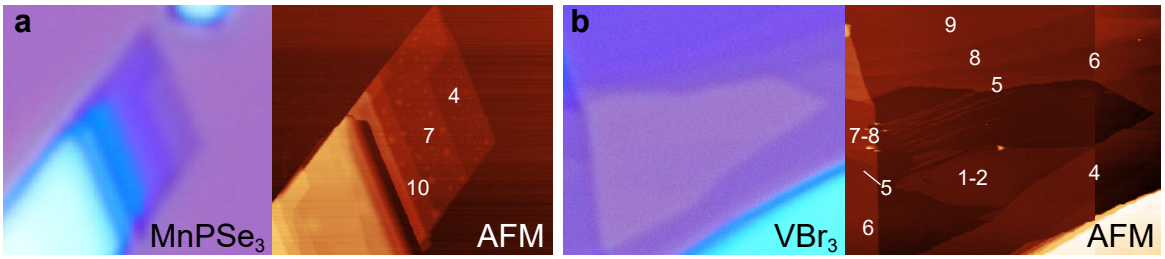


Figure 3.9: Mechanical exfoliation of vdW materials Few-layer regions of vdW magnets (**a**) $MnPSe_3$ and (**b**) VBr_3 identified using optical microscopy combined with atomic force microscopy. Numbers indicate the number of layers determined using AFM.

Materials). The substrate is pre-treated using RIE (20 sccm O_2, 60 mTorr, 30 W for 5 min) and baked for 3 h at 200 °C before exfoliation. O_2-plasma slightly increases the substrate's surface roughness to improve adhesion of flakes, while heating for an extended period inside the glovebox helps remove residual moisture from the surface. For efficient transfer from tape to Si substrate, the tape is gently pressed against the substrate to make good contact. After letting the assembly rest for about a minute, the tape is very slowly released from the chip at the lowest possible contact angle. A few exemplary exfoliation results are shown in Fig. 3.9. Exfoliated flakes are inspected under the optical microscope to identify specimen with only few layers, and their exact thickness is determined using an atomic force microscope (Nanosurf, Drive AFM) before further processing.

3.3.2 Isolation of flakes

Often times, the most interesting flakes—i.e., thin flakes in the few- to mono-layer limit, or flakes that feature multiple regions with different suitable layer-numbers and sufficient lateral size—are located within a dense "forest" of other flakes close-by. Having other flakes nearby can make picking up a given target flake very difficult, or in the worst case impossible. Pick-up is especially hard when flakes in vicinity are substantially thicker than the target object itself. In such cases, they do not only prevent making good contact between the stamp and target flake, but also complicate making a controlled approach as other flakes act as pinning sites for the contact line. In order to still be able to make a sample from such embedded flakes, we use a custom-made scribe holder (machine shop, in-house) which accepts tungsten carbide tips (item 10130–10, Fine Science Tools) with a tip diameter of 1 µm. The scribe holder can be mounted on the micromanipulator arm of the transfer setup. This does not only allow removal of material in the target's vicinity, but also dissection of the target with almost micrometer-precision as shown in Fig. 3.10. The procedure creates numerous smaller chippings from the flakes that are removed or dissected, and parts of the debris can be picked up and removed using a PC/PDMS (poly(bisphenol A carbonate)/polydimethyl siloxane) stamp.

3.3.3 Protection of vdW materials

After all required vdW materials are prepared—i.e. a magnetic flake and an hBN flake for encapsulation—the individual flakes can be picked up and stacked using a PC/PDMS stamp to form

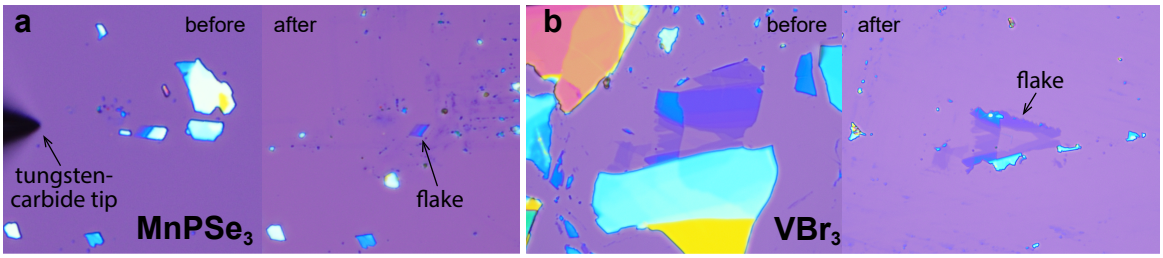


Figure 3.10: Mechanical isolation of flakes. Optical images of (**a**) $MnPSe_3$ and (**b**) VBr_3 before and after removal of adjacent material. Close-up views of the flakes of interest are shown in Fig. 3.9.

a protected magnetic vdW heterostructure. This way, the few-layer vdW magnet is protected from degradation by atmospheric H_2O and O_2 during mounting and alignment in the measurement setup which can take a few hours. We employ the dry transfer technique to stack vdW materials using a PC/PDMS stamp composed of a thin poly(bisphenol A carbonate) film tensioned over a polydimethyl siloxane pad.[270,271] This method provides excellent position and orientation control while stacking, allows fabrication of complex vdW heterostructures, and provides a controlled mechanism for drop off and placement of the final stack.[272] The production of PC/PDMS stamps, the method to pick up, stack, and transfer vdW flakes, and precision dicing are described in the following.

Production of PC/PDMS stamps

The stamp is assembled on a standard microscope slide, which serves as a rigid support for the PC/PDMS stack as schematically shown in Fig. 3.11. The PDMS pad is prepared from commercially available 0.4 mm-thick gel film (Gelpak, DGL film X4), cut into 2 mm × 30 mm strips. The strips are cleaned by immersion in acetone and subsequently in isopropyl alcohol for 1 min each, then dried on a microscope slide with the thinner side facing downward. The dried strips are exposed to O_3 in a UV–ozone cleaner for 10 min. They are then diced into ∼2 mm × 2 mm pieces and mounted onto a clean microscope slide at the center of the hole of previously attached adhesive tape (Scotch Double-Sided Tape), as shown in Fig. 3.11b. The PC film is prepared from a 30 % solution of

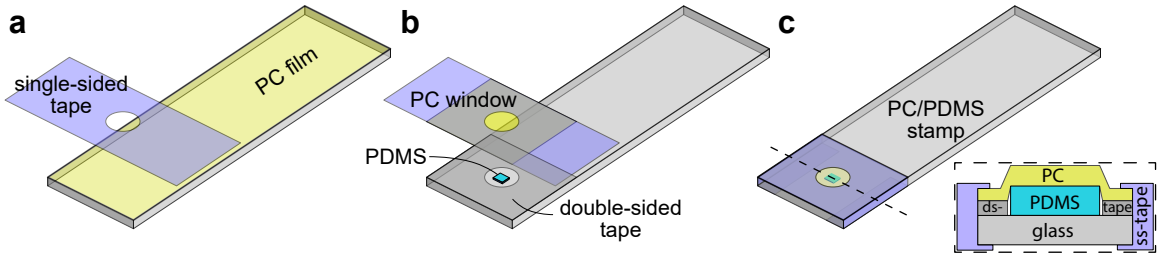


Figure 3.11: Production of PC/PDMS stamp. (**a**) Preparation of window made from PC film, (**b**) assembly of PC/PDMS stamp, and (**c**) product and cross-section view of complete PC/PDMS stamp.

poly(bisphenol A carbonate) in chloroform ($CHCl_3$). Five drops of the solution are dispensed onto a clean microscope slide, and a second clean slide is placed on top. After the solution has fully spread and wetted the interface between the slides, the top slide is removed using a swift, uniform motion. As the $CHCl_3$ evaporates, a thin PC film remains on the substrate. A "PC window" is then formed by using standard adhesive tape with a circular opening as a supporting frame. The framed PC film is aligned above the PDMS pad, slowly lowered, and gently tensioned across it. This yields the assembled PC/PDMS stamp, as schematically shown in Fig. 3.11c. For stamps intended for glove-box operation, the PC film is additionally punctured at a location far from the PC/PDMS stack. This venting prevents bulging of the tensioned PC membrane when the stamp is subjected to vacuum in the glove-box load-lock.

Stacking vdW materials

To cover an air-sensitive vdW magnet with a protective hBN layer, fabrication of the vdW stack begins by picking up the hBN flake first as schematically shown in Fig. 3.12a1 – a2. The PC/PDMS stamp is preferably aligned such that the hBN flake—and thus the final stack—lies close to the stamp's touch point, while remaining offset to allow the contact line to be advanced over the target flake in a controlled manner after initial contact. As the stamp approaches the substrate, a circular interference pattern becomes visible immediately before contact; its center defines the touch point. After contact is established, the temperature is increased to 60 °C, causing thermal expansion of the stamp and a radial growth of the contact area from the touch point. The contact line is allowed to advance until just before reaching the target flake. Further advance is inhibited by steadily retracting the stamp while it continues to expand. Images of the procedure are shown in Fig. 3.13.

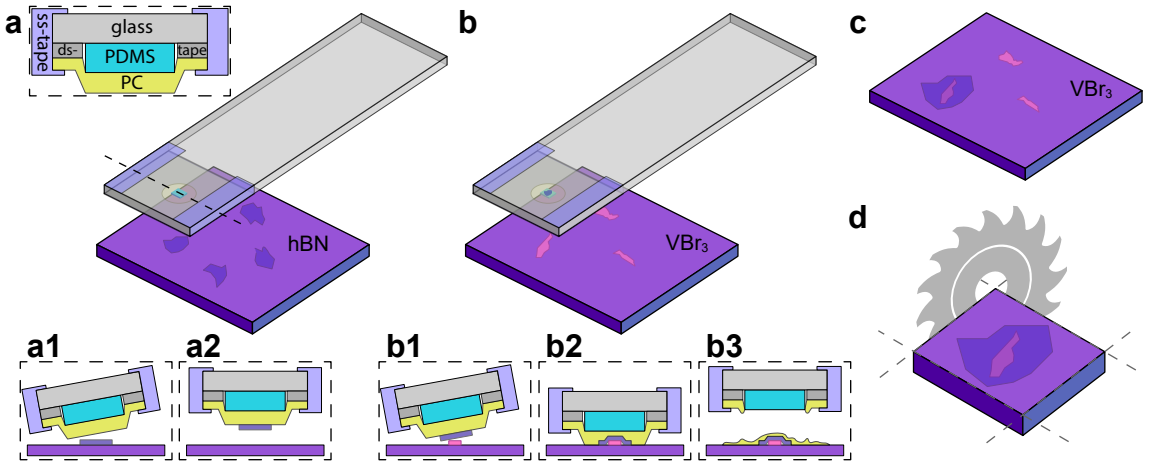


Figure 3.12: Stacking and transfer of vdW materials and precision dicing. (**a**) Pick-up of hBN flake, (**b**) transfer of hBN on top of magnetic vdW material by melting the PC film, (**c**) vdW material covered by hBN after removal of PC residues, and (**d**) precision dicing of chiplets to locate magnet near the chip edge.

The temperature is then increased to 90 °C, and the contact area is permitted to extend across the target flake and by an additional ∼100 – 150 µm. Any further propagation of the contact line is again suppressed by continuous, controlled retraction of the stamp during the temperature ramp. Once 90 °C is reached, the stamp is held in this configuration for 2 min to promote intimate contact between the PC film and the vdW flake, thereby improving adhesion.

Subsequently, the sample is cooled in 5 °C increments. During cooling, the stamp contracts and the contact line retracts slowly; the target flake is picked up as the contact line recedes.

The substrate chip can then be exchanged for a second chip carrying another exfoliated vdW material (e.g., VBr_3 or $MnPSe_3$), and the approach sequence is repeated: the PC/PDMS stamp is brought into contact, the contact line is advanced across the flake, and the stamp is subsequently retracted to retrieve the target flake. Iterating this procedure enables stepwise assembly of a vdW heterostructure on the stamp.[270–272]

Deterministic transfer

Finally, after picking up either a single flake or many flakes to form a multilayer vdW heterostructure, the material can be transferred to a designated target position using a temperature-controlled release sequence, as illustrated in Fig. 3.12b1 – b3. The stamp is first brought into contact with the target substrate surface. The flake/heterostructure is then released by heating to 170 °C, where the PC melts and the flake/heterostructure is deposited onto the substrate. During melting, the PC film detaches from the PDMS, allowing the stamp to be retracted slowly while leaving the sample on the

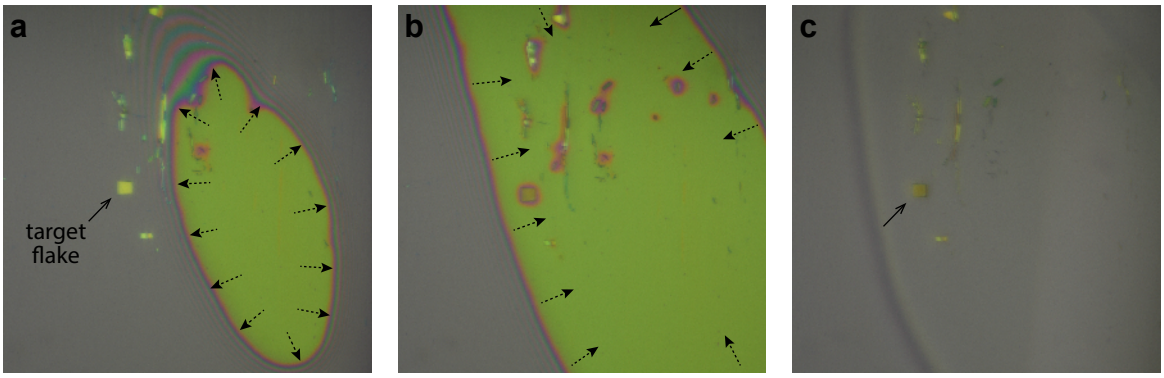


Figure 3.13: Pick-up of vdW flake. (**a**) Before advancing the contact line across the target flake, (**b**) before retracting the contact line, and (**c**) after pick-up.

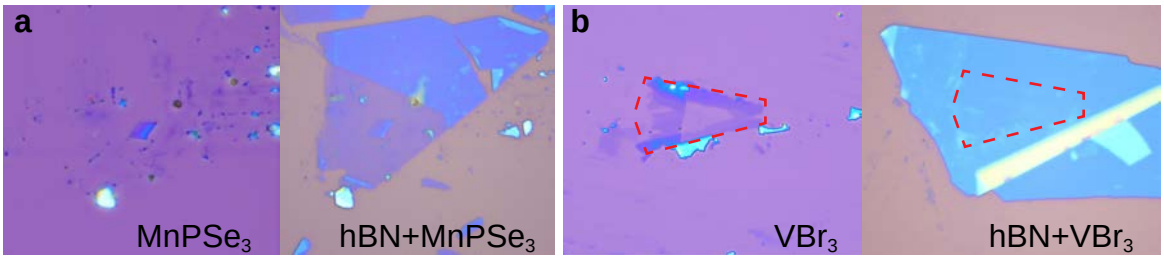


Figure 3.14: Encapsulation of vdW magnet with hBN. (**a**) $MnPSe_3$ and (**b**) VBr_3 before and after capping with hBN.

chip together with residual PC (Fig. 3.12b3).

Residual PC is removed by immersing the entire chip in dichloromethane (CH_2Cl_2) for 10 min at room temperature. Gentle immersion with minimal agitation reduces the likelihood of detaching the sample during this cleaning step. Examples of hBN capping are shown for $MnPSe_3$ and VBr_3 in Fig. 3.14.

For air-sensitive vdW materials, optimal protection is achieved by full, double-sided encapsulation with hBN or graphene and is essential for highly sensitive materials, particularly in the few-layer limit.[273] This provides superior sealing due to the atomically flat interfaces, while in contrast, partial encapsulation can still permit gradual ingress of air through microscopic channels associated with the finite roughness of the substrates SiO_2 surface. Nevertheless, if a sensitive flake cannot be retrieved (and full encapsulation is therefore not feasible), one-sided hBN coverage can serve as a fallback approach and may provide transient protection, depending on how air-sensitive the material is.[273,274]

Precision dicing

Sometimes, flakes of interest cannot be retrieved with the PC/PDMS stamp because their adhesion to the Si exfoliation substrate is too strong. Consequently, such flakes cannot be incorporated into a vdW heterostructure or deterministically positioned at a defined location on the target chip. For measurements with our nanowire magnetic force microscopy setup, the vdW magnet must be located within approximately 50 µm of the chip edge. When deterministic transfer fails to meet this positional requirement, we define the chip geometry by precision dicing.

Prior to dicing, the chip surface carrying the vdW sample is protected with a ∼230 nm layer of PMMA 950K (Kayaku Advanced Materials), spin-coated at 4000 rpm for 40 s and cured at 180 °C for 60 s. The chip is then diced using an automatic dicing saw (DAD 3240, Disco), as illustrated in Fig. 3.12d. The dicing blade has a width of 45 µm, which sets the width of the cutting trench. After dicing, the PMMA is removed by immersing the sample in acetone for several minutes. This procedure enables placement of vdW heterostructures in close proximity to the chip edge with high precision and high yield; two representative examples are shown in Fig. 3.15.

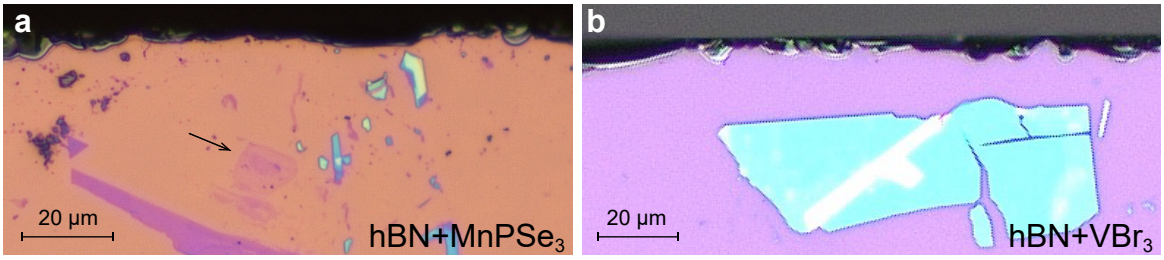


Figure 3.15: Precision dicing of Si chips. Examples of (**a**) $MnPSe_3$ and (**b**) VBr_3 positioned within 30–40 µm from the chip edge after dicing. Chipping near the newly created edge happens on the order of about 5 µm away from the cutting trench.

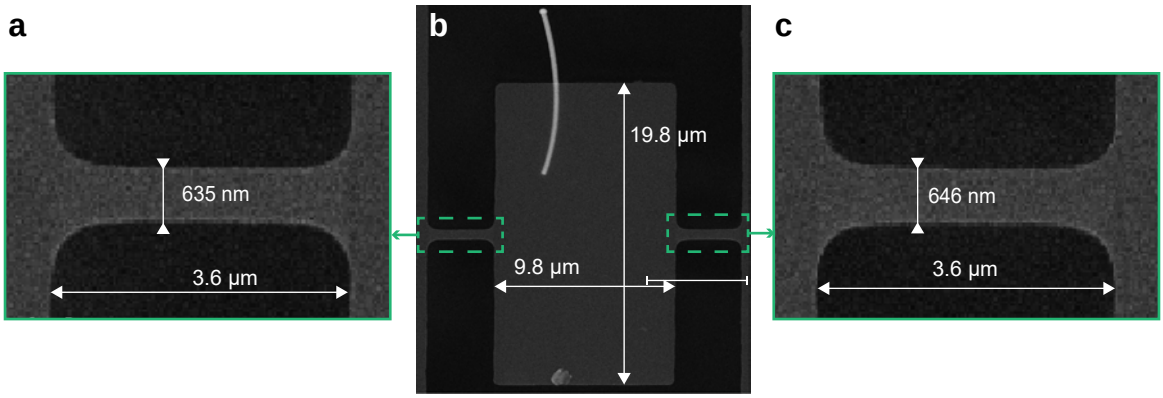


Figure 3.16: SEM micrographs of torsion paddle 1. (**a**) Left bridge, (**b**) complete device, and (**c**) right bridge.

3.4 Results

Following the fabrication of SiN_x-based torque transducers with and without phononic crystals (PnCs) in Sec. 3.2 and the preparation of few-layer samples of magnetic vdW materials in Sec. 3.3, we present the corresponding results. We first report the fabrication outcomes for the simple torsional paddles, and subsequently for the more complex torsional transducers integrated into a PnC. The section concludes with the results of preparing magnetic vdW materials in the few-layer to monolayer regime, including their protective encapsulation with hBN.

3.4.1 Standalone torsional paddles

SEM images of the first SiN_x torsional paddles fabricated using standard microfabrication procedures—PECVD of SiN_x, lithography, dry etching, and wet etching—are shown in Fig. 3.16. We refer to this device as torsion paddle 1. Ellipsometry of the SiN_x film yields a nominal thickness of (198 ± 10) nm, in good agreement with the thickness reduction expected from SiN_x loss during wet etching.

The lateral dimensions of the bridge segments in torsion paddle 1 are up to 0.4 µm smaller than specified in the lithography design. Consistent with this reduction, the corresponding bridge spans are slightly longer than intended. In addition, the abutments and midspan junctions are rounded rather than forming sharp right angles, which we attribute to the finite spot size of the direct laser writer. The measured span widths of 635 nm and 646 nm are on the order of the laser writer's resolution (∼1 µm).

Following mechanical characterization of torsion paddle 1, we further refine the bridge spans by focused ion beam (FIB) milling. After this post-processing step, the span width is reduced to ∼219 nm, and the abutments and midspan junctions exhibit well-defined right angles. This yields a transducer with bridge dimensions well below the direct laser writer's resolution. The resulting

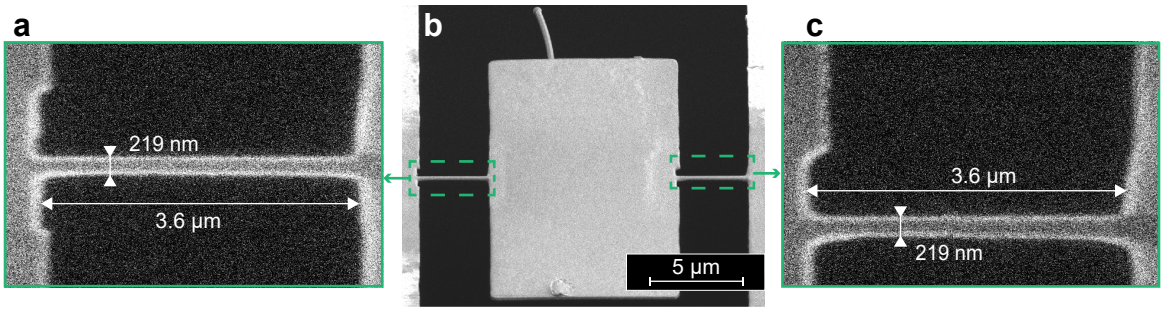


Figure 3.17: SEM micrographs of torsion paddle 2 after FIB milling. (**a**) Left bridge, (**b**) complete device, and (**c**) right bridge. Micrographs are acquired at a tilt; therefore, the paddle width (vertical axis) appear reduced. Images (**a**) and (**c**) were cosmetically edited to remove measurement annotations only; the unmodified originals are provided in Appendix A.1.1.

Table 3.1: Dimensions of torsion paddles 1 and 2. Comparison of design and fabricated dimensions, including percent deviations. Averaged values are given for the bridge segments.

torsional paddle	data	d [nm]	d^{err} [%]	w_{b} [nm]	$w_{\mathrm{b}}^{\mathrm{err}}$ [%]	l_{b} [µm]	$l_{\mathrm{b}}^{\mathrm{err}}$ [%]	w_{p} [µm]	$w_{\mathrm{p}}^{\mathrm{err}}$ [%]	l_{p} [µm]	$l_{\mathrm{p}}^{\mathrm{err}}$ [%]
1	design	200	−1	1000	−36	3.1	16	20.0	−1	10.0	−2
	fabrication	199		641		3.6		19.8		9.8	
2	design	—	—	200	10	3.6	0	—	—	—	—
	fabrication			219		3.6					

Note: d denotes the thickness, w (l) the width (length), subscript b (p) the bridge (paddle), and — indicates data not available.

device is shown in Fig. 3.17 and is referred to as torsion paddle 2.

Measured dimensions for torsion paddles 1 and 2 are summarized in Tab. 3.1, together with the corresponding design values and relative deviations. Overall, FIB reshaping enables the fabrication of torque transducers with bridge segments only a few hundred nanometers wide. This advantage comes at the cost of gallium implantation and low throughput, since FIB processing is performed serially on individual devices, in contrast to parallel lithographic fabrication.

3.4.2 Torsional paddles embedded in a PnC

The SiN_x torque transducers embedded in a PnC that are investigated in this work are shown in Fig. 3.18a – c. As a first design iteration, we fabricated a single, comparatively large torsional paddle with long bridge spans located at the center of the PnC; this device is referred to as PnC paddle 1.

The second device incorporates seven torsional paddles with equal platform size and different bridge-span widths. This multi-paddle layout is motivated by the observation that feature sizes defined by optical lithography can deviate by up to ±0.6 µm from the nominal design, primarily due to small variations in the laser focus between exposures. By fabricating seven paddles in parallel, each with a different bridge-span width, we increase the likelihood of obtaining a resonator with a bridge width close to the target value of 2.0 µm, such that the fundamental torsional resonance lies within the phononic band gap. This device is denoted PnC paddle 2.

Finally, we fabricated a third device in which the central defect forms a double-clamped flexural beam, referred to as PnC beam 1. This design is used to assess whether the second-harmonic of flexural mode of the beam can serve as the sensing mode for dynamic torque magnetometry. Measured dimensions of all PnC devices—PnC paddles 1 and 2, and PnC beam 1—are summarized in Tab. 3.2, together with the corresponding design values (see also Fig. 3.8) and the resulting percent deviations. Overall, the fabricated lateral dimensions agree well with the designs, with percent deviations below 24 %. The largest apparent deviation, up to 2 µm in l_b for PnC paddle 1 and PnC beam 1, occurs for measurements performed with a 20x objective, indicating a larger measurement uncertainty compared to measurements acquired with 50x or 100x objectives. Restricting the analysis to data obtained with 50x and 100x objectives, the maximum deviation is 0.6 µm, comparable to the photolithographic transfer fidelity previously observed for torsion paddle 1 in Sec. 3.4.1.

A detailed analysis of the SiN_x thickness for PnC paddle 2 and PnC beam 1 is provided in App. A.2, and the results are given in Tab. 3.2. The SiN_x thicknesses are estimated from the etch rates of SiN_x in aqueous KOH and the exposure time during device suspension. For PnC paddle 1, we do not provide a thickness estimate because uncontrolled exposure of the device layer—caused by etchant leakage into the wet-etch chuck cavity during the first backside wet etch—results in substantial, poorly constrained uncertainty in the thickness estimate.

In contrast, the SiN_x thicknesses of PnC paddle 2 and PnC beam 1 are calculated based on well-controlled etch conditions, giving final values of (116 ± 10) nm and (108 ± 10) nm, respectively. These values are close to the designed target value of 100 nm, corresponding to percent deviations of (16 ± 10) % for PnC paddle 2 and (8 ± 10) % for PnC beam 1. Disregarding the SiN_x thickness of PnC paddle 1, the designed PnC geometries are reproduced with high fidelity, with deviations of only a few percent. The PnC unit cell is well defined, with dimensions of ∼175 µm × 301 µm. Moreover,

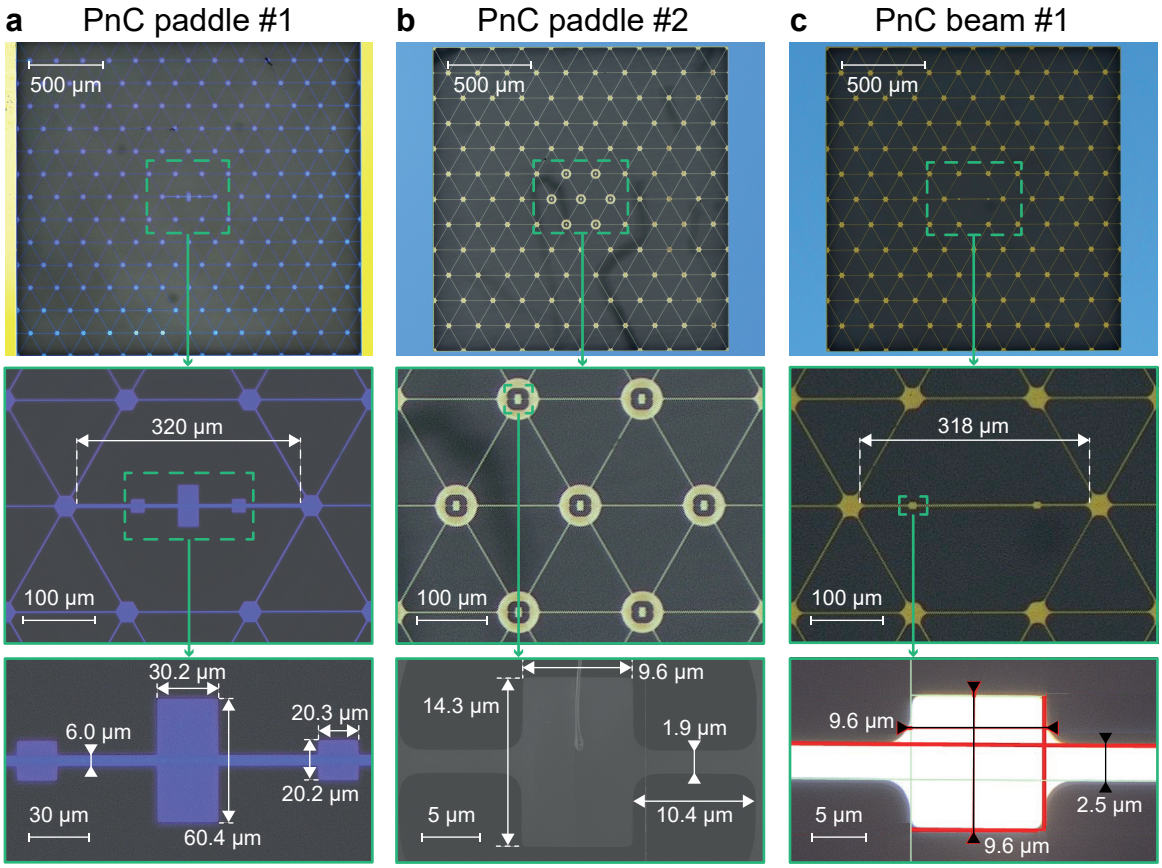


Figure 3.18: SiN_x torque transducers in a PnC surround. (**a**) PnC paddle 1, (**b**) PnC paddle 2, and (**c**) PnC beam 1. The bottom image in (**c**) was cosmetically edited to remove measurement annotations only; the unmodified original is provided in Appendix A.1.1.

the lateral offset between the Si frame and the SiN_x window is on the order of 1 µm, as shown in Fig. 3.19. This offset arises because the Si window etched from the backside becomes slightly larger than intended, rather than from a front-to-back alignment error. Indeed, the back-to-front alignment between the cavity defined in the mask layer and the PnC membrane in the device layer is excellent. The dimensions of the hexagonal PnC platforms and tethers are likewise well controlled and agree with the design to within 0.2 µm.

Table 3.2: Dimensions of PnC paddle 1, PnC paddle 2, and PnC beam 1. Comparison of design and fabricated dimensions, including relative errors.

PnC	data	d [nm]	d^{err} [%]	w_{b} [µm]	$w_{\mathrm{b}}^{\mathrm{err}}$ [%]	l_{b} [µm]	$l_{\mathrm{b}}^{\mathrm{err}}$ [%]	w_{p} [µm]	$w_{\mathrm{p}}^{\mathrm{err}}$ [%]	l_{p} [µm]	$l_{\mathrm{p}}^{\mathrm{err}}$ [%]
paddle 1	design	175	—	6.0	0	319	0	60.0	1	30.0	1
	fabrication	—		6.0		320		60.4		30.2	
paddle 2	design	100	16	2.5	−24	10.0	4	15.0	−5	10.0	−4
	fabrication	116 ± 10		1.9		10.4		14.3		9.6	
beam 1	design	100	8	3.0	−17	316	1	10.0	−4	10.0	−4
	fabrication	108 ± 10		2.5		318		9.6		9.6	

Note: d denotes the thickness, w (l) the width (length), subscript b (p) the bridge (paddle), and — indicates data not available.

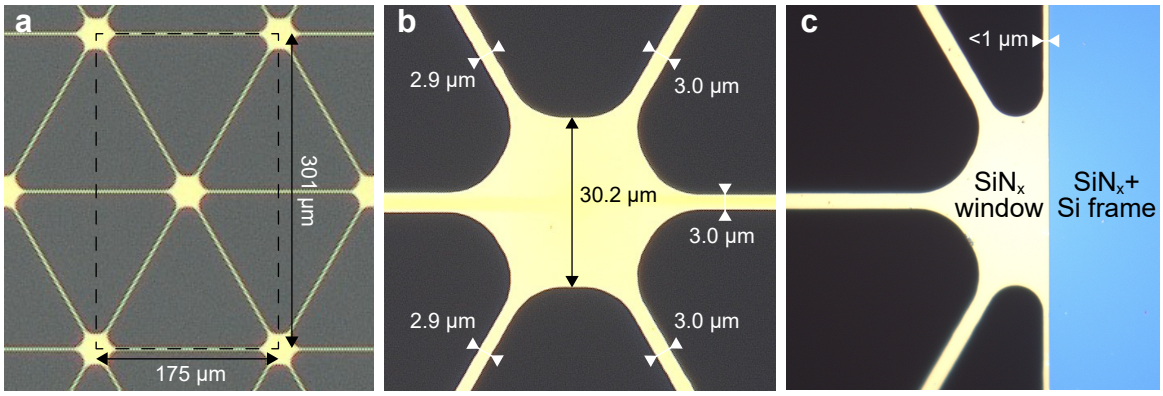


Figure 3.19: PnC structure and back-to-front alignment. (**a**) PnC unit cell. (**b**) PnC platform and bridge segments. (**c**) Back-to-front alignment between the suspended PnC membrane and supporting Si frame.

3.4.3 Few-layer samples from vdW materials

By following the exfoliation and protection protocol described in Sec. 3.3, we can prepare few-layer flakes of the vdW magnets $MnPSe_3$ and VBr_3 and temporarily mitigate air-induced degradation by capping them with hBN. Precision dicing further enables reliable positioning of a selected flake close to the edge of a substrate chip. In three trials, this approach succeeded in all cases where dry transfer using a PC/PDMS stamp failed. Representative samples are shown in Fig. 3.14, with corresponding AFM characterization in Fig. 3.9.

We also evaluated direct stamping of vdW material onto free-standing SiN_x membranes using the vdW magnet CrSBr. Despite the membrane thickness of only 50 nm, we found that vdW flakes can be transferred onto the membrane without rupturing it. An example of successful placement using dry viscoelastic transfer is shown in Fig. 3.20. Notably, the membrane remains intact even when the PC/PDMS stamp establishes extended contact across the full area of the suspended SiN_x window.

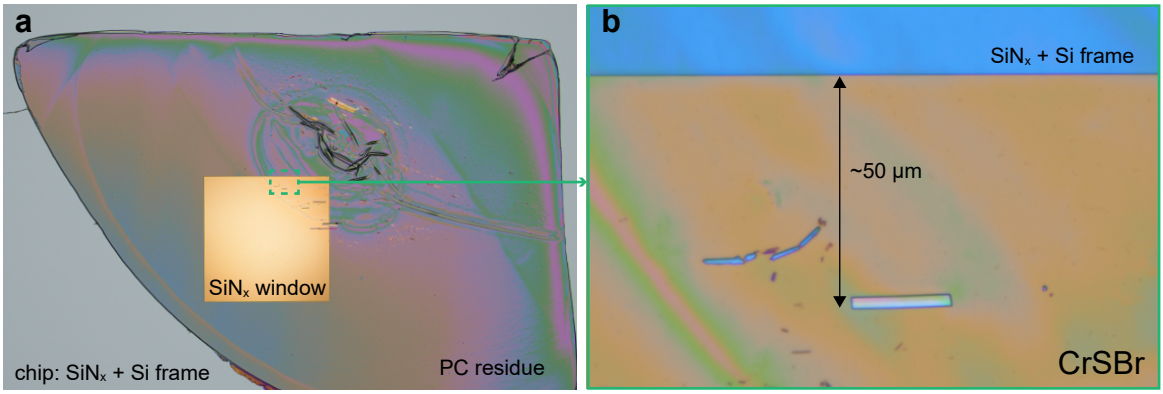


Figure 3.20: Stamping vdW material CrSBr directly onto a suspended SiN_x membrane. (**a**) Overview of 50 nm-thick SiN_x window after transfer of the vdW magnet CrSBr. (**b**) Magnified view of the same sample.

3.5 Discussion

Our results demonstrate the fabrication of suspended SiN_x torque transducers both with and without an integrated PnC surround. Using standard microfabrication processes—PECVD deposition of SiN_x, optical lithography, reactive ion etching, and wet etching of Si—we obtain SiN_x-based mechanical torque transducers with high dimensional accuracy and good reproducibility. Lateral feature dimensions defined above the direct laser writer resolution limit are formed with high fidelity, exhibiting deviations below 24 % relative to the nominal design. The fabrication method yields SiN_x

thicknesses close to the target value of 100 nm, with deviations below ∼16 % under controlled Si wet-etch conditions. Back-to-front alignment of features—for opening the cavity from the wafer backside and patterning the PnC structure on the frontside—is excellent, with negligible offset and rotational registration errors, while the size mismatch is on the order of ∼1 µm.

Run-to-run dimensional imprecision is primarily attributed to changes in the effective laser spot size arising from small variations in focus settings. Such focus variations can translate into dimensional offsets of up to ±0.6 µm while working comfortably above the laser writer's resolution limit. One strategy to mitigate this sensitivity is to pattern multiple transducers with deliberately varied dimensions within a single device, as implemented for PnC paddle 2. In this approach, bridge widths are distributed around a target value, thereby increasing the likelihood of obtaining at least one device within the desired tolerance.

Finally, we show that an already-fabricated torque transducer—initially defined by lithography followed by dry and wet etching—can be further refined by FIB milling. This post-processing enables SiN_x resonator features below the direct laser writer's resolution limit, as demonstrated by torsion paddle 2 with a bridge width of only ∼200 nm. Ga FIB milling, however, introduces gallium implantation, which can cause material swelling and modify the intrinsic film stress. Moreover, FIB processing is inherently serial and therefore limited to reshaping individual devices rather than enabling parallel batch fabrication.

We also describe the preparation of few-layer flakes from bulk vdW magnets—using $MnPSe_3$ and VBr_3 as representative examples—by standard micromechanical cleavage. Since these materials degrade in air, the flakes are transiently protected by capping with hBN. Notably, the highly air-sensitive vdW materials, such as CrI_3, have been reported to still degrade rapidly even after top-capping and therefore require encapsulation from on sides. Finally, we show that when flakes of interest are surrounded by larger flakes that obstruct pick-up or capping, the excess material can be efficiently removed with a tungsten carbide micro-needle, enabling recovery of the target flakes. For nanowire-MFM studies, the magnetic flake must be positioned near a chip edge. We show that, when dry viscoelastic transfer fails to achieve the required placement, precision dicing provides a robust alternative. Using this approach, samples can be positioned reproducibly within 30 µm of the chip edge. The resulting cut trench exhibits minor edge chipping extending up to 8 µm laterally into the substrate; therefore, even smaller sample–edge distances may be achievable.

The fabrication capabilities established in this chapter form the foundation for producing SiN_x torque transducers integrated into PnCs and for preparing few-layer magnetic vdW samples. Together, these developments enable the integration of vdW magnets with engineered mechanical transducers toward torque sensors with the sensitivity required to probe minute magnetic moments. A key remaining challenge is the attachment of vdW flakes to the delicate, fully suspended PnC devices. Once the structures are released, viscoelastic transfer is no longer applicable. However, vdW flakes can be transferred onto the device after patterning of the device layer but prior to final suspension. At this stage, the residual thinned Si layer beneath the SiN_x film still provides sufficient mechanical support to tolerate stamping.

In this integration scheme, the vdW stack must withstand the subsequent release step in aqueous KOH. For air-sensitive materials, encapsulation is required in any case and the chemically resistant hBN provides protection during alkaline etching. Nevertheless, the stack could still be displaced from the SiN_x surface during the final suspension and rinse steps. If this proves limiting, additional fixation strategies will be required, for example by forming local clamps via focused electron-beam-induced deposition (FEBID) of Pt, or by applying a small PMMA droplet to secure the flake.

4

Mechanical characterization of torque transducers

In this chapter, the torque transducers fabricated in Ch. 3 are characterized in terms of their mechanical properties and, when possible, their dynamic torque-sensing performance. After a brief introduction in Sec. 4.1, the characterization procedure is described in Sec. 4.2. This is followed by the characterization of torque transducers in Sec. 4.3, and concludes with discussing the results in Sec. 4.3.

4.1 Introduction

Dynamic torque magnetometry relies on ultra-sensitive mechanical resonators to transduce a minute torque into a detectable shift in the resonator resonance frequency. The minimal torque sensitivity of such transducers is set by its mechanical properties, in particular the moment of inertia and stiffness, and the mechanical dissipation of the sensing mode. SiN_x resonators are an attractive platform in this context, as they combine low mass, stiffness, and intrinsic high Q with the compatibility for integrating nanoscale samples and also electronic contacts. In addition, embedding a defect resonator in a PnC structure has been proposed as a route to suppress radiative losses to the environment, thereby strongly enhancing the quality factor via acoustic shielding.

Here, we report a systematic characterization of PECVD SiN_x torque transducers fabricated in this work—ranging from standalone torsional paddles to devices embedded in a PnC structure—using broadband spectroscopy, ring-down measurements, dynamic torque magnetometry, and finite-element modeling. Standalone torsion paddles 1 and 2 achieve minimum torque sensitivities of $9 \cdot 10^{-22}$ and $6 \cdot 10^{-22}\,\mathrm{Nm}/\sqrt{\mathrm{Hz}}$, respectively, comparable to state-of-the-art Si cantilevers. We confirm robust engineering of phononic band gaps and, for PnC paddle 2, placement of the torsional defect mode inside the stop band at 450 – 690 kHz. Under cryogenic conditions, this mode has $f_0 = 522\,\mathrm{kHz}$, $Q = 6.6 \cdot 10^3$, and achieves a minimum torque sensitivity of $\tau_{\mathrm{min}} = 1.2 \cdot 10^{-22}\,\mathrm{Nm}/\sqrt{\mathrm{Hz}}$, slightly surpassing highly sensitive state-of-the-art Si cantilevers. We find that dissipation in our devices is dominated by intrinsic dissipation, with clamping losses contributing only weakly. An additional PnC beam device confirms phononic band-gap formation but reveals strong nonlinearities and limited drive efficiency for an acoustically protected defect mode, constraining its utility for torque magnetometry. Overall, we conclude that significant improvement of torque sensitivity of the present devices will primarily require reducing intrinsic dissipation rather than relying on phononic isolation.

4.2 Characterization procedure

The torque transducers introduced and fabricated in Ch. 3 are characterized using the DCM measurement setup described in Sec. 2.3.1. After mounting the sample, the sample chamber is evacuated to a pressure $<10^{-6}$ mbar and cooled down to 5 – 8 K depending on thermal coupling. In a first step,

the driving frequency is swept across a large frequency range in order to probe the overall frequency response of the mechanical resonator. For torsion paddle 1 and 2, and PnC paddle 1 and 2, the goal is to identify the fundamental torsional resonance, and for PnC beam 1, the second-harmonic flexural resonance. Furthermore, for all PnC devices, we aim to confirm the presence of a phononic band gap and check if the relevant mechanical mode is located inside the phononic band gap. In a second step, the mechanical characteristics of each device are studied in more detail in order to determine the exact mode frequency f_0 and quality factor Q_0. This is achieved by sweeping the driving frequency across specific response peaks with high resolution while recording the corresponding out-of-plane displacement signal. Measurement results and mode-assignments are further validated by reconstructing the measured response using FEM modeling in *COMSOL Multiphysics*. In addition, the FEM model is used to determine the effective moment of inertia J_{eff} of transducers, which—together with f_0—is used to determine the effective spring constant k_{eff}. After data collection, response peaks are fitted using a Lorentzian lineshape which provides a good approximation to the response of a simple driven damped harmonic oscillator in the high-Q regime. Treating the problem in Fourier space, the displacement signal is proportional to the AC voltage $\hat{U}_{\text{PD}}$ detected by the photodiode (PD) via interferometric laser readout and it follows the relations

$$\hat{U}_{\text{PD}}(\omega) \;\propto\; \hat{x}(\omega) = \frac{\hat{\tau}}{J_{\text{eff}}} \; \frac{1}{\omega_0^2 - \omega^2 + i\frac{\omega_0 \omega}{Q}}, \tag{4.1}$$

where ω_0 is the angular resonance frequency, Q is the mechanical Q-factor, and $\hat{\tau}$ denotes the driving torque. The composite term $\hat{\tau}/J_{\text{eff}}$ determines the displacement amplitude times Q/ω_0^2 at resonance. Fitting is performed treating ω_0, $\hat{\tau}/J_{\text{eff}}$, and Q as free parameters, and the resonance frequency is deduced from resulting fit parameters. Q-factors are further determined more accurately using the ring-down method and fitting the observed exponential mode decay. When possible—i.e., when the mechanical mode is well defined, as is the case for simple paddles 1 and 2, and PnC paddle 2—dynamic torque magnetometry is also performed to assess the transducers' dynamic torque-sensing performance.

4.3 Results

Characterization results are presented in this section; it starts with the assessment of plain transducers without PnC—torsion paddle 1 and 2—in Sec. 4.3.1 and continues with the results of transducers embedded in a PnC—namely, PnC paddle 1 in Sec. 4.3.4, PnC paddle 2 in Sec. 4.3.5, and PnC beam 1 in Sec. 4.3.8.

4.3.1 Mechanical properties of torsion paddle 1

In a first step, the driving frequency is swept from 10 kHz – 1 MHz in order to identify the fundamental torsional mode of torsion paddle 1. Mechanical response spectra recorded at room temperature (RT) and after cooling down to 7 K are shown in Fig. 4.1a and b. Using the piezoelectric drive for mechanical actuation excites a large number of mechanical modes, which makes identification of the fundamental torsional mode difficult. On the other hand, driving mechanical motion inductively leads to a much cleaner spectrum, which allows direct identification of the displacement signal associated with the fundamental torsional mode. As the piezoelectric actuator shakes the entire sample, excitation is unspecific and a variety of modes are excited. For inductive actuation, the applied AC magnetic field interacts with the magnetic moment of the magnetic CoFeB nanotube, and thus, primarily excites mechanical motion of the torsional paddle. Resonance peaks of the fundamental torsional mode at RT and at 7 K are presented in Fig. 4.1c together with their fitted response. We observe that the frequency of the fundamental torsional mode slightly increases by about ∼2.5 kHz when cooling from RT to cryogenic conditions. This behavior can be explained in terms of thermal contraction and material stiffening of SiN_x associated with lower temperatures. Based on Lorentzian fitting, we determine fundamental torsional frequencies of 513.5 kHz and 516.1 kHz at RT and 7 K, respectively. Additionally, the signal amplitude increases and the linewidth becomes more narrow which is expected since mechanical dissipation is suppressed at cryogenic temperature.

Table 4.1: Mechanical characteristics of fundamental torsional mode of torsion paddles 1 and 2. Model predictions based on the lumped parameter model (Eq. (2.7)) and *COMSOL* are included for comparison. Values refer to cryogenic conditions at 7 K if not denoted differently.

torsional paddle	data	k_{eff} [Nm]	J_{eff} [kg m^2]	f_0 [kHz]	$Q_{7\mathrm{K}}$ [a.u.]	Q_{RT} [a.u.]	τ_{min} [Nm/$\sqrt{\mathrm{Hz}}$]
1	lumped model	$7.2 \cdot 10^{-11}$	$3.2 \cdot 10^{-24}$	764	—	—	$8.7 \cdot 10^{-22}$
	COMSOL	$5.2 \cdot 10^{-11}$	$4.9 \cdot 10^{-24}$	518	—	—	—
	experiment	$^*5.2 \cdot 10^{-11}$	—	516	7914	5624	$8.8 \cdot 10^{-22}$
2	lumped model	$1.4 \cdot 10^{-11}$	$3.1 \cdot 10^{-24}$	335	—	—	$6.6 \cdot 10^{-22}$
	COMSOL	$5.3 \cdot 10^{-12}$	$5.3 \cdot 10^{-24}$	160	—	—	—
	experiment	$^*5.2 \cdot 10^{-12}$	—	158	5864	2145	$5.9 \cdot 10^{-22}$

Note: Values marked with * are calculated using the measured f_0 and FEM-derived J_{eff}. — indicates data not available.

4.3.2 Torque sensitivity and mechanical properties of torsion paddles 1 and 2

In this section, the torque sensitivities of torsion paddle 1 and 2 are assessed. To this aim, we develop a finite-element model (FEM) in *COMSOL* and optimize the model by adjusting device dimensions such that the frequency prediction agrees with the frequency observed for the fundamental torsional modes. Fundamental torsional frequencies $f_{t,0}$ are taken from the DPM responses recorded at 7 K and zero field which is presented in Fig. 4.2 and 4.3 in Sec. 4.3.3. Minimal torque sensitivities τ_{min} normalized to a 1-Hz bandwidth are calculated using Eq. (2.24) on the basis of experimentally observed torsional resonance frequency $f_{t,0}$, quality factor Q determined at 7 K. The effective rotational inertia of the fundamental torsional mode $J_{t,0}$ is taken from the *COMSOL* model which also includes the weight of the magnetic specimen. Experimental torsional spring constants reported in Tab. 4.1 are calculated using $k_{t,0} = J_{t,0}\omega_{t,0}^2$. Mechanical characteristics of torsion paddle 1 and 2 are summarized in Tab. 4.1 where experimental data is accompanied by values predicted by the lumped parameter model from Eq. (2.7) and the *COMSOL* model based on device dimensions reported in Tab. 4.2. Qs are determined based on fitting the mode decay from ring-down measurements, and torque sensitivities are calculated based on the resulting Q-factors. Ring-down measurements are provided in App.B.1. In case of torsion paddle 1, the modeled and observed resonator characteristics are in

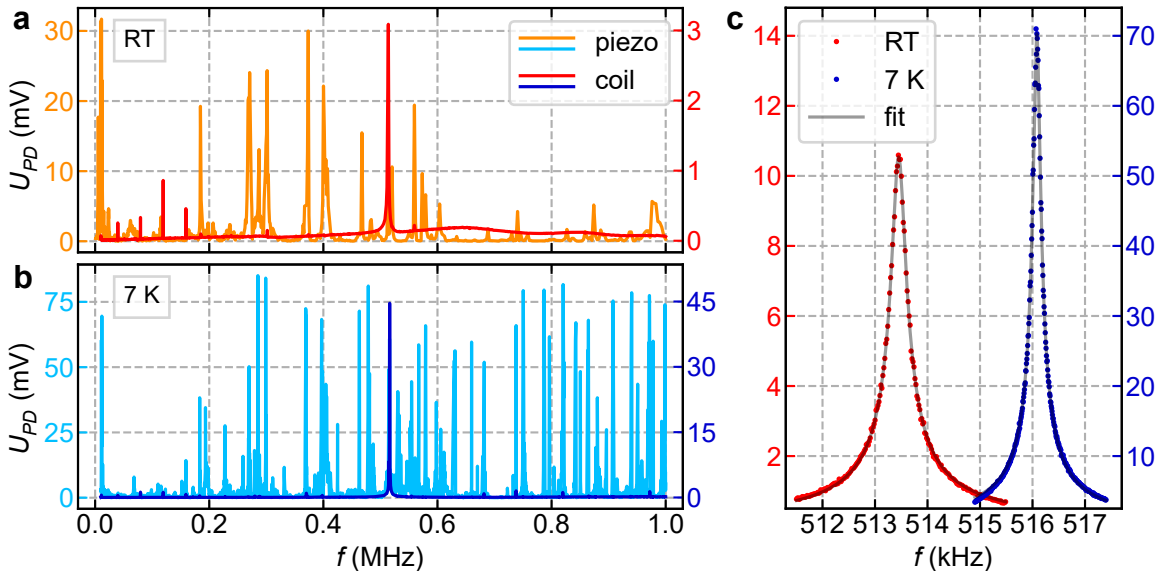


Figure 4.1: Identification of fundamental torsional resonance. Response spectra recorded using piezoelectric and magnetic-torque actuation (**a**) at RT and (**b**) at 7 K. (**c**) Measured resonance peaks with fitted curves.

Table 4.2: Measured and modeled device dimensions. *COMSOL* model dimensions are adjusted to reproduce measured frequencies. The deviation from measured dimensions is particularly striking in case of torsion paddle 2 which requires a 32 % reduction in thickness of bridge segments.

torsional paddle	data	d [nm]	w_b [nm]	l_b [µm]	w_p [µm]	l_p [µm]	d_{Au} [nm]
1	measured	198	641	3.6	19.8	9.8	—
	COMSOL	185	620	3.6	19.8	9.7	—
2	measured	198	219	3.5	19.8	9.8	2
	COMSOL	185 (d_b=135)	195	3.5	19.8	9.7	3

Note: d denotes the thickness, w (l) the width (length), subscript b (p) the bridge (paddle), subscript Au the gold film, and — indicates data not available.

relatively good agreement. Spring constant, fundamental torsional frequency and torque sensitivity are well approximated by use of the lumped model (Eq. (2.7)) with results being in the correct order of magnitude and differing by less than a factor of 2. The fundamental frequency is slightly overestimated by the lumped model which to a small degree can be attributed to the fact that the model does not account for the weight of the magnetic NT attached to the paddle. As a consequence the effective rotational inertia is systematically underestimated, which then translates to errors in frequency and sensitivity. The effect of the NT is further modeled in *COMSOL*, and the additional mass of the NT is observed to lower the fundamental torsional frequency by less than 20 kHz. Thus, the *COMSOL* model needs further tuning within error margins associated with measured device dimensions in order to reproduce the experimentally observed fundamental torsional frequency. After a few iterations, good approximation is achieved based on implementation of the device dimensions given in Tab. 4.2, and resonator characteristics predicted by this *COMSOL* model are included in Tab. 4.1.

With torsion paddle 2, the discrepancy between prediction of the lumped model and observed oscillator metrics is quite large considering frequency and torsional stiffness. Considerations made above for torsion paddle 1 concerning systematic errors in modeling the rotational inertia within the lumped model, do also apply here. Moreover, torsion paddle 2 is covered with an additional gold film which is at least 2 nm thick. Again, weights of the magnetic specimen and the gold film are neglected by the lumped model. And since torsion paddle 2 also features thinner bridge segments, and therefore, makes a much softer torsional spring, errors derived from previously described shortcomings of the lumped model have now a bigger weight. Correspondingly, the measured fundamental torsional frequency is much lower, i.e. about half the value predicted by the lumped parameter model (Eq. (2.7)). In keeping with this, the effective torsional spring constant associated with the experimental data is two times softer than predicted.

Again, an FEM model is developed in *COMSOL* including the gold film and the magnetic specimen. Pushing once more the limits of uncertainty in observed device measures, the observed fundamental torsional frequency is retrieved. Corresponding resonator characteristics and device measures are again given in Tabs. 4.1 and 4.2, respectively. It must be emphasized, that obviously there are numerous device dimensions which could reproduce the measured spring constants and frequencies. Nevertheless, by constructing the model within the limits of uncertainty associated with determination of device dimensions, the constructed model represents the best approximation that we have. The need to substantially reduce the thickness of bridge segments t_r in the optimized *COMSOL* model hints to potential damage caused by FIB milling during bridge refinement. Incident ions may have changed the elastic properties of SiN_x which could arise from damaged chemical bonds and ions being implanted into the substrate. Correspondingly, bridges seemingly appear to be more flexible than expected based on their size in response to damage impaired along the contours defined using FIB.

Considering Qs, a decrease is observed with an increase in temperature due to thermoelastic loss and coupling to defects in the material. Qs deduced for torsion paddle 2 lie below the ones of torsion paddle 1. This most likely again arises from ion implantation during FIB milling or a potential

increase of dangling bonds on top of the gold film compared to the bare SiN_x surface. With this, refinement of bridge segments using FIB milling did not bring about a higher Q torque sensor.

Regarding torque sensitivity, torsion paddle 2 achieves an about 30 % improved sensitivity compared to torsion paddle 1, despite its lower Q. The two prototype paddle microbridges fabricated and reported as torsion paddles 1 and 2 are promising for their use in torque sensing applications, achieving torque sensitivities on the order of $\sim 6 \cdot 10^{-22}\,\mathrm{Nm}/\sqrt{\mathrm{Hz}}$ with torsion paddle 2. This does not surpass the benchmark of $4 \cdot 10^{-22}\,\mathrm{Nm}/\sqrt{\mathrm{Hz}}$ set by currently available Si cantilevers. Nevertheless, in the prospect of further refinement of the fabrication process regarding the accuracy in defining device dimensions and the capacity to make also thinner devices, prototype devices described so far resemble an important stepping stone towards development of the next generation of torque sensors with improved torque sensitivity. Sensitivities calculated based on the lumped parameter model described by Eq. (2.7) are in very good agreement with the ones determined from the measurement, and therefore, it can be used as a simple, but useful tool to roughly estimate τ_{min} despite its shortcomings in predicting $f_{t,0}$ and $J_{t,0}$. It should be noted, however, that application of the lumped model should be restricted to device geometries that (i) satisfy the condition $d < w$ and (ii) exhibit a sufficiently large ratio $2l_\mathrm{b}/l_\mathrm{p}$ such that the employed mode-shape function can be regarded as a valid approximation.

4.3.3 Dynamic torque magnetometry with torsion paddles 1 and 2

DPM responses of torsion paddles 1 and 2 are discussed individually below followed by a brief comparison. DPM measurements are performed by sweeping the magnetic field from 1.5 T to −1.5 T and back with increments of 10 mT. At each point of the magnetic field, the driving frequency is swept through the fundamental torsional resonance using the same drive amplitude, and the response is then fitted in order to extract the resonance frequency.

Torque sensing with torsion paddle 1

Easy axis DPM measurements are recorded with the external field aligned parallel to the paddle surface, such that the field points along the NT's magnetic easy axis, i.e., the magnetization vector's

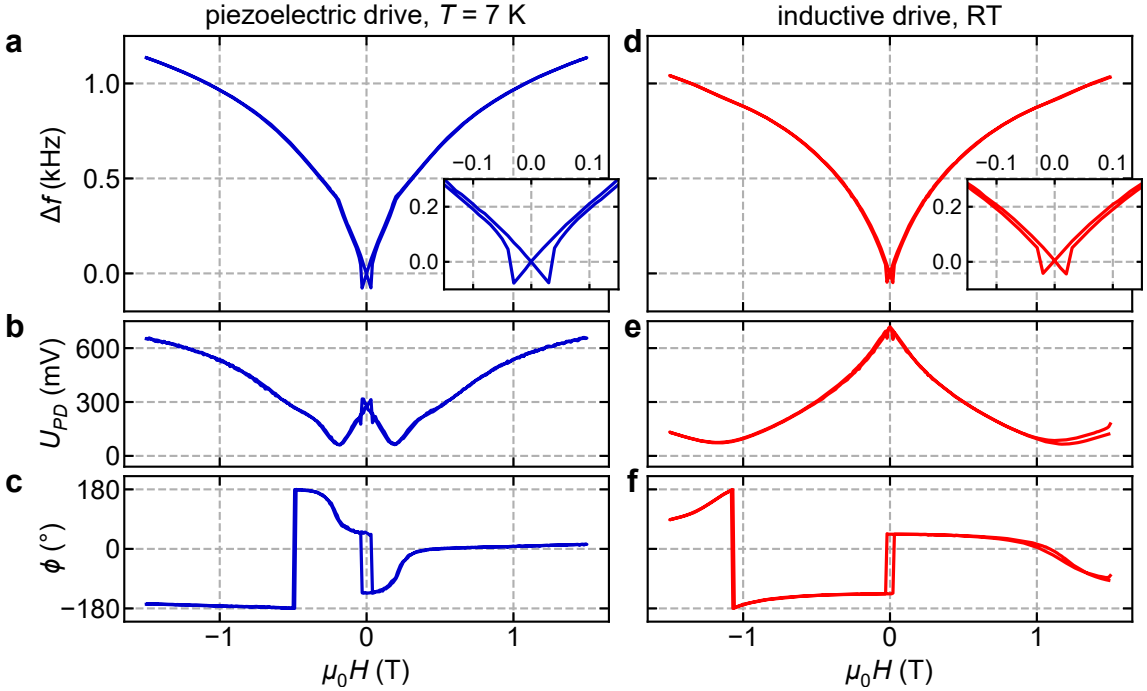


Figure 4.2: DPM response of torsion paddle 1. Hysteresis loops recorded by sweeping H along the NT easy axis with piezoelectric and magnetic actuation (**a**) – (**c**) at 7 K and (**d**) – (**f**) at RT, respectively. Tick labels in the inset are given in units of millivolts.

preferred orientation. Frequency shifts Δf as a function of the applied magnetic field $\mu_0 H$ are shown in Fig. 4.2 together with signal amplitudes U_{PD} and phase shifts ϕ between drive and response signal. Data is shown for both, piezoelectric and inductive actuation of the fundamental torsional mode at 7 K and RT, respectively. Irrespective of the type of actuation, DPM responses display expected easy axis signatures as observed and analyzed in Refs. 70, 74, 75. Based on the analysis of DCM hysteresis of CoFeB NTs reported by Gross *et al.* in Ref. 70, the small kinks in Δf observed around ± 200 mT in Fig. 4.2a can be attributed to nucleation and disappearance of oppositely oriented vortices at the NT ends. As $|H|$ is reduced nucleation is guided by a reduction of the NT's magnetostatic energy, while vortex disappearance is driven by a reduction of the Zeeman energy as $|H|$ increases. Further, hysteresis around $B = 0$ T is well resolved. Slight drift is present when using the inductive drive, as can be seen from misalignment of amplitude and phase signal between down- and upward sweeps. The drift can be attributed to a change in temperature of $\sim$0.5 K which occurs due to heating from electric currents running through the coil when the system is at RT and the temperature is not controlled. Hence, the frequency drift in Δf is compensated using a simple temperature-weighted drift correction which is further described in App. B.2.

The detected signal amplitudes U_{PD} differ substantially depending on whether the piezoelectric shaker or the coil is used for inductive actuation. This behavior can be understood from the following considerations: (i) The piezoelectric actuation strength depends on the locations of the piezoelectric element's own resonances in frequency space, together with the transfer function that determines what motion reaches the paddle. (ii) Coil actuation, in turn, depends on the resonance characteristics of the electrical circuit in which the coil is embedded, as well as on the magnitude and orientation of **M** with respect to **H**. (iii) Taken together, (i) and (ii) imply that U_{PD} can exhibit very different behavior for the two actuation schemes. (iv) In addition, magnetic dissipation may reduce U_{PD}, which depends strongly on the magnetic specimen and would, in principle, be an interesting quantity to probe.

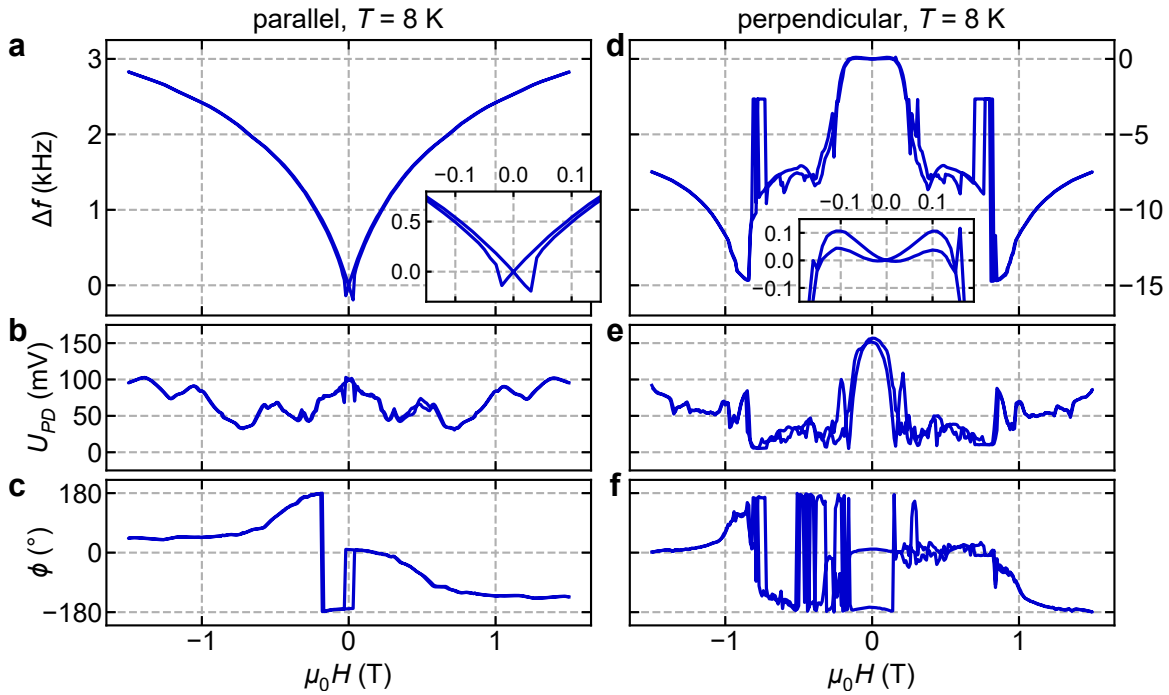


Figure 4.3: DPM response of torsion paddle 2. Hysteresis loops recorded by sweeping **H** oriented (**a**) – (**c**) parallel and (**d**) – (**f**) perpendicular relative to the NT easy axis. Data sets are recorded at 8 K and motion is driven using piezoelectric actuation. The tick labels in the inset are given in units of millivolts.

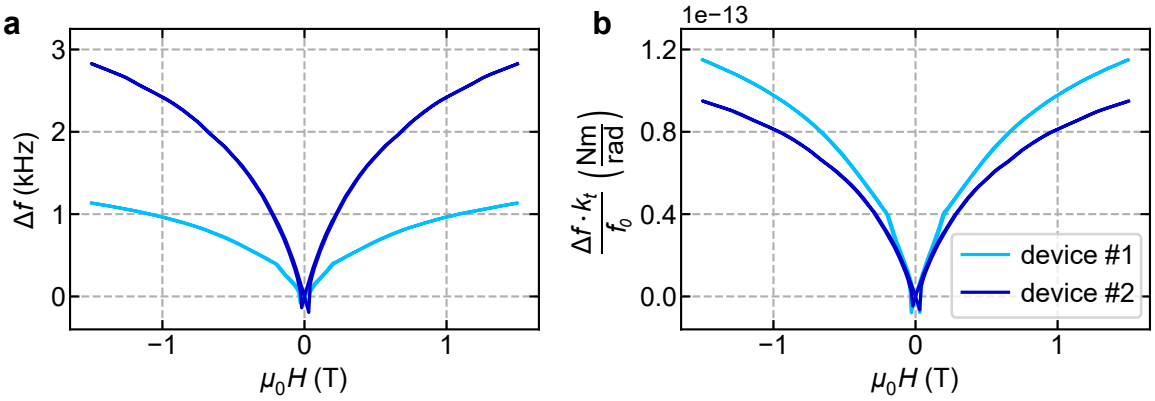


Figure 4.4: Comparison between DPM curves of torsion paddles 1 and 2 recorded at cryogenic temperature. (a) DPM data reproduced from Figs. 4.2 and 4.3. (b) DPM curves normalized with respect to fundamental torsional frequency and torsional spring constant.

Torque sensing with torsion paddle 2

DPM measurement results along the easy and hard axis are presented in Fig. 4.3 accompanied by their associated signal amplitudes and phase shifts. In the hard axis configuration the magnetic field is aligned perpendicular to the paddle surface, and therefore, also perpendicularly oriented with respect to the magnets preferred direction for magnetization. Mechanical modes of torsion paddle 2 are excited using the piezoelectric drive in both data sets, and both sets are recorded at 8 K.

As was the case for torsion paddle 1, a characteristic easy axis DPM response is also observed with torsion paddle 2. Considering the DPM response recorded along the hard axis, characteristic features are reproduced as reported with.[70,74] Note, that some data points are recorded with a very small amplitude very close to 0 mV. In these regions, at applied fields between $\pm 0.7 - \pm 0.9$ T, the signal amplitude potentially drops below the detection limit, and thus, fitting a Lorentzian lineshape to the resonance peak fails and extracted resonance frequencies are subject to substantial error.

Comparison between DPM curves recorded with torsion paddles 1 and 2

Easy axis DPM curves of both devices are plotted together in Fig. 4.4a. Frequency shifts of about 1.2 kHz and 2.5 kHz are observed with devies 1 and 2, respectively. Hence, they differ by a factor of $\sim$2. The shift in frequency is guided by Eq. (2.43). Correspondingly, DPM curves are normalized with respect to fundamental torsional frequencies and spring constants are derived from the *COMSOL* models defined in Tab. 4.1. The normalized DPM curves are shown in Fig. 4.4b. Since the magnetic specimen is identical, differences in the normalized curves can only be attributed to either an error in the calculated spring constant or measurement errors. After normalization, the amplitude of Δf for torsion paddle 1 exceeds the one of torsion paddle 2. In keeping with previously discussed uncertainty in determination of the torsional spring constant of torsion paddle 2, its lower normalized DPM curve substantiates the conjecture that the experimental spring constant given in Tab. 4.1 is indeed underestimated. The normalized DPM curves show an almost perfect match in terms of their shape besides their amplitude and minor deviations in hysteresis for intermediate field values.

4.3.4 Mechanical properties of PnC paddle 1

Mechanical response spectra for PnC paddle 1 are recorded at RT before and after integrating the magnetic CoFeB NT. Before attachment, we use piezo-driven excitation and the frequency-dependent displacement amplitude is detected while sweeping the drive frequency from 1 kHz to 1 MHz. Measurements are performed with the laser spot focused on the large platform at the defect center (yellow), the small platform next to it (orange), and also on the first (red) and second (purple) platforms of the surrounding PnC lattice. The data and color-coded locations are shown in Fig. 4.5. With the laser readout positioned in a single location, signal detection is limited to mechanical modes that cause an out-of-plane displacement at this specific location. Hence, by measuring the

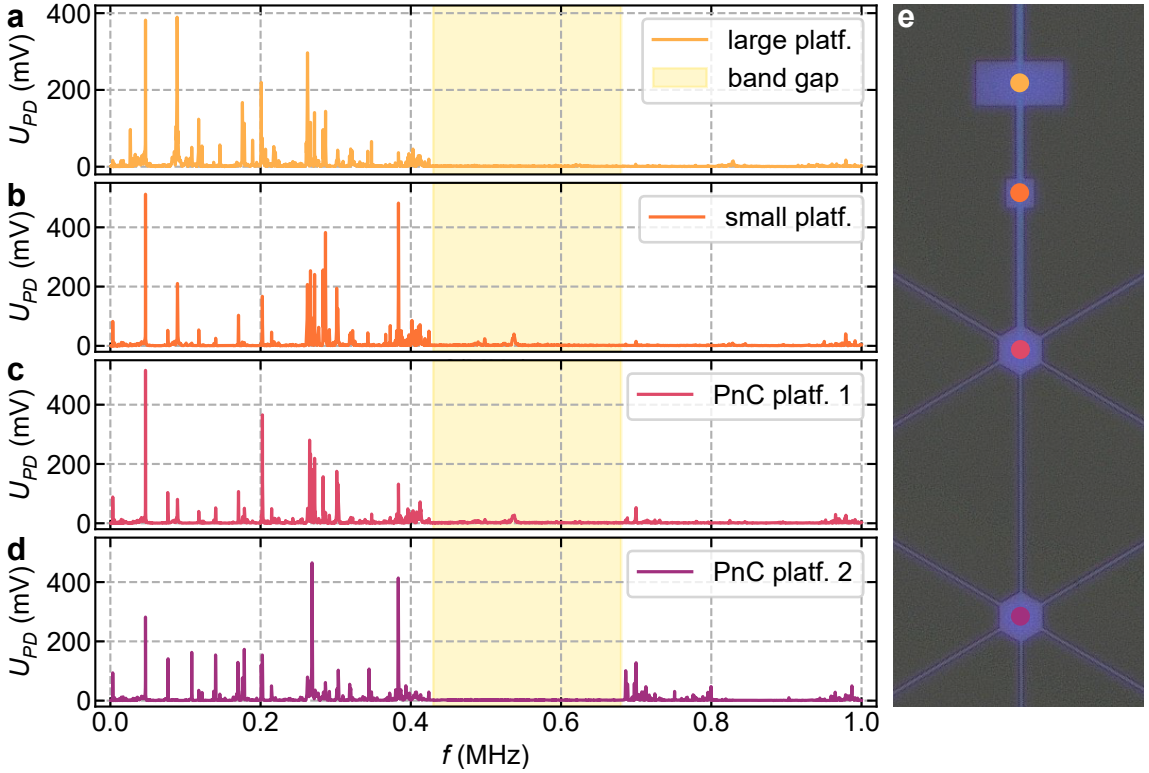


Figure 4.5: Frequency response of PnC paddle 1 before attaching a CoFeB NT. A phononic band gap opens between 430 – 680 kHz. Spectra were recorded at RT with the laser readout focused on (**a**) the large defect platform, (**b**) the small defect platform, (**c**) the first PnC platform, and (**d**) the second PnC platform. (**e**) Color code.

displacement at multiple positions, we obtain a more complete picture of all mechanical modes excited in the full PnC membrane.

A distinct phononic band-stop signature is observed in all location channels, starting at 430 nm and continuing up until about 680 nm, with the upper frequency bound visible in the displacement detected via the second PnC platform. This confirms the presence of a phononic band gap in PnC paddle 1, which marks a first small success and presents the first time that a phononic shield has been implemented for a 2D resonator design at the department of physics of University Basel. A one-dimensional PnC beam has previously been pioneered by C. Spinnler at our research institution.[275,276] The frequency response obtained from piezo-driven excitation is complex and difficult to interpret.

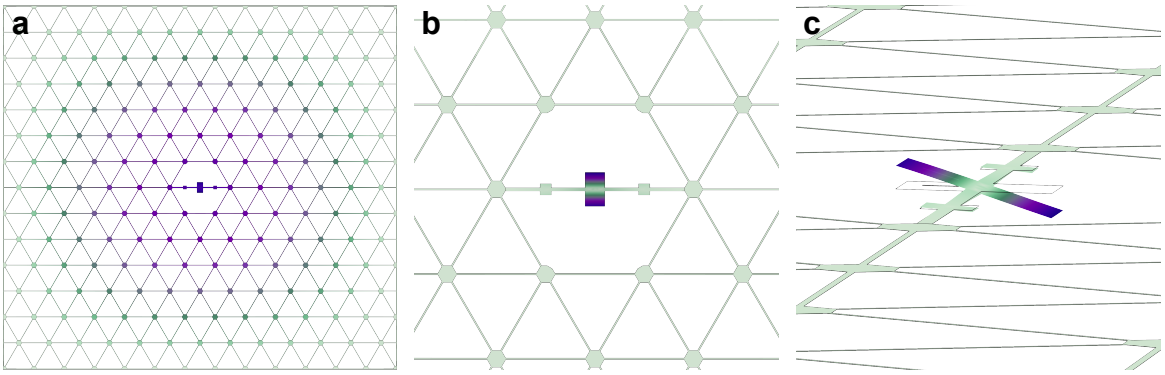


Figure 4.6: Mode shapes of PnC paddle 1. Finite-element (*COMSOL*) mode shapes showing (**a**) the fundamental flexural mode of the complete PnC membrane, (**b**) the fundamental torsional mode of the defect platform, and (**c**) a side view of the same torsional mode illustrating strong localization within the defect region.

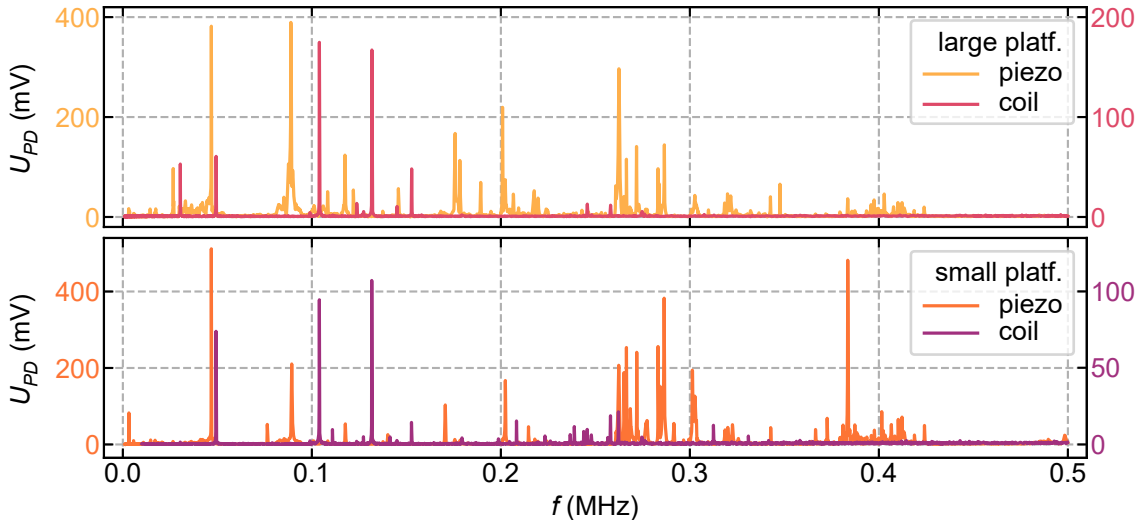


Figure 4.7: Frequency response of PnC paddle 1 before and after attaching the CoFeB NT. The bare resonator is driven using piezoelectric actuation. After integration of the CoFeB NT, the resonator motion is driven via magnetic-torque actuation.

As the signal peak at 47 kHz appears with large amplitude across all readout locations, it can be reasonably attributed to the fundamental flexural mode of the collective PnC membrane. The mode shapes relevant to this section are shown in Fig. 4.6.

After attaching the CoFeB NT, the resonator is driven via magnetic-torque actuation. Frequency responses are recorded with the laser spot positioned on the large and small defect platforms. The resulting spectra are shown in Fig. 4.7, together with measurements acquired at the same locations prior to mounting the magnet. Surprisingly, the putative fundamental flexural resonance of the full PnC membrane appears slightly shifted upward by 2 kHz upon attaching the magnet, and the origin of this upward shift remains unclear.

Further, the frequency response measured under magnetic-torque actuation exhibits several new peaks that were not observed under piezoelectric driving. The two most prominent peaks occur at 104 kHz and 132 kHz. Because magnetic-torque actuation couples directly to the defect paddle and efficiently excites modes with angular displacement—as previously observed for torsion paddles 1 and 2—the signal at 104 kHz most likely corresponds to the fundamental torsional resonance of the defect, whereas the peak at 132 kHz is attributed to a higher-order mode.

PnC paddle 1 provides the first proof of successful design and fabrication of a phononic band gap. However, because the fundamental torsional defect mode lies well outside the acoustically isolated band and the SiN_x thickness of this device is subject to substantial uncertainty, we conclude the characterization at this stage and refrain from performing FEM modeling as well as additional ring-down and dynamic torque magnetometry measurements.

4.3.5 Mechanical properties of PnC paddle 2

The frequency response of PnC paddle 2 is studied after integration of a magnetic CoFeB NT. We sweep the drive frequency from 5 kHz – 1 MHz using both piezoelectric and magnetic drive and record response spectra at RT and 5 K. The measured spectra are shown in Fig. 4.8a and b, together with the fitted resonance peaks of the fundamental torsional mode in Fig. 4.8c. We observe the opening of a phononic band gap spanning a range from about 450 – 690 kHz. The fundamental torsional resonance is centered at 516.6 kHz at room temperature and at 522.4 kHz at 5 K, and in both cases lies well within the phononic band gap. The small number of peaks detected under inductive drive, together with the fact that the peak exhibits the highest intensity, allows an unambiguous assignment of this resonance to the fundamental torsional mode of the defect paddle. While the fundamental torsional mode of torsion paddle 1 was susceptible to mechanical excitation using piezoelectric actuation, this time we cannot observe a corresponding piezo-driven excitation for PnC paddle 2. This observation

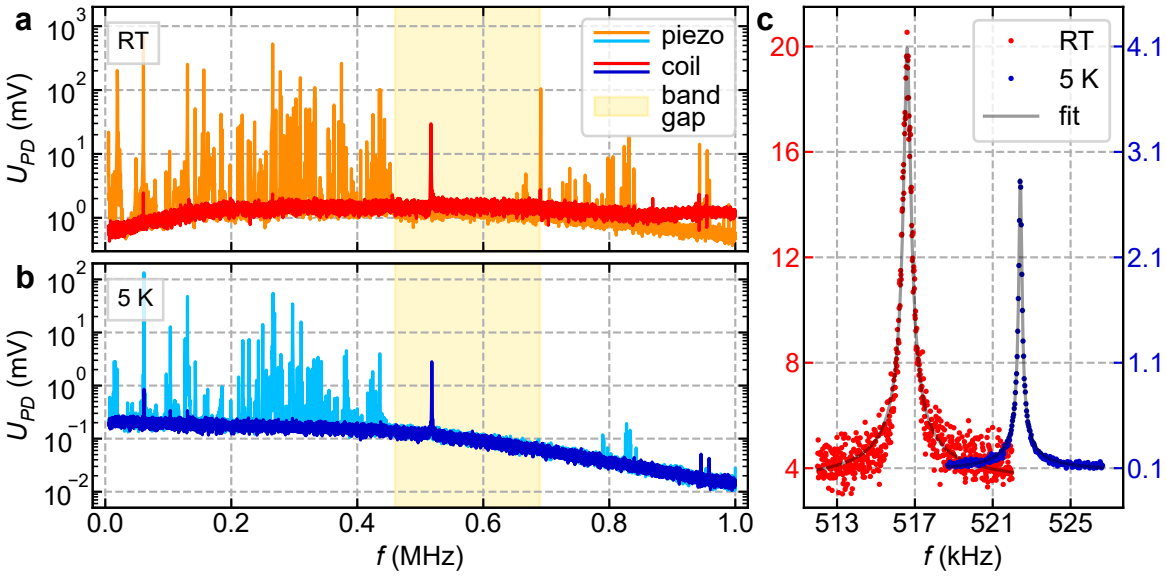


Figure 4.8: Frequency response of PnC paddle 2. The phononic band gap extends from 450 kHz and 690 kHz. Spectra were recorded using piezoelectric (magnetic) actuation with drive amplitude of 50 mV (3 V) (**a**) at RT and (**b**) at 5 K. (**c**) Measured resonance peaks with fitted curves.

suggests that mechanical coupling between the surrounding Si chip and the defect mode is strongly suppressed, confirming the effectiveness of the added PnC structure in providing acoustic isolation.

We further analyze the mechanical properties of the defect's fundamental torsional mode by sweeping the drive frequency across the resonance with smaller frequency increments between data points, thereby determining the resonance frequency more accurately. The measured and fitted responses at RT and 5 K are shown in Fig. 4.8c and we find $f_0 = 516.7$ kHz at RT and $f_0 = 522.4$ kHz at 5 K. We can further see from fitting that Q increases by roughly a factor of 2 from about 1500 to 3800 at cryogenic temperatures compared to RT. This is a well-known and often described behavior and is attributed to suppression of internal dissipation at low temperature.[277–279] In addition, we determine the mechanical quality factor more precisely by performing ring-down measurements at 5 K and find $Q = 6600$ and the corresponding ring-down data is provided in App. B.1.2.

Based on the measured dimensions of PnC paddle 2 given in Tab. 3.2, we set up a finite-element model in *COMSOL* to reconstruct the observed mechanical response. Again, we optimize the simulated mechanical response by varying device dimensions roughly within their limits of uncertainty and include the mass of the attached magnetic specimen. For PnC paddle 2, the lateral device dimensions

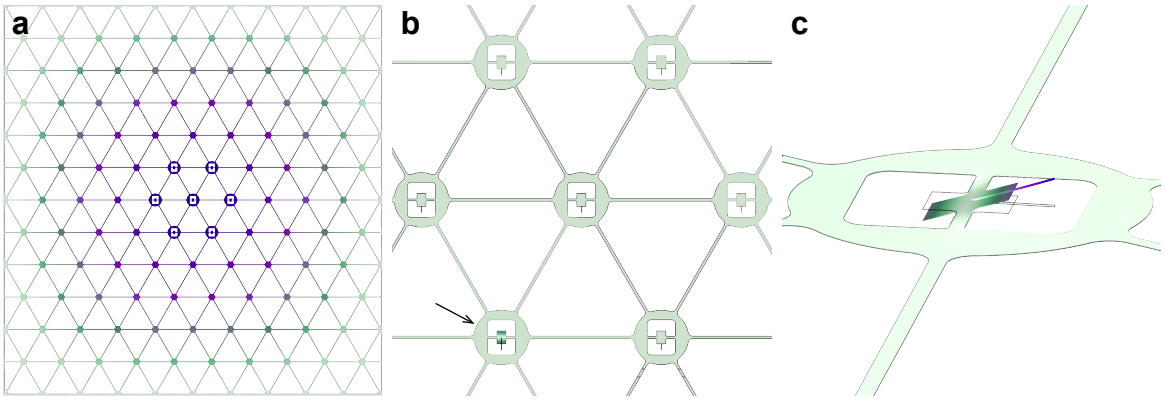


Figure 4.9: Mode shapes of PnC paddle 2. Simulated mode shapes showing (**a**) the fundamental flexural mode of the complete PnC membrane, (**b**) the fundamental torsional mode of the defect platform at the readout location, and (**c**) a side view of the same torsional mode illustrating strong localization within the defect region.

are well constrained; therefore, we only vary the thickness of the PnC membrane. Mode shapes relevant to the peak assignment are shown in Fig. 4.9. Excellent agreement between simulation and measurement is obtained by reducing the SiN_x thickness to 106 nm, which predicts a fundamental flexural frequency of the full PnC membrane of 61 kHz. In addition, prediction of the fundamental torsional frequency of the defect also matches the signal peak observed at 522 kHz very nicely within an error of about 1 kHz. And at last, also the modeled band gap is predicted between 460 – 720 kHz which fits the experimental observed range of 450 – 690 kHz well. Matching the three key features—the fundamental PnC frequency, the fundamental torsional frequency, and the phononic band gap range—provides strong validation of the finite-element model.

4.3.6 Torque sensitivity and mechanical dissipation of PnC paddle 2

From the finite-element model developed in Sec. 4.3.5, we deduce the effective moment of inertia for the fundamental torsional mode of PnC paddle 2 and find $J_{\text{eff}} = 1.0 \cdot 10^{-25}\,\text{kg}\,\text{m}^2$. Combined with the observed resonance frequency, the torsional spring constant is determined $k_{\text{eff}} = 1.1 \cdot 10^{-12}\,\text{Nm}$. Based on this result and Q determined from ring-down measurements, we calculate the minimal torque sensitivity using Eq. (2.24) and find $\tau_{\text{min}} = 1.2 \cdot 10^{-22}\,\text{Nm}/\sqrt{\text{Hz}}$ for a 1 Hz measurement BW which is comparable to values previously reported for the plain device architectures without PnC structure represented by torsion paddles 1 and 2.

The fact that we do not observe any noticeable improvement in Q despite acoustic isolation of the torsional resonance by structuring a PnC around it suggests that mechanical dissipation of the fundamental torsional mode of the plain device is not dominated by radiative or clamping losses at the device boundaries. Instead it may be dominated by dissipative contributions from internal and surface loss channels. To assess whether the measured quality factor of our torsional mode is limited by clamping losses or by intrinsic dissipation, we first compare it to the intrinsic loss expected from the surface-loss model of Villanueva and Schmid[117] described in Eq. (2.26). This analytical model describes the intrinsic Q-factor of thin pre-stressed silicon nitride films, using $Q_{\text{surf}} = \beta d$ with $\beta \approx (6 \pm 4) \cdot 10^{10}\,\text{m}^{-1}$ and $Q_{\text{vol}} \approx 2.8 \cdot 10^4$ extracted from a large set of low- and high-stress LPCVD silicon nitride resonators at room temperature. Applying this model to our film thickness, $d = 116\,\text{nm}$, yields an intrinsic quality factor

$$Q_{\text{int}}(d = 116\,\text{nm}) = \left(\frac{1}{\beta d} + \frac{1}{Q_{\text{vol}}}\right)^{-1} \approx 10^3\text{–}10^4\,,$$

where the range reflects the uncertainty in β and also the fact that the model is calibrated at room temperature on LPCVD rather than PECVD films.

At cryogenic temperatures ($T \approx 10\,\text{K}$), measurements on PECVD amorphous SiN_x films report cryogenic loss angles in the range from low 10^{-4} to low 10^{-3}, corresponding to intrinsic quality factors $Q_{\text{int}} \sim 10^3$–10^4 in a similar thickness range and for measurement frequencies up to 7 kHz.[280] While PnC paddle 2 operates at substantially higher frequency, these values provide a useful order-of-magnitude reference for cryogenic dissipation in PECVD SiN_x. Our PECVD film is therefore expected, both from the room-temperature surface-loss model and from direct cryogenic PECVD measurements, to have a Q_{int} in this range. The measured quality factor of the fundamental torsional mode $Q_{\text{meas}} \approx 6.6 \cdot 10^3$ at $f_0 = 522\,\text{kHz}$ and $T = 5\,\text{K}$ lies comfortably within this expected intrinsic range, indicating that intrinsic surface and bulk losses are sufficient to account for the observed dissipation.

Considering that intrinsic and clamping (radiation) losses add in parallel as

$$\frac{1}{Q_{\text{meas}}} = \frac{1}{Q_{\text{int}}} + \frac{1}{Q_{\text{clamp}}},$$

a Q_{int} of order 10^4 or larger implies a clamping-limited quality factor $Q_{\text{clamp}} \gtrsim 10^4$. Thus clamping (radiation) loss can contribute at most a modest fraction of the total dissipation. The fact that embedding the resonator in a PnC and placing the torsional mode well inside the band gap does not increase Q is therefore consistent with the fundamental torsional defect mode being predominantly intrinsic-loss-limited rather than clamping-loss-limited, even under cryogenic conditions.

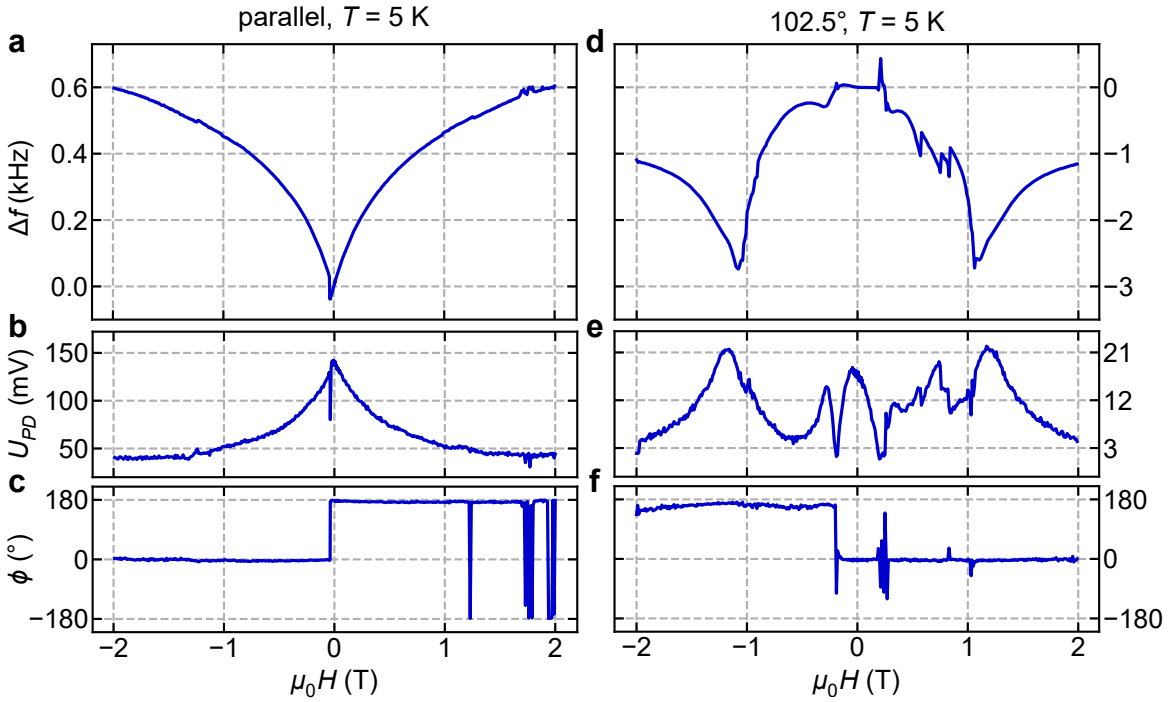


Figure 4.10: DPM response of PnC paddle 2 at 5 K using piezoelectric excitation. Measurements with **H** oriented (**a**) – (**c**) parallel to the easy axis with the field swept from 2 T to −2 T and (**d**) – (**f**) at 102.5° with the field swept up from −2 T to 2 T.

4.3.7 Dynamic torque magnetometry with PnC paddle 2

With previous observations in mind, we perform dynamic torque magnetometry measurements with PnC paddle 2 to assess its capacity for magnetic torque sensing. At each field step, the drive frequency is swept across a 1 kHz wide window positioned around the fundamental torsional frequency with constant driving amplitude. The response amplitude is fitted using Eq. (4.1) and the resonance frequency is deduced from fitting. This procedure is very time-consuming, and therefore, we limit our investigation to recording only half a hysteresis curve, i.e., perform an unidirectional magnetic field sweep from 2 T to −2 T or vice versa. Since the fundamental torsional mode cannot be excited for a strictly perpendicular field orientation, the direction of the applied field **H** is tilted from 90° to 102.5°. This orientation remains close to the perpendicular configuration, approximates the nominal magnetic hard axis, and allows us to probe the DCM response in a geometry that closely reflects the hard-axis condition. DPM measurements are shown Fig. 4.10. The observed Δf is on the order of 0.6 kHz and the DPM response recorded with **H** in parallel orientation produces a typical V-shaped dynamic torque response.[70]

4.3.8 Mechanical properties of PnC beam 1

In contrast to previous PnC devices, the defect center of PnC beam 1 is not structured as a torsional paddle but forms a double-clamped flexural beam and we aim to probe the mechanical properties of the second-harmonic flexural out-of-plane mode. Accordingly, the laser readout is positioned on one of the small platforms located at 1/4 beam length in order to maximize sensitivity to this specific mode. Dynamic torque magnetometry fundamentally requires that the magnetic probe undergoes an angular displacement with respect to the applied magnetic field. For the second-harmonic flexural mode, the central bridge segment remains nearly flat and primarily undergoes rotation about the beam's midline. With the CoFeB NT located at the bridge center and oriented parallel to the bridge as shown in Fig. 4.11, we investigate (i) wether the second harmonic can be driven magnetically, and (ii) wether it can be employed for dynamic torque magnetometry.

Frequency responses measured by sweeping the excitation frequency from 25 – 800 kHz at RT and

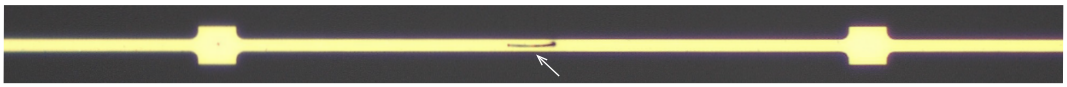


Figure 4.11: Position of the CoFeB NT. The magnetic specimen is precisely centered on PnC beam 1, with its long axis aligned along the resonator axis.

5 K are shown in Fig. 4.12. The abrupt stop and clear absence of signals detected above 400 kHz visually indicates the presence of a phononic band gap which continues up to a frequency of about 660 kHz. It must be emphasized, though, that in this readout configuration detection is only sensitive to modes that cause an out-of-plane displacement in the readout location. The fundamental out-of-plane flexural mode of the collective PnC membrane can be expected to behave similarly as the one of PnC paddle 2 with an identical PnC structure. Therefore, the signal observed at 56 kHz can be readily assigned to the PnC's fundamental flexural mode. Mode shapes relevant to the peak assignment are shown in Fig. 4.13. In the RT measurement shown in Fig. 4.12a, an isolated signal within the band gap near 490 kHz is detected under both actuation schemes. This differs from our previous observation for the fundamental torsional mode of PnC paddle 2 which could only be driven magnetically. This behavior can be understood intuitively by noting that piezoelectric driving induces out-of-plane chip motion, which couples more efficiently to flexural out-of-plane modes. After cooling the sample down to 5 K the same resonance is no longer detected in wide range frequency sweeps as shown in Fig. 4.12b irrespective of the actuation method.

By scanning the corresponding frequency range more closely, the signal is retrieved at $f = 489.96$ kHz and we apply a magnetic field to examine if the frequency changes in response, and thus, is sensitive to a magnetic torque. The magnetic field is nominally applied parallel with the CoFeB tube's magnetic easy axis and as Fig. 4.14a shows, a negligible frequency shift of only 6 Hz is observed by stepping from 0 T up to 2 T. This is about two orders of magnitude below the dynamic torque amplitudes previously reported for this type of sample with currently available highly-sensitive Si cantilevers.[70]

In addition, already at low displacement amplitudes of only few tens of millivolts the resonance peak shifts to higher frequencies and becomes asymmetric, indicating a Duffing-type hardening nonlinearity of the mode which gives rise to the typical "shark fin"-shaped response as depicted in Fig. 4.14b. The asymmetry persists down to driving the resonator at very small displacement amplitudes just above

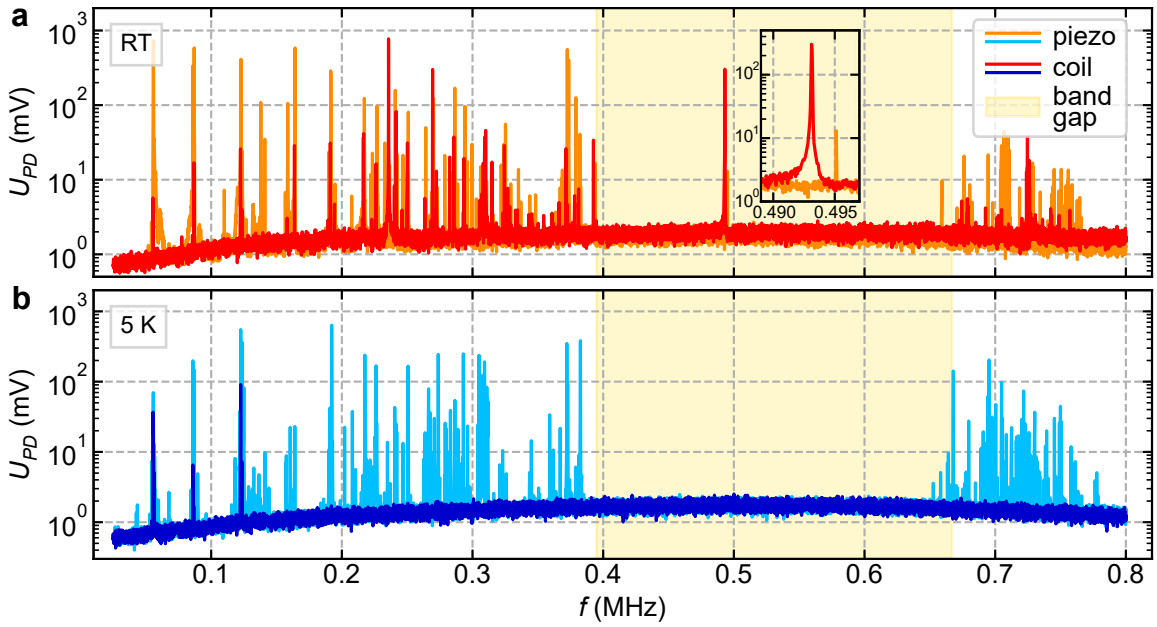


Figure 4.12: Frequency response of PnC beam 1. The phononic band gap is observed between 395 kHz and 665 kHz. Spectra were recorded with piezoelectric (magnetic) actuation with drive amplitudes of 100 mV (10 V) (**a**) at RT and (**b**) at 5 K.

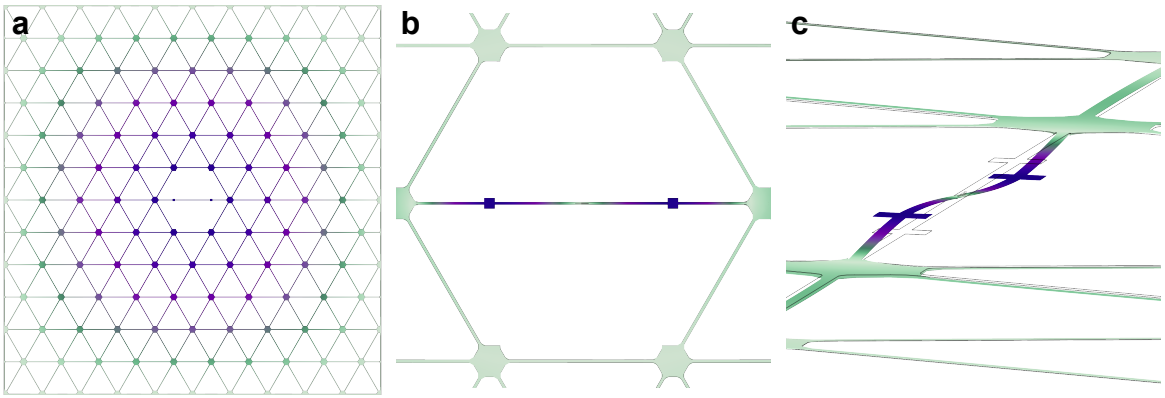


Figure 4.13: Mode shapes of PnC beam 1. Simulated mode shapes showing (**a**) the fundamental flexural mode of the complete PnC membrane, (**b**) the second-harmonic flexural mode, and (**c**) a side view of the same flexural mode illustrating that it is predominantly localized in the defect beam with a weak evanescent decay into the surrounding PnC.

the noise floor which makes performing dynamic torque magnetometry impossible with this device.

We build a finite-element model using *COMSOL* based on measured device dimensions reported in Tab. 3.2 in Sec. 3.2 and tune device dimensions within the limits of uncertainty in order to optimize matching between model and measurement. The phononic band gap is readily predicted between 450 – 720 kHz in reasonable agreement with the measured frequency response simply by implementation of the measured device dimensions. But in stark contrast to previous FEM reconstructions performed for torsion paddles 1 and 2, and PnC paddles 1 and 2, we cannot find a geometry within reasonable limits that produces the observed fundamental PnC membrane mode near 56 kHz and the supposed second flexural harmonic of the defect near 490 kHz. By reducing device thickness to 90 nm, the fundamental flexural frequency of the PnC membrane can be lowered to 62 kHz which is still off by 6 kHz and in this scenario the second flexural harmonic of the defect stays far too high at 615 kHz. As another way to model the observed behavior, we consider that the intrinsic film stress of our PECVD SiN_x film is potentially lower than the nominal 0.25 GPa. By reducing film stress by 20 % to only 0.2 GPa, prediction of the fundamental flexural frequency of the full PnC can be matched with the observed response within a deviation of 1 kHz. But even in this extreme scenario, the second harmonic is predicted far too high at 568 kHz. Based on sampling a large parameter space including various combinations of device geometries and intrinsic film stresses, the second harmonic cannot be matched with the observed signal at 490 kHz, and therefore, the idea of having a SiN_x film with a substantially lower film stress is unlikely. All things considered, we are not able to clearly assign the signal observed at 490 kHz to a specific mode.

Even without a comprehensive finite-element model for PnC beam 1, examination of this device architecture shows that the putative second-harmonic flexural mode of a double-clamped beam cannot be efficiently driven with piezoelectric or magnetic-torque driving, albeit for different reasons. Coupling from the piezoelectric shaker to the central defect is suppressed by the PnC. The assumption that the second-harmonic flexural mode can be driven efficiently using magnetic-torque actuation has been a hypothesis from the beginning which we can now refute based on our observation. In light of this, further attempts in examining defect modes in PnC structures would be well advised to employ photothermal excitation via modulation of optical radiation intensity instead.[281]

The vanishing torque sensitivity displayed by a negligible frequency shift observed with applied magnetic field, signature of a Duffing-type hardening nonlinearity, and FEM results that do not allow clear assignment of the mechanical mode detected inside the band gap; all this demonstrates that the device does not satisfy the requirements for dynamic torque magnetometry and ends our examination of PnC beam 1.

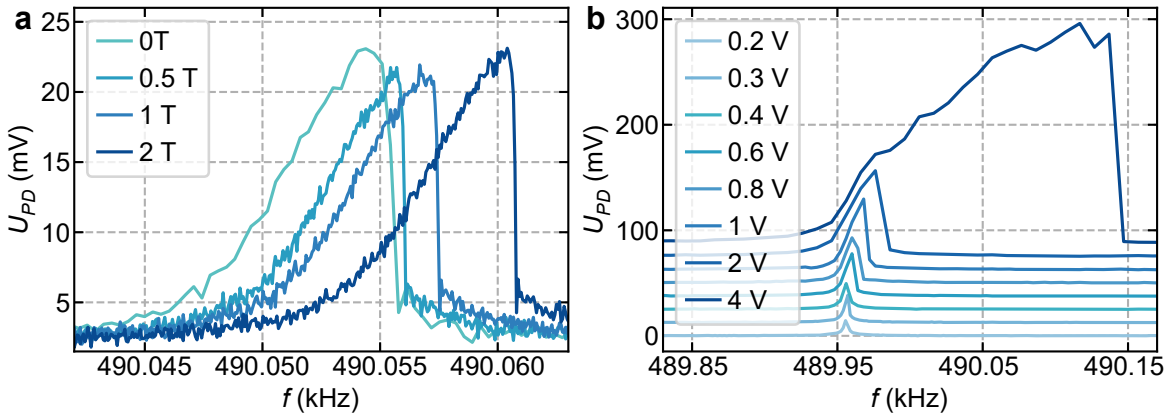


Figure 4.14: Frequency shift with applied field and non-linearity observed in PnC beam 1. Response of mechanical mode near 490 kHz, measured at 5 K under magnetic driving. (**a**) Frequency-shift with **H** oriented parallel to the magnetic easy axis. (**b**) Duffing-type hardening nonlinearity.

4.4 Discussion

In this chapter we have characterized the mechanical properties and torque-sensing performance of PECVD SiN_x torque transducers ranging from simple torsional paddles to devices embedded in a phononic crystal. By combining broadband spectroscopy, ring-down measurements, dynamic torque magnetometry, and finite-element modeling, we have assessed both the performance and torque sensitivities for working devices.

For the simple torsion paddles 1 and 2, we identified the fundamental torsional modes, quantified their resonance frequencies and Q-factors at cryogenic temperatures, and validated the experiment against a finite-element model. Torsion paddle 1 reaches a minimal torque sensitivity of $\tau_{\min} = 9 \cdot 10^{-22}\,\mathrm{Nm}/\sqrt{\mathrm{Hz}}$, while the softer, FIB-refined torsion paddle 2 improves this to $\tau_{\min} = 6 \cdot 10^{-22}\,\mathrm{Nm}/\sqrt{\mathrm{Hz}}$ despite a reduced Q. The comparison between analytic modeling, *COMSOL* simulations and dynamic torque magnetometry measurements indicates that FIB processing softens the bridges and increases internal dissipation. These prototype paddles operate close to the torque sensitivity of state-of-the-art Si cantilevers and provide robust, well-understood platforms for dynamic torque magnetometry, and we demonstrate that their use for dynamic torque magnetometry produces a well-defined DCM response.

For the first phononic device, PnC paddle 1, we demonstrated for the first time at our institute the fabrication of a two-dimensional phononic band gap in a suspended SiN_x membrane with a stop band from roughly 430 – 680 kHz and clear localization of defect modes. However, the fundamental torsional defect mode lies far outside the band gap and therefore no further characterizations of its torque sensing properties are performed.

The central result of this chapter is the detailed characterization of PnC paddle 2. Here, the torsional defect mode is deliberately engineered to lie well inside a well-defined band gap ranging from 450 – 690 kHz, and we confirm this picture experimentally and via FEM simulations that consistently reproduce the fundamental PnC flexural mode, the defect torsional frequency, and the band-gap edges. At $T \approx 5\,\mathrm{K}$ the fundamental torsional mode exhibits a resonance frequency $f_0 = 522\,\mathrm{kHz}$ and a quality factor $Q \approx 6.6 \cdot 10^3$. From the FEM-derived moment of inertia and the measured Q, we infer a minimal torque sensitivity $\tau_{\min} = 1.2 \cdot 10^{-22}\,\mathrm{Nm}/\sqrt{\mathrm{Hz}}$ in a 1 Hz bandwidth. This is comparable to or slightly better than the minimal torque sensitivity achieved by the standalone SiN_x torsional paddles, however, this does not result from an improved Q but rather originates from a smaller effective moment of inertia compared to torsion paddles 1 and 2. Further, this minimal torque sensitivity slightly surpasses state-of-the-art highly sensitive Si cantilevers which benchmark at $\tau_{\min} = 4 \cdot 10^{-22}\,\mathrm{Nm}/\sqrt{\mathrm{Hz}}$. A comparison of the measured Q with surface- and volume-loss models for SiN_x and reported cryogenic loss angles shows that the observed dissipation is fully compatible with intrinsic surface and bulk loss in our PECVD film, and that any additional clamping (radiation) loss must correspond to $Q_{\mathrm{clamp}} \gtrsim 10^4$. The absence of a Q enhancement upon embedding the paddle

in a PnC thus reveals that for our current film quality and thickness, mechanical dissipation of the torsional mode of the plain torsional paddles is dominated by intrinsic losses rather than by clamping losses.

Finally, the device PnC beam 1 confirms again the formation of a phononic band gap and shows an isolated mode within the gap, but exhibits strong Duffing nonlinearity, an ambiguous mode assignment, and an almost vanishing magnetic-field-induced frequency shift. These features make it unsuitable for sensitive dynamic torque magnetometry. Further, our observations with of PnC beam 1 combined with PnC beam 2 show that driving defect modes that are effectively shielded by a PnC are hard to drive using piezoelectric actuation, while magnetic actuation is efficient, albeit only for torsional defect modes.

In summary, this chapter establishes that (i) simple SiN_x torsional paddles achieve torque sensitivities on the order of $10^{-22}\,\mathrm{Nm}/\sqrt{\mathrm{Hz}}$, comparable to those obtained with torsional resonators embedded in a PnC. (ii) Phononic structuring around a torsional defect can be implemented reliably, and the torsional mode can be engineered to lie within the phononic stop-band, but (iii) in our present devices the fundamental torsional modes are intrinsically loss-limited, such that further improvements in torque sensitivity will primarily require reducing intrinsic dissipation as, for example, via optimized film deposition or surface treatment rather than relying on phononic isolation. Another route is to use high-stress stoichiometric LPCVD Si_3N_4, which provides lower defect density and has been widely employed to fabricate ultrahigh-Q mechanical resonators. Owing to its substantial intrinsic tensile film stress, this approach would require a different resonator geometry that prevents stress relaxation and thereby avoids the formation of high-loss regions, as is the case, for example, for string, trampoline or binary tree resonators. Furthermore, optimizing the flexural defect mode in a PnC structure—similar to PnC beam 1—rather than using a torsional paddle geometry would enable dissipation dilution and soft-clamping via strain-engineering to yield magnetic-torque transducers with ultrahigh Qs from high-stress stoichiometric LPCVD Si_3N_4.

5

Magnetic properties of an individual *Magnetospirillum gryphiswaldense* cell

This chapter is adapted from:
Claus, M. M., Wyss, M., Schüler, D., Poggio, M. & Gross, B. Magnetic properties of an individual *Magnetospirillum gryphiswaldense* cell. *Phys. Rev. E* **113**, 014408 (2026)

License and copyright notice: This chapter is excluded from the Creative Commons license stated in the front matter of this thesis. Reuse is subject to the copyright conditions of the original publication.

5.1 Summary

Many bacteria share the fascinating ability to sense Earth's magnetic field — a process known as magnetotaxis. These bacteria synthesize magnetic nanoparticles, called magnetosomes, within their own cell body and arrange them to form a linear magnetic chain. The chain, which behaves like a compass needle, aligns the microorganisms with the geomagnetic field. Here, we measure the magnetic hysteresis of an individual bacterium of the species *Magnetospirillum gryphiswaldense* via ultrasensitive torque magnetometry. These measurements, in combination with transmission electron microscopy and micromagnetic simulations, reveal the magnetic configurations of the magnetosomes, their progression as a function of applied field, as well as the total remanent magnetic moment and effective magnetic anisotropy of a chain within a single bacterium. Knowledge of these properties is crucial both for understanding the mechanisms behind magnetotaxis and for the design of systems exploiting magnetotactic bacteria in biomedical applications.

5.2 Introduction

Nature has invented an incredible mechanism to lead magnetotactic bacteria such as *Magnetospirillum gryphiswaldense* to its optimum feeding grounds: a compass needle in its cell body in the form of a chain of self-assembled magnetite crystallites, each a few tens of nanometers in diameter.[179,180,186] Even better than a compass, which only indicates the direction of the Earth's magnetic field, this chain of magnetosomes directly orients the bacterium along the field, as a result of the torque exerted. Using its flagella and a biological sensor for oxygen content,[282] the bacterium then propels itself along the magnetic field lines towards sources of nourishment in aquatic sediments. By restricting *M. gryph.*'s motion along one dimension, the chain of magnetosomes increases the efficiency of this search.[283,284]

The magnetism of a chain of magnetosomes within a single *M. gryph.* is complex: It consists of several tens of individual nanomagnets, one after another in a string-like arrangement. Because of their small size, each magnetosome can be approximated as a single-domain magnet, whose magnetism is determined both by the cubic anisotropy of magnetite and the magnetosome's shape. The fact that each magnetosome takes an unknown orientation in space adds further complexity. Finally—and crucially for the biological function of the chain—dipolar interactions between nearby magnetosomes result in a net preferred orientation along the chain axis. The competition between these anisotropies defines the orientation of each magnetosome's magnetic moment.

Precise measurements of the magnetic properties of magnetotactic bacteria, specifically anisotropy and total magnetic moment, are the key to understanding the mechanisms behind magnetotaxis.[285–291] One approach is to monitor the motion of either ensembles or individual bacteria in the presence of magnetic fields.[292–296] Reufer *et al.*[293] investigated the trajectories of *M. gryph.* swimming in a magnetic field, determining an average magnetic moment of $2 \cdot 10^{-16}\,\mathrm{A\,m^2}$ per bacterium. Zahn *et al.*[292] extracted the moment of about 150 bacteria in liquid by tracking and modeling the rotation and translation of individual bacteria under the influence of magnetic tweezers. Typically, however, magnetic properties deduced from such measurements rely on assumptions about the motion of the bacteria in liquid. The magnetic moment of ensembles of magnetotactic bacteria has been measured directly using a superconducting quantum interference device (SQUID).[297,298] Individual bacteria have also been studied via magnetic imaging techniques, including X-ray magnetic circular dichroism combined with scanning transmission X-ray microscopy[299–303] and electron holography.[304] In particular, Dunin-Borowski *et al.* used electron holography to visualize the magnetic stray fields of an individual *Magnetospirillum magnetotacticum* in remanence.[304]

The magnetic hysteresis of an individual bacterium, from which magnetic properties such as coercivity, anisotropy, and switching behavior can be determined, is challenging to measure due to the tiny magnetic moment of a single chain of magnetosomes.[300,305,306] Knowledge of these properties is especially important for applications involving magnetic actuation or sensing.

Dynamic cantilever magnetometry (DCM),[70,230,307,308] which is a particularly sensitive form of torque magnetometry, provides a method for measuring the magnetism of nanometer-scale magnetic systems. Gysin *et al.* first used DCM to measure the magnetic hysteresis of an ensemble of about 100 *M. gryph.*, resulting in a magnetic moment of $5 \cdot 10^{-16}\,\mathrm{A\,m^2}$[309] per bacterium. A few years later, using a more sensitive cantilever, the same group managed to measure the hysteresis of an individual *M. gryph.*,[305] however, low signal-to-noise ratio precluded a detailed analysis of the measurements.

By attaching a single *M. gryph.* to an ultrasensitive SiN cantilever, we resolve its magnetic hysteresis via DCM. Furthermore, based on transmission electron microscopy (TEM) images, we create a micromagnetic model for the bacterium's chain of magnetosomes and compare it to DCM measurements. This comparison allows us to determine the likely progression of the magnetosomes' magnetic configurations as a function of applied field, as well as determining components of the remanent magnetization, effective anisotropy, and switching field of the bacterium. In measurements of ensembles, the properties of individual bacteria are obscured by inhomogeneity in the size, shape, and orientation of the chains of magnetosomes.

5.3 Dynamic cantilever magnetometry

In DCM, as shown in Fig. 5.1, the sample under investigation is attached to the free end of a cantilever, which is driven into self-oscillation at its fundamental mechanical resonance frequency f. Similar to DPM introduced in Sec. 2.3.2, the DCM measurement consists of monitoring changes in the resonance frequency as a function of a uniform applied magnetic field $\Delta f(\mathbf{H})$, relative to the unperturbed resonance frequency f_0 at $\mu_0 H = 0\,\mathrm{T}$. Δf reveals the curvature of the magnetic system's free energy with respect to rotations about the cantilever oscillation axis[76,217] according to

$$\Delta f = \frac{f_0}{2k_0 l_{\mathrm{eff}}^2} \left(\frac{\partial^2 E_m}{\partial \theta_c^2}\bigg|_{\theta_c=0} \right),$$

where l_{eff} is the cantilever's effective length, and θ_c the cantilever's oscillation angle (see Eq. (2.43) for comparison with DPM). A detailed derivation of this equation can be found in the supplementary information of Ref. 72. This relation does not allow a direct link between magnetic moment and Δf, rather Δf can be intuitively understood in a thermodynamic framework[217] as an analogue to magnetic susceptibility: while susceptibility quantifies the magnetic response of a sample to changes in the magnitude of $\mathbf{H}$, Δf quantifies the response to changes in its orientation. Measurements of Δf are particularly useful for identifying magnetic phase transitions,[72,217,228] as well as providing information on the switching, saturation magnetization, coercivity, and the anisotropy of a magnetic system.[75]

The SiN cantilever used in this measurement has a quality factor of a few thousand at room temperature. Once the sample has been attached to the end of the cantilever, the cantilever is mounted in the measurement setup described in Sec. 2.3.1, and the cantilever's flexural motion is read out using 100 nW of laser light. For investigation of *M. gryph.*, the piezoelectric actuator mechanically drives the cantilever at f_0 with a constant oscillation amplitude of a few tens of nanometers using a feedback loop implemented by a field-programmable gate array. This process enables the fast and accurate extraction of Δf from the cantilever deflection signal.

5.4 Data acquisition and processing

The sampling time for measurements of cantilever frequency f vary between 1 and 5 s, a time which is limited by a slow time-dependent frequency drift, which adds to the magnetic contribution,

$$f = f_0 + f_{\text{magnetic}}(H) + f_{\text{drift}}(t).$$

The drift likely originates from liquid evaporating from the bacterial cell into the surrounding vacuum. This explanation is supported by the observation that f increases monotonically in time at room temperature (the expected effect of a loss of mass on the cantilever), while no drift is observed at cryogenic temperatures, when the sample is frozen. We approximate $f_{\text{drift}}(t)$ to be linear in time and subtract it from f. The measurement noise is close to the thermal limit of what is possible with the given setup and cantilever. For further details in Δf to be resolved, one would have to reduce the cantilever's mechanical dissipation and/or perform the measurements at lower temperatures.

The error of our measurement of the remanent magnetic moment is dominated by the uncertainty in determining the exact geometry of our cantilever. This uncertainty leads to a 5 % error in the determination of both the cantilever's spring constant k_0 and its effective length l_{eff}, ultimately affecting the uncertainty of the magnetic moment measurement. Cantilever geometry is estimated from TEM images and goes into *COMSOL* simulations determining k_0 and l_{eff}.

5.5 Sample preparation and cantilever properties

Cells of *M. gryph.* DSM 6361 are grown under anaerobic conditions in sealed Hungate tubes containing 10 mL of Flask Standard Medium under a headspace of N_2, as described before.[310,311] The cells are then fixed with formaldehyde. Next, a droplet of solution containing the cells is placed on the surface of a polytetrafluoroethylene sheet. A small permanent magnet placed under the sheet helps to retain bacteria, which contain magnetosomes. After 10 min, the droplet is dried with a gentle flow of compressed air. A micromanipulator system (Narishige) is used to pick up an individual bacterium from the surface, and transfer it to the free end of the ultra-soft cantilever. The bacterium is attached to the apex of the cantilever for magnetic characterization as shown in Fig. 5.1b, oriented roughly with the cantilever axis using the micromanipulator, and fixed in place with UV glue (Thorlabs).

The cantilever is commercially available (Nunano) and made of SiN. Its 1.94 µm width and 55.8 µm length are measured using scanning electron microscopy. Its nominal thickness is 50 nm. The experimentally observed resonance frequencies of the bacterium-loaded cantilever at zero field are $f_0 = 16.9$ kHz and $f_1 = 104.9$ kHz, where f_1 is the frequency of the first harmonic. We use the *COMSOL Multiphysics* software package to construct a finite element model of the cantilever and adjust its properties so that its calculated resonance frequencies match the measured frequencies.

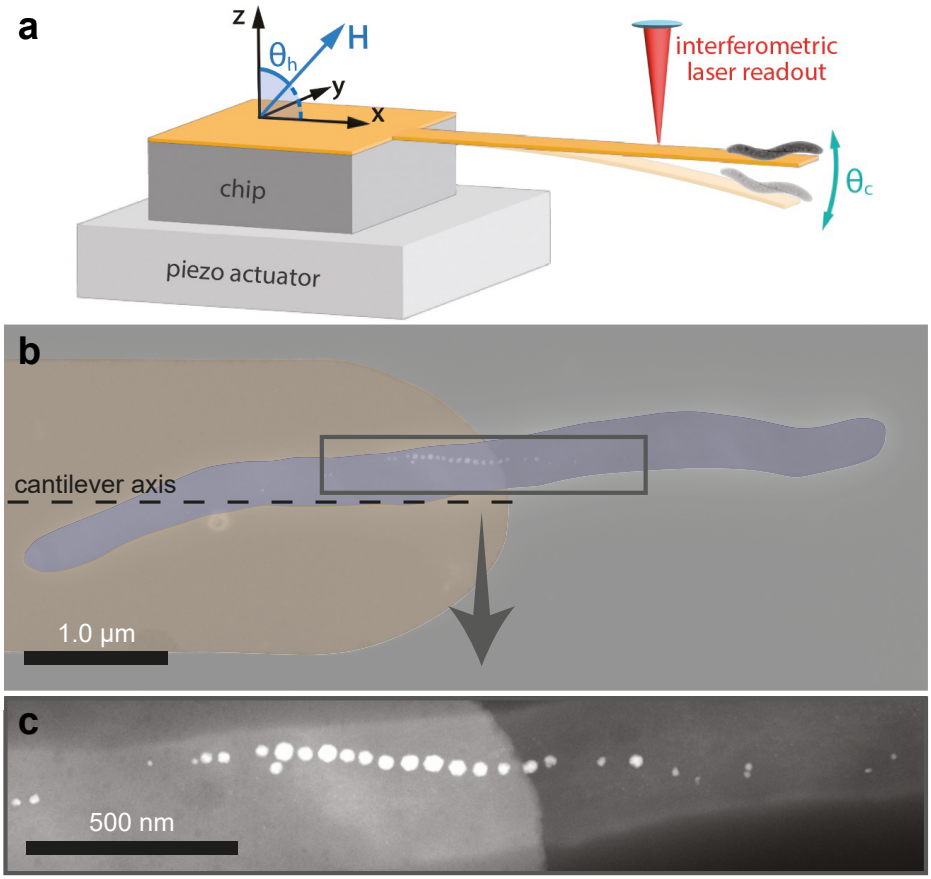


Figure 5.1: Measurement setup and bacterium-on-cantilever probe. (**a**) Schematic of a cantilever with a single bacterium attached at the tip, including the definition of the coordinate axes. (**b**) False color high-angle annular dark-field scanning transmission electron microscopy image showing the orientation of the magnetosome chain relative to the cantilever axis. (**c**) Close-up view of the magnetosome chain.

The Young's modulus of SiN is set to 250 GPa, its density to 3100 kg/m^3 and Poisson's ratio to 0.23. The bacterium is modeled as a 5 µm long bar with flat bottom and rounded top. Its width is 300 nm and its density is assumed to be the same as for water ($\rho = 1000\,\mathrm{kg/m^3}$). In order to match f_0 and f_1, a small, linear gradient in the thickness of the cantilever is introduced, such that it is thickest at its base (39.9 nm) and becomes thinner towards the tip (38.2 nm). Using this model, we calculate an effective length $l_{\mathrm{eff}} = 39.4\,\mu\mathrm{m}$ and a spring constant $k_0 = 44\,\mu\mathrm{N/m}$ for the cantilever.

5.6 Measurements

We perform two types of DCM measurements just below room temperature at $T = 284\,\mathrm{K}$. In the first, shown in Fig. 5.2, we monitor Δf as a function of the direction θ_h of a large field of constant magnitude $\mu_0 H = 3.5\,\mathrm{T}$ applied in the plane perpendicular to the cantilever's rotation axis (xz-plane). In a magnetic field H large enough to saturate the system, as in this case, the maxima and minima of $\Delta f(\theta_\mathrm{h})$ indicate the directions of the easy and hard axes, respectively.[70,76] The data plotted in Fig. 5.2 show the signatures of uniaxial anisotropy with the maximum and minimum separated by 90° and the maximum indicating the direction of the easy axis, which roughly coincides with the axis of the magnetosome chain.

In the second type of measurement, shown in Fig. 5.4, we measure Δf as we sweep H along a fixed direction from large positive to large negative values. Analysis of the resulting $\Delta f(H)$ hysteresis measurements allows for the extraction of information on the remanent magnetic moment as well as the system's magnetic switching behavior and the progression of magnetic configurations present as the system reverses. Measurements taken for $\theta_\mathrm{h} = 90°$ (along the axis of the magnetosome

chain), shown in Fig. 5.4a and b, and for $\theta_h = 0°$, shown in Fig. 5.4c and d, show the characteristic response of a magnetic system with uniaxial anisotropy with **H** applied along its easy and hard axes, respectively.[70] The sharp discontinuity seen in Fig. 5.4b is the signature of magnetic switching in reverse applied field allowing us to deduce a coercive field of around 20 mT for the chain.

Upon completion of the DCM measurements, the cantilever is transferred to a grid for subsequent high-resolution (HR)TEM, high-angle annular dark-field scanning transmission electron microscopy (HAADF-STEM) imaging, and TEM tomography. During this process, the cantilever is broken off of its base at its clamping point, making further DCM measurements impossible. TEM tomography in combination with a deep learning algorithm then allows the construction of a realistic three-dimensional (3D) model of the particles, revealing their position and morphology. Further details on HAADF-STEM and HRTEM imaging, as well as TEM tomography and subsequent development of the 3D model are provided in the following section.

5.7 Magnetosome chain

The process of developing a realistic physical model of the magnetosome chain is described in this section, including considerations about its shape, dimension, and orientation in 3D space, and also its magnetic properties for the construction of an accurate micromagnetic model.

5.7.1 Structural model

We use HRTEM and HAADF-STEM to image the position and morphology of each magnetosome in the chain. Individual magnetite magnetosomes, which are surrounded by biological tissue, are clearly resolved in the HAADF-STEM images, as shown in Fig. 5.1b and c. These images show the individual bacterium under investigation, which is still attached to the end of the SiN cantilever. The brightest contrast in the images corresponds to the projection of each magnetosome on the xy-plane. The image reveals the alignment of the magnetosome chain with the cantilever's long axis. HRTEM images of each individual magnetosome and their Fourier transforms also provide information on their crystallinity and orientation. Crystal planes visible in the images show that at least 25 of the 29 magnetosomes are in a crystalline state. We do not find correlations between the orientation of these planes and either the axis of the chain or the orientation of neighboring magnetosomes. Experimental circumstances prevented the extraction of the exact crystalline orientation of each magnetosome, which would have provided the orientation of each particle's magneto-crystalline anisotropy axes.

We then rely on TEM tomograms to fully determine their position and shape in 3D. These tomograms, which were recorded more than a year after the original images, show a $\sim$4 % increased distance between the magnetosomes. We attribute this to a deformation of the bacterium's cell body over time, and correct for this when reconstructing the morphology of the chain.

For technical reasons, we were able to reconstruct only the main part of the magnetosome chain, which contains 20 magnetosomes, via tomography. For these tomograms, we correct for the missing wedge artifact using the deep learning software package *IsoNet*,[312] which iteratively reconstructs the missing wedge information of each magnetosome. Missing wedge correction is of particular importance in the case of magnetic nanoparticles: without correction, the extracted morphology of the individual magnetosomes would show a systematic overestimation of their extent along the z-axis. This effect would introduce a spurious shape anisotropy along the z-axis. Note that the choice of threshold in the tomogram's intensity, which is used to set the boundary between a magnetosome and its surroundings, is chosen such that the resulting volume of the magnetosome chain yields a good match between the simulated and experimental $\Delta f(H)$ asymptotes at high field.

For 9 remote magnetosomes, which are not part of the central chain and constitute less than 5 % of its total volume, we were unable to fully reconstruct their 3D position and morphology from the tomograms. We set the position of these magnetosomes along the z-axis using the partial information from the tomogram combined with an extrapolation of their position in 3D based on their nearest neighbor's position and the overall shape of the chain. We further assume that their morphology is an ellipsoid of revolution, providing uniaxial anisotropy as the dominant shape anisotropy term, as shown for the magnetosomes of *M. gryph.*[313] The unknown extent of these magnetosomes along

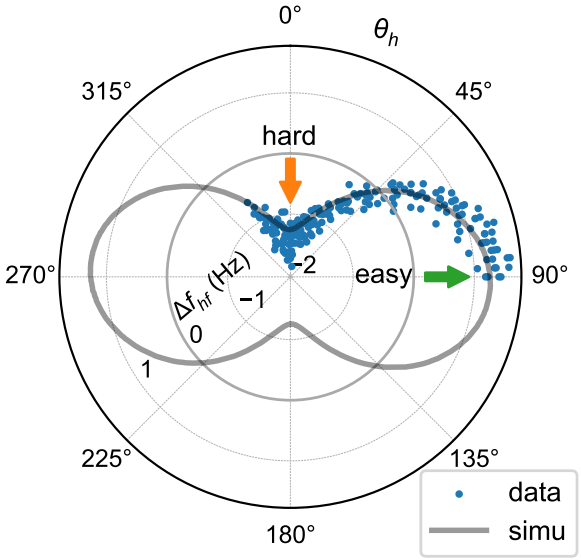


Figure 5.2: DCM field rotation measurement and simulation. $\Delta f(\theta_\mathrm{h})$ measured at $\mu_0 H = 3.5\,\mathrm{T}$ is plotted as blue points. Orange and green arrows indicate the hard and easy axes, respectively, as derived from the simulation shown in transparent grey.

the z-axis is then set to the average of the lateral extents, see Sec. 5.7.1. Because they constitute a small fraction of the total volume of the chain, these magnetosomes play a minor role in its magnetic behavior.

Ultimately, the procedure described above yields a 3D model of the magnetosome chain with ∼1.2 nm pixel size. A list of all magnetosomes and their properties along with TEM images of each magnetosome are provided in App. C.1 and C.2.

5.7.2 Micromagnetic model

Micromagnetic simulations are performed with the finite-difference software package *Mumax3*. Material parameters are taken from literature at the measurement temperature $T = 284\,\mathrm{K}$:[314] we set the exchange stiffness to $A_\mathrm{ex} = 13.5\,\mathrm{pJ\,m}$, the saturation magnetization to $M_\mathrm{s} = 483.9\,\mathrm{kA/m}$, and the first order cubic anisotropy constant to $K_\mathrm{c1} = -14.0\,\mathrm{kJ/m^3}$.

As discussed in the preceeding section, the morphology and position of the individual magnetosomes in 3D space are taken from TEM data. Because the orientation of each magnetosome's cubic anisotropy axes is unknown, we simulate the magnetosome chain with many configurations of different randomly chosen orientations of each magnetosome's crystalline anisotropy axes.

The simulated configuration that best matches the DCM measurements is presented in Sec. 5.8 and is chosen via an iterative process. We start by finding the 20 best matches to the high-field measurement of $\Delta f(\theta_\mathrm{h})$, shown in Fig. 5.2, from ∼1000 configurations of different randomly oriented cubic anisotropy axes. The best matches are determined by minimizing the root-mean-square deviation between the simulated and measured data. For each of these 20 configurations, we then simulate five $\Delta f(H)$ curves with the external field aligned along slightly different directions within a few degrees, which is our experimental error, of the easy (hard) axis. These small deviations are considered, because many features in the simulations depend sensitively on this alignment. Finally, we choose the configuration of magnetosome orientations, whose simulated hard- and easy-axis $\Delta f(H)$ curves best qualitatively match both measured curves. A match is judged by taking into account how well the simulation reproduces the high-field asymptotes, curve shape, and switching events of both the easy- and hard-axis measurements. To illustrate the effect of different configurations of anisotropy axis orientations within the magnetosome chain, Fig. 5.3 shows the $\Delta f(\theta_\mathrm{h})$ measured at $\mu_0 H = 3.5\,\mathrm{T}$ for the best match along with a model that was discarded, due to poor matching with the measurement. We also plot a configuration of the magnetosome chain, in which the ⟨111⟩-type axes for each magnetosome are aligned with the chain axis.

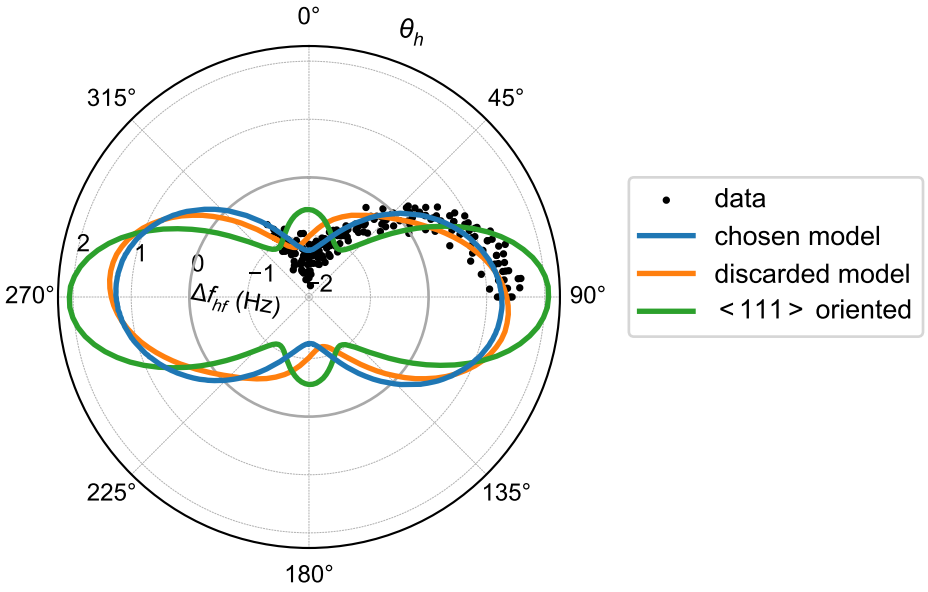


Figure 5.3: DCM field rotation measurement and simulations. $\Delta f(\theta_\mathrm{h})$ measured at $\mu_0 H = 3.5\,\mathrm{T}$ plotted together with simulations for different combinations of anisotropy-axis orientations assigned to the individual magnetosomes.

5.8 Results

DCM data plotted in Fig. 5.2 indicate the presence of an effective anisotropy along the chain of magnetosomes of uniaxial character. Detailed consideration is necessary to understand the role that all the involved magnetic anisotropies play. To do so, we construct a three-dimensional, micromagnetic model of the magnetosome chain using the software package *Mumax3*.[232,315] The software solves the space and time dependent Landau-Lifshitz-Gilbert equation using a finite-difference approach, i.e. we discretize space to 1.2 nm, and determine the relaxed state of each voxel's magnetic moment in an effective magnetic field. This effective field contains all relevant interactions and anisotropy contributions: exchange interactions, dipolar interactions, cubic magneto-crystalline anisotropy of the individual particles, and an externally applied magnetic field. Ultimately, this approach allows us to precisely model the magnetic behavior of the magnetosome chain from knowledge of the position, shape, and orientation of each magnetosome as measured by TEM. Using material parameters from the literature,[314] the model determines the equilibrium magnetic state of the chain for a set external magnetic fields. By including the geometry of the DCM experiment and the properties of the cantilever, we calculate Δf and use it to iteratively adjust the input parameters, optimizing the agreement between simulated and measured Δf. In this way, features in hysteresis curves of $\Delta f(H)$ such as jumps, dips, or humps can be associated with events such as magnetic switching or collective rotation of magnetic moments.

Our lack of knowledge of the orientation of the crystalline anisotropy axes of the individual magnetosomes forces us to fall back on a "best guess" strategy in order to construct a realistic model: We simulate 1000 iterations of the high-field $\Delta f(\theta_\mathrm{h})$ measurement shown in Fig. 5.2 with randomly oriented crystalline anisotropy axes for each magnetosome. The parameters from the 20 best matches are then used to simulate the $\Delta f(H)$ hysteresis measurements shown in Fig. 5.4 for a number of magnetic field orientations close to the experimental orientations. Further details on the simulations can be found in Sec. 5.7.2.

One set of parameters is found to provide the best match to the measurements, coinciding with both the experimental $\Delta f(\theta_\mathrm{h})$ and $\Delta f(H)$ data within the measurement noise, as shown in Figs. 5.2 and 5.4. The model allows the extraction of an effective uniaxial anisotropy constant for the chain as a whole, containing all contributions from the included anisotropies, $K_\mathrm{u} = 12.5\,\mathrm{kJ/m^3}$. This is in excellent agreement with the value obtained in Ref.[306] for a chain of non-interacting magnetic

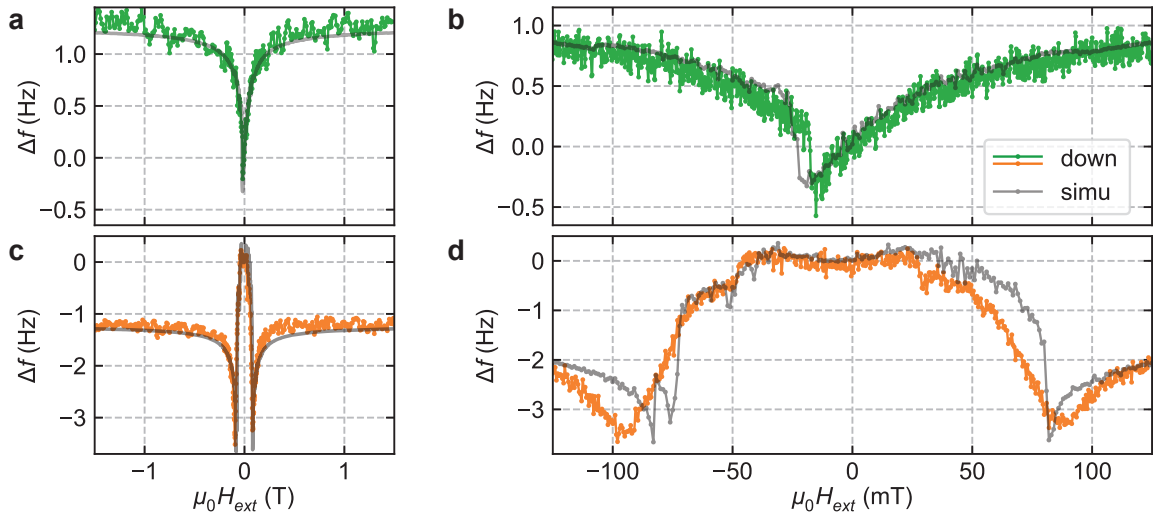


Figure 5.4: DCM hysteresis as a function of applied field. (**a**) and (**b**) Measured $\Delta f(H)$ with **H** parallel to the magnetic easy axis plotted in green for a wide and narrow field range, respectively. (**c**) and (**d**) Measured $\Delta f(H)$ with **H** perpendicular to the magnetic easy axis plotted in orange, for a wide and narrow field range, respectively. In all plots, the applied field $\mu_0 H_{\text{ext}}$ is swept from large positive values, through zero, to large negative values. Best-fit simulations are plotted in transparent grey.

dipoles. Note, however, that the model therein incorporates cubic crystalline anisotropy with one axis aligned to the chain axis for all magnetosomes, deviating from the model at hand. Typically, in literature,[179] only a minimal magnetic moment for effective magnetotaxis is given. The effective anisotropy of the magnetosome chain is, however, an equally important quantity, because it quantifies the stability of the magnetic moment along the chain axis against perturbation.

It is interesting to note that most of the 1000 simulated high-field rotation curves do not show the characteristic shape resulting from simple uniaxial magnetic anisotropy along the chain direction, as measured for this bacterium in Fig. 5.2. Rather, they show a more complex angular dependence with signatures of the shape and randomly oriented crystalline anisotropies of the individual magnetosomes. This finding highlights that anisotropies of the individual magnetosomes should not be neglected and suggests that the absence of features due to these anisotropies in the curve in Fig. 5.2 could be a coincidence due to the specific orientations of the magnetosomes in this chain or the result of an external process, such as the alignment of the magnetosomes during their growth in the *M. gryph.* cells. Nevertheless, even in iterations, in which the orientations of the individual magnetosomes result in more complex $\Delta f(\theta_{\text{h}})$, the dominant easy axis is always set by the direction of the magnetosome chain. The fact that the chain axis sets the global energetic minimum of the magnetic anisotropy energy, despite the competing anisotropies of individual magnetosomes, ultimately ensures that every bacterium's body aligns along magnetic field lines.

Some previous studies report the alignment of a ⟨111⟩-type axis of individual magnetosomes with the chain axis for several different types of magnetotactic bacteria,[306,313,316,317] including *M. gryph.* We tested the consistency of our measurements with such an alignment, by simulating a number of random orientations in which each magnetosome had a ⟨111⟩-type axis pinned along the chain direction. Under this constraint, no match to the measurements was found, with an exemplary result shown in Fig. 5.3. In fact, averaged over all magnetosomes, the simulation with the best match has an angle between the chain axis and the nearest ⟨111⟩-type axis of 23° with a standard deviation of 12°. We therefore conclude that no specific alignment of the ⟨111⟩ axes with the chain axis is present in the measured bacterium.

Measurements of the hysteresis of $\Delta f(H)$, shown in Fig. 5.4, are taken with **H** aligned along the magnetic easy and hard directions, as determined by the measurements shown in Fig. 5.2. In the limit of low fields, the component of the remanent magnetic moment parallel to the external magnetic field applied during the hysteresis cycle can be directly determined from $\Delta f(H)$ with

the knowledge of the cantilever properties.[70] We find $M_x \approx (1.84 \pm 0.54) \cdot 10^{-16}$ A m^2 after **H** is applied parallel to the chain axis, which is closely reproduced by our best-scenario micromagnetic model with $M_x \approx 1.73 \cdot 10^{-16}$ A m^2, for which the calculated $\Delta f(H)$ is also shown in Fig. 5.4. The saturation magnetic moment within the model is $2.0 \cdot 10^{-16}$ A m^2. Therefore, almost the full moment is preserved along x in remanence after **H** is applied parallel to the chain axis. After the application of perpendicular fields, M_z nearly vanishes: $M_z \approx (0.26 \pm 0.14) \cdot 10^{-16}$ A m^2. Note, however, that this measurement does not determine the remanent magnetic moment along the x or y directions. These values are consistent with the orientation of the effective anisotropy along the chain axis. Further, the magnitude of the saturation moment is in very good agreement with previous measurements done via optical microscopy[292,293] and DCM.[309]

Further insight can be deduced from a detailed analysis of the measured and simulated $\Delta f(H)$ shown in Fig. 5.4. In the measurement with the field applied along the easy-axis, shown in Fig. 5.4b, $\Delta f(H)$ monotonically decreases from high fields down to zero. In a reverse field of -17 mT, a jump occurs and thereafter the curve progresses symmetrically as for positive fields. Such behavior and the V-shape of the curve can be explained via a single macro-spin approximation:[70] all magnetic moments are aligned with the external field, coinciding with the easy-axis of the effective magnetic anisotropy and, shortly after field reversal, collectively flip their direction in a single switching event. Simulations reveal that this picture conceals a more complex behavior: as the applied field is swept from saturation down towards zero, some magnetosomes reorient the alignment of their magnetic moments from coinciding with the chain axis to coinciding with one of their local magnetic easy axes. In the given simulation, this process proceeds in the form of a smooth rotation with decreasing magnetic field. To illustrate the result of these rotations, Fig. 5.5a shows m_x and m_z of the remanent state of the magnetosome chain, where only the main part of the chain maintains close-to full alignment of the magnetic moments with the overall magnetic easy axis. Although the net remanent magnetic moment of the chain is nearly aligned along the chain's easy axis (only 1.8° off), the remanent moments of each individual magnetosome span an angle of about 34° with respect to this axis with a 29° standard deviation. This qualitatively confirms the observations of Ref.,[306] in which the remanent magnetic moment of a single magnetosome was tilted away from the overall easy axis. Although the noise level of the measurement does not allow for the confirmation of related switching events or rotations of magnetic moments in the measured $\Delta f(H)$, the slightly reduced remanent magnetic moment compared to the saturation moment is their direct experimental consequence. The simulations show that further sweeping H in the reverse field direction results in the full magnetic reversal of the chain via switching events of individual or a few magnetosomes, as illustrated in Fig. 5.5b.

When **H** is applied along the magnetic hard-axis, the form of the measured $\Delta f(H)$ is consistent with a gradual rotation of all magnetic moments from alignment with **H** towards the easy-axis for decreasing $|H|$ (compare Fig. 5.4c to Fig. 9 in Ref.70). The beginning of this rotation is marked by the strong dips around ± 100 mT. Deviations from this simple behavior appear in the discontinuities at 28 mT and -48 mT in the measured $\Delta f(H)$. The micromagnetic simulations, which reproduce these distinctive features at nearly the same fields, suggest that they originate in an abrupt reorientation of the magnetization of individual or groups of magnetosomes, cf. Fig. 5.5d and e. The discontinuity in d is connected to two individual magnetosomes in the chain reorienting its magnetization, while it corresponds in e to a switch of the magnetization of a group of three magnetosomes aligned with $\hat{x}$ towards $-\hat{x}$. Further switching events are either hidden in the noise of the measurement or the progression of the magnetic moments takes place slightly differently than in our best-guess simulation.

This analysis of the measurement along the magnetic hard-axis also suggests a specific remanent state, as shown in Fig. 5.5c. In this state, the magnetic moments on the left half of the chain orient their moments towards the left ($-\hat{x}$), while those on the right orient towards the right ($+\hat{x}$). Together, the moments compensate each other, leading to a very low remanent moment compared to the case with **H** applied along the easy-axis. Note, however, that in other simulations, which match similarly well with experiment, this state of low remanent moment is not evident, but a state rather close to what is shown in Fig. 5.5a is observed.

As the progressions of the chain's magnetic configuration for the two different orientations of the

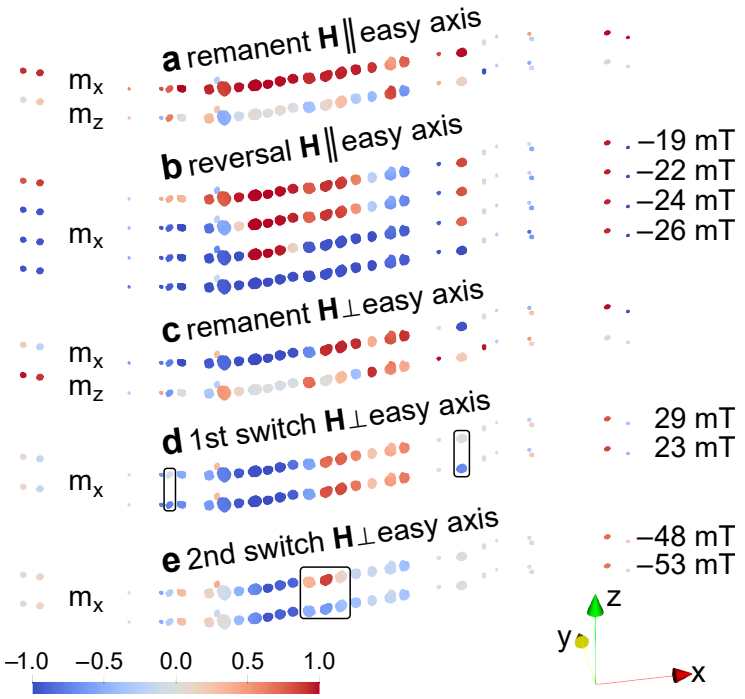


Figure 5.5: Visualization of simulated magnetic states of the magnetosome chain. The color bar applies to the component of the magnetization as indicated on the left of each of the visualizations.

external field show, the total magnetic moment at remanence depends strongly on the magnetic history of the chain. This dependence is a result of the relatively weak effective anisotropy, which fails to stabilize the magnetic moment in direction of the easy axis against the application of perpendicular fields larger than several tens of millitesla. Nevertheless, because in its natural habitat *M. gryph.* likely never experiences magnetic fields of this magnitude, this effective anisotropy is sufficient to stabilize its magnetic moment in direction of the magnetosome chain and ensure magnetotaxis. However, knowledge of the magnetic behavior for field magnitudes beyond earth's magnetic field may become decisive for applications of magnetotactic bacteria such as biological micro-robots, in which stronger fields are typically used.

5.9 Discussion

Via ultrasensitive torque magnetometry, combined with transmission electron microscopy and micromagnetic simulations, we determine the remanent magnetic moment of $(1.84 \pm 0.54) \cdot 10^{-16}$ A m^2 and a saturation moment of $2.0 \cdot 10^{-16}$ A m^2 of an individual *M. gryph.* cell. Furthermore, we determine an effective easy-axis anisotropy of 12.5 kJ/m^3 aligned along the bacterium's chain of magnetosomes. Analysis of the magnetic hysteresis shows that this anisotropy is strong enough to stabilize the remanent magnetic moment in Earth's magnetic field. Future experiments, making use of TEM tomography and diffraction to reveal the full morphology and crystal structure of the magnetosomes,[306] may allow for higher precision determination of the exact magnetic states of a single bacterium. Improved cantilever sensors could also enable the resolution of the switching of individual magnetosomes, further deepening our understanding of the magnetic reversal process. DCM Measurements of many more individual bacteria would also help to determine the homogeneity of saturation moment, remanent moment, and anisotropy across a population of bacteria.

6

Conclusions and Outlook

This work reports an initial effort toward the development of new silicon nitride based resonators aiming to provide ultrasensitive mechanical transducers with ultimate torque sensitivity in order to enable the study of magnetic 2D materials and complex vdW heterostructures via dynamic torque magnetometry. The approach builds on the prior works which have demonstrated ultrahigh-Q mechanical resonators based on employing PnC engineering to open a phononic band gap that acoustically isolates a defect mode while also soft-clamping the supports in order to suppress clamping losses.

In Ch. 3 we have established a reliable microfabrication route to produce SiN_x torque transducers, including standalone resonators as well as versions integrated in PnC surrounds. The method achieves high dimensional accuracy and good reproducibility for features above the laser writer's lithographic resolution limit, and focus-dependent spot-size variations is identified as the dominant source of run-to-run offsets near $\sim$0.5 µm. It further shows that post-processing by Ga FIB milling can be used to reshape bridge dimensions, albeit with trade-offs in stress modification and scalability. In parallel, previously reported preparation and handling protocols for few-layer vdW flakes are reproduced, with hBN capping applied for transient protection, and we demonstrate that viscoelastic stamping can be used to transfer vdW flakes to a suspended (unpatterned) SiN_x membrane. Utilizing precision dicing, the chips can be diced to position vdW flakes near the chip edge, enabling their study by nanowire MFM. Together, these capabilities provide the technical foundation for engineering SiN_x transducers embedded in a PnC toward ultrasensitive dynamic torque magnetometry of vdW materials and heterostructures, with the possibility to integrate electrical contacts. Microfabrication methods for defining electrical contacts as narrow as $\sim$100 nm on planar substrates are well established.

The remaining key fabrication challenge is integrating vdW samples with the PnC architecture, for which we foresee three routes, each requiring prior double-sided hBN encapsulation for maximal sample protection: (i) The sample can be stamped directly onto the device layer—either before or after patterning the device—prior to the final release step in aqueous KOH. At this stage, the thin Si layer beneath the patterned SiN_x provides structural support to the otherwise fragile resonator and its PnC surround, as well as the thermal conductance required to heat and melt the PC film for sample release. This approach may also require securing the flake—for example, using a droplet of PMMA or metal clamps formed by focused electron-beam-induced deposition (FEBID)—to ensure compatibility with the final release process in an alkaline solution. (ii) The sample can be stamped onto a separate SiN_x membrane. Predetermined breaking points can be patterned either before or after stamping, after which the intermediate SiN_x carrier can be broken out and transferred to the device using a micromanipulator. This method offers the advantage of being performed either before or after the final device release. If performed after the release step, vdW forces between films are expected to provide sufficient adhesion for firm attachment. (iii) Should approaches (i) and (ii) fail, the sample can be transferred using a wet-transfer method inspired by the works of Jäger *et al.* and

Forrer *et al.*, in which the flake is initially stamped onto a thin sacrificial dextran layer instead of a SiO_2 layer,[318,319] thereby avoiding bubble formation below the PMMA carrier in the absence of SiO_2 etching. This transfer scheme, however, is extremely delicate, error-prone, and requires immersing the suspended device in liquid, which carries a substantial risk of breaking parts of it, especially for high-contrast PnC geometries as presented in this work.

In Ch. 4 we have provided a comprehensive mechanical characterization of PECVD SiN_x torque transducers, from standalone torsional paddles to PnC devices with torsional and flexural defect modes, by combining broadband spectroscopy, ring-down measurements, dynamic torque magnetometry, and FEM modeling. Standalone paddles reach torque sensitivities in the medium $10^{-22}\,\mathrm{Nm}/\sqrt{\mathrm{Hz}}$ range, with FIB refinement improving sensitivity via reduced stiffness at the cost of increased mechanical dissipation. For PnC structures, we demonstrate robust formation of a phononic band gap and, for PnC paddle 2, successful engineering of a torsional defect mode within the stop band, yielding $\tau_{\mathrm{min}} = 1.2 \cdot 10^{-22}\,\mathrm{Nm}/\sqrt{\mathrm{Hz}}$ primarily through reduced effective inertia rather than enhanced Q compared to standalone geometries. This sensitivity slightly surpasses the sensitivity benchmark set by current state-of-the-art highly-sensitive cantilevers used in DCM. Our analysis of loss channels indicates that the torsional modes in our present devices are dominated by intrinsic dissipation. This finding implies that significant sensitivity gains—by orders of magnitude—envisioned for studies of vdW materials and heterostructures in the few-layer limit, will require improved material quality and surface engineering to reduce internal bulk and surface losses, rather than relying solely on phononic isolation, with the current PECVD SiN_x torsional-resonator platform.

An alternative route is to switch to stoichiometric LPCVD Si_3N_4, which has been widely used to engineer ultrahigh-Q resonators. Its intrinsically high tensile film stress, however, calls for strategies that prevent stress release upon device release; otherwise it can lead to out-of-plane deformation as well as the formation of high-loss defect regions. This can be achieved either by designing the defect geometry accordingly or by locally preventing stress release, for example by leaving a thin remaining Si support. Finally, Fedorov *et al.* reasoned, based on dissipation-dilution theory, that torsional modes do not experience dissipation dilution, which is at odds with recent experimental observations on mass-loaded strained Si_3N_4 nanoribbons reported by *Pratt et al.*[123,141] Fabricating such a torsional transducer, determining its Q-factor, and assessing its torque-sensing performance in dynamic torque magnetometry experiments would not only be interesting from a sensing perspective, but independent replication would provide a reliable reference point for future work.

In Ch. 5 we have demonstrated dynamic torque magnetometry as an excellent tool for the study of nanomagnets with outstanding torque sensitivity. By combining ultrasensitive torque magnetometry with transmission electron microscopy and micromagnetic simulations, we quantitatively determine the magnetic properties of an individual *M. gryph.* cell, finding a remanent moment of $(1.84 \pm 0.54) \cdot 10^{-16}\,\mathrm{A\,m^2}$ and a saturation moment of $2.0 \cdot 10^{-16}\,\mathrm{A\,m^2}$. We further extract an effective easy-axis anisotropy of $12.5\,\mathrm{kJ\,m^{-3}}$ aligned with the magnetosome chain, which is sufficient to stabilize remanence in Earth's magnetic field. These results establish torque magnetometry as a powerful route to resolving single-cell magnetic states and motivate future work. This includes using TEM tomography and diffraction to provide improved structural constraints and developing higher-performance torque transducers to experimentally resolve magnetosome-by-magnetosome switching. Further, collecting larger datasets will be a key element to assess cell-to-cell and species-to-species variability in the saturation moment, remanent moment, and anisotropy of *M. gryph.* and other magnetotactic bacteria. Fostering the understanding of magnetosomes, magnetosome chains, and whole magnetic bacteria will enable and accelerate their implementation in a host of technological application across disciplines.

Once fabrication and sensitivity challenges are overcome, dynamic torque magnetometry will become a key complement to today's leading experimental platforms in the study of few-layer vdW materials and heterostructures, unlocking their phenomenal potential for future spin-based computing and memory technologies.

A

Supplemental material: Micro- and nanofabrication

This section provides addition information about fabrication of the mechanical resonators fabricated and studied in this work. This includes step-by-step fabrication protocols for each device and a detailed analysis of SiN_x-thickness of PnC devices after final suspension.

A.1 Fabrication details

Devices were fabricated using a 2" (5.08 cm) Si substrate. It is (280 ± 10) µm thick, double-side polished, and undoped with <100> crystallographic orientation (University Wafer, item 2018). The substrate is float-zone type and has an electrical resistivity >10 kΩ cm. Fabrication protocols are provided in the following.

A.1.1 Protocol: Torsion paddles 1 and 2

Step 1: **Plasma-enhanced chemical vapor deposition (PECVD) of SiN_x**

Backside: Process time of 28 min 38 s → 400 nm
Frontside: Process time of 24 min 46 s → 340 nm

Step 2: **Patterning of SiN_x mask-layer** (backside)

a. Preparation of photoresist S1805:
The wafer is spin-coated with MICROPOSIT S1805 directly, without prior application of an adhesion promoter contrary to the generalized procedure given in the main text. S1805 is applied using a spin-coater set at 4500 rpm for 40 s. This results in an about 430 nm-thick resist layer which is then cured for 2 min at 125 °C using a hotplate.

b. Direct-laser lithography:
The photoresist on the wafer's backside is patterned using a µPG101 µMLA laser writer (Heidelberg Instruments). The exposure is horizontally aligned with <110> based on the wafer's major flat.

c. Lithography development:
The lithography pattern is developed using MICROPOSIT MF-319 for 1 min at room temperature.

d. Reactive ion etching of SiN_x:
At the time of fabricating torsion paddles 1 and 2, an old RIE 80 Plus system (Oxford Instruments) was used for dry-etching. Accordingly, the process parameters vary with respect to the ones described in the generalized procedure which uses a modern Plasma

Pro 80 RIE. Etching is performed with a mixture of CHF_3 (80 sccm) and O_2 (8 sccm), a pressure of 60 mTorr, and a forward RF power of 60 W. The process is run for 11 min 40 s in order to etch all the way through the SiN_x layer to expose the underlying Si substrate.

e. Removal of photoresist S1805:
Excess resist is removed with RIE using a soft O_2-plasma operating at 20 sccm, 60 mTorr, and a forward power of 60 W for 10 min.

Step 3: **Si wet etching with SiN_x mask-layer as etch mask**

Note, at the time of making torsion paddle 1, no wet-etch chuck was used, and therefore, the SiN_x film of the device-layer (frontside) is also exposed to etchant for the entire wet etching duration.

a. Wet etching in aq. NaOH:
In a first step, the sample is etched in 20 w% aq. NaOH solution for 1 h 32 min at 80 °C. Then the reaction was quenched by submersion in DI water for 10 min.

b. Wet etching in aq. KOH:
In a second step, the sample is etched in 25 w% aq. KOH solution for 2 h 5 min at 80 °C. The reaction is stopped as soon as alignment markers become fully transparent, and the reaction is again quenched by submersion in 60 °C-warm DI water for 40 min.

Step 4: **Patterning of SiN_x device-layer** (frontside)

a. Preparation of photoresist S1805:
Repeat step 2a.

b. Direct-laser lithography:
Repeat step 2b. This time, the lithography pattern is aligned with structures on the backside with help of the etched alignment markers.

c. Development:
Repeat step 2c.

d. Reactive ion etching of SiN_x:
Repeat step 2d, but this time for a reduced total duration of 9 min 50 s.

e. Removal of photoresist S1805:
Repeat step 2e.

Step 5: **Si wet etching in aq. KOH to suspend transducers**

a. Dicing of single chips:
After patterning the SiN_x film of the device-layer (frontside), single chips are removed from the substrate and further processed individually.

b. Suspension:
The device-layer is suspended with wet etching using a 25 w% aq. solution of KOH heated to 63 °C. The chip is fixed with tweezers and submerged for 1 h 55 min until the SiN_x window becomes fully transparent.

c. Quenching:
The reaction is quenched by exchanging the etchant with 70 °C-warm DI water while keeping the sample submerged at all times: Etchant is removed with a syringe until the level is just slightly above the chip, and then DI water is added very carefully again. This cycle is repeated 8 times for consecutive dilution and removal of KOH.

c. Solvent exchange:
DI water is again removed using a syringe until the level is just above the chip. Then, isopropyl alcohol (IPA) is carefully added on top, and DI water is fully removed from underneath while keeping the chip submerged in IPA. After 10 min, IPA is removed

until the level is just above the chip, and then IPA is again topped up. This step is repeated twice in order to further remove residual water.

d. IPA-drying
Finally, IPA is heated to 50 °C with the chip submerged. After reaching target temperature, the sample is kept submerged for another 10 min before lifting it out very carefully. The sample is now held just above the IPA level such that it can dry as slowly as possible in an IPA-enriched atmosphere which takes about 15 min.

Step 6: **Attachment of magnetic CoFeB nanotube**

A CoFeB nanotube is attached to the resonator using a micromanipulator (Narishige), and the sample is fixed with UV glue ((Norland Optical Adhesive, NOA 60). The glue is cured under UV light for 30 min. Manipulator arms are functionalized with extremely fine glass needles which are produced from simple glass rods (Narishige, G-1000) using a needle puller (Narishige, PC-100). This yields needles with a tip diameter of $\sim 0.5\,\mu m$.

Step 7: **FIB-milling of torsion paddle 2**

After characterization of torsion paddle 1, torsion paddle 2 is fabricated by refining the lateral dimension of bridge segments using a dual beam gallium FIB-SEM (FEI Helios Nano Lab 650) available at the Nano Imaging Lab (University Basel). Prior to FIB-milling, a 2 nm thick gold film is deposited on the device in order to remediate potential damage caused by electric charging of the SiN_x film. FIB-milling is performed using an acceleration voltage of 30 kV and a low beam current of 88 pA. Note, that since Ga^{3+}-ions are implanted in the SiN_x film, the entire FIB-milling procedure must be performed without taking any snap-shots with the FIB. By aligning the fields of view between the SEM and the FIB channel, progress in FIB-milling can still be tracked using the SEM channel exclusively.

A.1.2 Protocols: PnC devices

PnC paddle 1

Step 1: **Plasma-enhanced chemical vapor deposition (PECVD) of SiN_x**

Backside: Process time of 15 min 15 s → 200 nm
Frontside: Process time of 15 min 15 s → 200 nm

Step 2: **Patterning of SiN_x mask-layer** (backside)

a. Preparation of photoresist S1805:
The wafer is spin-coated with MICROPOSIT S1805 directly, without prior application of an adhesion promoter contrary to the generalized procedure given in the main text. S1805 is applied using a spin-coater set at 4500 rpm for 40 s. This results in an about 430 nm-thick resist layer which is then cured for 2 min at 125 °C using a hotplate.

b. Direct-laser lithography:
The photoresist on the wafer's backside is patterned using a µPG101 µMLA laser writer (Heidelberg Instruments). The exposure is horizontally aligned with <110> based on the wafer's major flat.

c. Lithography development:
The lithography pattern is developed using MICROPOSIT MF-319 for 1 min at room temperature.

d. Reactive ion etching of SiN_x:
The lithography pattern is transferred to the SiN_x of the mask-layer using a PlasmaPro 80 RIE (Oxford Instruments). Etching is performed with a mixture of CHF_3 (50 sccm) and O_2 (5 sccm), a pressure of 55 mTorr, and a forward RF power of 150 W. The process

is run for 9 min 20 s in order to etch all the way through the SiN_x layer to expose the underlying Si substrate.

e. Removal of photoresist S1805:
Excess resist is removed with RIE using a soft O_2-plasma operating at 20 sccm, 60 mTorr, and a forward power of 60 W for 10 min.

Step 3: **Si wet etching with SiN_x mask-layer as etch mask**

Note, at the time of making PnC paddle 1, a self-made wet etch chuck was used for protection of the SiN_x film of the device-layer instead of the commercial one by AMMT described in the main text. This wet-etch chuck was not leak-proof, and therefore, the frontside SiN_x was also exposed about 30 min after initial submersion in etchant.

a. Wet etching in aq. NaOH:
In a first step, the sample is etched in 20 w% aq. NaOH solution for 1 h 45 min at 80 °C. Then the reaction was quenched by submersion in DI water for 10 min.

b. Wet etching in aq. KOH:
In a second step, the sample is etched in 25 w% aq. KOH solution for 2 h 5 min at 80 °C. The reaction is stopped as soon as alignment markers become fully transparent, and the reaction is again quenched by submersion in 60 °C-warm DI water for 40 min.

Step 4: **Patterning of SiN_x device-layer** (frontside)

a. Preparation of photoresist S1805:
Repeat step 2a.

b. Direct-laser lithography:
Repeat step 2b. This time, the lithography pattern is aligned with structures on the backside with help of the etched alignment markers.

c. Development:
Repeat step 2c.

d. Reactive ion etching of SiN_x:
Repeat step 2d, but this time for a reduced total duration of 9 min.

e. Removal of photoresist S1805:
Repeat step 2e.

Step 5: **Si wet etching in aq. KOH to suspend transducers**

a. Dicing of single chips:
After definition of the PnC and the mechanical resonator at its center, single chips are removed from the substrate and further processed individually.

b. Suspension:
The device-layer is suspended with wet etching using a 25 w% aq. solution of KOH heated to 63 °C. The chip is fixed with tweezers and submerged for 2 h 20 min until the SiN_x window becomes fully transparent.

c. Quenching:
The reaction is quenched by exchanging the etchant with 70 °C-warm DI water while keeping the sample submerged at all times: Etchant is removed with a syringe until the level is just slightly above the chip, and then DI water is added very carefully again. This cycle is repeated 8 times for consecutive dilution and removal of KOH.

c. Solvent exchange:
DI water is again removed using a syringe until the level is just above the chip. Then, isopropyl alcohol (IPA) is carefully added on top, and DI water is fully removed from underneath while keeping the chip submerged in IPA. After 10 min, IPA is removed

until the level is just above the chip, and then IPA is again topped up. This step is repeated twice in order to further remove residual water.

d. IPA-drying
Finally, IPA is heated to 50 °C with the chip submerged. After reaching target temperature, the sample is kept submerged for another 10 min before lifting it out very carefully. The sample is now held just above the IPA level such that it can dry as slowly as possible in an IPA-enriched atmosphere which takes about 15 min.

Step 6: **Attachment of magnetic CoFeB nanotube**

A CoFeB nanotube is attached to the resonator using a micromanipulator (Narishige), and the sample is fixed with UV glue ((Norland Optical Adhesive, NOA 60). The glue is cured under UV light for 30 min. Manipulator arms are functionalized with extremely fine glass needles which are produced from simple glass rods (Narishige, G-1000) using a needle puller (Narishige, PC-100). This yields needles with a tip diameter of $\sim 0.5\,\mu m$.

PnC paddle 2

Step 1: **Plasma-enhanced chemical vapor deposition (PECVD) of SiN_x**

Backside: Process time of 15 min 15 s → 200 nm
Frontside: Process time of 12 min 50 s → 160 nm

Step 2: **Patterning of SiN_x mask-layer** (backside)

a. Preparation of photoresist S1805:
The wafer is spin-coated with MICROPOSIT S1805 directly, without prior application of an adhesion promoter contrary to the generalized procedure given in the main text. S1805 is applied using a spin-coater set at 4500 rpm for 40 s which is then cured for 2 min at 125 °C using a hotplate.

b. Direct-laser lithography:
The photoresist on the wafer's backside is patterned using a µPG101 µMLA laser writer (Heidelberg Instruments). The exposure is horizontally aligned with <110> based on the wafer's major flat.

c. Lithography development:
The lithography pattern is developed using MICROPOSIT MF-319 for 1 min at room temperature.

d. Reactive ion etching of SiN_x:
The lithography pattern is transferred to the SiN_x of the mask-layer using a PlasmaPro 80 RIE (Oxford Instruments). Etching is performed with a mixture of CHF_3 (50 sccm) and O_2 (5 sccm), a pressure of 55 mTorr, and a forward RF power of 150 W. The process is run for 10 min in order to etch all the way through the SiN_x layer to expose the underlying Si substrate.

e. Removal of photoresist S1805:
Excess resist is removed with RIE using a soft O_2-plasma operating at 20 sccm, 60 mTorr, and a forward power of 60 W for 10 min.

Step 3: **Si wet etching with SiN_x mask-layer as etch mask**

A commercially available wet etch chuck (single OW, AMMT) is used to protect the SiN_x film of the device-layer (frontside) during wet etching. With this sample, wet etching is performed using only aq. NaOH. Increased lateral etching in response to NaOH's lower anisotropy compared to KOH, is compensated by adjusting dimensions of features in the lithography pattern which is used to define the wet etch mask. The sample is etched in 20 w% aq. NaOH solution for 3 h at 85 °C until alignment markers

become fully transparent. The reaction is quenched by submersion of the sample in 60 °C-warm DI water for 40 min.

Step 4: **Patterning of SiN_x device-layer** (frontside)

a. Preparation of photoresist S1805:
Repeat step 2a.

b. Direct-laser lithography:
Repeat step 2b. This time, the lithography pattern is aligned with structures on the backside with help of the etched alignment markers.

c. Development:
Repeat step 2c.

d. Reactive ion etching of SiN_x:
Repeat step 2d, but this time for a reduced duration of 9 min.

e. Removal of photoresist S1805:
Repeat step 2e.

Step 5: **Si wet etching in aq. KOH to suspend transducers**

a. Dicing of single chips:
After definition of the PnC and the mechanical resonator at its center, single chips are removed from the substrate and further processed individually.

b. Suspension:
The device-layer is suspended with wet etching using a 25 w% aq. solution of KOH heated to 75 °C. The chip is fixed with tweezers and submerged for 1 h 30 min until the SiN_x window becomes fully transparent.

c. Quenching:
The reaction is quenched by exchanging the etchant with 70 °C-warm DI water while keeping the sample submerged at all times: Etchant is removed with a syringe until the level is just slightly above the chip, and then DI water is added very carefully again. This cycle is repeated 8 times for consecutive dilution and removal of KOH.

c. Solvent exchange:
DI water is again removed using a syringe until the level is just above the chip. Then, isopropyl alcohol (IPA) is carefully added on top, and DI water is fully removed from underneath while keeping the chip submerged in IPA. After 10 min, IPA is removed until the level is just above the chip, and then IPA is again topped up. This step is repeated twice in order to further remove residual water.

d. IPA-drying
Finally, IPA is heated to 50 °C with the chip submerged. After reaching target temperature, the sample is kept submerged for another 10 min before lifting it out very carefully. The sample is now held just above the IPA level such that it can dry as slowly as possible in an IPA-enriched atmosphere which takes about 15 min.

Step 6: **Attachment of magnetic CoFeB nanotube**

A CoFeB nanotube is attached to the resonator using a micromanipulator (Narishige), and the sample is fixed with UV glue ((Norland Optical Adhesive, NOA 60). The glue is cured under UV light for 30 min. Manipulator arms are functionalized with extremely fine glass needles which are produced from simple glass rods (Narishige, G-1000) using a needle puller (Narishige, PC-100). This yields needles with a tip diameter of $\sim 0.5\,\mu m$.

PnC beam 1

Step 1: **Plasma-enhanced chemical vapor deposition (PECVD) of SiN_x**

Backside: Process time of 20 min 4 s → 300 nm
Frontside: Process time of 12 min 50 s → 160 nm

Step 2: **Patterning of SiN_x mask-layer** (backside)

a. Preparation of photoresist S1805:
First, the wafer is pre-conditioned by spin-coating it with adhesion promoter AR 800-30 (Allresist). It is applied using a spin-coater set at 2000 rpm for 40 s and the resist is baked on a hotplate at 90 °C for 2 min. Then, MICROPOSIT S1805 is applied at 4500 rpm for 40 s and then baked for 2 min at 125 °C.

b. Direct-laser lithography:
The photoresist on the wafer's backside is patterned using a µPG101 µMLA laser writer (Heidelberg Instruments). The exposure is horizontally aligned with <110> based on the wafer's major flat.

c. Lithography development:
The lithography pattern is developed using MICROPOSIT MF-319 for 1 min at room temperature.

d. Reactive ion etching of SiN_x:
The lithography pattern is transferred to the SiN_x of the mask-layer using a PlasmaPro 80 RIE (Oxford Instruments). Etching is performed with a mixture of CHF_3 (50 sccm) and O_2 (5 sccm), a pressure of 55 mTorr, and a forward RF power of 150 W. The process is run for 15 min in order to etch all the way through the SiN_x layer to expose the underlying Si substrate.

e. Removal of photoresist S1805:
Excess resist is removed with RIE using a soft O_2-plasma operating at 20 sccm, 60 mTorr, and a forward power of 60 W for 10 min.

Step 3: **Si wet etching with SiN_x mask-layer as etch mask** A commercially available wet etch chuck (single OW, AMMT) is used to protect the SiN_x film of the device-layer (frontside) during wet etching. With this sample, wet etching is performed using only aq. NaOH. Increased lateral etching in response to NaOH's lower anisotropy compared to KOH, is compensated by adjusting dimensions of features in the lithography pattern which is used to define the wet etch mask. The sample is etched in 20 w% aq. NaOH solution for 3 h 50 min at 81 °C until alignment markers become fully transparent. The reaction is quenched by submersion of the sample in 70 °C-warm DI water for 40 min.

Step 4: **Patterning of SiN_x device-layer** (frontside)

a. Preparation of photoresist S1805:
Repeat step 2a.

b. Direct-laser lithography:
Repeat step 2b. This time, the lithography pattern is aligned with structures on the backside with help of the etched alignment markers.

c. Development:
Repeat step 2c.

d. Reactive ion etching of SiN_x:
Repeat step 2d, but this time with reduced total duration of 10 min.

e. Removal of photoresist S1805:
Repeat step 2e.

Step 5: **Si wet etching in aq. KOH to suspend transducers**

a. Dicing of single chips:
After definition of the PnC and the mechanical resonator at its center, single chips are removed from the substrate and further processed individually.

b. Suspension:
The device-layer is suspended with wet etching using a 25 w% aq. solution of KOH heated to 75 °C. The chip is fixed with tweezers and submerged for 1 h 50 min until the SiN_x window becomes fully transparent.

c. Quenching:
The reaction is quenched by exchanging the etchant with 70 °C-warm DI water while keeping the sample submerged at all times: Etchant is removed with a syringe until the level is just slightly above the chip, and then DI water is added very carefully again. This cycle is repeated 8 times for consecutive dilution and removal of KOH.

c. Solvent exchange:
DI water is again removed using a syringe until the level is just above the chip. Then, isopropyl alcohol (IPA) is carefully added on top, and DI water is fully removed from underneath while keeping the chip submerged in IPA. After 10 min, IPA is removed until the level is just above the chip, and then IPA is again topped up. This step is repeated twice in order to further remove residual water.

d. IPA-drying
Finally, IPA is heated to 50 °C with the chip submerged. After reaching target temperature, the sample is kept submerged for another 10 min before lifting it out very carefully. The sample is now held just above the IPA level such that it can dry as slowly as possible in an IPA-enriched atmosphere which takes about 15 min.

Step 6: **Attachment of magnetic CoFeB nanotube**

A CoFeB nanotube is attached to the resonator using a micromanipulator (Narishige), and the sample is fixed with UV glue ((Norland Optical Adhesive, NOA 60). The glue is cured under UV light for 30 min. Manipulator arms are functionalized with extremely fine glass needles which are produced from simple glass rods (Narishige, G-1000) using a needle puller (Narishige, PC-100). This yields needles with a tip diameter of ~ 0.5 µm.

A.2 Determination of SiN_x thickness after device fabrication

The final thickness of the released SiN_x devices is estimated from the deposited film thickness and the etching conditions, namely etch duration, temperature, and KOH concentration. De Vito determined the etch rate of the same PECVD SiN_x film used in this work and reported (0.5 ± 0.1) nm/min in 25 w% aqueous KOH at 80 °C.[249] We independently estimate the etch rate in 25 w% KOH at 75 °C by ellipsometry and obtain ∼0.4 nm/min. This value is based only on a single sample and should therefore be regarded as an approximate reference rather than a precise rate.

As the Si is fully removed toward the end of the release process, the PnC membranes are exposed to etchant from both sides during ∼20 min of over-etching. For PnC paddle 2, we determine a device thickness of 116 nm, and for PnC beam 1 a thickness of 108 nm, with an uncertainty of ∼10 nm. This uncertainty arises from uncertainties in the etch rates, temperature fluctuations during etching, and the fact that the reaction is not quenched instantaneously. Instead, the etchant is replaced with DI water through multiple dilution steps which takes ∼10 min. Results are summarized in Tab.,A.1. For PnC paddle 1, we do not estimate the thickness because uncontrolled exposure of the device layer introduces substantial uncertainty in the device thickness which is difficult to quantify.

Table A.1: Determination of SiN_x thickness: Results are shown for PnC paddle 2 and PnC beam 1 after suspension.

PnC device	t [min]	t_{over} [min]	T [°C]	$d_{deposited}$ [nm]	Δd [nm]	d_{final} [nm]
paddle 2	90	20	75	160	-44	116
beam 1	110	20	75	160	-52	108

Note: t denotes the single-sided etch time, t_{over} the over-etch time, T the temperature, d the thickness, and Δd the loss in thickness.

A.3 Original micrographs prior to cosmetic editing

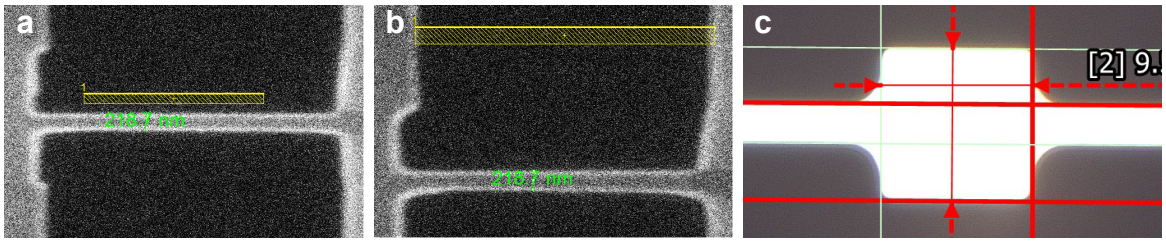


Figure A.1: Unedited micrographs. (**a**) and (**b**) show the unedited left and right bridges of torsion paddle 2 (see Fig. 3.17). (**c**) shows the unedited platform segment of PnC beam 1 (see Fig. 3.18).

B

Supplemental material: Mechanical characterization of torque transducers

In this section, ring-down data are shown for torsion paddles 1 and 2, and PnC paddle 2. Data are acquired under piezoelectric actuation with the resonator driven in self-oscillation. For each measurement, ten ring-down traces are recorded, and the quality factor Q is obtained by evaluating the average.

B.1 Ring-down measurements

B.1.1 Torsion paddles 1 and 2

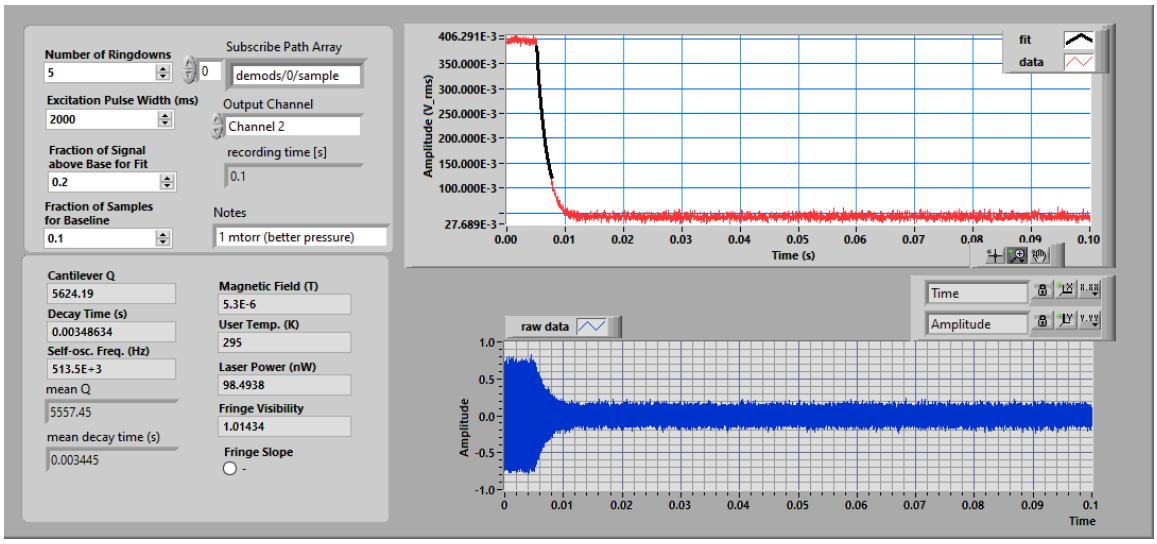


Figure B.1: Torsion paddle 1. Ring-down data measured at RT and fitted decay curve.

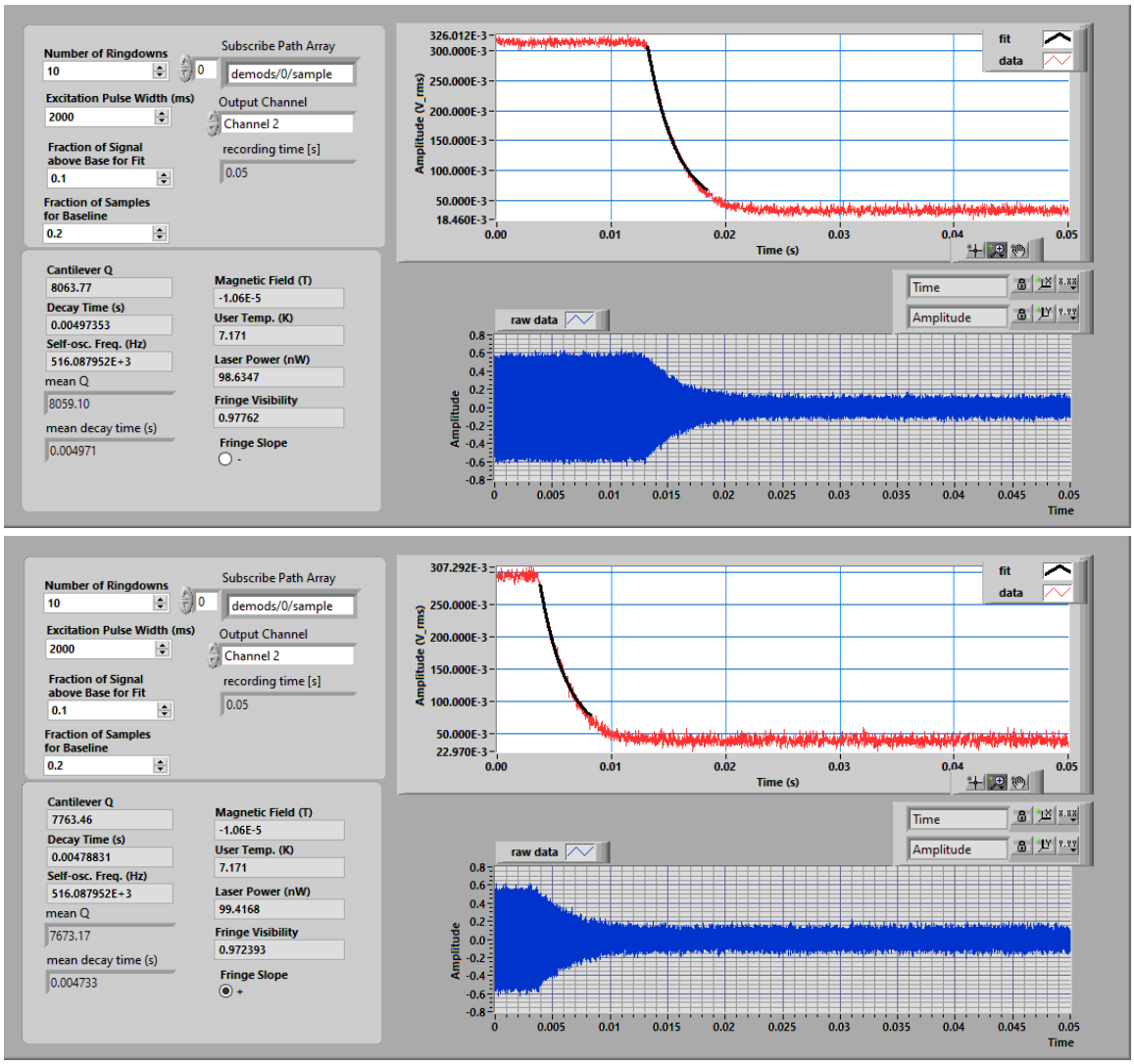


Figure B.2: Torsion paddle 1. Ring-down data measured at 7 K and fitted decay curve.

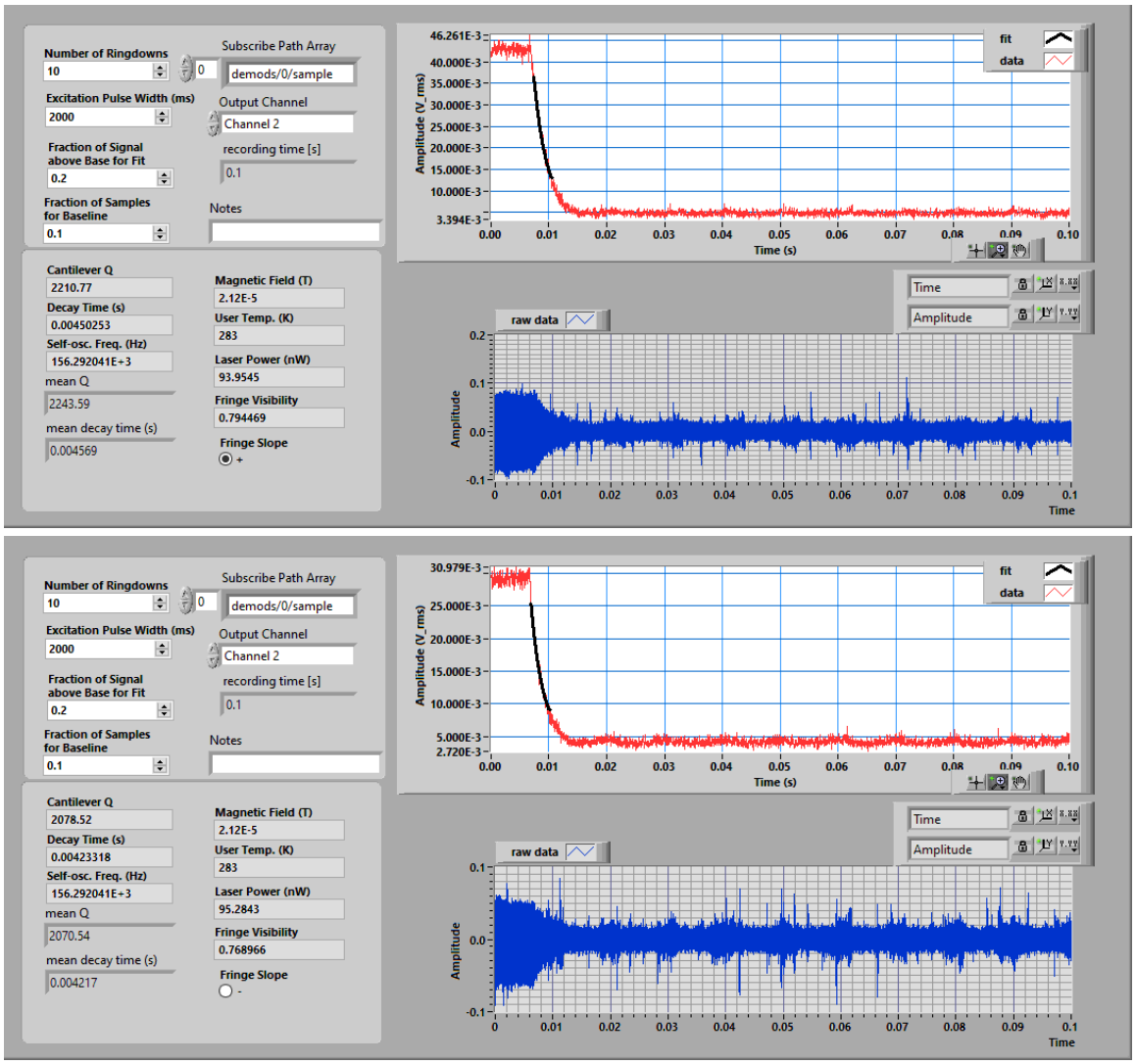


Figure B.3: Torsion paddle 2. Ring-down data measured at RT and fitted decay curve.

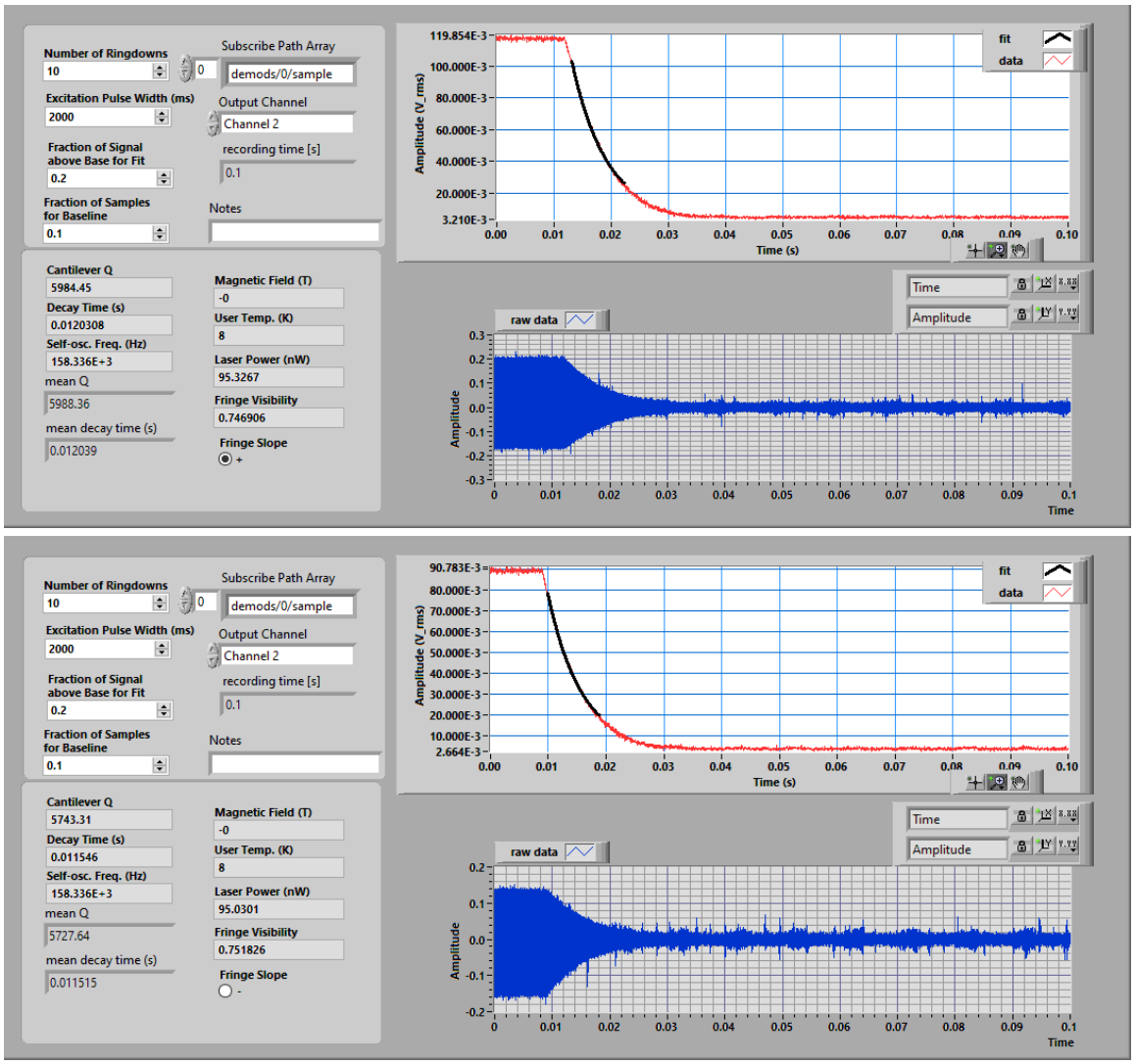


Figure B.4: Torsion paddle 2. Ring-down data measured at 8 K and fitted decay curve.

B.1.2 PnC paddle 2

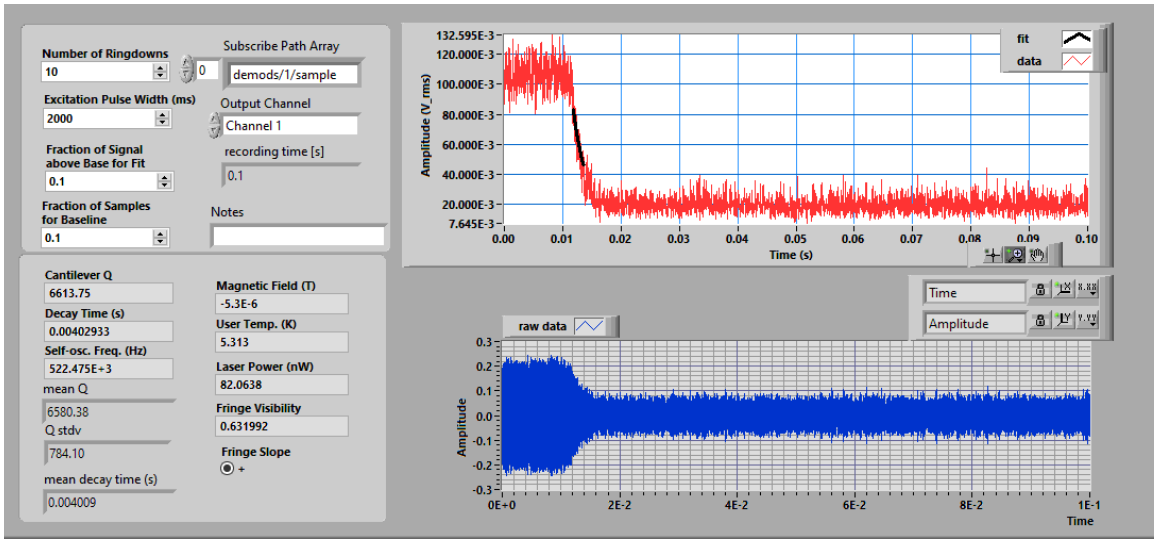


Figure B.5: Torsion paddle 2. Ring-down data measured at 5 K and fitted decay curve.

B.2 Temperature-weighted drift correction

A drift in frequency f is visible in the raw DPM data recorded at RT and using inductive actuation with torsion paddle 1. The raw frequency drift and temperature data is shown in Fig. B.6, and the data relates to the corrected frequency presented Fig. 4.2 under Sec. 4.3.3.

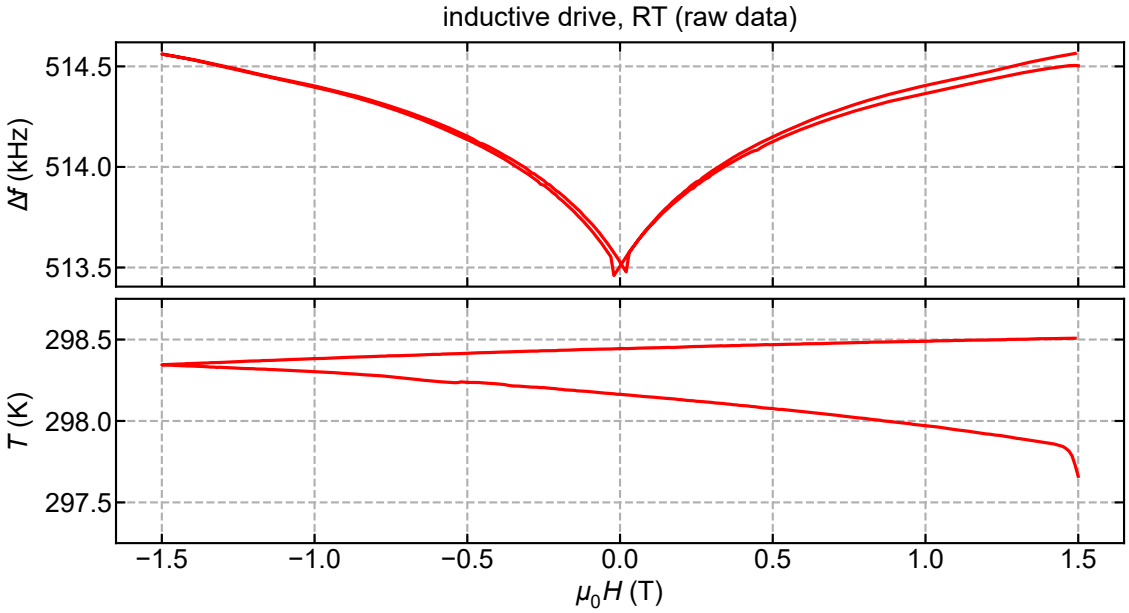


Figure B.6: Temperature-dependent frequency drift. Visible in DPM recorded with torsion paddle 1 at RT and using inductive actuation.

We approximate the observed frequency drift to be temperature-dependent which adds to the magnetic contribution, by

$$f = f_0 + \Delta f_{magnetic}(H) + \Delta f_{drift}(T)$$

where f_0 is the fundamental torsional frequency, $\Delta f_{magnetic}(H)$ is the field-dependent frequency shift, and $\Delta f_{drift}(T)$ is the temperature-dependent contribution. As both, T and f, are monotonously rising, a simple temperature-weighted drift correction can be performed for f. The approach evaluates the total drift in temperature $\Delta T_{drift} = T_{end} - T_{start}$ and in frequency $\Delta f_{drift} = f_{end} - f_{start}$ between start and end points of the data set. After choosing either the start or end point as reference, the corrected frequency f_{corr} is calculated by subtracting the temperature-weighted frequency drift according to

$$f_{corr} = f - \Delta f_{drift} \cdot w$$

with the temperature-weight

$$w = \frac{T - T_{ref}}{\Delta T_{drift}}$$

where $T - T_{ref}$ measures the local temperature difference between a given data point and the chosen reference.

C

Supplemental material: Magnetic properties of a single *M. gryphiswaldense* cell

C.1 List of magnetosomes

In Tab. C.1 we list properties of the individual magnetosomes as used in the best matching simulation.

Table C.1: List of magnetosomes and their properties. x, y, and z are the center-of-mass coordinates (assuming constant density), V denotes the volume, and `axis1` and `axis2` specify the crystalline anisotropy orientation. `Morph` indicates the origin of the data source used to define the morphology in the micromagnetic model; `img` = TEM image, `tomo` = TEM tomogram. `cp` denotes the crystal-plane visibility in TEM; `y` = yes, `n` = no, and `(fft)` = only visible in fast Fourier transform.

No	x [nm]	y [nm]	z [nm]	V[nm^3]	axis1	axis2	morph	cp
1	10.2	7.3	121.8	5812.8	[-0.39, 0.44, 0.58]	[0.01, 0.28, -0.20]	img	n
2	73.3	14.7	109.8	8529.4	[0.24, -0.36, 0.72]	[0.48, 1.36, 0.52]	img	y(fft)
3	411.4	108.0	67.4	774.1	[0.99, -2.33, -1.03]	[-0.71, -1.91, 3.64]	tomo/img	y
4	536.7	113.1	55.3	1850.0	[1.70, -1.18, -0.18]	[1.75, 2.20, 2.11]	tomo/img	y
5	567.5	117.1	53.7	8266.5	[1.12, -0.53, 0.35]	[0.25, 0.51, -0.03]	tomo	y
6	615.5	119.0	50.8	14590.4	[-0.64, -0.55, -0.98]	[-0.28, -3.17, 1.95]	tomo	y
7	722.3	135.4	46.5	23842.0	[-1.34, 2.04, -1.46]	[0.80, 2.76, 3.11]	tomo	n
8	760.3	95.8	51.9	7962.8	[-0.36, -1.77, -1.52]	[-1.06, 0.05, 0.19]	tomo	y
9	781.3	134.9	42.0	67320.5	[-0.47, -1.42, 0.24]	[1.46, -0.38, 0.58]	tomo	y
10	843.4	128.3	34.6	24036.4	[2.52, -0.16, 1.08]	[-0.20, -3.55, -0.07]	tomo	y(fft)
11	907.2	128.5	34.7	51546.8	[-1.34, 1.75, 0.20]	[-2.00, -1.32, -1.84]	tomo	y
12	961.8	125.5	31.6	22993.9	[1.44, -0.50, 1.94]	[-3.06, -2.14, 1.72]	tomo	y(fft)
13	1012.2	119.7	33.0	30640.0	[1.59, -1.43, -0.53]	[-0.65, -0.20, -1.40]	tomo	y
14	1067.2	112.3	32.3	28380.8	[-1.48, -0.19, 0.78]	[0.99, -5.14, 0.61]	tomo	y
15	1133.9	112.4	26.8	42773.0	[0.55, 0.90, -0.52]	[-1.29, 0.77, -0.04]	tomo	y(fft)
16	1206.6	110.1	25.7	41650.8	[-2.92, 0.44, -1.10]	[0.61, 0.99, -1.22]	tomo	y(fft)
17	1271.8	103.2	26.8	44221.1	[1.79, -1.26, -0.95]	[1.21, 0.31, 1.85]	tomo	y(fft)
18	1334.4	100.3	31.8	30477.0	[0.30, 1.41, -0.24]	[0.42, -0.31, -1.27]	tomo	y
19	1401.5	102.3	34.9	26110.4	[0.20, -0.18, -0.38]	[-0.07, -0.20, 0.05]	tomo	y
20	1478.5	109.7	48.0	48106.2	[1.20, 1.51, -0.71]	[1.79, 0.53, 4.16]	tomo	y
21	1531.5	117.9	58.1	29549.2	[-0.92, 1.41, -0.24]	[-0.02, 0.14, 0.90]	tomo	y
22	1679.0	118.4	76.4	1909.2	[1.98, -1.09, 0.77]	[-1.76, -2.22, 1.39]	tomo	n
23	1776.8	122.9	75.0	24419.7	[1.49, 1.76, 0.71]	[4.43, -3.17, -1.40]	tomo	y
24	1882.9	100.8	93.4	3605.5	[-1.38, 0.44, -1.09]	[-0.92, -0.75, 0.85]	tomo	y
25	1943.4	86.9	103.8	1138.9	[-1.86, -0.35, 1.00]	[-0.06, -2.03, -0.82]	tomo/img	y(fft)
26	2080.8	99.2	109.9	1729.6	[0.59, -0.79, 0.90]	[-0.53, -1.22, -0.73]	img	n
27	2085.1	115.4	96.9	3322.1	[-1.26, -0.04, -0.20]	[-0.12, 0.66, 0.63]	img	y(fft)
28	2435.0	107.9	79.1	4485.1	[1.62, -2.05, -0.54]	[0.02, 0.11, -0.35]	img	y
29	2508.3	142.5	73.1	1303.7	[1.19, -0.89, 2.49]	[1.80, 2.13, -0.10]	img	y

C.2 Transmission electron microscopy images of magnetosomes

High resolution (HR)TEM images of all magnetosomes are shown in Tabs. C.2 and C.3. For many of the images, crystal planes are visible, e.g. in images 3 and 4 in Tab. C.2. Some only show indications of crystal planes in the fast Fourier transform. A full list of these findings is given in Tab. C.1. The orientation of the crystal planes differ from image to image, but experimental conditions did not allow the exact spatial orientations of the magnetosomes' crystal structures to be determined.

Table C.2: HRTEM images of the individual magnetosomes 1-16. The scale bar in the images is 5 nm.

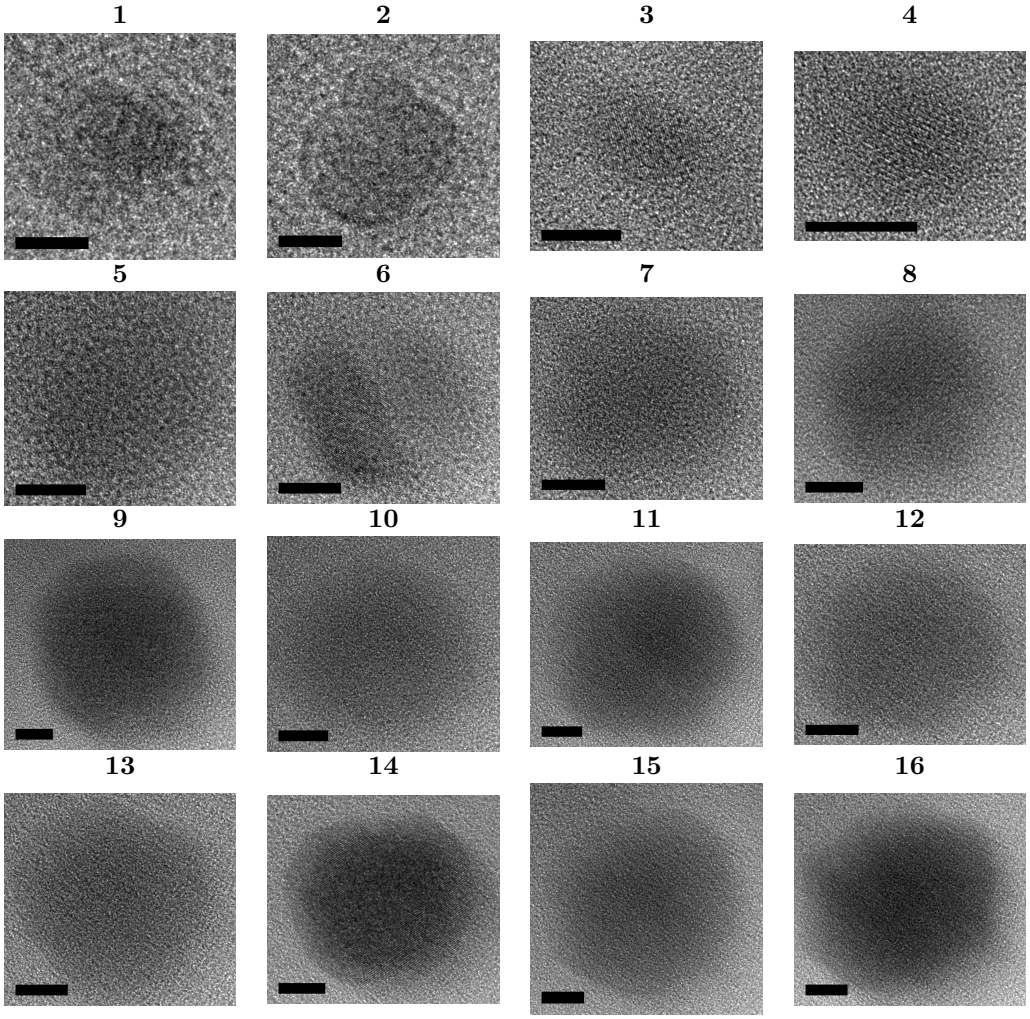
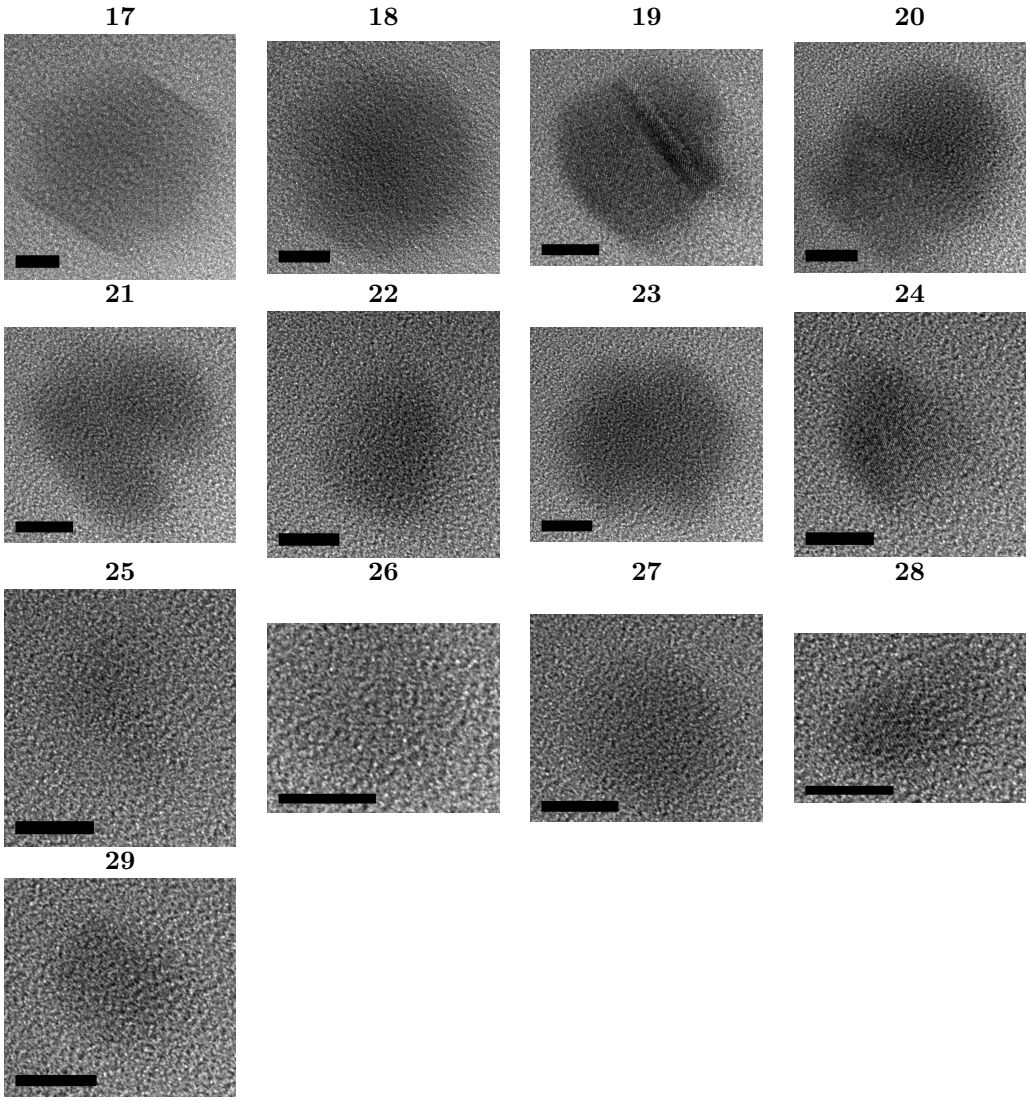


Table C.3: HRTEM images of the individual magnetosomes 17-29. The scale bar in the images is 5 nm.



Bibliography

[1] National Research Council. *Making IT Better: Expanding Information Technology Research to Meet Society's Needs* (National Academies Press, 2000).

[2] National Academies of Sciences, Engineering, and Medicine. *Information Technology Innovation: Resurgence, Confluence, and Continuing Impact* (National Academies Press, 2020).

[3] Hey, T., Tansley, S. & Tolle, K. (eds.) *The Fourth Paradigm: Data-Intensive Scientific Discovery* (Microsoft Research, 2009).

[4] Karpatne, A. *et al.* Ai-enabled scientific revolution in the age of generative ai: second nsf workshop report. *npj Artif. Intell.* **1**, 18 (2025).

[5] Copeland, B. J. The Modern History of Computing. In Zalta, E. N. (ed.) *The Stanford Encyclopedia of Philosophy* (Metaphysics Research Lab, Stanford University, 2020), Winter 2020 edn.

[6] Rojas, R., Darius, F., Göktekin, C. & Heyne, G. The reconstruction of konrad zuse's z3. *IEEE Ann. Hist. Comput.* **27**, 23–32 (2005).

[7] Morelli, M. *Dalle calcolatrici ai computer degli anni Cinquanta: I protagonisti e le macchine della storia dell'informatica* (FrancoAngeli, 2001).

[8] Rojas, R. Konrad zuse's legacy: The architecture of the z1 and z3. *IEEE Ann. Hist. Comput.* **19**, 5–16 (1997).

[9] Bardeen, J. & Brattain, W. H. The transistor, a semi-conductor triode. *Phys. Rev.* **74**, 230–231 (1948).

[10] Riordan, M., Hoddeson, L. & Herring, C. The invention of the transistor. *Rev. Mod. Phys.* **71**, S336–S345 (1999).

[11] Harris, J. R. TRADIC: The first phase. *Bell Lab. Rec.* 330–334 (1958).

[12] Brown, L. C. Flyable TRADIC: The first airborne transistorized digital computer. *IEEE Ann. Hist. Comput.* **21**, 55–61 (1999).

[13] Atalla, M. M. & Kahng, D. Silicon–silicon dioxide field-induced surface devices. IRE-AIEE Solid-State Device Research Conference (SSDRC).

[14] Kahng, D. Silicon–silicon dioxide surface device. In Sze, S. M. (ed.) *Semiconductor Devices: Pioneering Papers*, 583–596 (World Scientific, 1991). Reprint of Bell Laboratories Technical Memorandum to File 61-2821-1 (16 Jan. 1961).

[15] Sah, C.-T. Evolution of the MOS transistor—from conception to VLSI. *Proc. IEEE* **76**, 1280–1326 (1988).

[16] Bassett, R. K. *To the Digital Age: Research Labs, Start-up Companies, and the Rise of MOS Technology* (Johns Hopkins University Press, 2002).

[17] Moore, G. E. Cramming more components onto integrated circuits. *Electronics* **38**, 114–117 (1965).

[18] Dennard, R. H. *et al.* Design of ion-implanted MOSFET's with very small physical dimensions. *IEEE J. Solid-State Circuits* **9**, 256–268 (1974).

[19] Wong, H.-S. P., Frank, D. J., Solomon, P. M., Wann, C. H. J. & Welser, J. J. Nanoscale CMOS. *Proc. IEEE* **87**, 537–570 (1999).

[20] Doering, R. & Nishi, Y. Limits of integrated-circuit manufacturing. *Proc. IEEE* **89**, 375–393 (2001).

[21] Taur, Y. CMOS design near the limit of scaling. *IBM J. Res. Dev.* **46**, 213–222 (2002).

[22] Pedram, M. & Nazarian, S. Thermal modeling, analysis, and management in VLSI circuits: Principles and methods. *Proc. IEEE* **94**, 1487–1501 (2006).

[23] Shepard, K. L. & Narayanan, V. Noise in deep submicron digital design. In *Proc. IEEE/ACM Int. Conf. Comput.-Aided Des. (ICCAD)*, 524–531 (1996).

[24] Weste, N. H. E. & Harris, D. M. *CMOS VLSI Design: A Circuits and Systems Perspective* (Addison-Wesley, 2011), 4 edn.

[25] Chandrakasan, A. P., Sheng, S. & Brodersen, R. W. Low-power CMOS digital design. *IEEE J. Solid-State Circuits* **27**, 473–484 (1992).

[26] Rabaey, J. M., Chandrakasan, A. P. & Nikolić, B. *Digital Integrated Circuits: A Design Perspective* (Pearson Education, 2003), 2 edn.

[27] Vittal, A., Chen, L. H., Marek-Sadowska, M., Wang, K.-P. & Yang, S. Crosstalk in VLSI interconnections. *IEEE Trans. Comput.-Aided Des. Integr. Circuits Syst.* **18**, 1817–1824 (1999).

[28] Dong, G., Li, S. & Zhang, T. Using data postcompensation and predistortion to tolerate cell-to-cell interference in MLC NAND flash memory. *IEEE Trans. Circuits Syst. I* **57**, 2718–2728 (2010).

[29] Johnson, H. W. & Graham, M. *High-Speed Digital Design: A Handbook of Black Magic* (Prentice Hall, 1993).

[30] Wulf, W. A. & McKee, S. A. Hitting the memory wall: Implications of the obvious. *SIGARCH Comput. Archit. News* **23**, 20–24 (1995).

[31] Horowitz, M. 1.1 computing's energy problem (and what we can do about it). In *2014 IEEE Int. Solid-State Circuits Conf. (ISSCC) Dig. Tech. Papers*, 10–14 (2014).

[32] Sebastian, A., Le Gallo, M., Khaddam-Aljameh, R. & Eleftheriou, E. Memory devices and applications for in-memory computing. *Nat. Nanotechnol.* **15**, 529–544 (2020).

[33] Wolf, S. A. *et al.* Spintronics: A spin-based electronics vision for the future. *Science* **294**, 1488–1495 (2001).

[34] Žutić, I., Fabian, J. & Das Sarma, S. Spintronics: Fundamentals and applications. *Rev. Mod. Phys.* **76**, 323–410 (2004).

[35] Burch, K. S., Mandrus, D. & Park, J.-G. Magnetism in two-dimensional van der waals materials. *Nature* **563**, 47–52 (2018).

[36] Gibertini, M., Koperski, M., Morpurgo, A. F. & Novoselov, K. S. Magnetic 2D materials and heterostructures. *Nat. Nanotechnol.* **14**, 408–419 (2019).

[37] Geim, A. K. & Grigorieva, I. V. Van der waals heterostructures. *Nature* **499**, 419–425 (2013).

[38] Novoselov, K. S., Mishchenko, A., Carvalho, A. & Castro Neto, A. H. 2d materials and van der waals heterostructures. *Science* **353** (2016).

[39] Gong, C. & Zhang, X. Two-dimensional magnetic crystals and emergent heterostructure devices. *Science* **363**, eaav4450 (2019).

[40] Zhang, B., Lu, P., Tabrizian, R., Feng, P. X.-L. & Wu, Y. 2D magnetic heterostructures: spintronics and quantum future. *npj Spintronics* **2**, 6 (2024).

[41] Christensen, D. V. *et al.* 2024 roadmap on magnetic microscopy techniques and their applications in materials science. *J. Phys. Mater.* **7**, 032501 (2024).

[42] Birch, M. T. *et al.* History-dependent domain and skyrmion formation in 2d van der waals magnet Fe_3GeTe_2. *Nat. Commun.* **13** (2022).

[43] Meseguer-Sánchez, J. *et al.* Coexistence of structural and magnetic phases in van der waals magnet CrI_3. *Nat. Commun.* **12** (2021).

[44] Huang, B. *et al.* Layer-dependent ferromagnetism in a van der waals crystal down to the monolayer limit. *Nature* **546**, 270–273 (2017).

[45] Huang, B. *et al.* Electrical control of 2D magnetism in bilayer CrI_3. *Nat. Nanotechnol.* **13**, 544–548 (2018).

[46] Song, T. *et al.* Direct visualization of magnetic domains and moiré magnetism in twisted 2D magnets. *Science* **374**, 1140–1144 (2021).

[47] Jiang, S., Shan, J. & Mak, K. F. Electric-field switching of two-dimensional van der waals magnets. *Nat. Mater.* **17**, 406–410 (2018).

[48] Wu, J.-B., Wu, H. & Tan, P.-H. Magneto-optical interactions in layered magnets. *Adv. Funct. Mater.* **34**, 2312214 (2024).

[49] Deng, Y. *et al.* Gate-tunable room-temperature ferromagnetism in two-dimensional Fe_3GeTe_2. *Nature* **563**, 94–99 (2018).

[50] Song, T. *et al.* Giant tunneling magnetoresistance in spin-filter van der waals heterostructures. *Science* **360**, 1214–1218 (2018).

[51] Tschudin, M. A. *et al.* Imaging nanomagnetism and magnetic phase transitions in atomically thin CrSBr. *Nat. Commun.* **15**, 6005 (2024).

[52] Pellet-Mary, C. *et al.* Lateral exchange bias for néel-vector control in atomically thin antiferromagnets. *Nat. Commun.* **16** (2025).

[53] Fridman, N. *et al.* Anomalous thickness dependence of the vortex pearl length in few-layer $NbSe_2$. *Nat. Commun.* **16**, 2696 (2025).

[54] Zur, Y. *et al.* Magnetic imaging and domain nucleation in CrSBr down to the 2D limit. *Adv. Mater.* **35**, 2307195 (2023).

[55] Noah, A. *et al.* Interior and edge magnetization in thin exfoliated $CrGeTe_3$ films. *Nano Lett.* **22**, 3165–3172 (2022).

[56] Tschirhart, C. L. *et al.* Imaging orbital ferromagnetism in a moiré chern insulator. *Science* **372**, 1323–1327 (2021).

[57] Uri, A. *et al.* Mapping the twist-angle disorder and landau levels in magic-angle graphene. *Nature* **581**, 47–52 (2020).

[58] Vervelaki, A. *et al.* Visualizing thickness-dependent magnetic textures in few-layer $Cr_2Ge_2Te_6$. *Commun. Mater.* **5** (2024).

[59] Bagani, K. *et al.* Imaging strain-controlled magnetic reversal in thin CrSBr. *Nano Lett.* **24**, 13068–13074 (2024).

[60] Khan, M. Z. *et al.* Imaging magnetic order in a two-dimensional iron-rich phyllosilicate. *Commun. Mater.* **6** (2025).

[61] Mattiat, H. *et al.* Mapping the phase-separated state in a 2d magnet. *Nanoscale* **16**, 5302–5312 (2024).

[62] Leisgang, N. *et al.* Exchange energy of the ferromagnetic electronic ground state in a monolayer semiconductor. *Phys. Rev. Lett.* **133**, 026501 (2024).

[63] Rizzo, D. J. *et al.* Visualizing atomically-layered magnetism in CrSBr. *Adv. Mater.* **34** (2022).

[64] Niu, B. *et al.* Coexistence of magnetic orders in two-dimensional magnet CrI_3. *Nano Lett.* **20**, 553–558 (2020).

[65] Yu, W. *et al.* Chemically exfoliated VSe_2 monolayers with room-temperature ferromagnetism. *Adv. Mater.* **31** (2019).

[66] Li, H. *et al.* Investigation of MoS_2 and graphene nanosheets by magnetic force microscopy. *ACS Nano* **7**, 2842–2849 (2013).

[67] Marchiori, E. *et al.* Nanoscale magnetic field imaging for 2D materials. *Nat. Rev. Phys.* **4**, 49–60 (2022).

[68] Kuehn, S., Hickman, S. A. & Marohn, J. A. Advances in mechanical detection of magnetic resonance. *J. of Chem. Phys.* **128** (2008).

[69] Losby, J. *et al.* Nanomechanical torque magnetometry of permalloy cantilevers. *J. Appl. Phys.* **108**, 123910 (2010).

[70] Gross, B. *et al.* Dynamic cantilever magnetometry of individual CoFeB nanotubes. *Phys. Rev. B* **93**, 064409 (2016).

[71] Ma, Z. *et al.* Dynamic cantilever magnetometry of paramagnetism with slow relaxation. *Chin. Phys. Lett.* **39** (2022).

[72] Mehlin, A. *et al.* Stabilized Skyrmion Phase Detected in MnSi Nanowires by Dynamic Cantilever Magnetometry. *Nano Lett.* **15**, 4839–4844 (2015).

[73] Weber, D. P. *et al.* Cantilever magnetometry of individual ni nanotubes. *Nano Lett.* **12**, 6139–6144 (2012).

[74] Mehlin, A. *et al.* Observation of end-vortex nucleation in individual ferromagnetic nanotubes. *Phys. Rev. B* **97**, 134422 (2018).

[75] Philipp, S. *et al.* Magnetic hysteresis of individual Janus particles with hemispherical exchange biased caps. *Appl. Phys. Lett.* **119**, 222406 (2021).

[76] Gross, B. *et al.* Magnetic anisotropy of individual maghemite mesocrystals. *Phys. Rev. B* **103**, 014402 (2021).

[77] Ekinci, K. L. & Roukes, M. L. Nanoelectromechanical systems. *Rev. Sci. Instrum.* **76**, 13 (2005).

[78] Saulson, P. R. Thermal noise in mechanical experiments. *Phys. Rev. D* **42**, 2437–2445 (1990).

[79] Callen, H. B. & Welton, T. A. Irreversibility and generalized noise. *Phys. Rev.* **83**, 34–40 (1951).

[80] Unterreithmeier, Q. P., Faust, T. & Kotthaus, J. P. Damping of nanomechanical resonators. *Phys. Rev. Lett.* **105**, 027205 (2010).

[81] Rieger, J., Isacsson, A., Seitner, M. J., Kotthaus, J. P. & Weig, E. M. Energy losses of nanomechanical resonators induced by atomic force microscopy-controlled mechanical impedance mismatching. *Nat. Commun.* **5**, 3345 (2014).

[82] Yu, P.-L. *et al.* A phononic bandgap shield for high-Q membrane microresonators. *Appl. Phys. Lett.* **104**, 023510 (2014).

[83] MacCabe, G. S. *et al.* Nano-acoustic resonator with ultralong phonon lifetime. *Science* **370**, 840–843 (2020).

[84] Tsaturyan, Y., Barg, A., Polzik, E. S. & Schliesser, A. Ultracoherent nanomechanical resonators via soft clamping and dissipation dilution. *Nat. Nanotechnol.* **12**, 776–783 (2017).

[85] Fedorov, S. A., Beccari, A., Engelsen, N. J. & Kippenberg, T. J. Fractal-like mechanical resonators with a soft-clamped fundamental mode. *Phys. Rev. Lett.* **124**, 025502 (2020).

[86] Wollack, E. A. *et al.* Loss channels affecting lithium niobate phononic crystal resonators at cryogenic temperature. *Appl. Phys. Lett.* **118**, 123501 (2021).

[87] Xi, X. *et al.* Ising pairing in superconducting $NbSe_2$ atomic layers. *Nat. Phys.* **12**, 139–143 (2016).

[88] Bossoni, L., Carretta, P. & Poggio, M. Vortex lattice melting of a $nbse_2$ single grain probed by ultrasensitive cantilever magnetometry. *Appl. Phys. Lett.* **104**, 182601 (2014).

[89] Cleland, A. N. *Foundations of Nanomechanics.* Advanced Texts in Physics (Springer, 2003).

[90] Abdolvand, R., Bahreyni, B., Lee, J. E.-Y. & Nabki, F. Micromachined resonators: A review. *Micromachines* **7**, 160 (2016).

[91] Rao, S. S. *Vibration of Continuous Systems* (John Wiley & Sons, Hoboken, NJ, 2019), 2 edn.

[92] Sokolnikoff, I. S. *Mathematical Theory of Elasticity* (McGraw-Hill, New York, 1956), 2 edn.

[93] Timoshenko, S. P. & Goodier, J. N. *Theory of Elasticity* (McGraw-Hill, New York, 1970), 3 edn.

[94] Ugural, A. C. & Fenster, S. K. *Advanced Mechanics of Materials and Applied Elasticity* (Pearson, 2011), 5 edn.

[95] Roccia, B. A., Alturria Lanzardo, C. J., Mazzone, F. D. & Gebhardt, C. G. On the homogeneous torsion problem for heterogeneous and orthotropic cross-sections: Theoretical and numerical aspects. *Appl. Numer. Math.* **201**, 579–607 (2024).

[96] Tran, D.-B. Torsional shear stress with arbitrary cross-sections in homogeneous isotropic elastic material using finite element method. *Civ. Eng. J.* **2**, 409–420 (2021).

[97] Jog, C. S. & Mokashi, I. S. A finite element method for the saint-venant torsion and bending problems for prismatic beams. *Comput. Struct.* **135**, 62–72 (2014).

[98] Castigliano, C. A. *Elastic Stresses in Structures* (Cambridge University Press, 2014).

[99] Young, W. C. & Budynas, R. G. *Roark's Formulas for Stress and Strain* (McGraw-Hill, 2002), 7 edn.

[100] Lobontiu, N. *Mechanical Design of Microresonators: Modeling and Applications* (McGraw-Hill, 2005).

[101] Rayleigh, L. *The Theory of Sound* (Dover, 1945), 2 edn.

[102] Hauer, B. D., Doolin, C., Beach, K. S. D. & Davis, J. P. A general procedure for thermomechanical calibration of nano/micro-mechanical resonators. *Annals of Physics* **339**, 181–207 (2013).

[103] Imboden, M. & Mohanty, P. Dissipation in nanoelectromechanical systems. *Phys. Rep.* **534**, 89–146 (2014).

[104] Schmid, S., Villanueva, L. G. & Roukes, M. L. *Fundamentals of Nanomechanical Resonators* (Springer, 2016).

[105] Eichler, A. Ultra-high-Q nanomechanical resonators for force sensing. *Mater. Quantum Technol.* **2**, 043001 (2022).

[106] Seis, Y. *et al.* Ground state cooling of an ultracoherent electromechanical system. *Nat. Commun.* **13**, 1507 (2022).

[107] Mason, D., Chen, J., Rossi, M., Tsaturyan, Y. & Schliesser, A. Continuous force and displacement measurement below the standard quantum limit. *Nat. Phys.* **15**, 745–749 (2019).

[108] Rossi, M., Mason, D., Chen, J., Tsaturyan, Y. & Schliesser, A. Measurement-based quantum control of mechanical motion. *Nature* **563**, 53–58 (2018).

[109] Lifshitz, R. & Roukes, M. L. Thermoelastic damping in micro- and nanomechanical systems. *Phys. Rev. B* **61**, 5600–5609 (2000).

[110] Zener, C. Internal friction in solids. i. theory of internal friction in reeds. *Phys. Rev.* **52**, 230–235 (1937).

[111] Zener, C. Internal friction in solids ii. general theory of thermoelastic internal friction. *Phys. Rev.* **53**, 90–99 (1938).

[112] Harry, G. M. *et al.* Thermal noise in interferometric gravitational wave detectors due to dielectric optical coatings. *Class. Quantum Grav.* **19**, 897–917 (2002).

[113] Qiao, Y., Elhady, A., Arabi, M., Abdel-Rahman, E. & Zhang, W. Thermal noise-driven resonant sensors. *Microsyst. Nanoeng.* **10**, 90 (2024).

[114] Bachtold, A., Moser, J. & Dykman, M. I. Mesoscopic physics of nanomechanical systems. *Rev. Mod. Phys.* **94**, 045005 (2022).

[115] Rossi, N. *Force sensing with nanowires.* Phd thesis, University of Basel (2019).

[116] Aspelmeyer, M., Kippenberg, T. J. & Marquardt, F. Cavity optomechanics. *Rev. Mod. Phys.* **86**, 1391–1452 (2014).

[117] Villanueva, L. G. & Schmid, S. Evidence of surface loss as ubiquitous limiting damping mechanism in sin micro- and nanomechanical resonators. *Phys. Rev. Lett.* **113**, 227201 (2014).

[118] Nowick, A. S. & Berry, B. S. *Anelastic Relaxation in Crystalline Solids* (Academic Press, 1972).

[119] Remus, L. G., Blencowe, M. P. & Tanaka, Y. Damping and decoherence of a nanomechanical resonator due to a few two-level systems. *Phys. Rev. B* **80**, 174103 (2009).

[120] Ghadimi, A. H., Wilson, D. J. & Kippenberg, T. J. Radiation and internal loss engineering of high-stress silicon nitride nanobeams. *Nano Lett.* **17**, 3501–3505 (2017).

[121] Cole, G. D., Wilson-Rae, I., Werbach, K., Vanner, M. R. & Aspelmeyer, M. Phonon-tunnelling dissipation in mechanical resonators. *Nat. Commun.* **2** (2011).

[122] Bereyhi, M. J. *et al.* Hierarchical tensile structures with ultralow mechanical dissipation. *Nat. Commun.* **13**, 3097 (2022).

[123] Fedorov, S. A. *et al.* Generalized dissipation dilution in strained mechanical resonators. *Phys. Rev. B* **99**, 054107 (2019).

[124] Sun, Y., Fang, D. & Soh, A. K. Thermoelastic damping in micro-beam resonators. *Int. J. Solids Struct.* **43**, 3213–3229 (2006).

[125] Candler, R. N. *et al.* Impact of geometry on thermoelastic dissipation in micromechanical resonant beams. *J. Microelectromech. Syst.* **15**, 927–934 (2006).

[126] Corigliano, A. *et al.* Damping in microsystems. In *Mechanics of Microsystems*, 313–350 (John Wiley & Sons, 2018).

[127] Svitelskiy, O. *et al.* Pressurized fluid damping of nanoelectromechanical systems. *Phys. Rev. Lett.* **103**, 244501 (2009).

[128] Verbridge, S. S., Ilic, R., Craighead, H. G. & Parpia, J. M. Size and frequency dependent gas damping of nanomechanical resonators. *Appl. Phys. Lett.* **93**, 013101 (2008).

[129] Karabacak, D. M., Yakhot, V. & Ekinci, K. L. High-frequency nanofluidics: An experimental study using nanomechanical resonators. *Phys. Rev. Lett.* **98**, 254505 (2007).

[130] Boom, B. A., Bertolini, A., Hennes, E. & van den Brand, J. F. Gas damping in capacitive mems transducers in the free molecular flow regime. *Sensors* **21**, 2566 (2021).

[131] Keşkekler, A., Soshani, O., van der Zant, H. S., Steeneken, P. G. & Alijani, F. Tuning nonlinear damping in graphene nanoresonators by parametric–direct internal resonance. *Nat. Commun.* **12**, 1099 (2021).

[132] Catalini, L., Rossi, M., Langman, E. C. & Schliesser, A. Modeling and observation of nonlinear damping in dissipation-diluted nanomechanical resonators. *Phys. Rev. Lett.* **126**, 174101 (2021).

[133] Eichler, A. *et al.* Nonlinear damping in a nanomechanical resonator. *Nat. Nanotechnol.* **6**, 339–342 (2011).

[134] Zaitsev, V., Shtempluck, O., Buks, E. & Gottlieb, O. Nonlinear damping in a micromechanical oscillator. *Nonlinear Dyn.* **67**, 859–883 (2012).

[135] Beccari, A. *et al.* Strained crystalline nanomechanical resonators with quality factors above 10 billion. *Nat. Phys.* **18**, 436–441 (2022).

[136] Sementilli, L., Romero, E. & Bowen, W. P. Nanomechanical dissipation and strain engineering. *Adv. Funct. Mater.* **32**, 2105247 (2022).

[137] Ghadimi, A. H. *et al.* Elastic strain engineering for ultralow mechanical dissipation. *Science* **360**, 764–768 (2018).

[138] Reetz, C. *et al.* Analysis of membrane phononic crystals with wide band gaps and low-mass defects. *Phys. Rev. Appl.* **12**, 044027 (2019).

[139] Condos, C. A. *et al.* Ultralow loss torsion micropendula for chipscale gravimetry. *Phys. Rev. Lett.* **134**, 253602 (2025).

[140] Pluchar, C. M., Agrawal, A. R. & Wilson, D. J. Quantum-limited optical lever measurement of a torsion oscillator. *Optica* **12**, 418–423 (2025).

[141] Pratt, J. R. *et al.* Nanoscale torsional dissipation dilution for quantum experiments and precision measurement. *Phys. Rev. X* **13**, 011018 (2023).

[142] Engelsen, N. J., Beccari, A. & Kippenberg, T. J. Ultrahigh-quality-factor micro- and nanomechanical resonators using dissipation dilution. *Nat. Nanotechnol.* **19**, 725–737 (2024).

[143] Aharoni, A. *Introduction to the Theory of Ferromagnetism*. No. 109 in International Series of Monographs on Physics (Oxford University Press, 2001), 2 edn.

[144] Miltat, J. E. & Donahue, M. J. Numerical micromagnetics: Finite difference methods. In Kronmüller, H. & Parkin, S. S. P. (eds.) *Handbook of Magnetism and Advanced Magnetic Materials*, vol. 2, 742–764 (John Wiley & Sons, 2007).

[145] Hubert, A. & Schäfer, R. *Magnetic Domains: The Analysis of Magnetic Microstructures* (Springer, 1998).

[146] Brown, W. F. J. *Micromagnetics* (Interscience, New York, 1963).

[147] Guimarães, A. P. *Principles of Nanomagnetism*. NanoScience and Technology (Springer, 2009).

[148] Skomski, R. & Coey, J. M. D. *Permanent Magnetism*. Condensed Matter Physics (Institute of Physics Publishing, 1999).

[149] Novoselov, K. S. *et al.* Electric field effect in atomically thin carbon films. *Science* **306**, 666–669 (2004).

[150] Mermin, N. D. & Wagner, H. Absence of ferromagnetism or antiferromagnetism in one- or two-dimensional isotropic Heisenberg models. *Phys. Rev. Lett.* **17**, 1133–1136 (1966).

[151] Klein, D. R. *et al.* Probing magnetism in 2D van der waals crystalline insulators via electron tunneling. *Science* **360**, 1218–1222 (2018).

[152] Gong, C. *et al.* Discovery of intrinsic ferromagnetism in two-dimensional van der waals crystals. *Nature* **546**, 265–269 (2017).

[153] Somphonsane, R., Buapan, K. & Ramamoorthy, H. Advances in 2D material transfer systems for van der waals heterostructure assembly. *Appl. Sci.* **14**, 6341 (2024).

[154] Bhakta, S., Mazumder, K., Kumar, M. & Nayak, P. K. Recent development in the synthesis of twisted van der waals heterostructures. *Discov. Nano* **20** (2025).

[155] Wang, W. *et al.* Clean assembly of van der waals heterostructures using silicon nitride membranes. *Nat. Electron.* **6**, 981–990 (2023).

[156] Liang, S.-J., Cheng, B., Cui, X. & Miao, F. Van der waals heterostructures for high-performance device applications: Challenges and opportunities. *Adv. Mater.* **32**, 1903800 (2020).

[157] Papavasileiou, S. *et al.* Ferromagnetic elements in two-dimensional materials: 2D magnets and beyond. *Adv. Funct. Mater.* **34**, 2309046 (2024).

[158] Baibich, M. N. *et al.* Giant magnetoresistance of (001) Fe/Cr magnetic superlattices. *Phys. Rev. Lett.* **61**, 2472–2475 (1988).

[159] Fert, A. Nobel lecture: Origin, development, and future of spintronics. *Rev. Mod. Phys.* **80**, 1517–1530 (2008).

[160] Kent, A. D. & Worledge, D. C. A new spin on magnetic memories. *Nat. Nanotechnol.* **10**, 187–191 (2015).

[161] Belvin, C. A. *et al.* Exciton-driven antiferromagnetic metal in a correlated van der waals insulator. *Nat. Commun.* **12**, 4837 (2021).

[162] Behovits, Y. *et al.* Terahertz néel spin-orbit torques drive nonlinear magnon dynamics in antiferromagnetic mn2au. *Nat. Commun.* **14**, 6038 (2023).

[163] Jungwirth, T., Marti, X., Wadley, P. & Wunderlich, J. Antiferromagnetic spintronics. *Nat. Nanotechnol.* **11**, 231–241 (2016).

[164] Baltz, V. *et al.* Antiferromagnetic spintronics. *Rev. Mod. Phys.* **90** (2018).

[165] Guo, H. *et al.* Layer-dependent spin-orbit torque switching of néel vector in a van der waals antiferromagnet. *Nat. Commun.* **16**, 8911 (2025).

[166] Verwey, E. J. W. & de Boer, J. H. Cation arrangement in a few oxides with crystal structures of the spinel type. *Recl. Trav. Chim. Pays-Bas* **55**, 531–540 (1936).

[167] Verwey, E. J. W. & Haayman, P. W. Electronic conductivity and transition point of magnetite ($\{Fe\}_3\{O\}_4$). *Physica* **8**, 979–987 (1941).

[168] Levy, D., Giustetto, R. & Hoser, A. Structure of magnetite (fe3o4) above the curie temperature: a cation ordering study. *Phys. Chem. Minerals* **39**, 169–176 (2012).

[169] Morrish, A. H. & Watt, L. A. K. Coercive force of iron oxide micropowders at low temperatures. *J. Appl. Phys.* **29**, 1029–1033 (1958).

[170] Dunlop, D. J. Magnetite: Behavior near the Single-Domain threshold. *Science* **176**, 41–43 (1972).

[171] Dunlop, D. J. Superparamagnetic and single-domain threshold sizes in magnetite. *J. Geophys. Res.* **78**, 1780–1793 (1973).

[172] Butler, R. F. & Banerjee, S. K. Theoretical single-domain grain size range in magnetite and titanomagnetite. *J. Geophys. Res.* **80**, 4049–4058 (1975).

[173] Muxworthy, A. R. & Williams, W. Critical single-domain/multidomain grain sizes in noninteracting and interacting elongated magnetite particles: Implications for magnetosomes. *J. Geophys. Res.* **111**, 1–7 (2006).

[174] Dunlop, D. J. & Özdemir, Ö. *Rock Magnetism: Fundamentals and Frontiers* (Cambridge University Press, 1997).

[175] Bazylinski, D. A. & Moskowitz, B. M. Microbial biomineralization of magnetic iron minerals: microbiology, magnetism, and environmental significance. In Banfield, J. F. & Nealson, K. H. (eds.) *Geomicrobiology: Interactions Between Microbes and Minerals*, 181–224 (Mineralogical Society of America, 1997).

[176] Nguyen, M. D., Tran, H.-V., Xu, S. & Lee, T. R. Fe3o4 nanoparticles: Structures, synthesis, magnetic properties, surface functionalization, and emerging applications. *Appl. Sci.* **11**, 11301 (2021).

[177] Laurent, S. *et al.* Magnetic iron oxide nanoparticles: Synthesis, stabilization, vectorization, physicochemical characterizations, and biological applications. *Chem. Rev.* **108**, 2064–2110 (2008).

[178] de Souza Cabral, A. *et al.* Large-scale cultivation of magnetotactic bacteria and the optimism for sustainable and cheap approaches in nanotechnology. *Mar. Drugs* **21**, 60 (2023).

[179] Faivre, D. & Schüler, D. Magnetotactic Bacteria and Magnetosomes. *Chem. Rev.* **108**, 4875–4898 (2008).

[180] Lefèvre, C. T. & Bazylinski, D. A. Ecology, Diversity, and Evolution of Magnetotactic Bacteria. *MMBR* **77**, 497–526 (2013).

[181] Pósfai, M., Lefèvre, C. T., Trubitsyn, D., Bazylinski, D. A. & Frankel, R. B. Phylogenetic significance of composition and crystal morphology of magnetosome minerals. *Front. Microbiol.* **4** (2013).

[182] Bazylinski, D. A. & Frankel, R. B. Magnetosome formation in prokaryotes. *Nat. Rev. Microbiol.* **2**, 217–230 (2004).

[183] Ling, D. & Hyeon, T. Chemical design of biocompatible iron oxide nanoparticles for medical applications. *Small* **9**, 1450–1466 (2013).

[184] Bobo, D., Robinson, K. J., Islam, J., Thurecht, K. J. & Corrie, S. R. Nanoparticle-based medicines: A review of FDA-approved materials and clinical trials to date. *Pharm. Res.* **33**, 2373–2387 (2016).

[185] Roda, A. *et al.* Bioengineered bioluminescent magnetotactic bacteria as a powerful tool for chip-based whole-cell biosensors. *Lab Chip* **13**, 4881–4889 (2013).

[186] Uebe, R. & Schüler, D. Magnetosome biogenesis in magnetotactic bacteria. *Nat. Rev. Microbiol.* **14**, 621–637 (2016).

[187] Boucher, M. *et al.* Genetically tailored magnetosomes used as MRI probe for molecular imaging of brain tumor. *Biomaterials* **121**, 167–178 (2017).

[188] Yan, L. *et al.* Magnetotactic bacteria, magnetosomes and their application. *Microbiol. Res.* **167**, 507–519 (2012).

[189] Vargas, G. *et al.* Applications of magnetotactic bacteria, magnetosomes and magnetosome crystals in biotechnology and nanotechnology: Mini-review. *Molecules* **23**, 2438 (2018).

[190] Wang, X. *et al.* Magnetotactic bacteria: Characteristics and environmental applications. *Front. Environ. Sci. Eng.* **14**, 56 (2020).

[191] Alphandéry, E., Chebbi, I., Guyot, F. & Durand-Dubief, M. Use of bacterial magnetosomes in the magnetic hyperthermia treatment of tumours: A review. *Int. J. Hyperthermia* **29**, 801–809 (2013).

[192] Serantes, D. *et al.* Multiplying Magnetic Hyperthermia Response by Nanoparticle Assembling. *J. Phys. Chem. C* **118**, 5927–5934 (2014).

[193] Felfoul, O. *et al.* Magneto-aerotactic bacteria deliver drug-containing nanoliposomes to tumour hypoxic regions. *Nat. Nanotechnol.* **11**, 941–947 (2016).

[194] Ghosh, D. *et al.* M13-templated magnetic nanoparticles for targeted in vivo imaging of prostate cancer. *Nat. Nanotechnol.* **7**, 677–682 (2012).

[195] Gandia, D. *et al.* Unlocking the Potential of Magnetotactic Bacteria as Magnetic Hyperthermia Agents. *Small* **15**, 1902626 (2019).

[196] Mickoleit, F., Lanzloth, C. & Schüler, D. A Versatile Toolkit for Controllable and Highly Selective Multifunctionalization of Bacterial Magnetic Nanoparticles. *Small* **16**, 1906922 (2020).

[197] Chen, C., Chen, L., Wang, P., Wu, L.-F. & Song, T. Steering of magnetotactic bacterial microrobots by focusing magnetic field for targeted pathogen killing. *J. Magn. Magn. Mater.* **479**, 74–83 (2019).

[198] Khalil, I. S. M. & Misra, S. Chapter 4 - Control of magnetotactic bacteria. In Kim, M., Julius, A. A. & Cheang, U. K. (eds.) *Microbiorobotics*, Micro and Nano Technologies, 61–79 (Elsevier, 2017), 2 edn.

[199] Mishra, S. R., Dickey, M. D., Velev, O. D. & Tracy, J. B. Selective and directional actuation of elastomer films using chained magnetic nanoparticles. *Nanoscale* **8**, 1309–1313 (2016).

[200] Martel, S., Mohammadi, M., Felfoul, O., Lu, Z. & Pouponneau, P. Flagellated magnetotactic bacteria as controlled MRI-trackable propulsion and steering systems for medical nanorobots operating in the human microvasculature. *Int. J. Rob. Res.* **28**, 571–582 (2009).

[201] Jiang, X. *et al.* Bioinspired 1D Superparamagnetic Magnetite Arrays with Magnetic Field Perception. *Adv. Mater.* **28**, 6952–6958 (2016).

[202] Alphandéry, E., Faure, S., Seksek, O., Guyot, F. & Chebbi, I. Chains of magnetosomes extracted from AMB-1 magnetotactic bacteria for application in alternative magnetic field cancer therapy. *ACS Nano* **5**, 6279–6296 (2011).

[203] Ota, S. & Takemura, Y. Characterization of néel and brownian relaxations isolated from complex dynamics influenced by dipole interactions in magnetic nanoparticles. *J. Phys. Chem. C* **123**, 28859–28866 (2019).

[204] Usov, N. A. & Gubanova, E. M. Application of magnetosomes in magnetic hyperthermia. *Nanomaterials* **10**, 1320 (2020).

[205] Molcan, M. *et al.* Magnetic hyperthermia study of magnetosome chain systems in tissue-mimicking phantom. *J. Mol. Liq.* **320**, 114470 (2020).

[206] Mahmoudi, M. *et al.* Novel MRI contrast agent from magnetotactic bacteria enables in vivo tracking of ipsc-derived cardiomyocytes. *Sci. Rep.* **6** (2016).

[207] Harvell-Smith, S., Tung, L. D. & Thanh, N. T. K. Magnetic particle imaging: tracer development and the biomedical applications of a radiation-free, sensitive, and quantitative imaging modality. *Nanoscale* **14**, 3658–3697 (2022).

[208] Makela, A. V., Schott, M. A., Madsen, C. S., Greeson, E. M. & Contag, C. H. Magnetic particle imaging of magnetotactic bacteria as living contrast agents is improved by altering magnetosome arrangement. *Nano Lett.* **22**, 4630–4639 (2022).

[209] Li, L. *et al.* Magnetically induced magnetosome chain (MAGiC): A biogenic magnetic-particle-imaging tracer with high performance and navigability. *Sci. Adv.* **11** (2025).

[210] Kraupner, A. *et al.* Bacterial magnetosomes – nature's powerful contribution to MPI tracer research. *Nanoscale* **9**, 5788–5793 (2017).

[211] Schüler, D. Genetics and cell biology of magnetosome formation in magnetotactic bacteria. *FEMS Microbiol. Rev.* **32**, 654–672 (2008).

[212] Zheng, H. *et al.* Construction of Recombinant Magnetospirillum Strains for Nitrate Removal from Wastewater Based on Magnetic Adsorption. *Processes* **10**, 591 (2022).

[213] Zingsem, B. W. *et al.* Biologically encoded magnonics. *Nat. Commun.* **10**, 4345 (2019).

[214] Arató, B. *et al.* Crystal-size and shape distributions of magnetite from uncultured magnetotactic bacteria as a potential biomarker. *Am. Mineral.* **90**, 1233–1240 (2005).

[215] Thomas-Keprta, K. L. *et al.* Magnetofossils from Ancient Mars: a Robust Biosignature in the Martian Meteorite ALH84001. *Appl. Environ. Microbiol.* **68**, 3663–3672 (2002).

[216] Frankel, R. B. & Buseck, P. R. Magnetite biomineralization and ancient life on Mars. *Curr. Opin. Chem. Biol.* **4**, 171–176 (2000).

[217] Modic, K. A. *et al.* Resonant torsion magnetometry in anisotropic quantum materials. *Nat. Commun.* **9**, 3975 (2018).

[218] Blankenhorn, M. *et al.* Membrane-based torque magnetometer: Enhanced sensitivity by optical readout of the membrane displacement. *Review of Scientific Instruments* **88**, 094707 (2017).

[219] Moreland, J. Micromechanical instruments for ferromagnetic measurements. *Journal of Physics D: Applied Physics* **36**, R39–R51 (2003).

[220] Komori, K. *et al.* Attonewton-meter torque sensing with a macroscopic optomechanical torsion pendulum. *Phys. Rev. A* **101**, 011802 (2020).

[221] Cornia, A. *et al.* High-field torque magnetometry for investigating magnetic anisotropy in Mn_{12}-acetate nanomagnets. *J. Magn. Magn. Mater.* **226**, 2012–2014 (2001).

[222] Rugar, D., Mamin, H. J. & Guethner, P. Improved fiber-optic interferometer for atomic force microscopy. *Appl. Phys. Lett.* **55**, 2588–2590 (1989).

[223] Philipp, S. *Magnetism of Nano- to Micrometer-Sized Anisotropic Materials*. Phd thesis, University of Basel (2022).

[224] Mehlin, A. *Dynamic cantilever magnetometry of reversal processes and phase transitions in individual nanomagnets*. Phd thesis, University of Basel (2017).

[225] Buchter, A. *Hybrid Torque and SQUID Magnetometry of Individual Magnetic Nanotubes*. Phd thesis, University of Basel (2015).

[226] Weber, D. P. *Dynamic Cantilever Magnetometry of Individual Ferromagnetic Nanotubes*. Phd thesis, University of Basel (2014).

[227] Kamra, A., Schreier, M., Huebl, H. & Goennenwein, S. T. B. Theoretical model for torque differential magnetometry of single-domain magnets. *Phys. Rev. B* **89**, 184406 (2014).

[228] Gross, B. *et al.* Stability of Néel-type skyrmion lattice against oblique magnetic fields in GaV_4S_8 and GaV_4Se_8. *Phys. Rev. B* **102**, 104407 (2020).

[229] Geirhos, K. *et al.* Macroscopic manifestation of domain-wall magnetism and magnetoelectric effect in a néel-type skyrmion host. *npj Quantum Mater.* **5**, 44 (2020).

[230] Stipe, B. C., Mamin, H. J., Stowe, T. D., Kenny, T. W. & Rugar, D. Magnetic Dissipation and Fluctuations in Individual Nanomagnets Measured by Ultrasensitive Cantilever Magnetometry. *Phys. Rev. Lett.* **86**, 2874–2877 (2001).

[231] Vansteenkiste, A. & Van de Wiele, B. Mumax: a new high-performance micromagnetic simulation tool. *J. Magn. Magn. Mater.* **323**, 2585–2591 (2011).

[232] Vansteenkiste, A. *et al.* The design and verification of MuMax3. *AIP Adv.* **4**, 107133 (2014).

[233] Fischbacher, T., Franchin, M., Bordignon, G. & Fangohr, H. A systematic approach to multiphysics extensions of finite-element-based micromagnetic simulations: Nmag. *IEEE Trans. Magn.* **43**, 2896–2898 (2007).

[234] Rossi, N., Gross, B., Dirnberger, F., Bougeard, D. & Poggio, M. Magnetic force sensing using a self-assembled nanowire. *Nano Lett.* **19**, 930–936 (2019).

[235] Moser, J. *et al.* Ultrasensitive force detection with a nanotube mechanical resonator. *Nat. Nanotechnol.* **8**, 493–496 (2013).

[236] Braakman, F. R. & Poggio, M. Force sensing with nanowire cantilevers. *Nanotechnology* **30**, 332001 (2019).

[237] Enzian, G. *et al.* Phononically shielded photonic-crystal mirror membranes for cavity quantum optomechanics. *Opt. Express* **31**, 13040–13052 (2023).

[238] Planz, E., Xi, X., Capelle, T., Langman, E. C. & Schliesser, A. Membrane-in-the-middle optomechanics with a soft-clamped membrane at millikelvin temperatures. *Opt. Express* **31**, 41773–41782 (2023).

[239] Gisler, T. *et al.* Enhancing membrane-based scanning force microscopy through an optical cavity. *Phys. Rev. Applied* **22** (2024).

[240] Fogliano, F. *et al.* Ultrasensitive nano-optomechanical force sensor operated at dilution temperatures. *Nat. Commun.* **12**, 4124 (2021).

[241] Košata, J., Zilberberg, O., Degen, C. L., Chitra, R. & Eichler, A. Spin detection via parametric frequency conversion in a membrane resonator. *Phys. Rev. Applied* **14**, 014042 (2020).

[242] Fischer, R. *et al.* Spin detection with a micromechanical trampoline: towards magnetic resonance microscopy harnessing cavity optomechanics. *New J. Phys.* **21**, 043049 (2019).

[243] Adams, A. C. Silicon nitride and other insulator films. In Mort, J. & Jansen, F. (eds.) *Plasma Deposited Thin Films*, chap. 5 (CRC Press, Boca Raton, Florida, 1986). URL `https://doi.org/10.1201/9781351075817`.

[244] Williams, K. R., Gupta, K. & Wasilik, M. Etch rates for micromachining processing—part II. *J. Microelectromech. Syst.* **12**, 761–778 (2003).

[245] Kovacs, G. T. A., Maluf, N. I. & Petersen, K. E. Bulk micromachining of silicon. *Proc. IEEE* **86**, 1536–1551 (1998).

[246] Han, J., Yin, Y. J., Han, D. & Dong, L. Improved PECVD SixNy film as a mask layer for deep wet etching of the silicon. *Mater. Res. Express* **4**, 096301 (2017).

[247] Mikolajūnas, M. *et al.* A study of stacked PECVD silicon nitride films used for surface micromachined membranes. *Thin Solid Films* **516**, 8788–8792 (2008).

[248] Rasmussen, F., Geilman, B., Heschel, M., Hansen, O. & Jørgensen, A. Development and characterisation of KOH resistant PECVD silicon nitride for microsystems applications. In *Proceedings of the International Symposium on Dielectrics in Emerging Technologies*, vol. 2003-01 of *Proc. Electrochem. Soc.* (The Electrochemical Society, Pennington, NJ, 2003).

[249] de Vito, G. *Four terminal devices for anisotropic thermal transport experiments.* Phd thesis, University of Basel (2024).

[250] Kim, E. S., Muller, R. S. & Hijab, R. S. Front-to-backside alignment using resist-patterned etch control and one etching step. *J. Microelectromech. Syst.* **1**, 95–99 (1992).

[251] Zhang, X. G. *Electrochemistry of silicon and its oxide* (Springer New York, NY, 2001), 1 edn.

[252] Tan, S., Boudreau, R. & Reed, M. L. Anisotropic etching of silicon on {111} and near {111} planes. *Sens. Mater.* **13**, 303–313 (2001).

[253] Kashkoush, I., Rieker, J., Chen, G. & Nemeth, D. Process control challenges of wet etching large MEMS Si cavities. *Solid State Phenom.* **219**, 73–77 (2014).

[254] Pal, P. *et al.* High speed silicon wet anisotropic etching for applications in bulk micromachining: a review. *Micro Nano Syst. Lett.* **9**, 4 (2021).

[255] Yusof, N., Bais, B., Majlis, B. Y., Soin, N. & Yunas, J. Optimization of KOH etching process for MEMS square diaphragm using response surface method. *Indones. J. Electr. Eng. Comput. Sci.* **15**, 113–121 (2019).

[256] Seidel, H., Csepregi, L., Heuberger, A. & Baumgärtel, H. Anisotropic etching of crystalline silicon in alkaline solutions: I. orientation dependence and behavior of passivation layers. *J. Electrochem. Soc.* **137**, 3612–3626 (1990).

[257] Gosalvez, M. A., Nieminen, R., Kilpinen, P., Haimi, E. & Lindroos, V. K. Anisotropic wet chemical etching of crystalline silicon: atomistic monte-carlo simulations and experiments. *Appl. Surf. Sci.* **178**, 7–26 (2001).

[258] Karanassios, V. & Mew, G. Anisotropic wet chemical etching of si for chemical analysis applications. *Sens. Mater.* **9**, 395–416 (1997).

[259] Sato, K. *et al.* Characterization of orientation-dependent etching properties of single-crystal silicon: effects of KOH concentration. *Sens. Actuators A Phys.* **64**, 87–93 (1998).

[260] Laidler, K. J. *Chemical Kinetics* (Harper & Row, 1987), 3 edn.

[261] Palik, E. D., Glembocki, O. J., Heard, I., Bruno, P. S. & Tenerz, L. Etching roughness for (100) silicon surfaces in aqueous KOH. *J. Appl. Phys.* **70**, 3291 (1991).

[262] Kleptsyn, V. F. & Smits, J. G. Temperature dependent etching of (100) and (110) silicon in NaOH and in Tetramethyl-Ammonium Hydroxide. *Sens. Mater.* **14**, 415–428 (2002).

[263] Leva, C. V. *et al.* Localized nanopore fabrication in silicon nitride membranes by femtosecond laser exposure and subsequent controlled breakdown. *ACS Appl. Mater. Interfaces* **17**, 8737–8748 (2025).

[264] Yue, S. & Gu, C. Nanopores fabricated by focused ion beam milling technology. In *Proceedings of the 7th IEEE Conference on Nanotechnology (IEEE-NANO)* (IEEE, 2007).

[265] Zainal Ariffin, N. H., Yahaya, H., Shinano, S., Tanaka, S. & Hashim, A. M. Fabrication of conical micropore structure on silicon nitride/silicon using focused ion beam milling for biosensor application. *Microelectron. Eng.* **133**, 1–5 (2015).

[266] Sugiyama, M., Nakanishi, N. & Shiojiri, M. A review of focused ion beam technology and its applications in transmission electron microscopy. *J. Electron Microsc. (Tokyo)* **53**, 527–536 (2004).

[267] Müller, A. *et al.* Detailed investigation of silicon nitride phase plates prepared by focused ion beam milling. *Microsc. Microanal.* **25**, 900–901 (2019).

[268] Peltonen, A., Nguyen, H. Q., Muhonen, J. T. & Pekola, J. P. Milling a silicon nitride membrane by focused ion beam. *J. Vac. Sci. Technol. B* **34**, 062201–(6) (2016).

[269] Novoselov, K. S. *et al.* Two-dimensional atomic crystals. *Proc. Natl. Acad. Sci. U.S.A.* **102**, 10451–10453 (2005).

[270] Onodera, M. & Machida, T. Transfer of van der waals heterostructures of two-dimensional materials onto microelectromechanical systems. *Sens. Mater.* **35**, 1929–1939 (2023).

[271] Purdie, D. G. *et al.* Cleaning interfaces in layered materials heterostructures. *Nat. Commun.* **9**, 5387 (2018).

[272] Zhao, Q., Wang, T., Ryu, Y. K., Frisenda, R. & Castellanos-Gomez, A. An inexpensive system for the deterministic transfer of 2d materials. *J. Phys.: Mater.* **3**, 016001 (2020).

[273] Shcherbakov, D. *et al.* Raman spectroscopy, photocatalytic degradation, and stabilization of atomically thin chromium tri-iodide. *Nano Lett.* **18**, 4214–4219 (2018).

[274] Doganov, R. A. *et al.* Transport properties of pristine few-layer black phosphorus by van der Waals passivation in an inert atmosphere. *Nat. Commun.* **6**, 6647 (2015).

[275] Spinnler, C. *et al.* A single-photon emitter coupled to a phononic-crystal resonator in the resolved-sideband regime. *Nat. Commun.* **15**, 9509 (2024).

[276] Spinnler, C. *Exploiting Phonon and Coulomb Interactions in Semiconductor Quantum Dots*. Phd thesis, University of Basel (2023).

[277] Klaß, Y. S. *High Q Nanomechanical Resonators Fabricated from Crystalline Silicon Carbide*. Phd thesis, Technische Universität München, München (2022).

[278] Gisler, T. *et al.* Soft-clamped silicon nitride string resonators at millikelvin temperatures. *Phys. Rev. Lett.* **129**, 104301 (2022).

[279] Morell, N. *et al.* High quality factor mechanical resonators based on WSe_2 monolayers. *Nano Lett.* **16**, 5102–5108 (2016).

[280] Pan, H.-W. *et al.* Silicon nitride films fabricated by a plasma-enhanced chemical vapor deposition method for coatings of the laser interferometer gravitational wave detector. *Phys. Rev. D* **97**, 022004 (2018).

[281] Ramos, D., Tamayo, J., Mertens, J. & Calleja, M. Photothermal excitation of microcantilevers in liquids. *J. Appl. Phys.* **99**, 124904 (2006).

[282] Popp, F., Armitage, J. P. & Schüler, D. Polarity of bacterial magnetotaxis is controlled by aerotaxis through a common sensory pathway. *Nat. Commun.* **5**, 5398 (2014).

[283] Frankel, R. B., Bazylinski, D. A., Johnson, M. S. & Taylor, B. L. Magneto-aerotaxis in marine coccoid bacteria. *Biophys. J.* **73**, 994–1000 (2018).

[284] Schüler, D. The biomineralization of magnetosomes in *Magnetospirillum gryphiswaldense*. *Int. Microbiol.* **5**, 209–214 (2002).

[285] Frankel, R. B. Magnetic Guidance of Organisms. *Annu. Rev. Biophys. Bioeng.* **13**, 85–103 (1984).

[286] Kalmijn, A. Biophysics of geomagnetic field detection. *IEEE Trans. Magn.* **17**, 1113–1124 (1981).

[287] Zhu, X. *et al.* Angle sensing in magnetotaxis of Magnetospirillum magneticum AMB-1. *Integr. Biol.* **6**, 706–713 (2014).

[288] Klumpp, S. & Faivre, D. Magnetotactic bacteria. *Eur. Phys. J.: Spec. Top.* **225**, 2173–2188 (2016).

[289] Klumpp, S., Lefèvre, C. T., Bennet, M. & Faivre, D. Swimming with magnets: From biological organisms to synthetic devices. *Phys. Rep.* **789**, 1–54 (2019).

[290] Mohammadinejad, S., Faivre, D. & Klumpp, S. Stokesian dynamics simulations of a magnetotactic bacterium. *Eur. Phys. J. E* **44**, 40 (2021).

[291] Codutti, A. *et al.* Interplay of surface interaction and magnetic torque in single-cell motion of magnetotactic bacteria in microfluidic confinement. *eLife* **11**, e71527 (2022).

[292] Zahn, C. *et al.* Measurement of the magnetic moment of single Magnetospirillum gryphiswaldense cells by magnetic tweezers. *Sci. Rep.* **7**, 3558 (2017).

[293] Reufer, M. *et al.* Switching of Swimming Modes in Magnetospirillium gryphiswaldense. *Biophys. J.* **106**, 37–46 (2014).

[294] Le Sage, D. *et al.* Optical magnetic imaging of living cells. *Nature* **496**, 486–489 (2013).

[295] Nadkarni, R., Barkley, S. & Fradin, C. A Comparison of Methods to Measure the Magnetic Moment of Magnetotactic Bacteria through Analysis of Their Trajectories in External Magnetic Fields. *PLOS ONE* **8**, e82064 (2013).

[296] Bahaj, A., James, P. & Moeschler, F. An alternative method for the estimation of the magnetic moment of non-spherical magnetotactic bacteria. *IEEE Trans. Magn.* **32**, 5133–5135 (1996).

[297] Chemla, Y. R. *et al.* A New Study of Bacterial Motion: Superconducting Quantum Interference Device Microscopy of Magnetotactic Bacteria. *Biophys. J.* **76**, 3323–3330 (1999).

[298] Prozorov, R. *et al.* Magnetic irreversibility and the Verwey transition in nanocrystalline bacterial magnetite. *Phys. Rev. B* **76**, 054406 (2007).

[299] Lam, K. P. *et al.* Characterizing magnetism of individual magnetosomes by X-ray magnetic circular dichroism in a scanning transmission X-ray microscope. *Chem. Geol.* **270**, 110–116 (2010).

[300] Marcano, L. *et al.* Magnetic Anisotropy of Individual Nanomagnets Embedded in Biological Systems Determined by Axi-asymmetric X-ray Transmission Microscopy. *ACS Nano* **16**, 7398–7408 (2022).

[301] Kalirai, S. S., Lam, K. P., Bazylinski, D. A., Lins, U. & Hitchcock, A. P. Examining the chemistry and magnetism of magnetotactic bacterium Candidatus Magnetovibrio blakemorei strain MV-1 using scanning transmission X-ray microscopy. *Chem. Geol.* **300-301**, 14–23 (2012).

[302] Kalirai, S. S., Bazylinski, D. A. & Hitchcock, A. P. Anomalous Magnetic Orientations of Magnetosome Chains in a Magnetotactic Bacterium: Magnetovibrio blakemorei Strain MV-1. *PLOS ONE* **8**, e53368 (2013).

[303] Staniland, S., Ward, B., Harrison, A., van der Laan, G. & Telling, N. Rapid magnetosome formation shown by real-time x-ray magnetic circular dichroism. *Proc. Natl. Acad. Sci. U.S.A* **104**, 19524–19528 (2007).

[304] Dunin-Borkowski, R. E. *et al.* Magnetic Microstructure of Magnetotactic Bacteria by Electron Holography. *Science* **282**, 1868–1870 (1998).

[305] Wasem, M. *Atomic Force Microscopy of Nanoparticles and Biological Cells.* Phd thesis, University of Basel (2015).

[306] Orue, I. *et al.* Configuration of the magnetosome chain: a natural magnetic nanoarchitecture. *Nanoscale* **10**, 7407–7419 (2018).

[307] Rossel, C. *et al.* Active microlevers as miniature torque magnetometers. *J. Appl. Phys* **79**, 8166–8173 (1996).

[308] Harris, J. G. E. *et al.* Integrated micromechanical cantilever magnetometry of Ga1-xMnxAs. *Appl. Phys. Lett.* **75**, 1140–1142 (1999).

[309] Gysin, U. *et al.* Magnetic properties of nanomagnetic and biomagnetic systems analyzed using cantilever magnetometry. *Nanotechnology* **22**, 285715 (2011).

[310] Heyen, U. & Schüler, D. Growth and magnetosome formation by microaerophilic Magnetospirillum strains in an oxygen-controlled fermentor. *Appl. Microbiol. Biotechnol.* **61**, 536–544 (2003).

[311] Li, Y., Katzmann, E., Borg, S. & Schüler, D. The Periplasmic Nitrate Reductase Nap Is Required for Anaerobic Growth and Involved in Redox Control of Magnetite Biomineralization in Magnetospirillum gryphiswaldense. *J. Bacteriol.* **194**, 4847–4856 (2012).

[312] Liu, Y.-T. *et al.* Isotropic reconstruction for electron tomography with deep learning. *Nat. Commun.* **13**, 6482 (2022).

[313] Gandia, D. *et al.* Elucidating the role of shape anisotropy in faceted magnetic nanoparticles using biogenic magnetosomes as a model. *Nanoscale* **12**, 16081–16090 (2020).

[314] Ó Conbhuí, P. *et al.* MERRILL: Micromagnetic Earth Related Robust Interpreted Language Laboratory. *Geochem. Geophys. Geosyst* **19**, 1080–1106 (2018).

[315] Exl, L. *et al.* LaBonte's method revisited: An effective steepest descent method for micromagnetic energy minimization. *J. Appl. Phys* **115**, 17D118 (2014).

[316] Körnig, A. *et al.* Magnetite Crystal Orientation in Magnetosome Chains. *Adv. Funct. Mater.* **24**, 3926–3932 (2014).

[317] Mann, S., Frankel, R. B. & Blakemore, R. P. Structure, morphology and crystal growth of bacterial magnetite. *Nature* **310**, 405–407 (1984).

[318] Jaeger, D. *et al.* Mechanical mode imaging of a high-Q hybrid hBN/Si_3N_4 resonator. *Nano Lett.* **23**, 2016–2022 (2023).

[319] Forrer, L., Kamber, A., Knoll, A. W., Poggio, M. & Braakman, F. R. Electron-beam lithography of nanostructures at the tips of scanning probe cantilevers. *AIP Adv.* **13**, 035208 (2023).

Tools

[1] **ChatGPT (OpenAI), model GPT-5.2** (https://chatgpt.com; accessed January 19, 2026).

Used for language assistance (suggesting synonyms, clearer wording, and improving readability), grammar and spell checking, drafting and refining definitions/explanatory text, and supporting literature discovery (e.g., proposing search terms and potentially relevant papers).

Not used to generate data or produce scientific claims. All AI-assisted content was reviewed by the author; factual statements were checked against primary sources and are cited where appropriate.

[2] **DeepL Translate (DeepL SE)** (https://www.deepl.com; accessed January 19, 2026).

Used for translation support. All translations were reviewed and edited by the author for technical accuracy and consistency.

Acknowledgements

First and foremost, I am grateful to Martino Poggio for giving me the opportunity to pursue a PhD in the field of nanomechanical sensing and nanomagnetism under his supervision. It has been a great pleasure working in his research group, and I sincerely appreciate the scientific freedom he granted me, as well as his encouragement to follow my own curiosity. I would also like to thank Ilaria Zardo for serving as my second supervisor and for providing the resources that allowed me to learn and immerse myself in the art of micro- and nanofabrication of MEMS devices. Furthermore, I thank Alexander Eichler for agreeing to act as the external referee of this thesis, and I am pleased to have him on my defense committee.

I wish to thank Boris Gross, who has been my closest mentor throughout my PhD. He provided invaluable guidance and has been a constant source of inspiration—not only through his remarkable ability to solve problems and develop new ideas, but also through his calm and constructive approach when things did not go as planned. His support with the characterization and simulation of the mechanical and magnetic properties of our samples was indispensable to this thesis.

I would also like to thank Yashpreet Kaur and Simon Philipp. Yashpreet introduced me to micro- and nanofabrication, and without the skills she taught me, I would not have been able to fabricate the devices studied in this work. Simon introduced me to dynamic torque magnetometry, trained me on the DCM setup, and supported the characterization of our first torsional resonator. Thank you both for preparing me so well for this PhD journey.

I would also like to acknowledge collaborators not mentioned above who contributed to our study of the magnetic properties of *M. gryphiswaldense*, in particular Marcus Wyss and Dirk Schüler. I am especially grateful to Marcus also for the many hours he spent, teaching me how to operate the FIB.

I also thank Patrick Maletinsky for granting me access to his glovebox facilities. Special thanks go to Märta Tschudin, who introduced me to the system and taught me how to work with it.

Moreover, I thank Lukas Schneider and Aris Lafranca for introducing me to the nanowire MFM setup, and I thank Francesco Fogliano for his assistance with mode imaging and many other tasks.

I gratefully acknowledge the SNI PhD School, funded by the Canton of Aargau, for supporting my PhD project. I particularly thank Andreas Baumgartner for organizing the *Nano in the Snow* winter schools and other training events. Special thanks go to Claudia Wirth for her exceptional work as managing director of SNI and for her indispensable help with accounting during the organization of the International Nanoscience Student Conference (INASCON) 2023.

I would also like to thank all former and current members of the PoggioLab and the Nanophononics research groups whom I had the pleasure of working with or interacting with during these years.

On a personal note, my heartfelt thanks go to my family, and in particular, I thank my parents Erna and Ulrich Claus. Your constant encouragement and unbroken belief in me throughout all these years is by no means something I take for granted, and it means more to me than words can say.

Last, but most importantly, I am deeply grateful to Nadia Antoniadis. Your unwavering support, patience, and encouragement throughout these years have been the bedrock of this achievement. You were there during my most stressful and difficult moments to cheer me up and put a smile back on my face. You were also there in my happiest and most joyful moments, and sharing them with you has meant everything to me. I could not have done this without you. Because of you, the future looks bright.

List of publications

- S. Philipp, B. Gross, M. Reginka, M. Merkel, M. M. Claus, M. Sulliger, A. Ehresmann, M. Poggio, Magnetic hysteresis of individual Janus particles with hemispherical exchange biased caps, *Appl. Phys. Lett.* **119**, 222406 (2021)

- M. M. Claus, M. Wyss. D. Schüler, M. Poggio, B. Gross, Magnetic properties of an individual Magnetospirillum gryphiswaldense cell, *Phys. Rev. E* **113**, 014408 (2026)